1-1-2017

New Particle Formation in the Mid-Latitude Upper Troposphere

Duncan Axisa
University of Denver

New Particle Formation in the Mid-Latitude Upper Troposphere

_____

A Dissertation

Presented to

the Faculty of the Daniel Felix Ritchie School of Engineering and Computer Science

University of Denver

_____

In Partial Fulfillment

of the Requirements for the Degree

Doctor of Philosophy

_____

by

Duncan Axisa

June 2017

Advisor: Prof. James C. Wilson

Author: Duncan Axisa
Title: New Particle Formation in the Mid-Latitude Upper Troposphere
Advisor: Prof. James C. Wilson
Degree Date: June 2017

Abstract

Primary aerosol production due to new particle formation (NPF) in the upper troposphere and the impact that this might have on cloud condensation nuclei (CCN) concentration can be of sufficient magnitude to contribute to the uncertainty in radiative forcing. This uncertainty affects our ability to estimate how sensitive the climate is to greenhouse gas emissions. Therefore, new particle formation must be accurately defined, parametrized and accounted for in models.

This research involved the deployment of instruments, data analysis and interpretation of particle formation events during the Mid-latitude Airborne Cirrus Properties Experiment (MACPEX) campaign. The approach combined field measurements and observations with extensive data analysis and modeling to study the process of new particle formation and growth to CCN active sizes. Simultaneous measurements of O_3, CO, ultrafine aerosol particles and surface area from a high-altitude research aircraft were used to study tropospheric-stratospheric mixing as well as the frequency and location of NPF. It was found that the upper troposphere was an active region in the production of new particles by gas-to-particle conversion, that nucleation was triggered by convective clouds and mixing processes, and that NPF occurred in regions with high relative humidity and low surface area. In certain cases, mesoscale and

synoptic features enhanced mixing and facilitated the formation of new particles in the northern mid-latitudes.

A modeling study of particle growth and CCN formation was done based on measured aerosol size distributions and modeled growth. The results indicate that when SO_2 is of sufficient concentration NPF is a significant source of potential CCN in the upper troposphere. In conditions where convective cloud outflow eject high concentrations of SO_2, a large number of new particles can form especially in the instance when the preexisting surface area is low. The fast growth of nucleated clusters produces a particle mode that becomes CCN active within 24-hours.

Table of Contents

List of Tables

List of Figures

Chapter One: Introduction

1.1 Background

Aerosol particles form part of the atmosphere, the water cycle, and the atmospheric radiation budget. Aerosols particles are liquid or solid and suspended in air. They affect the global energy budget both directly by scatterinrg of radiation and indirectly by acting as cloud condensation nuclei (CCN). Aerosols scatter and absorb solar radiation (direct effect) and change the microphysical structure, lifetime, and coverage of clouds (indirect effect). An increase in aerosol concentration leads to cloud droplets of a smaller size and higher droplet concentration and thereby an increase in cloud albedo (first aerosol indirect effect (Twomey, 1977)). The smaller cloud droplets have lower collection efficiencies and delay the formation of drizzle and precipitation, leading to an increase in cloud coverage (aerosol second indirect effect (Albrecht, 1989)). An aerosol-induced decrease in cloud droplet radius delays the formation of warm rain (Rosenfeld et al., 2014) and increases the concentration of supercooled drops in deep convective clouds, which could lead to changes in the distribution of hydrometeors, precipitation type and intensity (Ilotoviz et al., 2016). Accounting for all these aerosol effects can result in rain suppression (Rosenfeld et al., 2008) as well as a slower hydrological cycle (Ramanathan et al., 2001).

The Fifth Assessment Report of the Intergovernmental Panel on Climate Change (IPCC) states, in its summary for policy makers, that "there is high confidence that aerosols and their interactions with clouds have offset a substantial portion of global mean forcing from well-mixed greenhouse gases" and that climate change projections "require information about future emissions or concentrations of greenhouse gases, aerosols and other climate drivers" (Stocker et al., 2013). Figure 1.1 shows the global averaged radiative forcing (RF) partitioned by emissions and drivers. The largest contribution to total radiative forcing is caused by the increase in the atmospheric concentration of CO_2. The largest uncertainty in RF is due to aerosol-cloud interactions, and the magnitude in RF for aerosol species (net cooling) are about as large as the heating effects of greenhouse gases. This uncertainty affects our ability to estimate how sensitive the climate is to greenhouse gas emissions. Climate models now include aerosol-cloud interaction processes, but the low confidence in the representation and quantification of these processes remains.

Aerosol-cloud interaction processes are complex, and the radiative forcing that relates to each of these processes can vary in magnitude. As shown in Figure 1.1, the physical and chemical processes that contribute to the RF attributed to "cloud adjustments due to aerosols" has an uncertainty that varies from -1.33 to - 0.06 W m^{-2}. This dissertation is concerned with primary aerosol production due to new particle formation in the upper troposphere and the impact that this might have on CCN concentration. Specifically, this research was motivated by the need to make a

quantitative link between in-situ aerosol production (or new particle formation) and aerosol-cloud interactions as a climate driver.

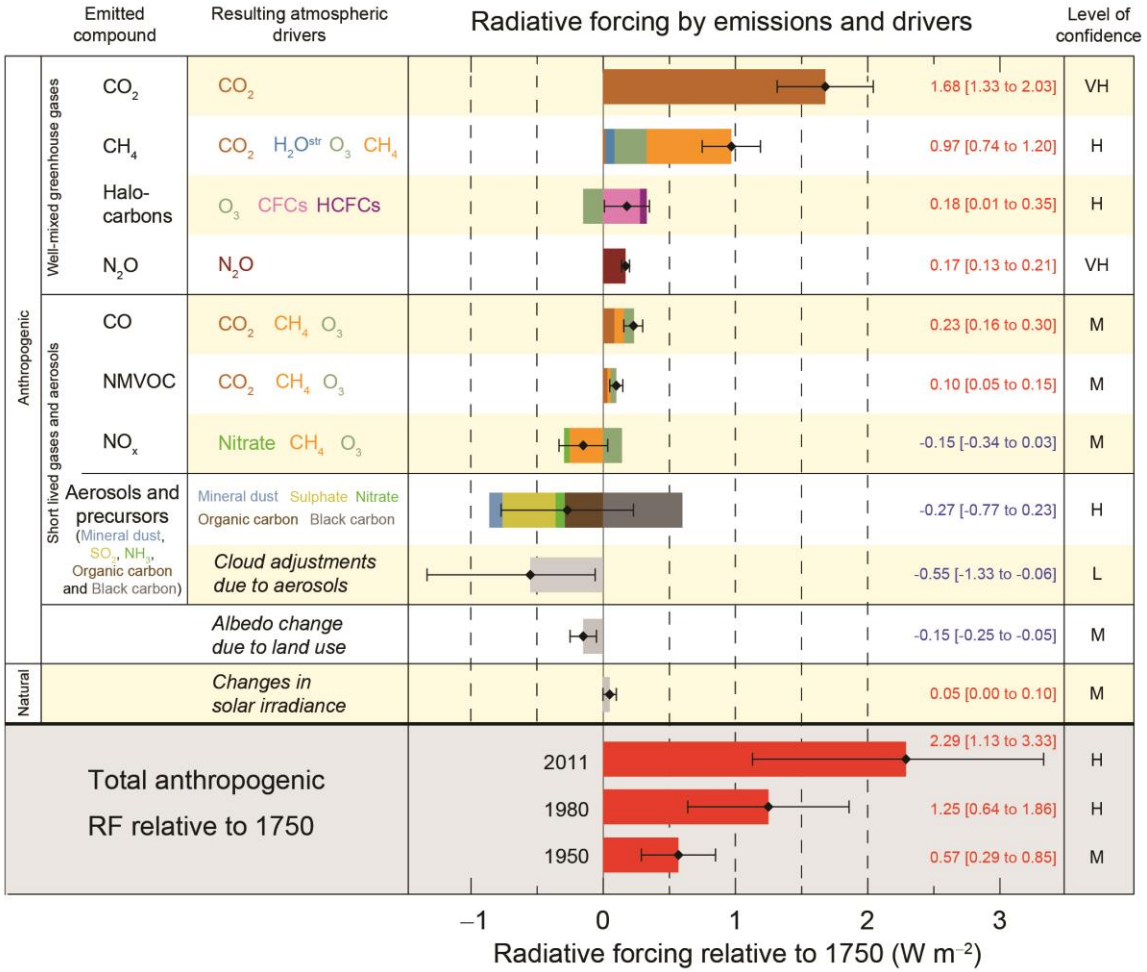

Figure 1.1. Global averaged radiative forcing (RF) partitioned by emissions and drivers. The best estimates of the net RF are shown as black diamonds with corresponding uncertainty interval. The size of the bar indicates the magnitude of RF of climate over the industrial period (relative to the year 1750).

Source: Stocker, T. F., Qin, D., Plattner, G. K., Tignor, M., Allen, S. K., Boschung, J., … & Midgley, P. M. (2013). IPCC, 2013: Summary for policymakers in climate change 2013: the physical science basis, contribution of working group I to the fifth assessment report of the intergovernmental panel on climate change.

In-situ aerosol production is a process where new particles form through gas to particle conversion. New particles form through oxidation of precursor gases to form

condensable species which condense to form particles. This is often referred to as new particle formation (NPF), a process that modifies the size distribution of airborne particles, which in turn changes the direct and indirect effect of aerosols. Aerosols have a direct radiative effect because they scatter and absorb solar and infrared radiation in the atmosphere. In general, Mie theory suggests that the light scattering of solar radiation depends on several factors including particle size, chemical composition (i.e. refractive index), and density. Therefore, to estimate the aerosol direct effect the aerosol size distribution and chemical composition must be accurately measured. Overall, IPCC estimates, with a medium to high level of confidence, that the total direct aerosol RF is -0.27 with an uncertainty that varies from -0.77 to 0.23 W m^{-2}. The uncertainty is related to the different scattering and absorbing properties of aerosol types; the optical properties of an aerosol of known aerosol composition are well constrained.

The aerosol effects on clouds and precipitation, or the indirect effects, are much more complex. Penner et al. (2001) describe the aerosol indirect effect as a series of processes linking various intermediate variables such as aerosol mass, CCN concentration, ice nuclei (IN) concentration, cloud hydrometeor type, concentration and size, and precipitation. A schematic of the processes involved that link aerosol mass to precipitation, cloud lifetime, cloud albedo and cloud optical depth is shown in Figure 1.2. Rather than discussing all the processes in Figure 1.2, it is most appropriate to link NPF with earth radiation budget, as this is most relevant for this dissertation. In the absence of primary aerosol emissions from land or ocean (e.g. in the upper troposphere), the key processes controlling aerosol number concentration are NPF from vapor precursors,

condensational growth, coagulation, and deposition. The evolution of the size distribution largely depends on these processes and may lead to an increase in aerosol number. Increases in aerosol number increase the concentration of background aerosol and contribute to the number of CCN that form cloud droplets (Kulmala et al., 2004). The effectiveness of an aerosol particle as a CCN depends on its size, chemical composition and in-cloud supersaturation (Dusek et al., 2006). Supersaturation in warm clouds depends on the microphysical and dynamical structure of the cloud environment and is initially dependent on the vertical velocity within the cloud. The resulting supersaturation often remains below 1% (Pruppacher and Klett, 1997). A modification in cloud droplet number and size by the introduction of additional CCN results in changes in cloud hydrometeor phase, type, concentration and size which effects precipitation phase and amount. As a consequence, the aerosol indirect effect has an impact on the optical properties and microphysical processes of clouds, inducing various feedback processes in clouds and precipitation. Therefore, one of the central challenges in climate assessment is to accurately describe the processes and spatial distribution of aerosols, including NPF, and its impact on CCN number.

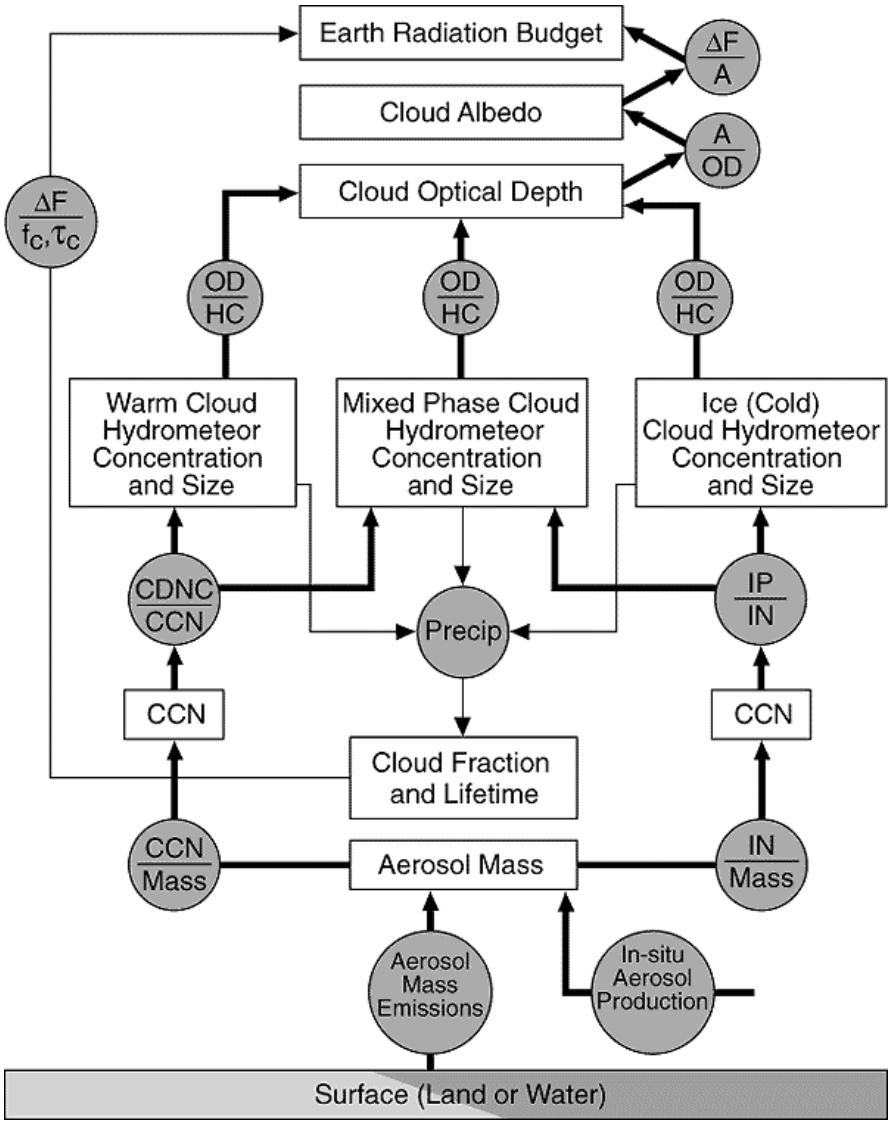

Figure 1.2. Flowchart showing processes linking aerosol emissions or production with changes in cloud optical depth and radiative forcing. Bars indicate the functional dependence of the quantity on top of the bar to that under the bar. Acronyms: CCN (cloud condensation nuclei); CDNC (cloud droplet number concentration); IN (ice nuclei); IP (ice particles); OD (optical depth); HC (hydrometeor concentration); A (albedo); f_c (cloud fraction); τ_c (cloud optical depth); ΔF (radiative forcing).

Source: Penner, J. E. and co-authors, 2001: Aerosols, their Direct and Indirect Effects. In Climate Change 2001: The Scientific Basis, Contribution of Working Group I to the Third Assessment Report of the Intergovernmental Panel on Climate Change, Cambridge, UK: Cambridge University Press, 289-348.

1.2 Aerosol Properties

Before discussing new particle formation and growth, it is important first to summarize aerosol size definitions and sources. Hinds (1999) defines an aerosol as "a collection of solid or liquid particles suspended in a gas." By definition, aerosols include particles that we refer to as smoke, soot, dust, smog, fog, mist and even clouds. Aerosol particles vary considerably in size, concentration, source, chemical composition, lifetime and distribution spatially and temporally. It is common practice to distinguish between aerosol and cloud, where clouds are considered to be a subset of aerosols that are composed of water. Aerosol diameters span over four orders of magnitude from a few nanometers to around 100 μm. Cloud particles that are suspended in the atmosphere can reach diameters of several centimeters. Primary atmospheric aerosols are particulates that are emitted directly into the atmosphere. Examples of primary aerosols are dust, sea salt, plant emissions, volcanic ash, smoke, and soot. Secondary atmospheric aerosols are particulates that form in the atmosphere by gas-to-particle conversion. For example, sulfates and nitrates are formed by gas-to-particle conversion. Once in the atmosphere, aerosols evolve in space and time as they may be transported with the atmospheric flow, removed by dry deposition, precipitation, clouds and gravitational sedimentation. Aerosols can change their size and composition due to physical and chemical transformation processes. Physical transformations involve nucleation, condensation, coagulation, and evaporation.

Aerosol nucleation is a process by which precursor gas condensable molecules aggregate together to form a molecular cluster. When the number of molecules inside the

cluster reaches a critical size, the cluster becomes stable and can grow larger by condensation (of additional molecules) into a nanoparticle. Homogeneous nucleation occurs when the gas nucleates without the aid of a surface while heterogeneous nucleation involves an existing surface such as a preexisting particle. Coagulation is a process by which particles collide and stick together to form a larger aerosol. An idealized schematic of the distribution of particulate matter and illustrations of their formation mechanisms and abundance is summarized in Figure 1.3. The concentration of nanoparticles is greatly affected by environmental conditions and depends strongly on the intensity of emission and the rate of formation.

Newly formed particles form part of the total aerosol size distribution. Size distributions describe the differences in number, surface area and volume as a function of size. A classic method used to simplify aerosol size distributions is that in which distributions are fit to three log-normal functions. Each of these functions describe three modes; “nuclei”, “accumulation”, and “coarse”, roughly corresponding to the size ranges below 0.1 μm, 0.1 to 1 μm, and above 1 μm, respectively (Whitby, 1978). An additional Aitken particle mode is identified between the nucleation and the accumulation particle modes. Four log-normal functions, three in the sub-micrometer range and one in the super-micron range, are often required to fit the entire size distribution. Each size mode has distinctive transformation mechanisms and deposition pathways (Seinfeld and Pandis, 1998). The largest number of aerosols are found in the smallest size range and the nucleation mode. Their surface to volume ratio is high, but their total surface area and volume is small when compared to the accumulation and coarse mode (Buseck and

Adachi, 2008). Overlapping with the nucleation mode are particles in the Aitken mode. The latter form by coagulation and condensation of nucleation mode particles. The accumulation and coarse modes make up the remainder of the size distribution. They contribute a significant volume and mass to the total aerosol and are critical in the formation of CCN because of their larger size.

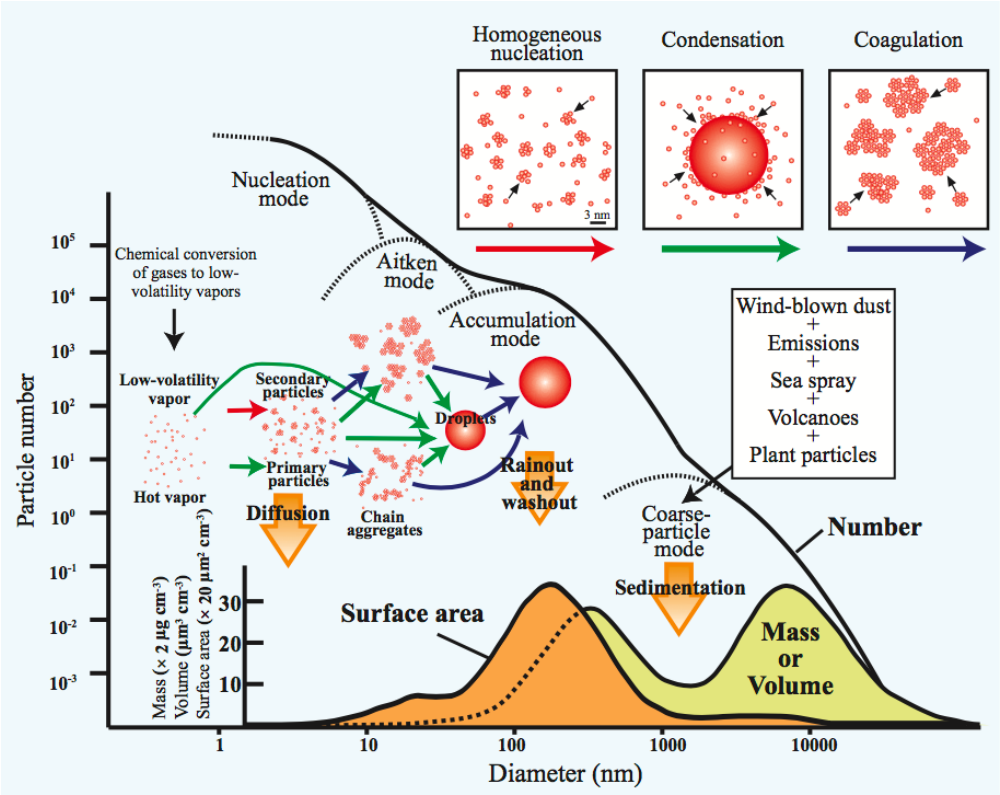

Figure 1.3. Schematic of the size distribution of aerosol particles for various parameters in an idealized atmospheric sample, together with illustrations of their formation mechanisms. The number, surface area, volume, and mass distributions, as well as the principal modes, sources, and particle formation and removal mechanisms, are adapted from Whitby (1978).

Source: Buseck, P. R. & Adachi, K. (2008). Nanoparticles in the atmosphere. Elements, 4(6), 389-394.

The atmospheric lifetimes of nanoparticles can be short. Frequent replacement by active nucleation processes means that the concentration of nanoparticles can be significant. Lifetimes can range from a few minutes to a few days, depending on their size and concentration (Anastasio and Martin, 2001). In general, smaller particles have a shorter lifetime as coagulation, and condensational growth removes them.

1.3 State of Knowledge of New Particle Formation in the Upper Troposphere

Aerosol nucleation from gas phase species is a source of particles. Freshly nucleated particles measure a few nanometers in diameter and their activity as CCN will depend on successful growth pathways to larger sizes of tens of nanometers. CCN formation will only occur if the aerosol is large enough and if the aerosol composition contains some soluble fraction. While CCN production associated with NPF is frequently observed in the continental boundary layer (Weber et al., 1997; Kulmala et al., 2005), NPF also occurs in the free and upper troposphere (Brock et al., 1995; Lee at al., 2003).

In classical theory, new aerosol particles are believed to form by the nucleation of water vapor in the presence of gaseous sulfuric acid and possibly other species (e.g., ammonia, halogens, ions and organics). Sulfuric acid is important in aerosol nucleation due to its low vapor pressure especially in cold temperatures (Hanson and Lovejoy, 2006). Laboratory experiments show that nucleation of sulfuric acid vapor is considerably enhanced in the presence of aromatic acids (Zhang et al., 2004). Sulfuric acid embryonic droplets are formed by gas-to-particle conversion, condense on preexisting aerosol and grow to form new small particles (McMurry and Friedlander,

1979; Shaw, 1989). Scavenging of the sulfuric acid molecules by preexisting aerosol competes with the growth of newly formed particles (Kerminen et al., 2001). Coagulation processes remove small particles, and their presence is indicative that gas precursors are present for nucleation to occur. The mechanisms for NPF are still the center of much debate. In general, it is believed that NPF events usually occur during the day, suggesting that they are driven by solar radiation (O'Dowd et al.,1998; Birmili and Wiedensohler, 2000; Hallar et al., 2011). The photochemical process that drives NPF is the OH-oxidation of aerosol precursor gases. Favorable conditions also include low preexisting aerosol concentrations, which may serve as a sink for condensable vapors, high vapor production rates, low temperature and mixing of air (Kulmala and Kerminen, 2008).

Newly formed particles are difficult to measure due to their small size, and it is not well known which nucleation mechanism is most active in the upper troposphere. The presence of new particles can only be detected after the particle has grown enough to be detected by available instruments. In the middle and upper troposphere the most likely nucleation mechanisms are: 1) binary homogeneous nucleation of sulfuric acid and water (e.g., Clarke et al., 1999; Weber et al., 1999); 2) ternary homogeneous nucleation of sulfuric acid, water and ammonia (e.g., Korhonen et al., 1999); and 3) ion-induced nucleation (Yu and Turco, 2001; Lee et al., 2003; Lovejoy et al., 2004; Kirkby et al., 2011). These mechanisms are governed by the probability of forming a critical cluster versus the trend of cluster decay that is inhibited by a free energy barrier (Clement and Ford, 1999).

1.3.1 Binary nucleation of sulfuric acid and water.

Binary nucleation is the spontaneous nucleation that can occur when the vapor pressure of sulfuric acid exceeds the saturation vapor pressure of the sulfuric acid-water mixture. This occurs when molecular clusters containing water and sulfuric acid evaporate or condense a water molecule or a sulfuric acid molecule, called a monomer. When an equal number of monomers evaporate and condense, the non-activated clusters are in equilibrium, and the saturation vapor pressure of the two components is constant. For the cluster to nucleate the local supersaturation must be reached, and the clusters get activated with the addition of an extra monomer. The supersaturation lowers the Gibbs free energy of the system and thus helps the cluster to overcome the nucleation energy barrier (Zhang, 2011). In this case, the concentration of sulfuric acid vapor is the limiting factor to nucleation since water vapor is present in the atmosphere at much higher concentrations (Kuang et al., 2008).

1.3.2 Ternary nucleation of sulfuric acid, water, and ammonia.

Homogeneous ternary nucleation (water - sulfuric acid - ammonia) is similar to the binary nucleation, but with the addition of ammonia in the water and sulfuric acid cluster. In certain cases observed high nucleation rates exceed those predicted by the binary nucleation scheme since the binary nucleation rate is too small (Kulmala et al., 2002). Ambient sulfuric acid concentrations can be too low for binary nucleation (Weber et al., 1999) but sufficient for ternary nucleation (Korhonen et al., 1999; Kulmala et al., 2002; Merikanto et al., 2007). Ternary nucleation gives higher nucleation rates at high

concentrations of ammonia and low temperature. In the upper troposphere, the temperature is low, but the ammonia concentration is also low. In the boundary layer, the ammonia concentration is higher, but the temperature is also higher. Hence, although the nucleation rates obtainable by ternary nucleation are higher than for binary nucleation, they are not sufficient to explain atmospheric nucleation rates during most circumstances in either the boundary layer or the upper troposphere (Yu et al., 2010). Organic acids are also important as their concentration is expected to be much higher than that of sulfuric acid due to photochemical oxidation of volatile organic compounds. The presence of organic acids could enable fewer sulfuric acid molecules to form a stable cluster and could explain the weaker dependence on sulfuric acid concentrations (Zhang, 2010).

1.3.3 Ion-induced nucleation.

Ion-induced nucleation reduces the nucleation energy barrier due to the stabilizing electrostatic interaction between the charged cluster and a molecule. Charged molecular clusters condensing around natural air ions can grow to stable clusters faster than neutral clusters (Yu and Turco, 2001). Ions increase the nucleation rate of sulfuric acid and water and can occur in the mid-troposphere (Kirkby et al., 2011). Ions quickly react with trace gases and organic species to form molecular clusters and sulfuric acid aggregates. The presence of ions limits ion-induced nucleation and hence the ion production rate must be sufficiently high. In the upper troposphere and the stratosphere the ion production rate is high, and thus ion-meditated nucleation is important. In the upper troposphere, ions are generated by galactic cosmic rays at the rate of ~ 20 - 30 ion-pairs/cm^3 (Reiter 1992).

Laakso et al. (2002) showed that ion-induced nucleation was capable of producing high concentrations of nucleation mode particles when the preexisting particle surface area was low. Kazil and Lovejoy (2004) and Modgil et al. (2005) report that ion-induced nucleation could be responsible for particle formation in the upper troposphere.

1.4 Growth of Nucleated Particles into CCN

Once particles form, particle growth occurs through coagulation and condensation and these particles eventually become large enough to act as CCN. Coagulation involves the collision of particles due to the motion between them. The size distributions in the atmosphere are polydispersed, and coagulation is effective between particles of different sizes. Condensation is a function of the saturation vapor pressure surrounding the particle and the preexisting particle surface area, both of which are related to particle size. Coagulation and condensation processes act separately and at different intensities depending on the environmental conditions and the preexisting size distribution (Kulmala et al., 2004). Analytical solutions have been developed for the coagulation and condensation of aerosol particles and are used in models to study the evolution of the size distribution.

1.4.1 Coagulation.

Hinds (1999) defines coagulation as "a process wherein particles collide with one another, due to a relative motion between them and adhere to form larger particles". Coagulation results in a decrease in particle number concentration but particle mass is

conserved through the formation of a single particle following a collision between two particles. Coagulation proceeds faster between particles of a different diameter than between particles of the same diameter. The greater the difference in particle diameter, the greater the effect. Hinds (1999) gives some examples of coagulation coefficients for various particle size combinations. In one example, polydispersed coagulation between 0.01 μm and 1.0 μm particles is 500 times more rapid than that for monodispersed 1.0 μm particles. In polydispersed coagulation, large particles act as a sink for the rapid collection of small particles. When a 1.0 μm particle collides with a 0.01 μm particle, a new particle is formed that has a volume 0.0001% greater than the original 1.0 μm particle. This means that the diameter of the new particle is 0.003% larger than that of the original 1.0 μm particle. These calculations get complicated when an aerosol of a given size has the probability of coagulating with particles of every other size in a polydispersed aerosol. If an aerosol size distribution is sufficiently wide, coagulation will narrow the distribution, reduce the number of small particles, and increase the number of larger particles. A stable size distribution will form after a long time, regardless of the initial size distribution (Lee et al., 1984).

1.4.2 Condensation.

Condensation is the primary method of aerosol growth and the most important mass-transfer process between the gas phase and the particulate phase (Hinds, 1999). Growth by condensation may involve various types of different trace gas species. In this case, sulfuric acid is the most relevant condensable species as organic species are more

likely to be destroyed during transport from the surface to the upper troposphere. In contrast, SO_2, which is the precursor of gaseous sulfuric acid, lives longer (about 10-20 days) and therefore sulfuric acid can persist in the upper troposphere for 10-20 days (Arnold, 2008). Therefore, newly formed clusters can grow by the condensation of sulfuric acid vapor, especially at low temperatures. Figure 1.4 shows a schematic representation of binary homogeneous nucleation of H_2SO_4 and H_2O. The process of condensation involves a supersaturated vapor that condenses on the nuclei and is transformed from the gaseous to particulate phase. When nucleation occurs, it produces a continuous flow of clusters. However, these are unstable and continuously disintegrate. If the supersaturation of condensable vapor is sufficient, the clusters increase in number, and frequent collisions produce agglomerate clusters. The greater the supersaturation, the more frequent is the formation of agglomerates of a certain diameter. If that diameter exceeds a critical diameter, a critical cluster forms and it becomes stable and grows by condensation to form a large particle and potentially a CCN. Growth by condensation is limited by the Kelvin effect and the available supersaturation. The Kelvin equation describes the change in vapor pressure due to the curved liquid-vapor interface on the droplet surface. For every size of the droplet, there is one saturation ratio that will exactly maintain that size of the particle, and supersaturation is required to prevent droplets from evaporating. This Kelvin effect is significant only for particles less than 0.1 μm (Hinds, 1999) and especially important for the smallest nucleated particles since their radii are very small and thus the curvature is enhanced.

The initial steps of growth following nucleation can occur via several processes and is discussed by Kulmala et al. (2004). The dominating particle formation mechanism after homogeneous nucleation is driven by the abundance of nucleating vapors. The driving force for early growth is the difference between vapor pressure at the critical conditions of nucleation (at the critical cluster size) and the actual size of the growing cluster. Growth occurs rapidly and then stays constant since the Kelvin effect is sensitive to cluster size. Besides those vapors that nucleate, other vapors can also participate in condensational growth. Also, the presence of ions and the electrical charge will enhance

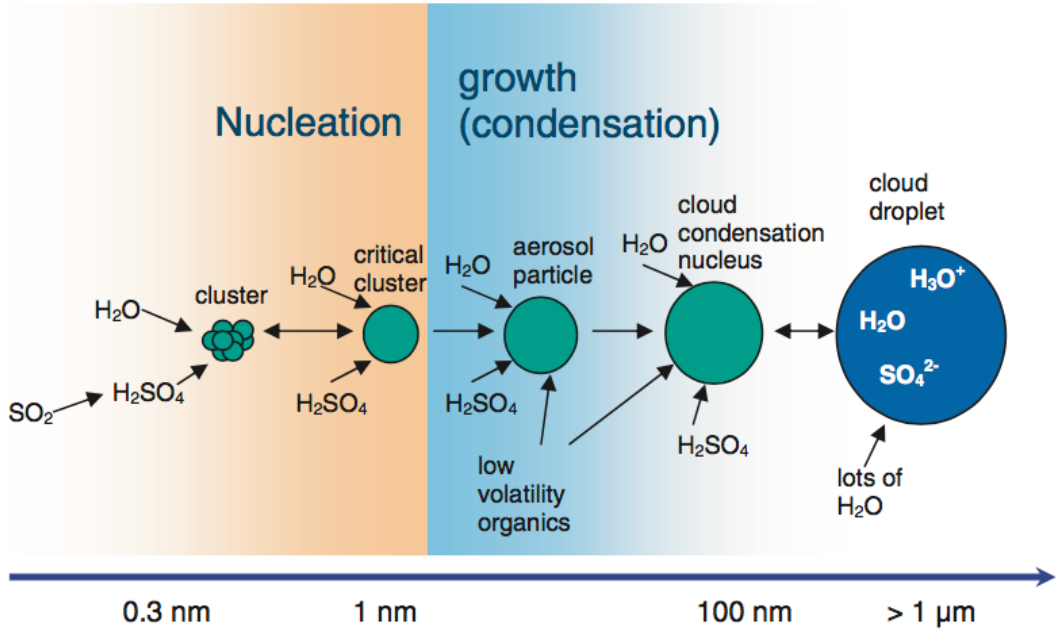

Figure 1.4. Schematic representation of the nucleation and subsequent growth process for atmospheric binary homogeneous nucleation of H_2SO_4 and H_2O. Once thermodynamically stable clusters larger than the critical cluster have formed, they grow by condensation.

Source: Curtius, J., 2009, Nucleation of atmospheric particles, The European Physical Journal Conferences 1, 199-209.

the growth rates of nanoparticles (Yu and Turco, 2001). The condensing vapor can be electrostatically attracted by charged particles, enhancing vapor condensation. This effect is size dependent and will decrease rapidly with increasing size.

1.5 Overview of Dissertation

The objectives of this work were to understand better the process by which new aerosol particles form in the upper troposphere, and how these particles grow to CCN sizes. The approach combined field measurements and observations with extensive data analysis and modeling to study the process of new particle formation, thereby increasing the predictive capability of atmospheric models.

The specific objectives of this dissertation are discussed in Chapter 2. This includes a description of the Mid-latitude Airborne Cirrus Properties Experiment (MACPEX) campaign and its objectives. The experimental methodology is detailed in Chapter 3. This describes a new stringent and statistically significant criterion that identifies NPF events from measurements of aerosols in the nucleation mode.

Chapter 4 discusses the measurements and results obtained from MACPEX. The first half of the chapter includes the identification of the tropopause layer by gas tracer relationships to examine stratospheric-tropospheric exchange. The final portion of the chapter examines the intensity of newly formed particles in relation to the tropopause.

Chapter 5 describes the method and results from model runs of the evolution of the aerosol size distribution using Model of Aerosols and Ions in the Atmosphere (MAIA) to evaluate the possible contribution of nucleated aerosol to the preexisting

aerosol and CCN concentrations. Chapter 6 provides an overall summary of the dissertation research and the major conclusions that can be drawn as a result. The significance of the research and the original contribution to the understanding of new particle formation in the upper troposphere is also discussed.

Chapter Two: Scientific Objectives and Experimental Design

2.1 Objectives and Scientific Issues

New particle formation and growth to active CCN may occur throughout the atmosphere. Merikanto et al. (2009) argued that the upper troposphere is a favorable location for these processes. Lee et al. (2003) and Brock et al. (1993) reported NPF in the upper troposphere and lower stratosphere (UT/LS). Here I present observations of NPF in the UT/LS and characterize the atmospheric conditions and meteorological processes favorable for the occurrence of NPF over the South Eastern United States in the spring season. I further demonstrate through modeling of air parcel trajectories and aerosol dynamics that these episodes can result in increases in CCN abundance. This increase results mainly from the growth of preexisting aerosol due to atmospheric photochemistry in the presence of sufficient precursor gases. The presence of NPF signals the occurrence of these processes and presence of precursors.

In addressing the main objectives of this research, the emphasis was placed upon the upper troposphere where cold temperatures and low preexisting aerosol concentration tend to facilitate new particle formation by the nucleation of H_2SO_4 and H_2O. Atmospheric ions produced by galactic cosmic rays may grow sufficiently to become stable aerosol particles and may also stabilize clusters thereby reducing the nucleation barrier. Other organic vapors, such as those from organic species and ammonia may also

stabilize clusters and weaken the dependence of nucleation on the abundance of H_2SO_4 vapor. However, these vapors are in limited supply in the upper troposphere.

The conditions for nucleation vary with airmass properties due to the variability in temperature, relative humidity, preexisting aerosol, ion concentration, precursor gases and stabilizing vapors. Distinct airmass properties are observed in the region of the tropopause where stratospheric air and tropospheric air mix. The identification of this layer, as well as the limits of the upper troposphere and the lower stratosphere, are important in identifying a source region where new particle formation occurs. These layers vary spatially and temporally with the synoptic meteorology.

The synoptic and mesoscale meteorology is also important in the formation of convective clouds. Deep convective clouds bridge the boundary layer with the upper troposphere and the mixing layer. Boundary layer precursor gases may entrain into convective clouds, lift through the clouds and exhaust from large outflow regions into the upper troposphere, transporting precursor gases. This process may be responsible for enhancements in the frequency of new particle formation.

The objectives of this work were to understand better the locations and conditions favorable to the formation of new aerosol particles in the upper troposphere, and how these particles grow to CCN sizes. The question on the influence of gas-to-particle formation processes on the formation of clouds is a topic of high scientific relevance. Especially of interest is the question of the impact of anthropogenic emissions on gas-to-particle conversion and therefore cloud formation, cloud microphysical properties, and precipitation. This research does not address the latter, but it does attempt to quantify the

impact of NPF in the upper troposphere, mixing layer and lower stratosphere on potential CCN. Conventional thinking is that the boundary layer supplies all the CCN needed for cloud formation, but this is not always the case. Even if a significant fraction of the CCN originated in the boundary layer, any additional CCN could potentially modify the cloud microstructure and precipitation efficiency.

Several studies have deployed instrumentation on airborne platforms to investigate the formation and growth of particles in different environments and discussed the importance of various mechanisms of particle formation and growth between the different environments. While several mechanisms have been proposed for new particle formation, the importance of each mechanism is still the center of much debate. One major problem hampering our understanding of new particle formation is that these new particles are smaller than the lowest detection limit of most deployed instruments. Another issue is that there are a very small number of new particle formation observations in the region close to the tropopause, due to the capabilities of research platforms to fly consistently at this high altitude equatorward of the mid-latitudes. Fewer studies have attempted to investigate the link of particle formation near the tropopause, subsequent growth and potential impact on CCN. In the introduction of Chapter 4, a literature review of the relevant studies was presented.

In this work, I have deployed instruments, performed data analysis and interpreted particle formation events during the Mid-latitude Airborne Cirrus Properties Experiment (MACPEX) campaign. The approach combined field measurements and observations with extensive data analysis and modeling to study the process of new particle formation,

thereby increasing the predictive capability of atmospheric models. The specific objectives of this dissertation were to: (1) successfully deploy a set of aerosol instruments on an airborne field campaign, (2) develop a new stringent and statistically significant criterion that identifies NPF events from measurements of aerosols in the nucleation mode, (3) identify the tropopause layer by using gas tracer relationships to examine stratospheric-tropospheric exchange, (4) examine the formation and intensity of NPF in relation to the origin of the air in which they were observed, (5) examine the formation and intensity of NPF in the vicinity of cloud, and (6) model the formation of new particles and their subsequent growth into a CCN active size range. The specific questions that I aim to address relate to aerosol new particle formation and particle growth in the mid-latitude upper troposphere. Based on the analysis and the current knowledge of nucleation mechanisms and particle growth, different science questions were addressed: (1) when, where and how often does NPF occur in the UTLS? (2) what is the role of airmass origin in the tropopause layer in the formation of new particles? (3) what is the impact of deep convection on NPF in the UT? (4) what is the impact of the newly formed particles on the concentration of potential CCN?

2.2 The MACPEX Experiment

2.2.1 Field campaign.

The MACPEX mission was an airborne field experiment designed to investigate cirrus cloud properties and the processes that affect their impact on radiation. Cirrus is a high level thin layered cloud that is composed of ice crystals. The airborne research

platform utilized during MACPEX was the NASA WB-57F operated out of Ellington Airport in Houston Texas and integrated 24 science instruments (see Figure 2.1). The month-long intensive campaign was conducted during April 2011. Science flights were flown over central North America and the Gulf of Mexico (see Figure 2.2) with a particular focus on sampling in the vicinity of the Department of Energy (DOE) Atmospheric Radiation Program (ARM) Southern Great Plains (SGP) site in Oklahoma. The WB-57F payload included a comprehensive cloud microphysics package to measure ice crystal size distributions, ice crystal habit, and ice water content. Several hygrometers were flown for measurements of water vapor. Also, aerosol size distributions and key trace gas species were also measured. Other instruments provided measurements of dynamics including pressure, temperature, vertical and horizontal winds. Flights were planned with an emphasis on ground-based and satellite observations for scientific utilization and validation. The aircraft in situ measurements also provided the cirrus microphysical information needed for improvement and evaluation of remote sensing retrievals and climate model cloud parametrizations. The instruments relevant to this analysis are described in more detail in Chapter 3.

Figure 2.1. The NASA WB-57F research aircraft at Ellington Field in Houston Texas during MACPEX.

The scientific objectives of the campaign were to (1) acquire accurate measurements of water vapor at low mixing ratios (below 10 ppm water vapor) in the UTLS (Rollins et al., 2014) and (2) investigate the microphysical and dynamical properties of mid-latitude cirrus clouds, the processes affecting these properties and their impact on radiation (Jensen et al., 2013). During flight operations, the aircraft targeted synoptic cirrus and thunderstorm anvil cirrus clouds using near real-time satellite imagery for guidance. Flights were 4.5 to 6 hours in duration. In this dissertation, I studied six flights: 3 April, 14 April, 16 April, 20 April, 25 April and 26 April 2011. This is when both instruments, the NMASS and FCAS, operated well throughout the flight. The aircraft flew up to a maximum altitude of 17.9 km and made 26 tropopause crossings in ascending and descending flight segments on the six flights (see Figure 2.3).

Several other investigators participated in the field campaign, deployed their instrumentation and reported on their results. Some of the highlights reported by the other investigators include:

- An intercomparison of a large group of in situ hygrometers to evaluate measurement agreement. Differences between values reported by the water vapor instruments were nonnegligible and on the order of 20% or 0.8 ppm (Gao et al., 2011; Al-Saadi et al., 2012; Rollins et al., 2014).

- The impact of physical processes on synoptically forced cirrus ice concentrations were studied using a one-dimensional model and obtained good agreement between simulated and observed ice concentrations frequency distributions (Jensen et al., 2013).

- Cloud radiative impact was studied by comparing simulations using a cloud microphysics model with in situ sensor data to distinguish among cloud formation mechanisms (Luebke et al., 2012).

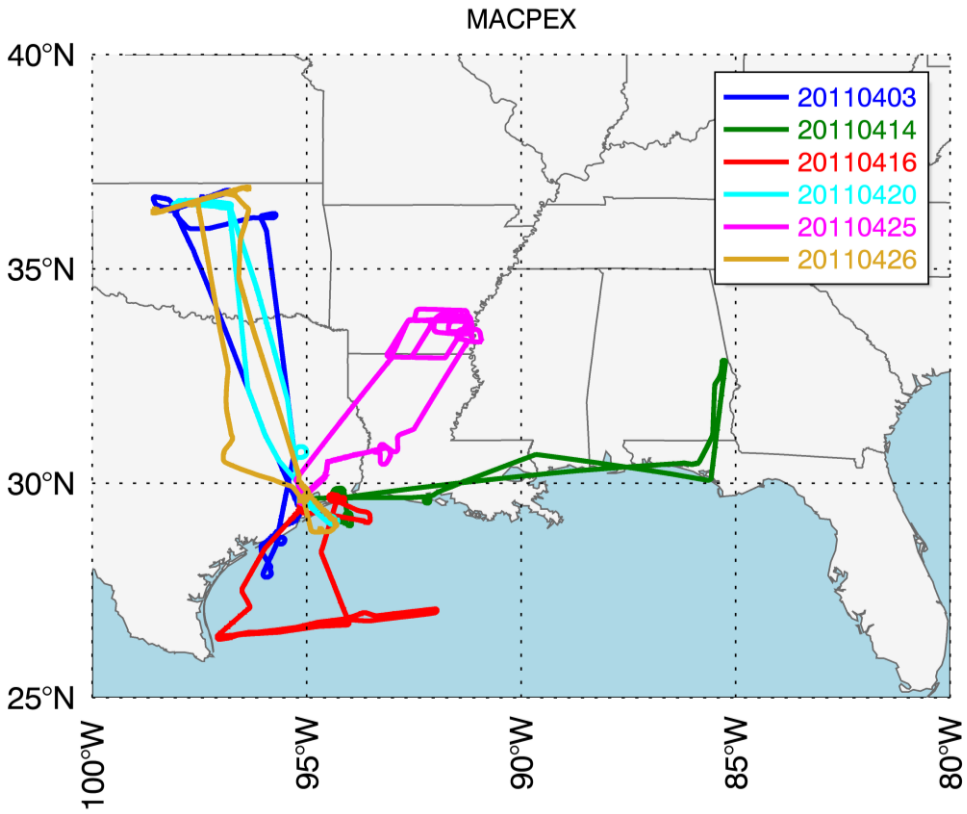

Figure 2.2. The NASA WB-57F flight tracks during MACPEX in April 2011.

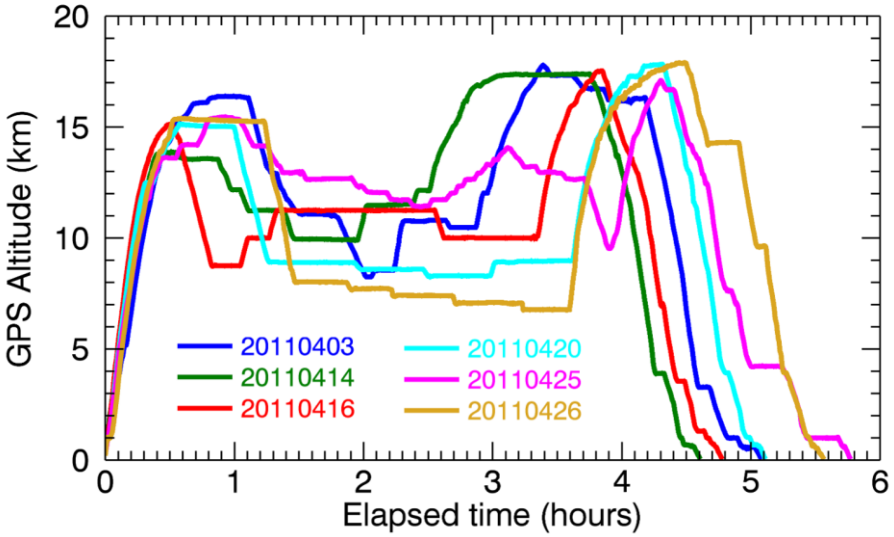

Figure 2.3. The NASA WB-57F flight profiles during MACPEX in April 2011. The profiles are color coded by date as in Figure 2.2.

- Cloud microphysics observations were used to constrain the parametrizations of the formation and growth of ice crystals in the Community Atmospheric Model version 5 (CAM5) (Liu et al., 2012).

- Measurements of chemical and physical properties of the aerosols on which cirrus ice crystals formed in situ and real time was made using a laser ablation single particle mass spectrometer. Mineral dust and metallic particles were highly enhanced in the ice phase when compared to their abundance outside of cloud (Cziczo et al., 2012).

- A Bayesian optimal estimation methodology was applied to retrieve the time-varying ice particle mass–dimensional relationships using the in-situ ice particle probe data (Xu and Mace, 2017).

- Ice particle probe data were used to investigate the frequency of occurrence of smooth and rough ice crystals in cirrus clouds (Schmitt et al., 2016).

2.2.2 Meteorological context.

Research studies over the last few decades have shown that the upper troposphere and the lower stratosphere are strongly coupled through transport processes driven by synoptic weather and large-scale circulation (Holton et al., 1995). Transport processes play a critical role in the mixing of chemical species across the tropopause. Meteorological phenomena such as Rossby waves, gravity waves, jets and fronts modify the tropopause layer and the mixing that occurs through that layer. Transport of chemical species between the upper troposphere and lower stratosphere is therefore linked to the upper-air meteorology.

The synoptic weather pattern over the contiguous United States during April 2011 featured prevailing westerly flow across the mid-latitudes with periodic disturbances from embedded short wave energy producing troughs or closed lows. When far enough south, these troughs or upper level closed lows produced areas of low pressure at the surface resulting in relatively slow moving cold fronts. Zonal storm tracks were associated with the westerly flow, with low-level jets of deep Gulf of Mexico moisture flowing inland in a southerly surface airflow that generated deep convection week after week over the Central and Southern Plains states. In Appendix A an upper air meteorological analysis was presented for each of the flight days in this study.

The cirrus sampled during MACPEX often developed in a region of uplift and moist air. The moist air was linked with wave motions associated with synoptic and mesoscale features. Wave motions varied from the near-planetary scale uplift of air from the tropics to cirrus altitudes, to synoptic-scale mid-latitude cyclones, to gravity waves (Jensen et al., 2013). Mid-latitude cyclones often entered the area of study and produced deep convection. The dominant cirrus forming mechanisms that are relevant to this study were jet stream dynamics and convective anvils.

Table 2.1 provides a coarse classification of the synoptic meteorology and the cloud type sampled during the campaign. The cases on 3 April, 14 April, and 16 April were associated with high altitude jet stream cirrus. The other case days were associated with intense spring convective systems. A mesoscale convective system (MCS) and convective supercell formed on 25 April and 26 April, respectively. This classification was done by the analysis of 250 mb and 500 mb geopotential height contour maps as well as satellite images. An example 500 mb map for 25 April 2011 is shown in Figure 2.4. Satellite images for each flight in this study are shown in Figure 2.5. The 250 mb geopotential height streamline analysis is shown in Appendix A.

Table 2.1. Meteorological classification of flights during MACPEX in April 2011

Date	Synoptic conditions	Clouds sampled [altitude sampled]
3 April	Entrance region of strong southwesterly jet stream with streamline divergence at upper troposphere	Fast moving jet stream cirrus [11 km]
14 April	Weakening subtropical jet stream maximum over Gulf Coast with cut-off low over central US	Jet stream cirrus [10 – 11 km]
16 April	Exit region of subtropical jet stream over Gulf of Mexico	Thin patchy jet stream cirrus [10 – 11 km]
20 April	Streamline divergence in upper air waves and troughs in zonal flow	Cirrus layer with embedded isolated convection [9 km]
25 April	Deep trough with strong positive vorticity advection over southern plains	Cirrus anvil with MCS and overshooting tops [12 – 13 km]
26 April	Amplified short wave trough with strong positive vorticity advection over southern plains	Cirrus anvil with deep convection and overshooting tops [7 – 8 km]

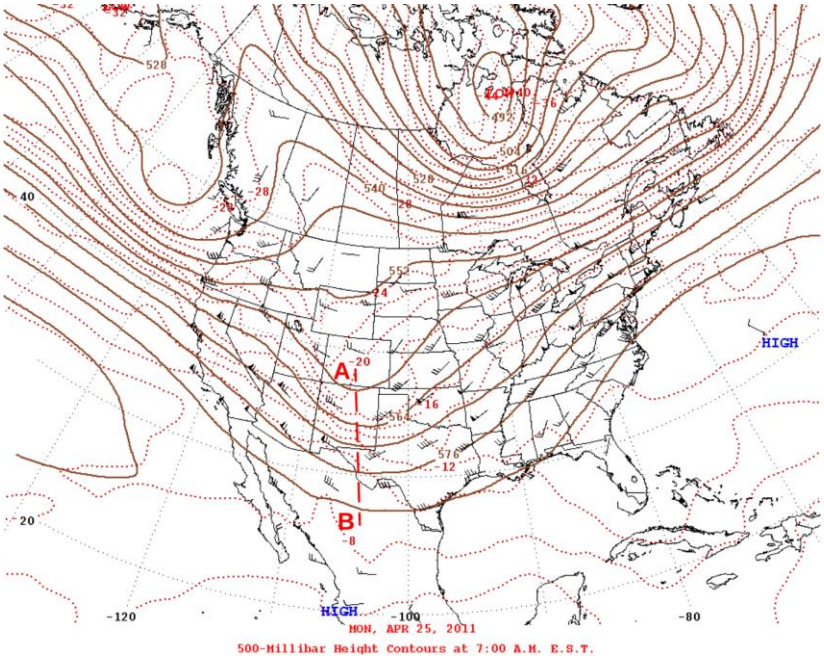

Figure 2.4. 500 mb geopotential height contours valid 12:00 GMT on 25 April 2011. The line AB shows a through axis that is approaching the study area. The region east (upstream) of the through experiences upper-level divergence which creates large-scale instability. In this case, a large MCS formed over the south-central US.

The image was obtained from the NOAA National Centers for Environmental Information, https://www.ncdc.noaa.gov

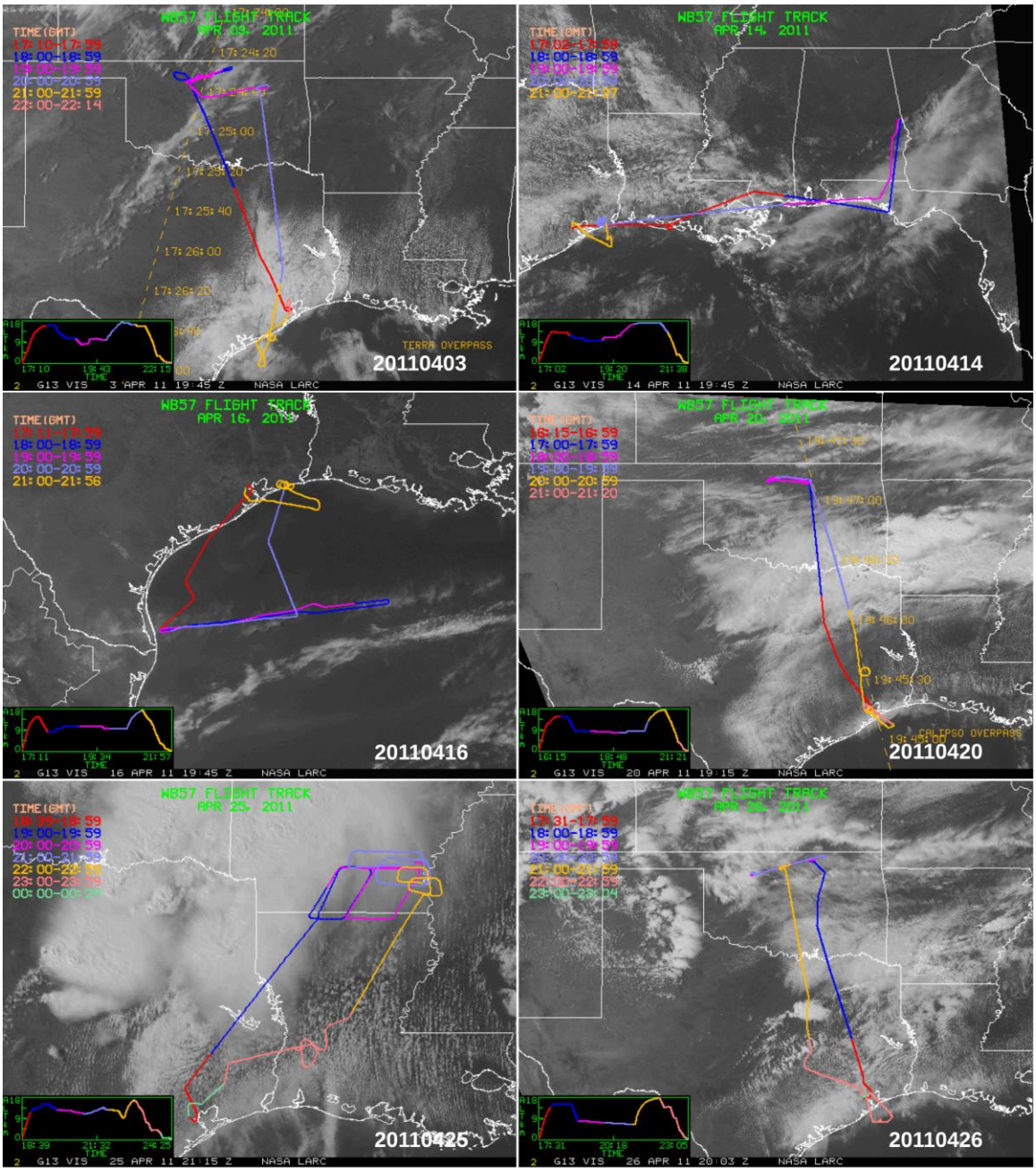

Figure 2.5. Satellite images for each flight in this study. The whole aircraft track is shown with flight tracks colored by time segment. The date and time of the satellite images are 19:45 GMT on 3 April, 19:45 GMT on 14 April, 19:45 GMT on 16 April, 19:15 GMT on 20 April, 21:15 GMT on 11 April and 20:03 GMT on 26 April.

The images were obtained from the NASA Langley Cloud and Radiation Research Group, http://angler.larc.nasa.gov/satimage/products.html

2.2.3 Meteorological reanalysis data.

Additional meteorological data analysis was needed to visualize the measurements in the synoptic scale and to derive other parameters that cannot be calculated from the aircraft data alone. This was done by sampling a meteorological reanalysis dataset. Reanalysis (or retrospective analysis) presents a clear picture of past weather events, independent of the variety of instruments used to make the measurements. Through a variety of methods, observations from different instruments are assimilated to a regularly spaced grid of data. Reanalysis data are created by data assimilation schemes and models that ingest all available observations. Placing all instrument observations onto a regularly spaced grid makes comparing the actual observations with other datasets easier.

In this work, the NASA Modern-Era Retrospective Analysis for Research and Applications (MERRA; Rienecker et al., 2011) reanalysis dataset was used. MERRA is a NASA global reanalysis for the satellite era (1979 to present) generated with the Goddard Earth Observing System Data Assimilation System Version 5 (GEOS-5) atmospheric model and data assimilation system. Specifically, the GOES-5 implements incremental analysis updates (Bloom et al., 1996) to adjust the model states toward the observed state. It was developed with NASA instrument teams and the science community as the user group. The MERRA resolution is 0.5° latitude and 0.667° longitude with 72 vertical levels, from the surface to 0.01 hPa, and extends through the stratosphere. The vertical resolution in the lower stratosphere is near 1 km. The MERRA data files available from NASA's Global Modeling and Assimilation Office (GMAO) are described by Lucchesi

(2012). The various data types used in MERRA include satellite radiance information, profiles from radiosondes and dropsondes (winds, temperature, and humidity), radar winds, surface meteorological data from automatic weather stations, ships and buoys, and wind and temperature reports from aircraft.

The objective of sampling MERRA was to retrieve temperature profiles and vorticity fields that were collocated in space and time with the aircraft data. The MERRA temperature and vorticity fields were linearly interpolated to match the position of the aircraft. The MERRA derived temperature was used to calculate the thermal tropopause. The identification of the dynamic tropopause was done by using potential vorticity (PV) as a diagnostic, which cannot be provided by any measurement system. MERRA PV contours for each flight in this study are shown in Figure 2.6 along with the aircraft flight track. These PV values vary from 0 close to the ground to 50 standard PV units (PVU) in the stratosphere, where 1 PVU = 10^{-6} K m^2/kg s. The value for PV in MERRA is the Ertel potential vorticity. The PV was derived from the MERRA relative vorticity, temperature, and pressure fields. Potential vorticity is defined by Holton et al. (1995) as (1),

$$P = (\xi_\theta + f)\,(-g\partial\theta/\partial p) \tag{1}$$

where ξ_θ is Rossby's "isentropic relative vorticity", a vorticity-like quantity approximately equal to the component of relative vorticity normal to an isentropic surface; f is the Coriolis paremeter (twice the local vertical component of the Earth's angular velocity); θ is the potential temperature; and g is the gravitational acceleration. Since $-\partial p/\partial\theta$ may be interpreted as a local measure of the depth (in pressure units) of the layer between two potential temperature surfaces, an increase in $-\partial p/\partial\theta$ implies

stretching of vortex tubes and in increase in absolute vorticity. In Chapter 4, this definition of PV was used to diagnose the tropopause as a surface of constant PV.

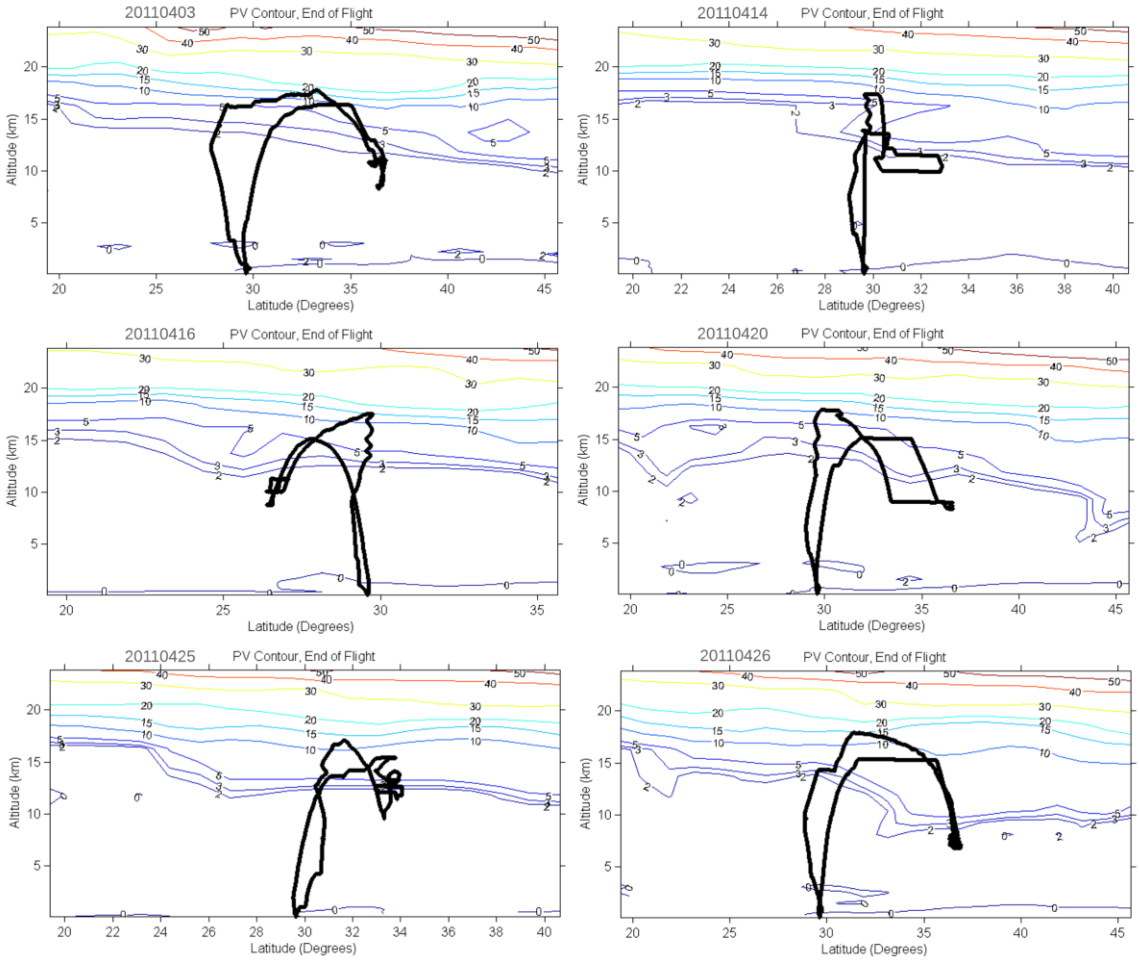

Figure 2.6. Flight track mapped on MERRA PV altitude – latitude profile. The dynamical background of the flights is shown by PV (contours). Flights were 4.5 to 6 hours in duration while the MERRA PV data are at the time step closest to the end of flight.

The MERRA data were obtained from Global Modeling and Assimilation Office (GMAO) and GES DISC, https://disc.gsfc.nasa.gov/daac-bin/DataHoldings.pl

Figure 2.6 shows that the PV contours increase in height equatorward. The PV gradient is sharp near 2 PVU. This is the conventional PVU found to be remarkably close to the tropopause (Holton et al., 1995). With this in mind, some general features were

observed. The tropopause, if assumed at 2 PVU, was above 15 km at the 20 º N latitude and dropped to about 10 km at the 40º N latitude. This drop in the tropopause is a discontinuity that is found in the vicinity of the subtropical jet and the polar jet. On certain flights the decrease in PV was sharp and it occurred over a short latitudinal distance. For example, on 20 April a drop in 2 PVU was observed at 22º N and 43º N latitude. The analysis chart of the 21 April 00:00 GMT 250 mb geopotential streamlines showed a jet maximum over the central US and another over the Gulf of Mexico (see Figure A6 in Appendix A). These correspond with the height changes in PV contours at the same latitude. Similar features were observed on 26 April. The subtropical jet and the polar jet were both analyzed on the 250 mb geopotential upper air chart (see Figure A8 in Appendix A). This time the polar jet was of large amplitude and positioned in south central US at latitude 32º N, while the position of the subtropical jet is approximately the same at latitude 22º N. This synoptic feature of deep throughing is common in spring and often produces severe weather in the southeastern United States. The features described as drops in PV are deep stratospheric intrusions, called "tropopause folds", that coincide with the frontal zone beneath the jet stream. Deep folds can extend down into the top of the boundary layer and are regions of intense mixing between the stratosphere and the troposphere (Danielsen, 1968).

In this study, I examine whether PV diagnostics provide an improved understanding of mixing between tropospheric air and stratospheric air in the tropopause layer. In this layer mixing between distinct airmasses of tropospheric and stratospheric origin occurs. Potential vorticity is a dynamic meteorological feature that describes the

limits of the upper troposphere and the lower stratosphere, as well as the location of the jet stream. It is the aim of this work to identify the variation of the tropopause layer and to determine the source region where new particle formation occurs relative to this layer.

Chapter Three: Methodology

3.1 Introduction

The Mid-latitude Airborne Cirrus Properties Experiment (MACPEX) mission permitted observations of aerosol size distributions in the 4 to 1000 nm diameter range, cloud particles, trace gases and water vapor in and around clouds in the mid-latitude upper troposphere. Newly formed aerosol particles were detected from measurements made by the University of Denver Nucleation Mode Aerosol Size Spectrometer (NMASS). The particle surface area was calculated from measurements made by the University of Denver Focused Cavity Aerosol Spectrometer (FCAS). Cloud particle size and concentration was measured using cloud drop spectrometers and optical array probes. These cloud data were used to determine when the aircraft was in and out of cloud. Water vapor, carbon monoxide, and ozone trace gas spectrometers were used to identify and quantify tropospheric and stratospheric mixing in the UTLS. These MACPEX data were used to characterize new particle formation events in relation to their proximity to cloud and the tropopause. Recent new particle formation was detected by using a relative difference method. In this chapter, I describe the instruments used in this study and the methodology developed to detect the formation of new particles.

3.2 Instrumentation and Experimental Setup during MACPEX

3.2.1 Aerosol sampling on the NASA WB-57 aircraft.

The NMASS and FCAS were installed on a pallet bay that attached to the bottom fuselage of the NASA WB-57F aircraft. Figure 3.1 shows a schematic and final installation of the NMASS and FCAS in the pallet of the WB-57F during MACPEX. The aerosol was sampled through an instrumented, forward-facing, passive, near-isokinetic inlet that was mounted on the fuselage of the aircraft and aligned with the direction of the flow. The inlet consisted of a double diffuser flow system that slows the air to about 5 ms^{-1}. A calibrated exit flow meter permits size-dependent corrections for anisokinetic sampling when it occurs (Jonsson et al., 1995). During instrument sampling and transport, the aerosol is warmed which dries the aerosol. The ambient size is calculated from the measured size, ambient and instrument cavity temperatures and water vapor mixing ratio assuming that the particles are solutions of H_2SO_4 and H_2O (Jonsson et al., 1995). These assumptions are suitable for this study as I investigate particle formation rates due to binary nucleation of H_2SO_4 and H_2O.

3.2.2 The nucleation mode aerosol size spectrometer (NMASS).

Newly formed aerosol particles were detected from measurements made by the University of Denver NMASS. The NMASS consists of five continuous flow condensation particle counters (CPCs) operating in parallel and using 3M™ FC-43 Fluorinert™ as a working fluid. The pressure inside the NMASS was maintained at 60 mb, which makes this instrument suitable for high-altitude measurements. Each CPC

maintained a different supersaturation so that aerosol particles of different size range can be detected. The d_{p50} (50% lower size detection efficiency diameter or "cut-off diameter") for each of the CPCs are 5.3 nm, 8.4 nm, 15 nm, 30 nm and 53 nm with the lowest detection limit of 4.0 nm.

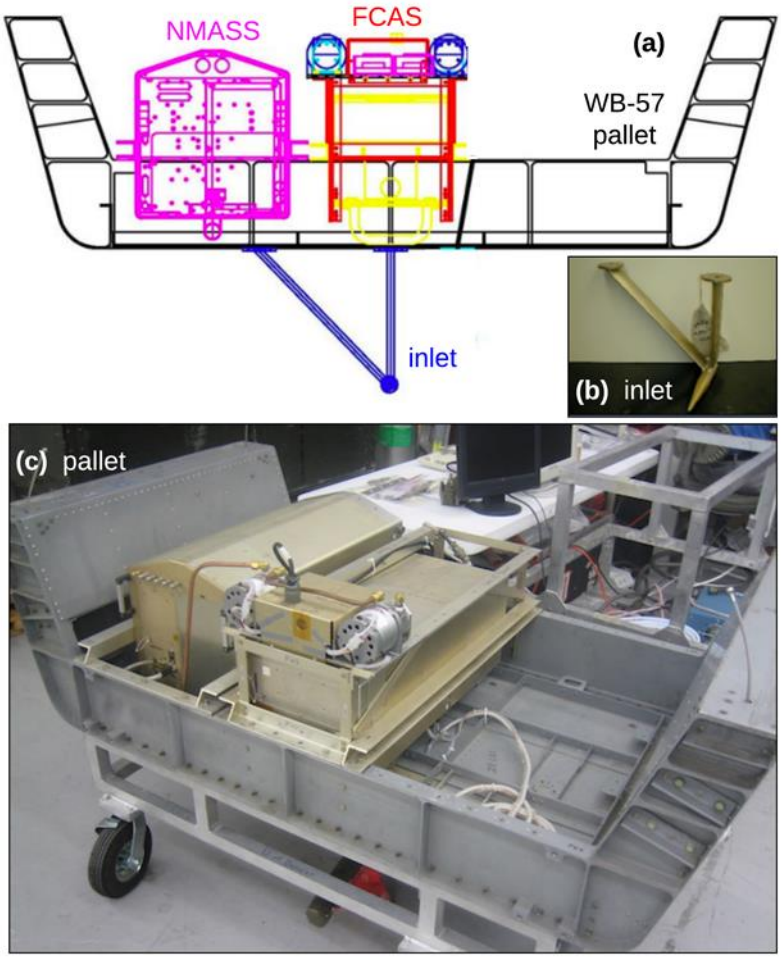

Figure 3.1. (a) Schematic of NMASS (magenta) and FCAS (red/yellow) pallet installation looking aft. The inlet (blue) is shown installed on the pallet. (b) Inlet used during MACPEX. (c) The NMASS and FCAS as installed in the WB-57F pallet during MACPEX. The NMASS is on the left and FCAS on the right.

The principal of the CPC consists of three processes: (1) creation of a supersaturated vapor from a working fluid, (2) rapid growth of aerosol particles by condensation of the supersaturated vapor, and (3) optical detection of the particles after their growth. Different types of CPCs have different techniques of creating vapor supersaturation. The design of the CPC module in the NMASS is based on the University of Minnesota condensation nucleus counter that was flown on the NASA U-2 aircraft (Wilson et al., 1983a). Wilson et al. (1983a, 1983b) were concerned with developing a CPC that performed well in aircraft for studies of stratospheric aerosol. Their design goals included fast time response and improved counting accuracy at low pressure. Filtered sheath air was introduced by Wilson et al. to confine the sample aerosol to the center streamline of the condenser to ensure that all the aerosol in the sample was exposed to the same supersaturation maximum and hence more consistent particle growth behavior. The sheath air design by Wilson et al. was crucial in the future development of the CPC. Another significant innovation was the use of the Kelvin curvature effect to change the detection efficiency and have different aerosol cut-off diameters. The University of Denver Aerosol Group applied this Kelvin-effect sizing method to develop a nuclei mode aerosol size spectrometer to obtain fast-time response airborne measurements (Brock, 1998).

In the NMASS each of the five CPCs samples the aerosol in parallel. Figure 3.2 shows a schematic of the design of the CPC. When the aerosol enters the sample tube it is separated into sample flow and sheath flow (Figure 3.2 step 1). The sheath flow is filtered (Figure 3.2 step 2), removing all particles, and passes through the temperature controlled

saturator. The saturator is maintained at 35°C and is filled with FC-43 Fluorinert^{TM} liquid which diffuses into the airstream (Figure 3.2 step 3). The vapor-laden particle-free sheath flow passes through the vertical cylinder growth tube, the condenser, where the sample air is surrounded by the vapor rich sheath air (Figure 3.2 step 4). The temperature of the condenser is maintained at a value lower than that of the saturator, and the rapid decrease in temperature causes the vapor to saturate and nucleate on the aerosol particles. The aerosol quickly grows by condensation into droplets and reach a size large enough to be detected by an optical particle counter (Figure 3.2 step 5). Subsequently, the sample is filtered and passes through a pump (Figure 3.2 step 6) and exhausted outside the CPC (Figure 3.2 step 7). Each CPC module in the NMASS produces a count rate of particles that can be converted to concentrations by measuring the pressure drop in the capillary flow meter and calibrating it to volumetric flow rate.

Each aerosol particle has a critical supersaturation and a critical diameter for droplet growth. An aerosol particle will activate into a droplet only if the vapor supersaturation surrounding the particle exceeds its critical supersaturation. Once this occurs, vapor rapidly condenses on the droplet resulting in droplet growth. The minimum particle detected in each CPC module depends on the maximum vapor saturation that is reached in the condenser at that particular temperature, pressure, and flow rate. At a fixed pressure and flow rate, this supersaturation is controlled by the absolute temperature of the saturator and the temperature difference between the saturator and condenser (Brock, 1998). By varying the temperatures of the condensers (and fixing pressure, flowrate and saturator temperature), each channel of the NMASS can be tuned to provide a different

minimum detectable diameter. The five CPC channels are tuned so that their detection efficiency can be set from 4 to 60 nm in diameter.

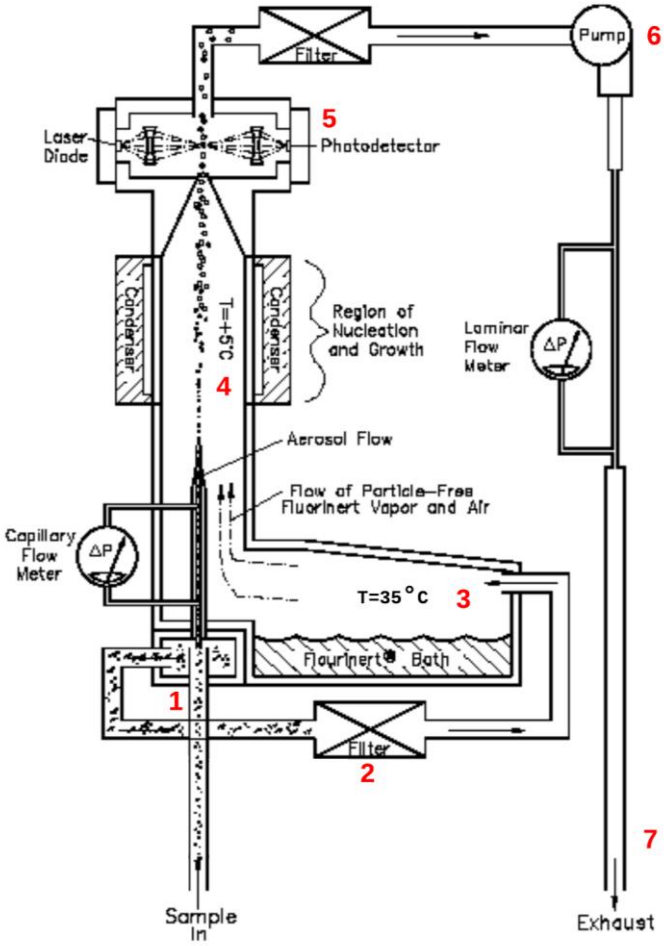

Figure 3.2. Schematic of the CPC module in the NMASS. There are five of these CPCs in the NMASS instrument each with a different size detection efficiency diameter.

Figure 3.3 shows a schematic of the NMASS with the five CPC modules arranged to sample the aerosol in parallel. The instrument features an integrated data acquisition and control system. The physical layout is constrained by space, weight and structural limitations imposed by the aircraft operator and aviation regulations. The instrument is designed for autonomous operation. Two pilots fly the WB-57F aircraft. The instruments

are simply switched on and off and reset if instrument status indicates a problem. To maintain proper flow and pressure as the airplane changes altitude, pumps, and a valve are controlled. The sample flow enters through an orifice, and the pressure of the sample flow is reduced to 60 mb in this orifice. Since the instrument functions to approximately 70 mb and the pumps are small, three orifices are required, and the correct one is inserted depending upon pressure. The pumps run continuously in flight. Total CPC flow is about 150 cm^3s^{-1} at 60 mb. The few seconds of data during orifice changes were rejected.

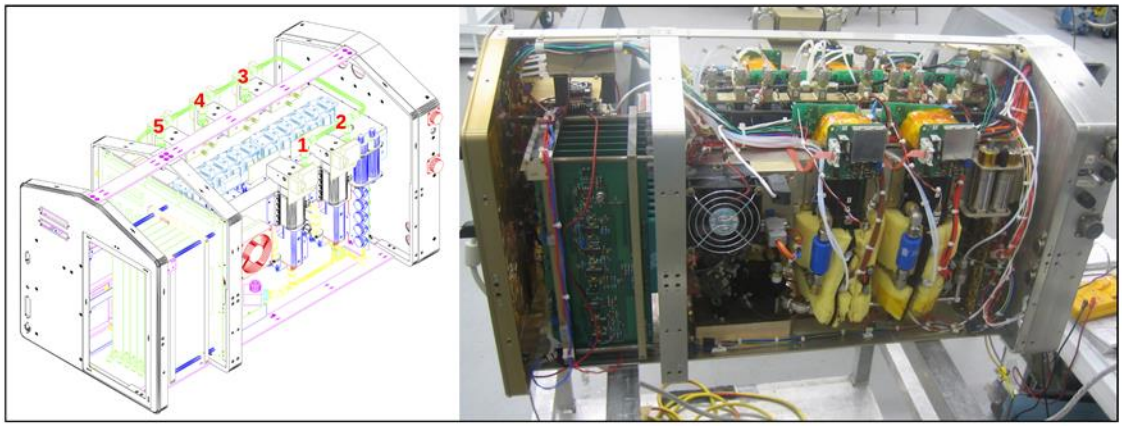

Figure 3.3. Schematic of the five CPC modules (or channels) in the NMASS (left) and the NMASS instrument with covers removed (right).

A numerical inversion technique is used to provide a more continuous size distribution (2). Each of the NMASS channels *i* records a single concentration value X_i,

$$X_i = \int_0^\infty N(D_p)\, K_i(D_p) dD_p \qquad (2)$$

where N is the particle size distribution function, and $K_i(D_p)$ the response function of instrument i to a particle of size D_p. The smoothed Twomey (STWOM) algorithm (Markowski, 1987) is used to solve for $N(D_p)$. This matrix inversion technique generates a 20-bin finite difference representation of $N(D_p)$. The STWOM algorithm uses a nonlinear

technique to choose one smooth, non-negative solution that minimizes the discrepancy between the predicted and actual instrument response. A convergence criterion and a smoothing parameter are required for this inversion procedure and these are determined using laboratory experiments with known aerosol size distributions.

The response function, $K_i(D_p)$, of each channel of the NMASS has been studied in the laboratory against particles of a known size, concentration, and composition. Figure 3.4 shows the results of the laboratory calibrations done by Brock (1998). Ammonium sulfate particles were generated and classified by a TSI 3071A differential mobility analyzer (DMA) into a nearly monodisperse aerosol. The concentration of particles at the NMASS inlet was determined by a TSI 3025A ultrafine CPC. The aerosol size was varied by the DMA in a scanning mode, starting at 3.9 nm and increasing the size. The NMASS response in each channel was then compared to the TSI 3025A CPC measurements. The measured response of each channel of the NMASS is shown in Figure 3.4. The cut-off diameter (d_{p50}) for each of the CPC channels was determined from Figure 3.4, and they are 5.3 nm, 8.4 nm, 15 nm, 30 nm and 53 nm.

During normal operation, the NMASS counts particles at 10 Hz and these data are then reported at 1 Hz. In this study, I have analyzed all NMASS data at 1 Hz and replaced all in-cloud values by not-a-number. The data in cloud are prone to contamination by ice-crystal fragments that can make it through the forward-facing inlet. It is very difficult to determine which data are not contaminated when the aircraft was in cloud and as such these data are flagged and not used in the analysis.

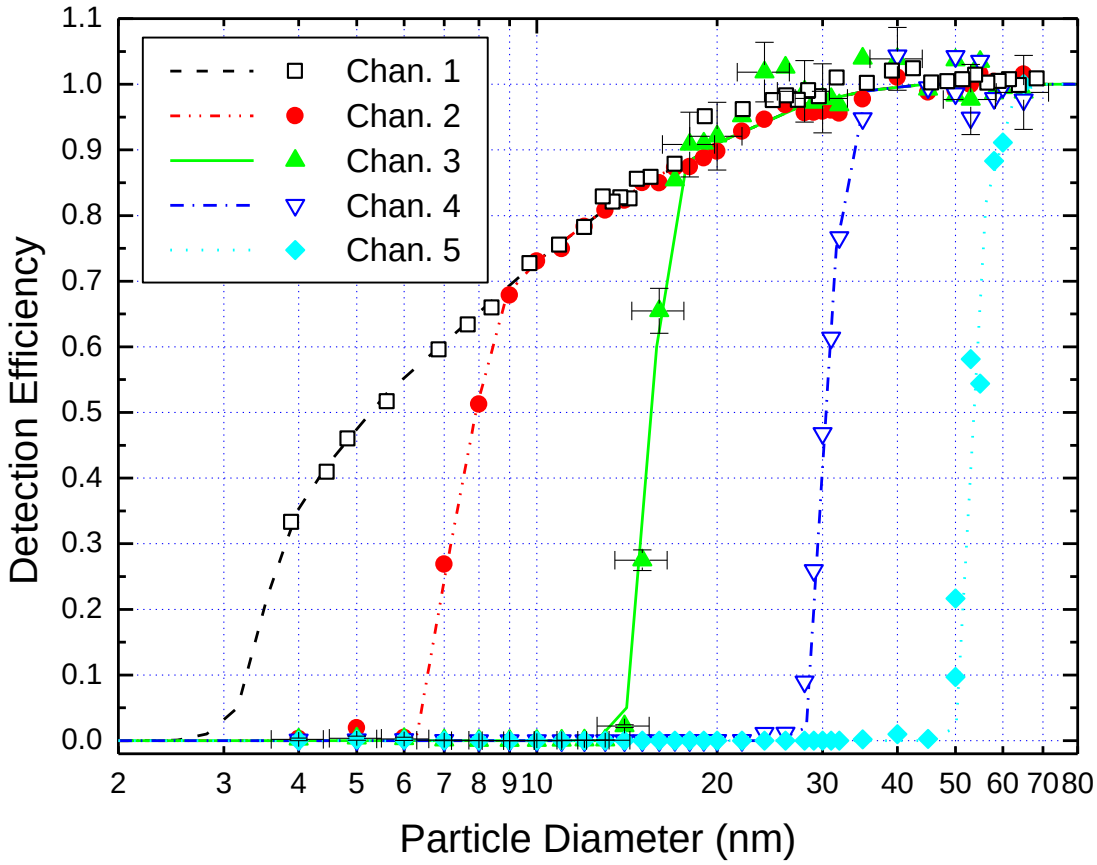

Figure 3.4. Response functions for the five channels of the N-MASS instrument as determined in laboratory experiments at the University of Denver Aerosol Group laboratory. The experimental uncertainties shown for channel 3 represent those for all channels.

Source: Brock, C. A. (1998). A fast-response nuclei mode spectrometer for determining particle size distribution in the 3-100 nm diameter range: technical description. Technical Report, University of Denver, Denver, CO.

3.2.3 The focused cavity aerosol spectrometer (FCAS).

The Focused Cavity Aerosol Spectrometer (FCAS; Jonsson, et al., 1995) was used to measure aerosol size distributions in the diameter range from 100 to 1000 nm. The FCAS instrument has provided accurate measurements of aerosol size distributions throughout the evolution of the volcanic cloud produced by the eruption of Mt. Pinatubo

(Wilson et al., 1993). Near coincidences between FCAS II and the Stratospheric Aerosol and Gas Experiment (SAGE) II observations show good agreement between optical extinctions calculated from FCAS size distributions and those measured by SAGE II (Reeves et al., 2008). The FCAS instrument, originally constructed by Particle Measuring Systems, Inc., is an improved version of the Passive Cavity Aerosol Spectrometer (PCAS; Wilson et al., 1992). Both instruments use a HeNe laser to illuminate particles as they cross the laser. The main improvement of the FCAS over the PCAS was to focus the laser beam inside the passive cavity to increase its intensity and sensitivity to smaller particle sizes.

The FCAS is an optical spectrometer that determines the size of aerosol particles based on the light scattering properties of small spherical particles. The light scattered by a spherical particle that is comparable in diameter to the wavelength of the incident laser light is a unique function of the particle diameter and refractive index. A measurement of the light intensity scattered by a particle as it traverses a monochromatic beam of light of known intensity and wavelength is an indication of the particles size, assuming that its refractive index is known. Therefore, to size a particle, it must be assumed that: (1) the aerosol is spherical, and (2) its chemical composition is known. Since the composition of the aerosol in the UTLS is predominantly sulfuric acid and water, the refractive index of the particles can be determined.

During MACPEX the FCAS was installed as shown Figure 3.1. The FCAS shares an inlet with the NMASS and suffers from the same cloud contamination issues. Particles are sampled through the same inlet as shown in Figure 3.1. They then pass through a laser

beam, and the light scattered by individual particles is measured. Particle size is determined from the intensity of the scattered light. The optical system of the FCAS is described by Jonsson et al. (1995). Its main components are a high-order multimode He-Ne laser, a passive cavity, two sets of collecting (Mangin) mirrors, and two detector arrays. A quartz crystal inside the passive cavity vibrates at high frequency and drives up the intensity of the laser. The particles enter the cavity through a slit orifice. The Mangin mirrors collect the fraction of scattered light into coaxial cones of 45° half-angles and project an image of the scatter onto the photodiode arrays. The signal from the photodiode arrays are processed by three signal amplifiers with different gains and passed to pulse height analyzers where they are sorted into 31 size groups.

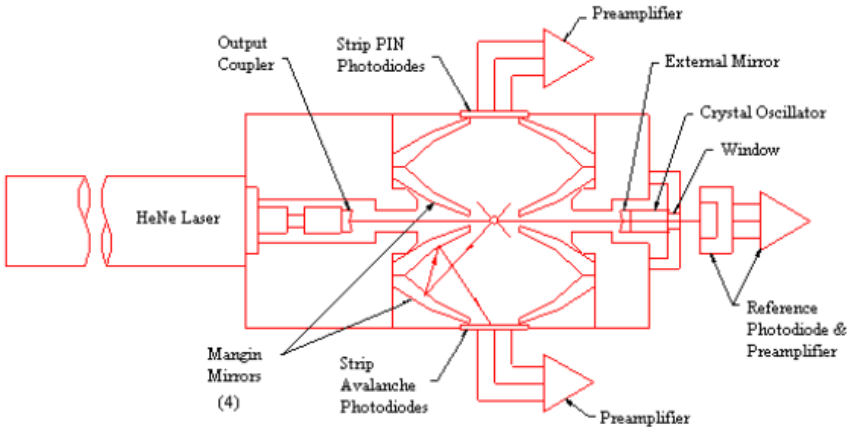

Figure 3.5. Schematic of the FCAS optical system. A converging lens on the output of the laser and an external converging mirror form a focusing cavity. Sample air with particles is injected perpendicular to the plane of the image.

Source: Jonsson, H. H., Wilson, J. C., Brock, C. A., Knollenberg, R. G., Newton, T. R., Dye, J. E., ... & Woods, D. C. (1995). Performance of a focused cavity aerosol spectrometer for measurements in the stratosphere of particle size in the 0.06–2.0 µm diameter range. Journal of Atmospheric and Oceanic Technology, 12(1), 115-129.

The response of the FCAS depends on the refractive index of the aerosol particles. The FCAS was calibrated at the University of Denver Aerosol Group laboratory with over 490 test aerosols. The test aerosol was generated with an atomizer and classified with a DMA. A low-pressure CPC determined the concentration of the test aerosol classified by the DMA. The median of the absolute values of the discrepancies between the FCAS and test aerosol for diameter and concentration was 3% and 11% respectively (Wilson et al., 2008).

The FCAS data reduction is described in Jonsson et al. (1995). The data reduction for the FCAS takes into account the water that is evaporated from the particle during sampling, sampling efficiency, optical and electronic noise and the effects of anisokinetic sampling. The data reduction method (Markowski, 1987) involves a Twomey method matrix inversion. The inversion procedure of the response matrix is determined from calibrations with nearly monodisperse DMA aerosol. The net effect of the data reduction procedure is: (1) the corrected size distributions are smoother, (2) the particle concentrations are lower due to the anisokinetic sampling correction, and (3) the particles are generally larger than in the raw data due to evaporation correction. As in the NMASS, FCAS data were analyzed at 1 Hz and all in-cloud values were replaced by not-a-number.

3.2.4 Cloud particle sensors.

Cloud sensors were needed to determine in-cloud flight segments. These sensors consisted of the Harvard water vapor (HWV; Weinstock et al., 2009), Forschungszentrum Juelich lyman-a photofragment fluorescence hygrometer (FISH total water; Zöger et al.,

1999), SPEC 2D Stereo optical array probe (2DS; Lawson et al., 2006), University of Colorado closed-path tunable diode laser hygrometer (CLH; Davis et al., 2007), NCAR video ice particle sampler (VIPS; McFarquhar and Heymsfield, 1996) and Karlsruhe Institute of Technology small ice detector (SID; Cotton et al., 2010). The NASA GOES-13 visible infrared solar-infrared split-window technique (VISST; Minnis et al., 1995) derived cloud-top data was used to determine whether the aircraft was flying above cloud top or below cloud top and to calculate the distance from cloud.

3.2.5 Trace gas sensors.

Trace gas mixing ratios of ozone (O_3) and carbon monoxide (CO) were used to estimate the location of the tropopause and mixing in the UTLS. The O_3 measurements were made with the NOAA dual-channel UV absorption spectrometer (Gao et al., 2012). CO was measured by the Jet Propulsion Laboratory (JPL) aircraft laser infrared absorption spectrometer (ALIAS; Scott et al., 1999). Chapter 4 has a detailed discussion on the importance of these data in identifying airmass origins and mixing in the UTLS.

3.3 Detection of Aerosol New Particle Formation

NPF occurs when nucleated particles grow to a detectable size. In most ultra-fine CPC instruments the minimum detectable size is 3 nm. While nucleation starts with the molecular growth of clusters (as discussed in Chapter 1), NPF is defined to occur when particle growth to the detection limit exceeds particle loss from coagulation with preexisting aerosol. Therefore, cluster nucleation may be active, but the loss rate may

also be large enough that cluster growth is inhibited. In this case, the conditions needed for nucleation are present, but NPF is not detected due to the growth limitation. There is a distinction between nucleation and new particle formation. In this study, NPF is the process when nucleation leads to particle growth of at least 3 nm in diameter. The presence of particles in the 3 to 8 nm minimum detectable size range by the NMASS is an indicator of recent NPF. Past identifications of NPF have used rather arbitrary criteria. In a study by Weigel et al. (2011) an NPF event is defined if $(0.85)(N_6) - (1.15)(N_{15}) > 0$ where N_6 and N_{15} correspond to the concentration of aerosol particles greater than 6 nm and the concentration greater than 15 nm respectively (for the aerosol spectrometer used in that study). Lee et al. (2003) identified NPF from the NMASS size distributions by two factors: (i) number concentration from 4 to 6 nm exceeding those from 6 to 9 nm, and (ii) number concentration from 4 to 9 nm exceeding 1 cm^{-3}. These methods use differential properties of the size distribution to identify new particles but do not consider the probability that such identification may result due to counting statistics.

In this study, I present a statistical approach to identifying NPF. The mixing ratio of particles in each NMASS channel is equal to b_iC_i where b_i is a function of flow, pressure and temperature and C are counts recorded by each CPC while sampling the populations. Therefore $M_i = b_iC_i$ where i corresponds to any of the CPC channels between 1 and 5. The mixing ratio of particles reported by the second channel (M_2) is subtracted from that reported by the first channel (M_1) to determine if there are particles in the size range from ~5 nm to ~8 nm. The variance of CPC counts for a fixed concentration is governed by Poisson statistics and can lead to NPF artifacts caused by

statistical fluctuations in nearly equal counts. The distributions that would result from repeated sampling with each CPC are Poisson distributions with a mean nearly equal to C_i and a variance equal to C_i. This assumption is equivalent to assuming that the variance in the observed C values are due solely to counting statistics.

Negative as well as positive values of M_1 - M_2 are expected in samples where the long-term averages of M_1 and M_2 are equal. The ratio of the reported difference (M_1 - M_2) to the standard deviation in this value expected to result from the counts can be defined as "relative difference" (3),

$$\text{Relative Difference} = \frac{M_1 - M_2}{\sqrt{(b_1^2 C_1 + b_2^2 C_2)}} \quad (3)$$

where *b* is a function of flow, pressure and temperature and *C* are particle counts detected by each CPC. It is expected that the counts in any channel vary according to Poisson statistics in the absence of microphysical or geophysical factors (such as new particle formation or spatial and temporal variation) that would drive variation. The aerosol mixing ratio M_i is proportional to the counts C_i with the proportionality containing the sample flow in each CPC, the temperature, and pressure. Each sample period for each of the CPCs produces a count that is a sample drawn randomly from an ensemble of counts whose mean approximates the long-term average one would get if the same aerosol were sampled for a long time. Therefore, any variation in M_1 - M_2 where $M_1 > M_2$ outside that expected by Poisson statistics would be due to new particle formation. Since Gaussian distributions approximate Poisson distributions for large counts, the properties of the Gaussian distribution can estimate the probability that $M_1 > M_2$ resulted from counting statistics alone. The further a measurement is from the mean (i.e. towards either end of

the distribution), the less likely it is being measured at random, and the less likely the signal is due to a small fluctuation in the background. If "relative difference" is greater than 3, then the probability that the positive difference M_1 - M_2 occurred due to counting statistics is less than 0.13% or a certainty of 99.87%. A criterion was established where NPF is assumed to occur when "relative difference" is greater than 3.

Using this new criterion for new particle formation, the relative difference was calculated at 1 Hz. Also, the relative difference was smoothed with a boxcar average of 60 seconds. An NPF event was further constrained by the requirement for the 60 second "smooth" relative difference to be greater than 3. This ensures that spikes in the data were not interpreted as NPF and also allows for the identification of events of extended duration and significant strength. When the relative difference falls below -3, the data are erroneous. In this case, M_2 is greater than M_1 which is an artifact in the instrument. This was observed to occur on rare occasions during sampling of cloud with high hydrometeor concentration and is likely due to shattering of ice particles on the inlet tip. By removing all in-cloud samples, most instances when the relative difference was less than -3 were also removed.

The frequency distributions of M_1 - M_2 for all out-of-cloud MACPEX data points are shown in Figure 3.6. All out-of-cloud data points (n=71,569) are shown in black, data with no NPF in blue (n=55,600) and data with NPF in red (n=15,969). Of all the out-of-cloud data points 22% indicated NPF. A Gaussian fit was applied to the main body of the distributions. Figure 3.6a shows that the data was distributed around 0 with a skewed distribution due to higher frequencies at larger mixing ratios. When $M_1 < M_2$ the data

points fell along the Gaussian fit indicating that this is counting statistics. When $M_1 > M_2$ the large end tail of the distribution was spread out away from the mode and therefore less likely to be random fluctuations. When the data with NPF (i.e. relative difference > 3) were over-plotted, a mode appeared that accounted for the tail in the frequency distribution that included all measurements. Figure 3.6b shows the data points with and without NPF. Here it was quite evident that the data without NPF followed the Gaussian fit, although a tail was still apparent at low frequency. This may be due to NPF that is undetected since the criteria for relative difference are at the 3-sigma level. Figure 3.7 shows the same information as in Figure 3.6 but with a relative difference at the 2-sigma level. In this case, 27% of all out-of-cloud data contained NPF. It was also evident in Figure 3.7b that the data without NPF had less of a tail compared to Figure 3.6b where the relative difference is at the 3-sigma level. When the relative difference is at 2-sigma, the probability that $(M_1 - M_2) > 0$ occurred due to counting statistics is less than 2.5%. For this study, I selected a statistically significant and stringent threshold for NPF at 3-sigma.

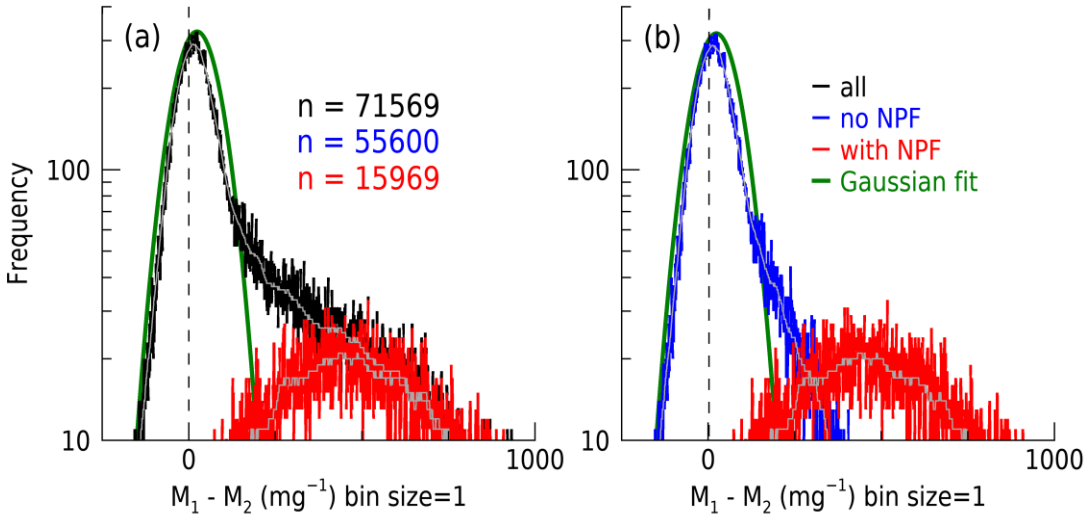

Figure 3.6. Frequency distribution of mixing ratio of particles reported by the second channel (M_2) subtracted from that reported by the first channel (M_1) with relative difference > 3. (a) Distribution of all measurements (black) and those with NPF (red). (b) Distribution of measurements with no NPF (blue) and with NPF (red). A Gaussian fit is applied in all cases in (a) and no NPF cases in (b). The gray traces are smoothed distributions of the plotted data. The bin size for the distribution on the abscissa is equal to 1 mg^{-1}. All data are out of cloud.

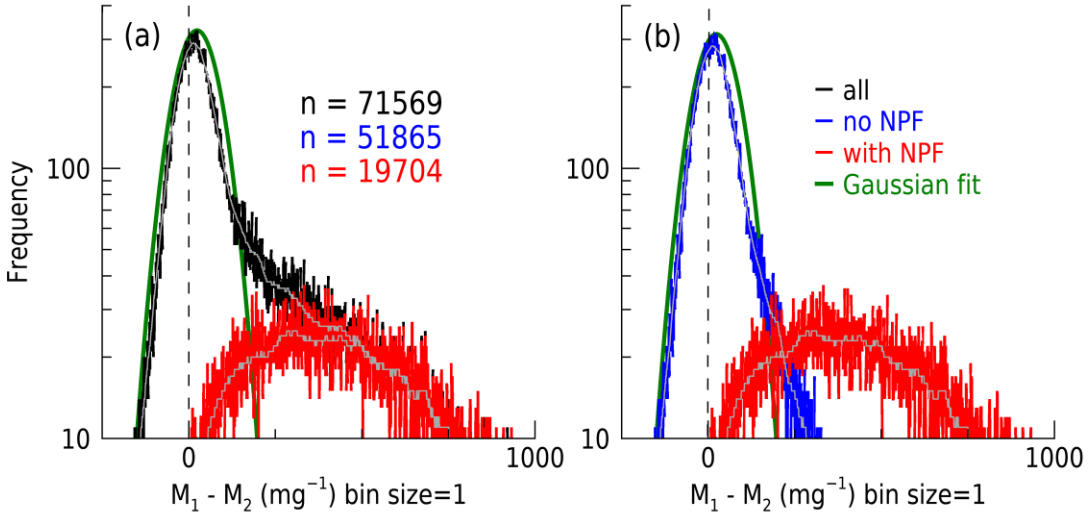

Figure 3.7. Same as in Figure 3.6 but with relative difference > 2.

Figure 3.8 shows the number of out-of-cloud 1 Hz samples collected as a function of altitude and relative difference during MACPEX. Most of the samples were measured at an altitude of 13 km to 17 km. The relative difference at high number density (75 percentile) was just above 0 at an altitude of 15 km. The 50 percentile number density had a range in relative difference of -0.3 to 0.7. The altitude with a relative difference greater than 3 was most contained in the 8 km to 13 km range. This is the region of the upper troposphere and the tropopause. In Chapter 4 the origin of NPF in relation to the tropopause is explored in detail.

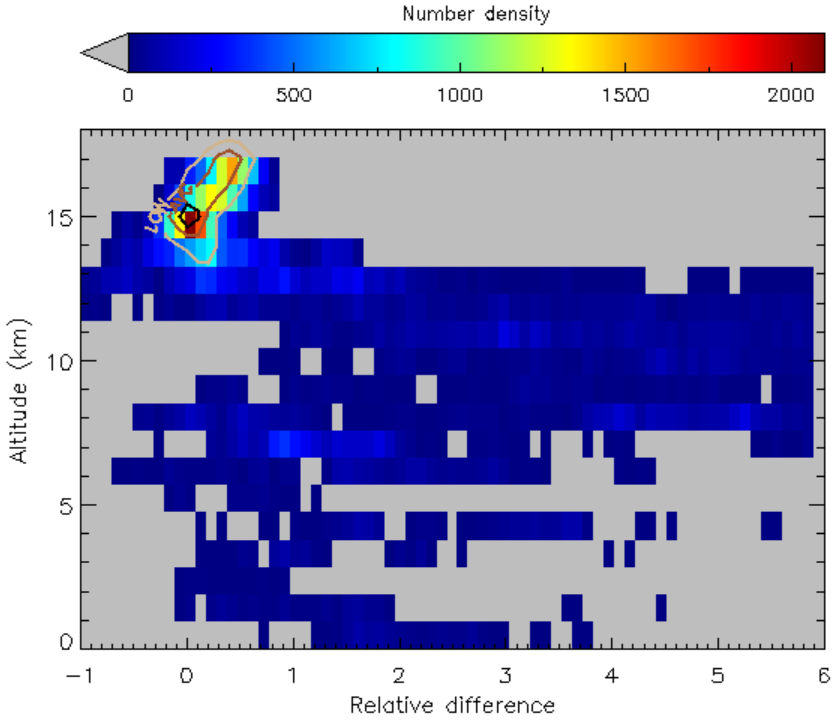

Figure 3.8. Number of 1 Hz out-of-cloud samples and corresponding 60-second smooth relative difference (n = 71,569). The samples were binned in 1 km altitude and 0.1 relative difference. The contour labeled ‘LOW’ defines 25 percentile of the density, ‘AVG’ defines 50 percentile of the density and ‘HI’ defines 75 percentile of the density.

The application of the new NPF criteria with a relative difference at 3-sigma is shown in Figure 3.9 and Figure 3.10. Two very similar methods were tested to identify the NPF events and their duration. The first method was to simply assign an NPF event for each data point with relative difference > 3 (Figure 3.9c and Figure 3.10c). This worked very well when the frequency distribution of counts was contained between -3 and 3. There are time segments, such as the period 74000 to 74300 seconds in Figure 3.10a, where the modal relative difference was slightly above 0. This shifted the distribution upward and increased the frequency of data points with relative difference > 3.

The second method that was tested involved applying a smooth function with a boxcar average of 60 seconds to the relative difference. This is shown in Figure 3.9b and Figure 3.10b. The criteria is not very sensitive to a shift in the mode of the distribution when smoothing is used, as can be seen by the lack of false NPF identification in the period 74000 to 74300 seconds in Figure 3.10b. The smoothing method was judged to be superior since it ensures that statistical outliers in the data were not interpreted as NPF. It also allows for the identification of events of extended duration and significant strength. This method was used for the analysis, but testing did not show significant differences in the results when switching between methods.

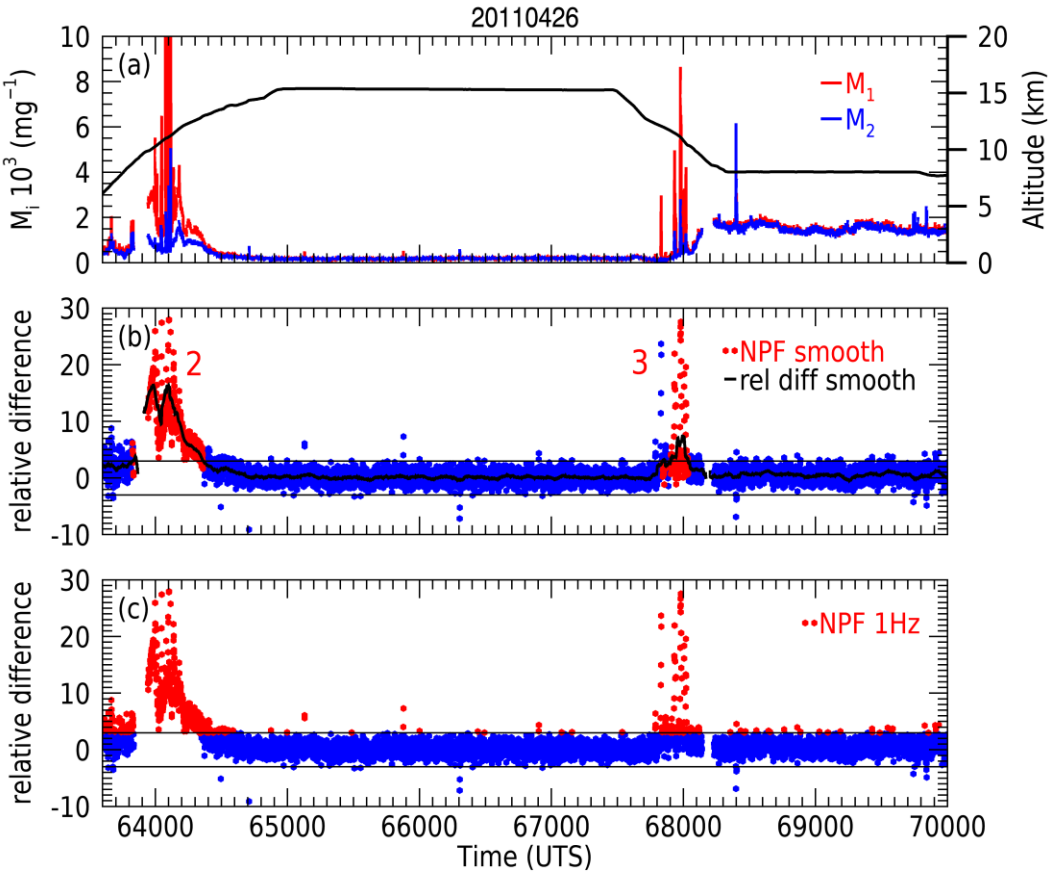

Figure 3.9. Application of new NPF criteria for a time segment on 20110426. (a) The mixing ratio of particles reported by the first channel M_1 (red), mixing ratio of particles reported by the second channel M_2 (blue) and aircraft altitude (black). (b) Relative difference (blue/red), 60-second boxcar smoothed relative difference (black) and NPF events (red). The NPF criteria are applied when smoothed relative difference > 3. NPF events are number 2 and 3. (c) Same as (b) but smoothed relative difference does not apply and the NPF criteria are applied at 1 Hz when relative difference > 3.

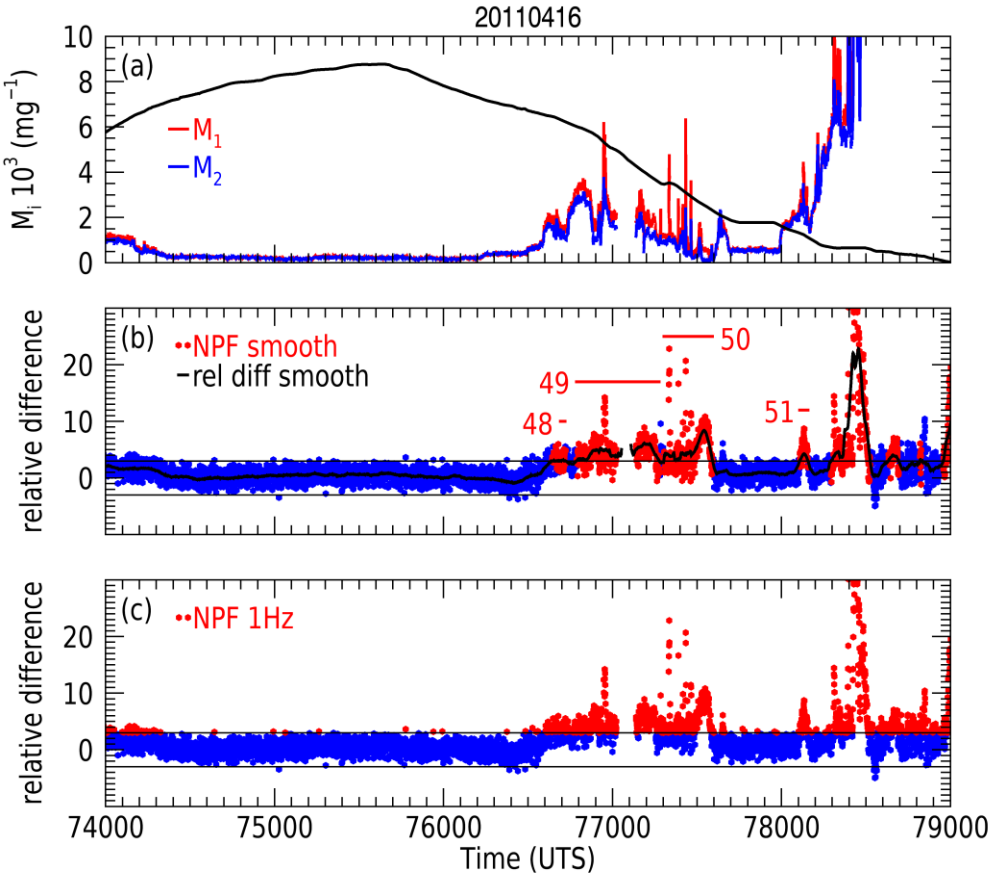

Figure 3.10. As in Figure 3.9 but for a time segment on 20110416. The horizontal red lines in (b) show the identification and duration of NPF events 48, 49, 50 and 51.

In total for the six MACPEX flights, 188 NPF events were detected using the smoothed relative difference 3-sigma criteria (in-cloud and out-of-cloud total). Figure 3.11 shows the number of events detected during each flight and the distance traversed by the aircraft to fly through each event. Out of the 188 events, 121 were traversed in a flight distance greater than 1 km. A quarter of the NPF events (47 events) were detected for a distance greater than 15 km. The event that covered the largest distance was detected on 20110414 and extended to 119 km (NPF number 19), with part of the event being through cloud (see long NPF event in Figure 3.12 from 68609 to 70541 seconds). The next section details how in-cloud data points were detected.

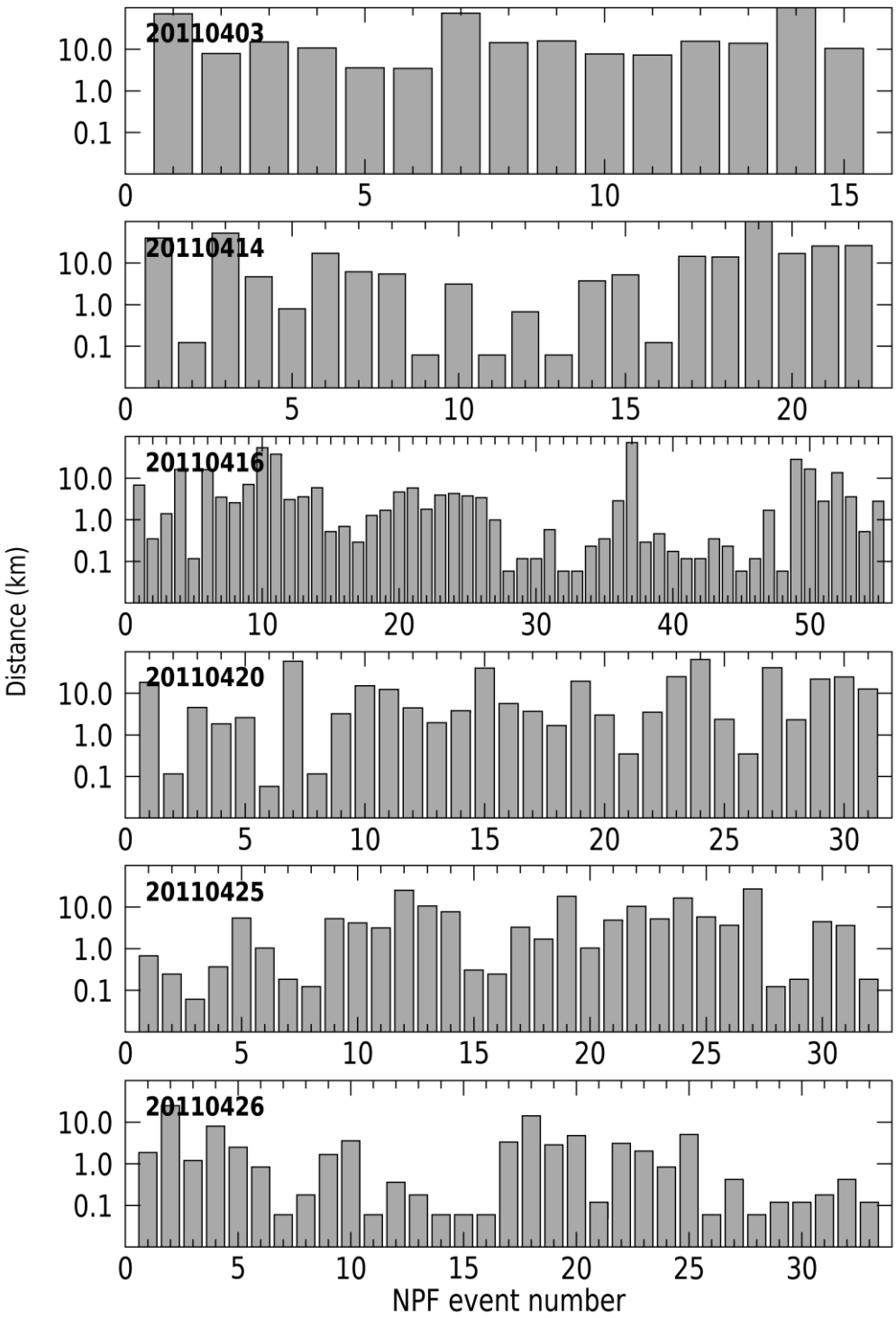

Figure 3.11. Barplots of the NPF events and the distance covered by the aircraft during these events for each flight in MACPEX.

3.4 Identification of Cloud Boundaries

The forward-facing sampling inlet for the NMASS and FCAS cannot discriminate between an aerosol particle and a cloud particle. When the aircraft penetrates cloud, a mixture of aerosol and cloud particles is passed through the inlet and the sampling systems downstream. Artifacts during cloud sampling are thought to arise from ice particles that shatter on impaction with the leading surfaces of the inlet and do not completely evaporate during transport to the instruments. In this study, cloud sensors were needed to determine in-cloud flight segments.

Figure 3.12 and Figure 3.13 show examples of the impact of cloud particles on sampling. The relative difference was observed to be consistently greater than -3 throughout the MACPEX NMASS data. The only exception was in cloud penetrations. Figure 3.12 and Figure 3.13 both show segments when the relative difference drops to below -3. These instances were related to cloud penetrations with high ice water content (IWC). It was observed that when the IWC was greater than 0.1 g m^{-3} the relative difference was below -3. By definition, this occurs when M_2 is greater than M_1 and can only occur due to counting statistics less than 0.13% of the time.

To look at this further the 2DS optical array probe particle inter-arrival time data were processed and analyzed to determine the fraction of particles that were shattered. The 2DS was mounted external to the aircraft on a wing pod, and ice particles were sampled as they crossed a laser beam through the probe arms. When shattering occurs on the probe arms, the particles arrive at the laser at a different time than the true airspeed. The technique by Field et al. (2006) was used to identify fragmented particles by the

analysis of particle-by-particle inter-arrival time. The inter-arrival times of particles measured by optical array probes (as in the 2DS) can be bimodal. The long inter-arrival time mode represents real cloud structure while the short inter-arrival time mode results from fragments of shattered ice particles. By assuming that particles are randomly distributed in space Field et al. (2006) showed that a function representing two Poisson processes was a good fit to the observed distributions of inter-arrival times. By comparing the mean inter-arrival time of the two Poisson distributions, the fraction of particles with short inter-arrival times, or the fraction of shattered particles, can be estimated. This fraction is shown as a percentage in Figure 3.12b and Figure 3.13b. The percentage of shattered particles had an impact on relative difference. It can be seen that when this percentage reached 40% for an extended period, the relative difference was less than -3.

Although it cannot be assumed that when shattering occurred at the 2DS probe, the same amount of shattering occurred at the aerosol inlet, it was evident that some shattering at the aerosol inlet produced artifacts in the NMASS. A cloud flag had to be formulated to determine when the aircraft was penetrating cloud. Figure 3.12c and Figure 3.13c show cloud flags as horizontal bars that span along the time axis. Individual cloud flags are shown for the 2DS and CLH. The 2DS and CLH both measure IWC but in a different way. The 2DS is an optical array probe and measures the particle area. By assuming a mass dimensional relationship and ice density, the IWC can be calculated. The CLH uses a heated inlet and flow path to evaporate cloud particles. The water vapor is then detected using infrared spectroscopy and direct absorption. The 2DS and CLH had

a linear correlation coefficient of 0.9 during MACPEX. Examination of time series of IWC from both instruments for all the flights revealed that both instruments performed well in ice clouds. In the case of the 2DS and CLH, a threshold of 1 mg m^{-3} IWC was chosen to indicate cloud. This threshold was at the right side of the noise distribution for all flights. At times the CLH had a high dry term due to extreme wetting in high IWC. In Figure 3.13c this can be observed in the time segment 74000 to 74800 seconds. When this occurred, it was useful to compare the 2DS with the VIPS and SID.

In the VIPS and SID, cloud was determined to be present when the hydrometeor concentrations exceeded 1 L^{-1}. This threshold was also determined by assuming a normal distribution to the noise of the instrument and picking a threshold at the right side of the noise. The HWV which measures water vapor (i.e. gas phase water only) and FISH which measures total water (i.e. gas phase water plus ice water content) were used to calculate relative humidity over ice (RH_{ice}) and $RH_{ice,enh}$. The latter represents gas phase water plus the over-sampled ice crystals expressed as relative humidity. The ratio $RH_{ice,enh}/RH_{ice}$ is used as the "cirrus parameter" where cirrus ice cloud is determined to be present when $RH_{ice,enh}/RH_{ice} > 1$ and $RH_{ice} > 100\%$ (Krämer et al., 2009). All the cloud flags (including 2DS, CLH, VIPS, SID, and cirrus parameter) were passed through a data quality routine with weight given to the best performing instruments, and a "composite flag" was formulated that aggregated each of the individual flags. As a final precaution against including cloud edges in the sample, the data within two seconds (~ 300 m) of all cloud edges were also excluded. The "composite cloud flag" is shown in Figure 3.12c

and Figure 3.13c. This cloud flag was then used to omit all NMASS and FCAS in-cloud data from the analysis.

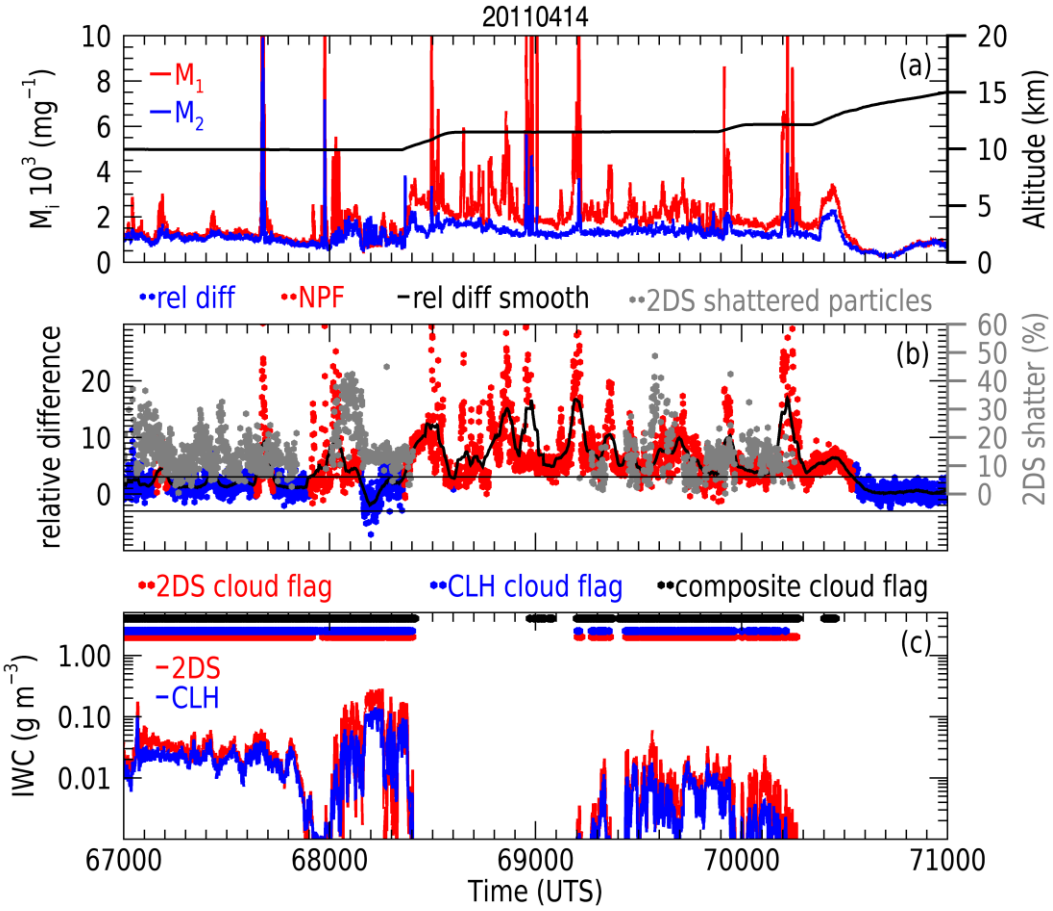

Figure 3.12. Cloud detection and effect of cloud on NPF criteria for a time segment on 20110414. (a) The mixing ratio of particles reported by the first channel M_1 (red), mixing ratio of particles reported by the second channel M_2 (blue) and aircraft altitude (black). (b) Relative difference (blue/red), 60-second boxcar smoothed relative difference (black), NPF events (red). The fraction of ice particles that were shattered in the 2DS is given in percent (gray). The NPF criteria are applied when smoothed relative difference > 3. (c) 2DS ice water content (red), CLH ice water content (blue), 2DS cloud flag (red), CLH clould flag (blue) and composite cloud flag (black).

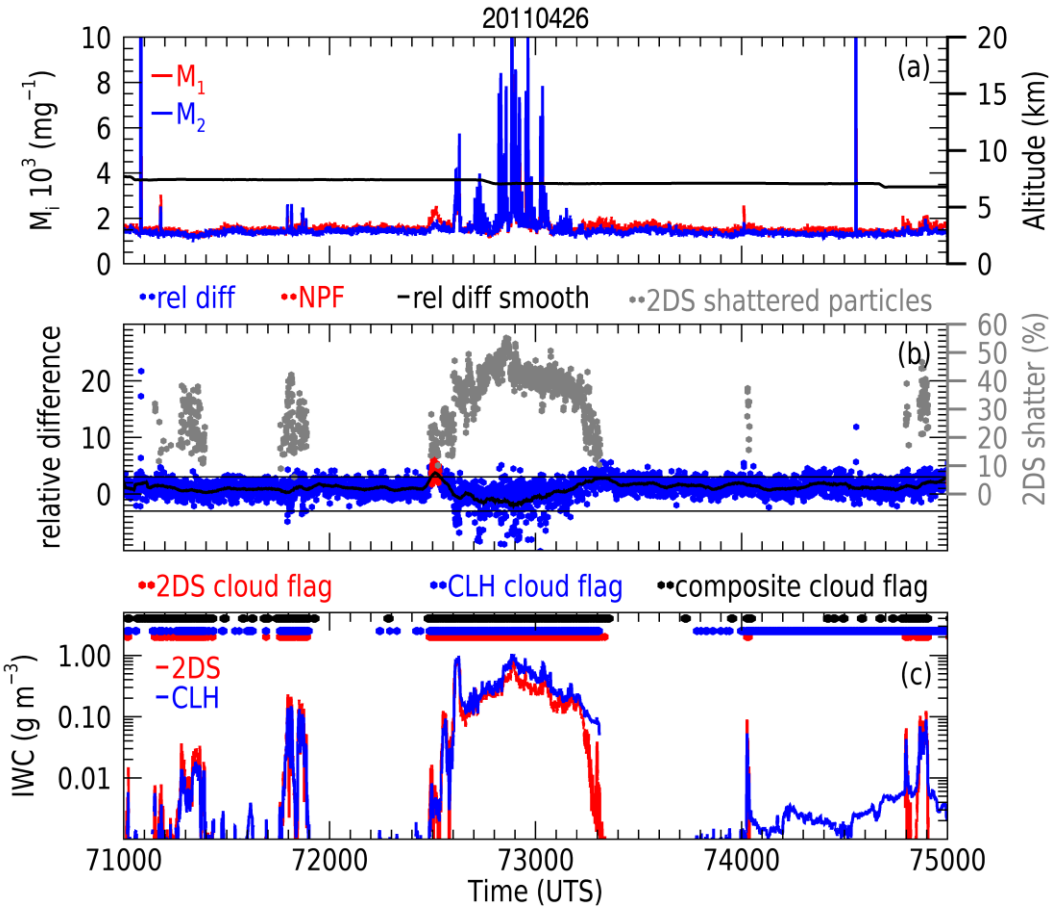

Figure 3.13. Same as in Figure 3.12 but for a time segment on 20110426.

The cloud flag together with the NASA GOES-13 VISST cloud-top height were used to determine the nearest distance from cloud. VISST is a satellite-based retrieval method that determines the cloud-top height at 4 km resolution. The VISST height data was collocated with the flight track of the aircraft. The method to calculate the nearest distance to/from cloud was by calculating the shortest distance between in-cloud and out-of-cloud flag determinations and comparing that to the distance between the aircraft and cloud top. If the vertical distance between the aircraft and cloud top was less than the horizontal distance determined by the cloud flag, then the distance between the aircraft and cloud top was used as the nearest distance. When the aircraft penetrated cloud, an

entry point (φ_1, θ_1) and an exit point (φ_2, θ_2) was recorded, where φ and θ correspond to latitude and longitude, respectively. The horizontal distance of the great circle across the Earth's surface connecting the aircraft to the exit point of cloud *p*, and the entry point of cloud *p+1* were calculated. The length of the shortest path between them was used as the nearest distance unless the absolute vertical distance between the aircraft and the VISST cloud top was less. Previously a method that calculated the nearest distance based on the aircraft airspeed along the flight path was used, but this was found to be inaccurate. The advantage of the horizontal distance of the great circle was that it accounts for turns during flight. By using the VISST cloud-top height, the vertical proximity to cloud can also be estimated. It is possible that clouds on the sides of the aircraft that were not penetrated would have been missed. However, they would also have to miss the 4-km resolution of VISST. There was no way to account for all clouds and their possible influences on NPF.

Figure 3.14 shows the number of 1 Hz samples collected as a function of altitude and distance to cloud. In general, the number of samples collected away from clouds exceeded those near clouds. The highest number density was at an altitude of 15 km and a distance of 14 km away from cloud. This was associated with the aircraft sampling the region above the tropopause and in the lower stratosphere. Although cloud tops can push into the lower stratosphere, these intrusions were isolated in area. Another maximum was observed at an altitude of 11 km where it appears that the aircraft collected samples very close to the cloud edge. Over the period of the project the aircraft targeted cirrus clouds and conducted many cloud penetrations, so a maximum at the level of cirrus formation

and deep convective outflow is expected. Of interest is the mean number density at 7 km altitude close to the cloud edge. This altitude is typical of convective cloud top outflow below the polar jet. It is apparent that the two peaks near cloud, one at 11 km and the other at 7 km, are linked with sampling cloud development associated with the subtropical jet and the polar jet, respectively.

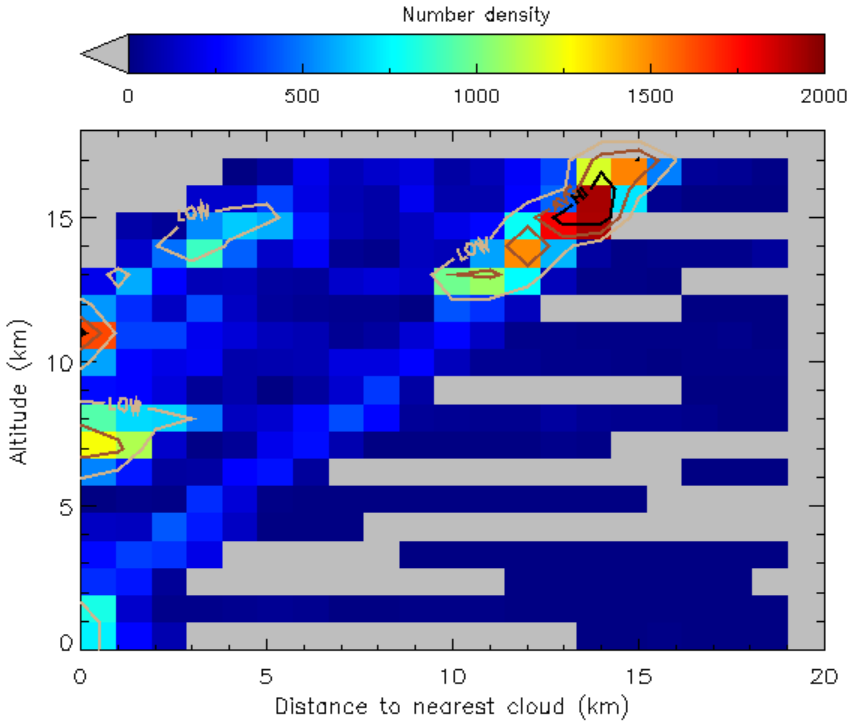

Figure 3.14. Number of 1 Hz out-of-cloud samples and their distance to the nearest cloud (n = 70,787). The samples were binned in 1 km altitude and 1 km distance to cloud. The contour labeled 'LOW' defines 25 percentile of the density, 'AVG' defines 50 percentile of the density and 'HI' defines 75 percentile of the density.

3.5 Aerosol Size Distributions

The NMASS and FCAS measurements were combined to produce a size distribution for particles with D_p in the range 4 to 1000 nm. An inversion code based on the nonlinear technique of Markowski (1987) was used to solve for $N(D_p)$. As discussed

earlier, the NMASS response matrix consists of the fraction of particles counted by each CPC for nearly monodispersed aerosol. The FCAS response matrix is based on pulse heights resulting from measurements of the fraction of particles counted for monodisperse test aerosol. The data reduction and inversion include corrections for passing efficiency through the sampling inlet. Once the corrected size distributions were produced the samples that were determined to be in-cloud are replaced with not-a-number.

Figure 3.15 shows the combined NMASS and FCAS size distributions with NPF that were measured in the upper troposphere. A total of 12,010 out of cloud size distributions were measured in this layer. In the figure, one size distribution is plotted every 60 samples. The 25 percentile, median and 75 percentile values for the size distribution are shown along with the mean. The median and mean values were calculated for each bin in the size distribution. The median is the 50 percentile value in each bin while the spread is captured by the 25 and 75 percentile values. The individual size distributions indicate the amplitude range. As expected, the mean was above the median in all size bins. At sizes larger than 0.4 μm the mean diverges from the 75 percentile and is skewed towards the maximum values at the large end tail of the size distribution. Because of this divergence, the mean was not used for the fitting procedure described in Chapter 5. Rather, the 25 percentile, median, and 75 percentile values were used. This is due to the high sensitivity of the model simulation to the preexisting surface area which is highly impacted by the number of particles in the large end tail of the size distribution.

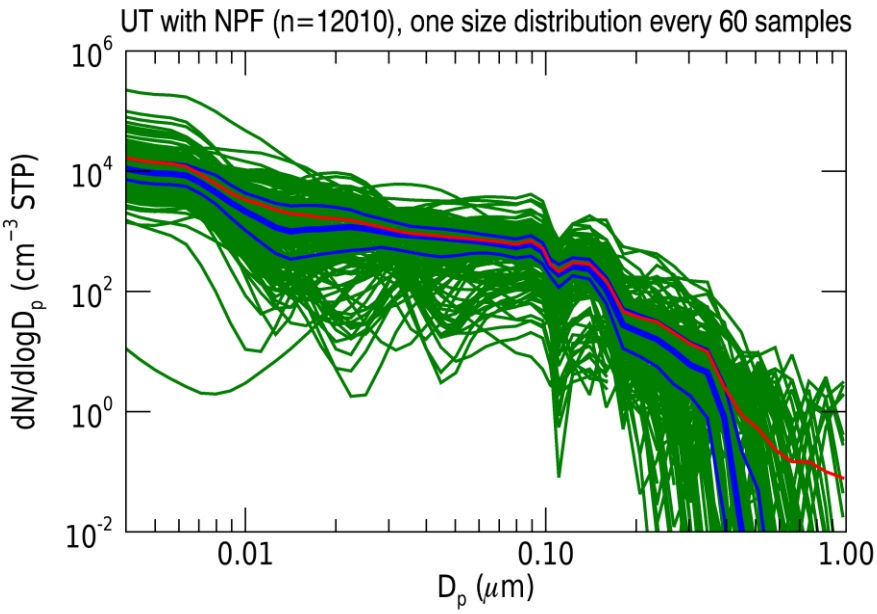

Figure 3.15. Measured aerosol size distributions with NPF in the upper troposphere (UT). The number of samples (n) is 12,010. One size distribution is plotted every 60 samples. The red line is the mean. The thick blue line is the median, and the thin blue lines are the 25 and 75 percentile values. All data are out of cloud.

3.6 Summary

In this chapter, I have described the instrumentation and data processing procedures that were used in obtaining a size distribution that was not impacted by cloud artifacts. To do this, clouds had to be detected by the analysis of multiple cloud hydrometeor spectrometers and water vapor hygrometers. This dissertation is also concerned with the proximity of cloud to NPF and as such the nearest distance to cloud had to be calculated. This calculation does not account for all clouds and their possible influences on NPF. The objective was to limit the likelihood that cloud artifacts modified aerosol size distributions and to minimize the impact of cloud processing on the modes of the size distribution. A new diagnosing parameter called “relative difference” is formulated to detect the fraction of potential new particles that fall at 3-sigma above the

mean of the probability distribution function. The probability that the positive difference in mixing ratio of particles between ~5 nm to ~8 nm occurred due to counting statistics is less than 0.13%. A criterion was established, and it was used to detect NPF. In Chapter 4 I analyzed the MACPEX trace gas data to identify the tropopause and the mixing layer between the troposphere and the stratosphere. Based on the new stringent and statistically significant criteria for nucleation and the identification of the tropopause, I described NPF events in relation to the origin of the air in which they were observed.

Chapter Four: New Particle Formation Observations in the Mid-Latitude Upper Troposphere

4.1 Introduction

Aerosols exhibit large temporal and spatial variability in the atmosphere. As outlined in Chapter 1, the importance of the aerosol radiative forcing is well recognized, but gaps exist in modeling aerosols in the free troposphere (FT), upper troposphere and lower stratosphere (UTLS). While nucleation in the boundary layer has been the focus of several studies, few experiments have investigated the frequency of NPF in the UTLS. Brock et al. (1995) identified a region of enhanced particle number mixing ratio in the mid-latitude lower stratosphere above the tropopause and attribute this enhancement to particles produced in the upper tropical troposphere by homogenous binary nucleation of sulfuric acid and water vapor transported to the lower mid-latitude stratosphere. Particle nucleation in the UTLS was found to be sensitive to the preexisting particle number concentration and water vapor mixing ratio in the mid-latitudes (de Reus et al., 1998). Lee et al. (2003) identified a local source of new particles in the UTLS through ion-induced nucleation when there is sufficient sun exposure and low surface area. Several factors favor ion-production in the UTLS including the presence of gas-phase ions generated by galactic cosmic rays, low temperature, and relatively low surface area of preexisting aerosol. New particle formation in the UTLS has been observed in mid-latitude tropopause folds where nucleation rates are increased with mixing of

stratospheric and tropospheric air (Young et al., 2007). Weigel et al. (2011) identify numerous NPF events in the UT Tropical Tropopause Layer (TTL) and the outflow of tropical convection. They narrow the altitude of the main source region of NPF to the level of main tropical convection outflow at the bottom of the TTL. After growth, the nucleation mode particles may act as CCN or enter the stratosphere where they maintain the stratospheric background aerosol.

Since frontal systems frequent the mid-latitudes, deep convection often develops, and convective cloud tops reach the UT. In several measurement studies (Radke and Hobbs, 1991; Schröder and Ström, 1997; Clark et al., 1998; Clark et al., 1999; Ström et al., 1999; Wang et al., 2000; de Reus et al., 2001; Twohy et al., 2002; Clement et al., 2002; Lee et al., 2004; Weigelt et al., 2009; Frey et al., 2011; Weigel et al., 2011) high number concentrations of aerosol particles were found in the vicinity of deep convection. Radke and Hobbs (1991) reported regions of high humidity and high aerosol concentrations producing an Aitken nuclei "halo" around cumulus clouds. Easter and Peters (1993) found that turbulent fluctuations of temperature and water vapor showed new particle formation peaking at conditions of lower temperature and higher relative humidity. Their modeling results predict that a 2°C change in temperature or 6% change in relative humidity would be sufficient to increase nucleation rates by an order of magnitude even when the preexisting surface area is high. Bigg (1996) suggested that very sudden mixing events associated with breaking waves in strong thermally stratified atmospheric layers, wind shear and gravity waves may lead to particle formation due to the sensitivity of binary nucleation rates to relative humidity and temperature. Nilsson

and Kulmala (1998) studied the formation of sulfate aerosol particles due to mixing and found that the nucleation rate is enhanced by two orders of magnitude when two air parcels with different temperature and relative humidity mix with each other. They find that mixing increases particle nucleation due to the curvature on the H_2SO_4 vapor pressure diagram and identified that mixing can dominate the effect proposed by Easter and Peters (1993) where fluctuations in temperature and relative humidity are a prerequisite for enhancement in nucleation. DeFelice and Cheng (1998) suggest that droplet fragmentation of evaporating cloud drops could be a source of new particle formation. Enhanced concentrations of H_2SO_4 and freshly formed 3-4 nm particles were measured near cloud in droplet-free air in a region of upwelling short wave UV radiation (Weber et al., 2001). This new particle formation activity was attributed to enhanced OH concentrations above clouds relative to cloud-free regions.

In most cases, it is suggested that binary homogeneous nucleation in the vicinity of convective clouds is the nucleation mechanism that is active (Clark et al., 1999). de Reus (2001) used back trajectory analysis and satellite-retrieved cloud top temperatures to show that ultra-fine particles originated from the outflow of large convective systems. Twohy et al. (2002) observed greatly enhanced particle concentrations above and downwind of the cirrus anvil associated with a large mesoscale convective system. These particles were likely small sulfate particles produced by high concentrations of gas-phase precursors that traveled through the convective region from lower in the atmosphere. The high relative humidity and low preexisting particle number concentration in the outflow

region of convective clouds and the strong decrease in temperature of the air as it rapidly rises through convection are thought to trigger new particle formation.

Intrigued by some of these observations of nucleation, Kulmala (2006) designed a laboratory experiment to simulate this process of NPF in the vicinity of clouds. It was found that ambient water insoluble trace gases were able to produce new aerosol particles by homogeneous nucleation under cloud like conditions, which is a plausible explanation for new particle production inside cloud anvils and cloud outflows. The nucleation of water insoluble trace gases after cooling can explain the new aerosol production and observed aerosol number concentrations in the UTLS region (Kulmala et al., 2006). Unfortunately, the identity of vapors participating in nucleation and subsequent growth remains unknown.

Weigelt et al. (2009) investigated the influence of clouds on aerosol particles in the upper troposphere statistically, from the tropics to mid-latitudes as part of the Civil Aircraft for the Regular Investigation of the Atmosphere Based on an Instrument Container (CARIBIC) project. This study concludes that over the Arabian Sea and the Caribbean the majority of clouds act as a source of new particles. The clouds over the Arabian Sea act as a sink for Aitken and accumulation mode particles and as an indirect source for Aitken mode particles by the growth of the freshly nucleated particles with time. Clouds over the Middle East seem not to act as a source for new particles due to the less frequent occurrence of deep convection. Over the mid-latitude North Atlantic Ocean, the majority of the clouds do not influence nucleation mode aerosol concentration. Nevertheless, a few clouds provide such a strong contribution to the formation of new

particles that the nucleation mode aerosol concentration is increased up to 175% above the background level (Weigelt et al., 2009). Since several types of clouds occur at mid-latitudes, there could be varying effects on the aerosol particles.

High concentrations of condensation nuclei have frequently been observed in the vicinity of clouds. Lee et al. (2004) found high concentrations of ultra-fine particles interstitially in cirrus clouds suggesting that cirrus clouds in the UT may provide favorable conditions for NPF, such as low temperatures, high relative humidity with respect to ice, and high OH production. However, ice crystal particles shatter upon impact, and the generation of secondary artifact particles by sampling inlets can contaminate aerosol samples (Murphy et al., 2004). Weber et al. (1998) claim that measurements of elevated concentrations of condensation nuclei reported by Clarke et al. (1998) were not authentic, but instead, a sampling artifact, likely related to fragmentation of cloud drops impacting the aerosol inlet. In this case measurement artifacts from fragmented droplets were observed at temperatures down to -20°C, spanned a broad size range with diameters down to 3 nm, and were correlated with liquid water (Weber et al., 1998). In another study, Kojima et al. (2004) measured aerosol particles in the UTLS using transmission electron microscopy (TEM) during the Cirrus Regional Study of Tropical Anvils and Cirrus Layers-Florida Area Cirrus Experiment (CRYSTAL-FACE) and found that in-cloud samples contained abundant zinc-rich particles. Their origin was unclear, but it was suggested that they are contaminants that originated through impact by ice cloud particles on the sampling system (Kojima et al., 2004). Zinc particles were found to increase in number with the amounts of ice particles and were related to the

volumes of ice crystals detected in the sampling period. These findings show that great care must be taken when reporting aerosol measurements from airborne platforms in and around clouds, and is particularly pertinent to NPF studies by homogeneous nucleation in the vicinity of clouds.

In this dissertation, episodes of NPF that occurred during the Mid-latitude Airborne Cirrus Properties Experiment (MACPEX) campaign were identified, and the characteristics of the particle formation events in relation to whether they were observed in stratospheric, tropospheric or mixing layer air were examined. The identification of the tropopause layer followed studies that use gas tracer relationships to examine stratospheric-tropospheric exchange (Boering et al., 1994; Fischer et al., 2000; Hoor et al., 2002; Zahn et al., 2000, 2004; Pan et al., 2004; Pan et al., 2007a, 2007b). A focus of this chapter was to identify the mixing layer between the troposphere and the stratosphere using observations of trace gases. Based on the new stringent and statistically significant criteria for nucleation (see Chapter 3) and the identification of the tropopause, I describe NPF events in relation to the origin of the air in which they were observed.

4.2 Defining the Tropopause

The aerosol above and below the tropopause is expected to differ in residence time, composition, source region, and formation mechanism. Tropospheric and stratospheric air differ significantly. However, the effort to precisely define when one goes from the troposphere to the stratosphere is fraught with difficulty. As Edwin Danielsen said, “The tropopause is not made of Saran Wrap.” The point at which the

transition from the troposphere to the stratosphere is judged to happen depends upon the property upon which the judgment is based. In this work, I investigate the origins of particles which were formed in response to the presence of precursor gases and reactive species, low temperatures, high supersaturations of water vapor, sunlight, preexisting aerosol surface and other factors in varying proportions. The key variables change as one moves from tropospheric to stratospheric air, and they change in different ways depending on the property. In this study, it was useful to focus on a chemical tropopause and to attend to mixing between tropospheric and stratospheric air.

There is no unique way to define the tropopause, and the results of the definition may depend on the method used. The tropopause has been described using different algorithms due to the uncertainty in defining this boundary. Empirical definitions are incomplete since each of them is primarily based on isolated properties of the tropopause boundary. The analysis approach was to use different definitions of the tropopause to allow a more thorough characterization of this layer. The approach was to use tracer-tracer correlations to separate tropospheric air from the stratospheric air and the mixing layer. To demonstrate that the troposphere, stratosphere and mixing layer were adequately identified the dynamic tropopause and thermal tropopause definition was used to describe the tropopause layer.

4.2.1 Determination of chemical tropopause by tracer-tracer correlations.

The correlation between a tropospheric and a stratospheric tracer has been used to identify the chemical transition across the tropopause (Fischer et al., 2000; Hoor et al.,

2002; Zahn et al., 2000; Pan et al., 2004). To determine the location of the tropopause both the O_3 - CO and O_3 - H_2O correlations have been analyzed. O_3 and CO are the classical pair of tracers used to study O_3 transport in the stratosphere as well as the photochemical formation of O_3 in the troposphere. Here the two contrasting tracers were used to identify tropospheric and stratospheric air near the tropopause: O_3 marking stratospheric air and CO marking tropospheric air. It is well known that O_3 and CO exhibit a strong gradient across the tropopause and as such can be used as tracers of mixing between tropospheric and stratospheric air (Hoor et al., 2002). The abundance of CO in the stratosphere is due to the transport of CO from the troposphere to the stratosphere, the production of CO in the stratosphere and destruction of CO in the stratosphere. In the troposphere, CO is produced by the partial oxidation of carbon-containing compounds. In the stratosphere, CO is produced from the oxidation of CH_4 by OH and removed by oxidation with OH. The removal of CO is faster in the stratosphere than the temperature dependent CO production (Crutzen, 1979). The predominant removal of CO in the stratosphere leads to a stable equilibrium between the production and destruction of CO on a timescale of months (Hoor et al., 2002). Therefore, in the absence of recent mixing with tropospheric air, CO concentrations are at their lowest (~ 20 – 40 ppbv) and are strongly influenced by transport processes. O_3 is produced in the stratosphere by the photolysis of oxygen molecules by energetic UV light. It has a lifetime of one year in the lower stratosphere at mid-latitudes (Solomon et al., 1985). Therefore the gradients of CO and O_3 near the tropopause are opposite in sign.

Since the objective of the campaign was to target mid-latitude cirrus, the aircraft often flew near the jet stream and within anvil cirrus where the highly variable structure of CO and O_3 are often observed. To identify tropospheric and stratospheric air, the correlations between CO and O_3 were used. If no mixing is assumed between the troposphere and the stratosphere, the CO and O_3 mixing ratio should exhibit compact relations. The nearly constant value of CO with increasing O_3 indicates the stratospheric branch while increasing CO and nearly constant O_3 indicates the tropospheric branch. This idealized relationship between CO and O_3 can be expected to display an L-shape in a scatter plot of O_3. vs. CO. Mixing between tropospheric and stratospheric air can be identified by deviations from this L-shape formed by the CO and O_3 trend lines (Fischer et al., 2000; Hoor et al., 2002). Figure 4.1 shows CO and O_3 data for the six MACPEX flights that were analyzed. The stratospheric branch was identified by low CO concentrations and strongly increasing O_3 ranging from 100 to 820 ppbv. The tropospheric branch was characterized by low O_3 and CO concentrations varying from 70 to 190 ppbv. Trend lines are shown in the stratospheric and tropospheric branch in Figure 4.1. If these trend lines were extended towards decreasing values, they would intersect at an O_3 mixing ratio of about 40 ppbv and CO of 48 ppbv. This is a region of the curve with no data indicating that the correlation is non-linear. This occurs at the tropopause where mixing between the troposphere and the stratosphere results in linear mixing lines connecting the stratosphere and the troposphere regions. Figure 4.1 shows trend lines that cross the tropospheric and stratospheric branch. In the concept of tracer-tracer correlations such mixing lines will only form if the mixing is irreversible (Hoor et al.,

2002). Due to the vertical stability that is a characteristic of lower stratospheric air, the "mixing layer" can be observed just above the local tropopause as a mixture of stratospheric and tropospheric air (Fischer et al., 2000). On the stratospheric branch, the steep slope and tight correlation at O_3 > 400 ppbv indicate that no recent mixing with tropospheric air had occurred in this region. The quasi-horizontal tropospheric branch was identified for O_3 < 130 ppbv and a CO > 70 ppbv. Between the two branches, the scatterplot shows data points in the mixing layer with slightly curved mixing lines of intermediate slope. The linearity of these mixing curves indicates a rapid and frequent mixing of the tropospheric and stratospheric air masses (Hoor et al., 2002), which is expected considering the aircraft flew near the jet stream. Each measurement was flagged to identify it as being made in the stratosphere, troposphere or mixing layer.

O_3 and H_2O correlations can also be used to identify the region of the mixing layer between the troposphere and the stratosphere. As in O_3 - CO correlations an L-shape is expected in O_3 vs. H_2O plots as a result of the strong gradients of the tracers across the tropopause, the limited cross-tropopause mixing of tropospheric H_2O and slow ascent of air. Therefore, water vapor in the stratosphere decreases as the tropopause is approached from the troposphere and often coincides with the decrease in CO and increase in O_3 (Fueglistaler et al., 2009).

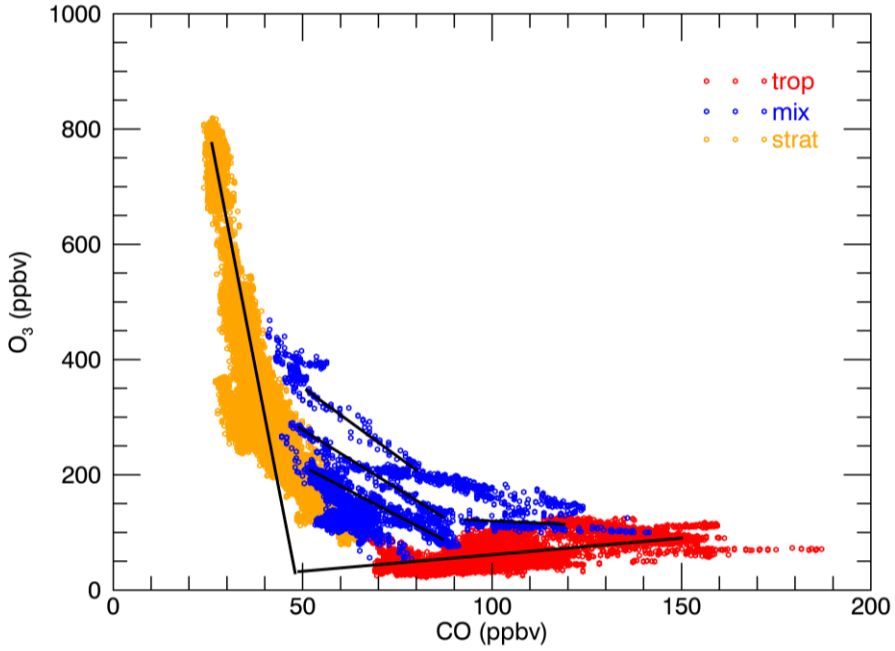

Figure 4.1. Scatter plot of CO and O_3 for six MACPEX flights. The red points show the tropospheric relationship between CO and O3 (trop), orange points show the stratospheric relationship (strat) and the blue show the result of mixing (mix).

Figure 4.2 shows the O_3 - H_2O scatter plot. The tropospheric branch was contained at H_2O > 13 ppmv and O_3 < 110 ppmv. The tropospheric branch was mostly contained at H_2O < 10 ppmv with a more compact correlation at O_3 > 400 ppmv. However, with flight segments penetrating the jet stream, it is expected that mixing lines occur. These are apparent as lines that cross from the tropospheric to the stratospheric branch. The nearly straight segments between the tropospheric and stratospheric branches of the scatter plot are interpreted as demonstrating mixing between reservoirs of trace species with abundances represented by the end points of the segments. Moving along the line from the tropospheric reservoir to the stratospheric reservoir shows the change in

the composition of the air shifting nearly linearly from the tropospheric abundances to the stratospheric abundances.

Using the troposphere, mixing and stratosphere identifications determined from the O_3 and CO plot, O_3 and H_2O were plotted to see whether the same thresholds apply. The mixing layer data points in Figure 4.2 (blue data points) are located in the region between the two branches, but appear to be less defined especially when the mixing lines approach the stratospheric branch. It should be noted that H_2O vapor is not as good a long-lived tracer as O_3 and CO. H_2O vapor is not conserved as an air parcel experiences colder temperatures in the upper troposphere where phase transitions and removal by sedimentation can occur. Heterogeneous freezing processes are temperature dependent, impacting H_2O mixing ratio. High-altitude cirrus cloud formation can dehydrate the rising air near the tropopause (Jensen et al., 1996). Since the aircraft targeted cirrus clouds, there is some uncertainty when classifying these data in the mixing layer. This could be one of the reasons why some of the stratospheric air points appear on mixing lines in Figure 4.2. Regardless O_3 - H_2O correlations have been used to identify the mixing of stratospheric and tropospheric air near the tropopause (e.g. Krebsbach et al., 2006; Pan et al., 2007a, 2007b).

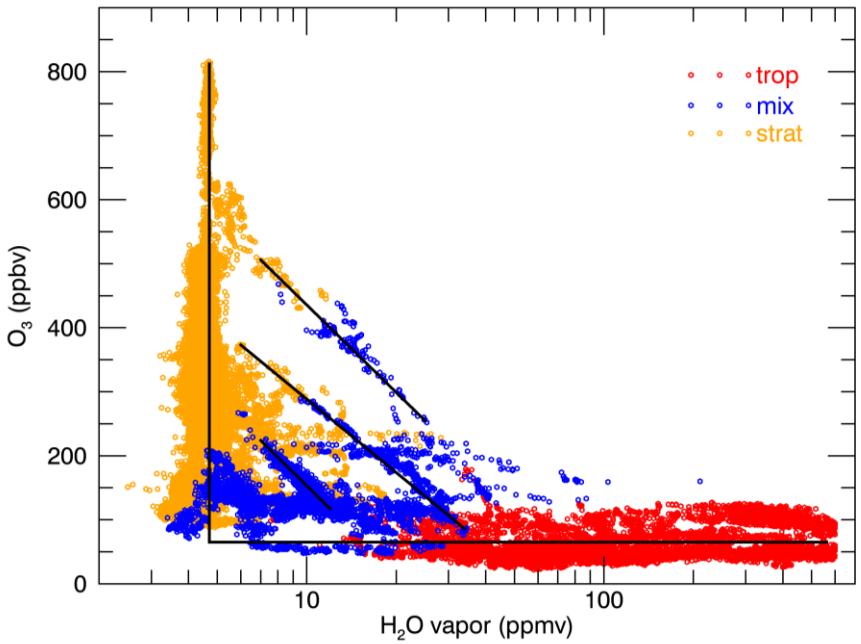

Figure 4.2. Scatter plot of H_2O and O_3 for MACPEX data. The red points show the tropospheric relationship between O_3 and H_2O (trop), orange points show the stratospheric relationship (strat) and the blue show the result of mixing (mix).

4.2.2 Determination of dynamic and thermal tropopause.

The determination of the dynamic and thermal tropopause is made by the analysis of mesoscale thermodynamic features. The spatial and temporal evolution of the mesoscale and synoptic meteorology was discussed in Chapter 2. In this section, I use temperature profiles and vorticity fields obtained from the NASA Modern-Era Retrospective Analysis for Research and Applications (MERRA) reanalysis dataset (described in Chapter 2). The thermal tropopause heights were determined using the World Meteorological Organization (WMO) definition as "the lowest level at which the lapse rate decreases to 2 °C/km or less, provided that the average lapse rate between this level and all higher levels within 2 km does not exceed 2 °C/km" (WMO, 1957). This

same definition is in use for the tropopause determination using routine sounding measurements.

The dynamic tropopause, defined using isentropic potential vorticity (PV), locates the continuous surface that separates the chemically distinct tropospheric and stratospheric air masses (e.g. Danielsen, 1968; Shapiro, 1980; Holton et al., 1995, Pan et al., 2004; Pan et al., 2007a). The PV of an air parcel is conserved following its motion under adiabatic and frictionless flow (Holton, 1992). It is well suited to characterize barriers to transport (Ploeger et al., 2015). Regions of enhanced PV gradients are indicative of suppressed transport (Nash et al., 1996; Ploeger et al., 2015). A range of PV values have been used to define the dynamic tropopause, and most are in the range of 1.5 – 3.5 PVU (Pan et al., 2004). In this study, the dynamic tropopause was set to the altitude where the potential vorticity is equal to 2.5 PVU (1 PV = 10^{-6} K m^2/kg s). To analyze the MACPEX data, many of the measured parameters were averaged and normalized to the dynamic tropopause.

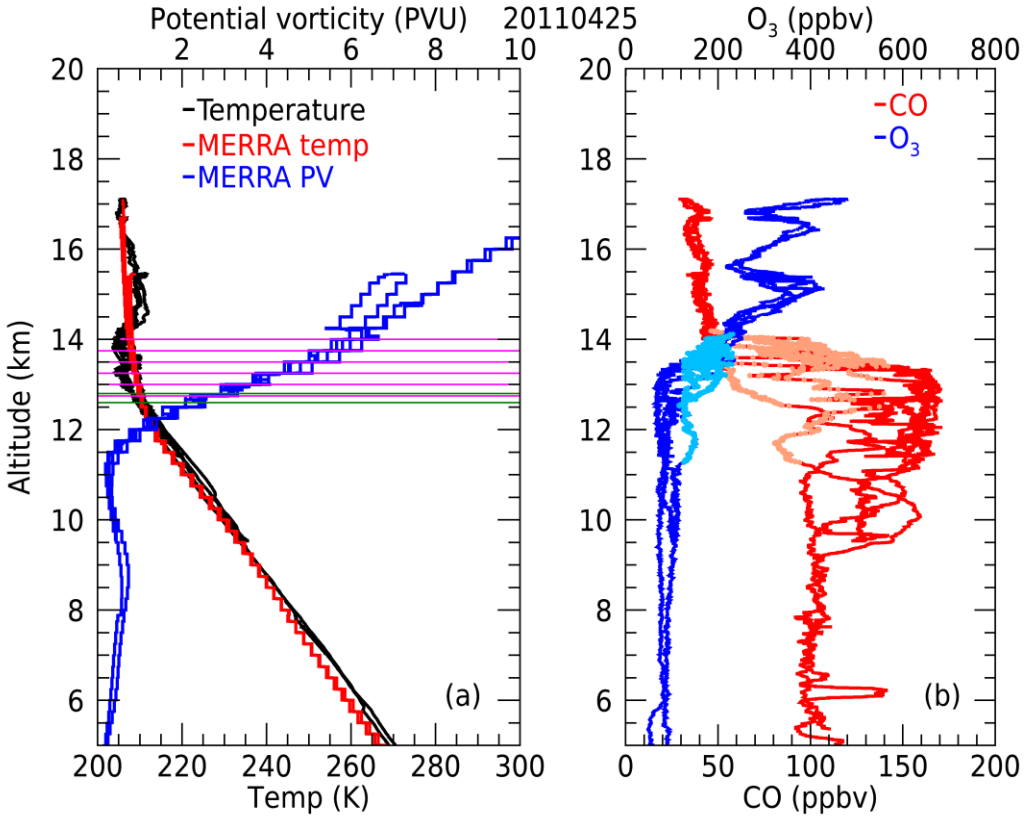

Figure 4.3. Vertical profile on 25 April 2011 from 5 to 17 km. (a) Vertical profile of measured temperature (black trace), MERRA temperature (red trace) and MERRA potential vorticity (blue trace). The magenta lines show instances when the thermal tropopause was diagnosed. The green lines show instances when the dynamic tropopause was diagnosed. (b) Vertical profile of measured CO (blue trace) and O_3 (red trace). The CO trace in the mixing layer is colored light red and that of O_3 light blue.

An example of the diagnosis of the thermal tropopause and the dynamic tropopause for the flight on 25 April 2011 is shown in Figure 4.3a. The magenta lines show instances when the change of the temperature lapse rate indicated the presence of a thermal tropopause. In this case, the thermal tropopause was diagnosed by the analysis of the MERRA temperature lapse rate when it decreased to 2 °C/km or less as defined by WMO. The green lines show instances when the MERRA PV was equal to 2.5 PVU and the presence of the dynamic tropopause. The thermal tropopause and the dynamic

tropopause were determined at 1 Hz using the MERRA data but the green and magenta lines were plotted every 1000 seconds so as to not clutter the plot. Figure 4.3b shows the traces of CO and O_3. It can be seen from the light red and light blue coloring of the CO and O_3 that mixing between these tracers was contained within the altitude range of ~ 11.5 km to ~ 14 km. Figure 4.3 shows that the sorting of the troposphere, mixing and stratosphere produces a coherent picture of the tracers and the dynamic tropopause. Appendix B Figure B1 shows the vertical profile for each flight.

Figure 4.4 shows the mixing ratio profiles of CO, O_3 and H_2O vapor relative to the altitude with respect to the thermal tropopause and dynamic tropopause. The contrast between the tropospheric air and stratospheric air is immediately apparent in both the thermal (Figure 4.4a-4.4c) and dynamic (Figure 4.4d-4.4f) tropopause. When the data points are organized by their altitude relative to the dynamic tropopause height a clear separation can be observed at the dynamic tropopause. The mixing layer was approximately centered at the dynamic tropopause (at a mean of 0.35 km above the dynamic tropopause) and below the thermal tropopause (at a mean of 1.5 km below the thermal tropopause). In this dataset, the dynamic tropopause best identifies the discontinuity in chemical composition between the troposphere and the stratosphere. The clear separation of the data points according to troposphere, mixing and stratosphere and their location with respect to the dynamic tropopause shows that the choice of the dynamic tropopause at 2.5 PVU and the identification of the points was consistent. The thermal tropopause as calculated from the MERRA analysis identified the cold point tropopause with the top of the tropopause layer at 0.19 km. The bottom of the

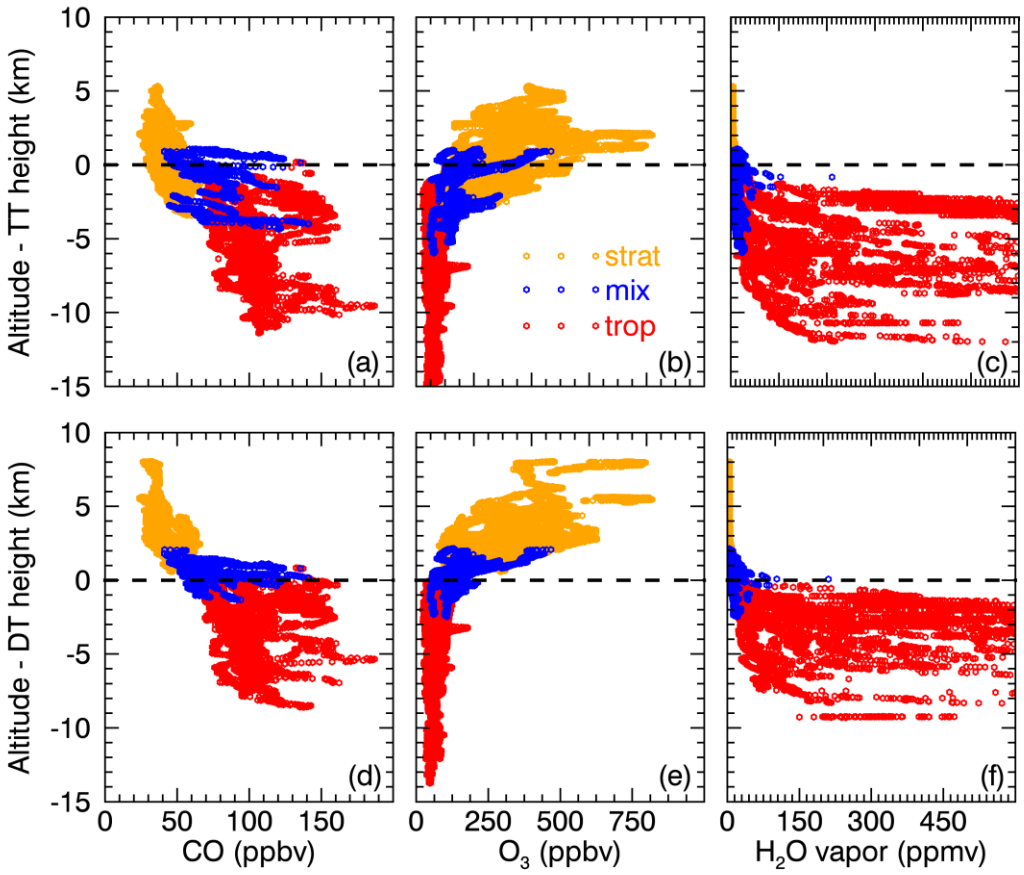

Figure 4.4. CO, O_3 and H_2O vapor mixing ratio profiles as a function of relative altitude with respect to thermal tropopause (TT) and dynamic tropopause (DT). The red data points have been classified as 'trop' for tropopause, blue as 'mix' for mixing layer and orange as 'strat' for stratosphere.

stratospheric layer was at 3.5 km below the thermal tropopause, the bottom of the mixing layer was at 6.0 km below the thermal tropopause, and the top of the mixing layer was at 1.1 km above the thermal tropopause. This indicates that most of the mixing was occurring below the thermal tropopause and (by definition) below the cold point tropopause. Since the aircraft was flying in cirrus and near to the jet stream, it is likely that more than one cold point tropopause was present. Pan et al. (2004) found that the

thermal tropopause is discontinuous in the vicinity of the subtropical jet and can have two values simultaneously. This is caused by the tropical air overlapping the mid-latitude airmass on either side of the jet, each separating tropospheric and stratospheric air. Since WMO (1957) identifies the thermal tropopause at "the lowest level at which the lapse rate decreases", it is likely that in the region where jet dynamics is present, stratospheric air intrudes below that level. This is consistent with the finding that the bottom of the stratospheric layer is below the thermal tropopause.

4.3 New Particle Formation Relative to the Tropopause

To provide an overview of the aerosol properties in the UTLS and the free troposphere during MACPEX, the aerosol data were presented in vertical profiles with altitude relative to the dynamic tropopause. The dynamic tropopause best defines the discontinuity in chemical composition between the troposphere and the stratosphere. The analysis proceeds to determine how the aerosol properties differ vertically and in the region of the tropopause and the mixing layer. Figure 4.5 shows the NMASS number concentration data for all six MACPEX flights. The five NMASS CPC channel number concentrations (N_5, N_8, N_{16}, N_{30} and N_{52}) are plotted relative to the dynamic tropopause. Each channel includes all the particles detected by the CPC. This diameter range extends from the lower detection limit to about 1 micron. Figures 4.6a-d show the total number concentration (N_5), ultra-fine particle concentration (N_5-N_8), the ratio of ultra-fine particles to the rest of the size distribution (N_5-N_8)/N_5 and the FCAS total surface area. All these data are grouped into three categories according to their classification as

tropospheric, mixing or stratospheric. The ratio $(N_5-N_8)/N_5$ was calculated to characterize the relative importance of the ultra-fine mode (or particles in the 5 to 8 nm size range) to the total number size distribution. To show the variability in the observations, the 25 and 75 percentile are also plotted. Figures 4.7a-4.7d show the nearest distance to cloud, the relative humidity with respect to liquid water (RH liquid), the relative humidity with respect to ice (RH ice), and the CO mixing ratio, respectively. Wind speed and direction vectors are plotted for the troposphere, mixing layer and the stratosphere. Figures 4.8a-d show the frequency of NPF in the troposphere, mixing layer and the stratosphere. Figure 4.8d expresses this frequency in percent by taking the ratio of the number of samples with NPF to the total number of samples in each 100-meter bin.

All reported data are out of cloud. The data were divided into 100 m altitude bins and median values calculated for each bin. Wind vectors were binned in 500 m. All aerosol number and surface area concentrations were reported at standard temperature and pressure (STP; temperature of 273.15 K and pressure of 1013.25 hPa). Table 4.1 reports median, mean and standard deviation values for various observed parameters in different layers observed during MACPEX.

The median N_5 in the troposphere ranged from 640 to 47,154 cm^{-3}, 517 to 2509 cm^{-3} in the mixing layer and 188 to 782 cm^{-3} in the stratosphere. High concentrations were found in the boundary layer from the surface up to 8.4 km below the dynamic tropopause (at -8.4 km or approximately 6.2 km above the surface). The maximum median concentration of 47,154 cm^{-3} was at -12 km (or approximately 2.6 km above the surface). The boundary layer total aerosol concentration had a decreasing trend

with increasing height. The median N_5 was 3685 cm^{-3} from -14.6 km to -8.4 km. Figure 4.6a shows that the variation in N_5 was small, as can be seen from the relatively small difference in the 25 and 75 percentile values, indicating similar altitude profiles for all six flights. Also, all five CPC channels of the NMASS (N_5, N_8, N_{16}, $N_{30,}$ and N_{52}) do not differ much in concentration suggesting that a significant fraction of the particles were in the accumulation mode (particles > 100 nm). The exception was the N_5 peak at 2.6 km above the surface that can be related to a narrow peak in ultra-fine particles (N_5-N_8) which also coincided with a peak in (N_5-N_8)/N_5. The peak in ultra-fine particles and the peak in ratio (N_5-N_8)/N_5 suggests that NPF produced these particles. This is related to a layer where measurements were being done at a distance of 15-35 km away from cloud, as shown in Figure 4.7a by the increase in distance to cloud at -12 km (upper quartile trace). Therefore, the boundary layer can be characterized as a region impacted by cloud with episodic NPF occurring in the boundary layer. Nucleation is mostly limited to the lower boundary layer close to the surface (where diurnal temperature inversions are typical) but was also present in thin layers (< 0.5 km deep) in the middle (-11.5 km) and the top (-9.7 km) of the layer at distances 15-35 km away from cloud.

Most variable were the N_5, and N_5-N_8 concentrations in the layer immediately above the boundary layer. Total aerosol number concentrations (N_5) dropped to a median value of 852 cm^{-3} at -8.3 km and increased steadily to a median value of 1181 cm^{-3} at -4.7 km. This layer from -8.3 km to -4.7 km had a median N_5 of 928 cm^{-3} and (N_5-N_8)/N_5 of 0.16. It was classified as middle troposphere due to its distinct properties compared to the boundary layer and the upper troposphere. It is not immediately impacted by cloud as the

aircraft remained on average (median) about 2-18 km at 50 percentile and 7-52 km at 75 percentile away from cloud. Figure 4.5 shows an order of magnitude difference between N_5 and N_{52}, a large variation in N_5-N_8 and (N_5-N_8)/N_5 in Figure 4.6b and 4.6c, as well as an increasing trend with height in the frequency of NPF in Figure 4.8a. On average, the median fraction of measurements with NPF increased from 3.7% in the boundary layer to

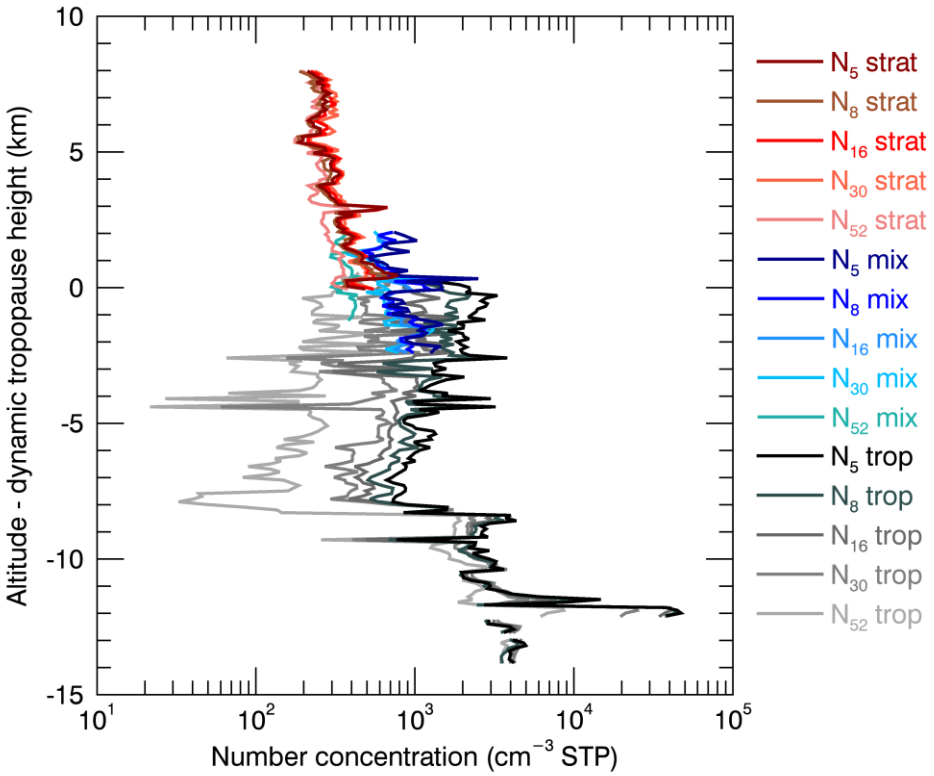

Figure 4.5. NMASS median altitude profiles in the troposphere (gray colors), mixing (blue colors) and stratosphere (red colors) for all five channels. The five NMASS CPC channels are N_5, N_8, N_{16}, N_{30} and N_{52}. All NMASS concentration units are in standard number of particles per cubic centimeter (cm^{-3} STP). The curves show concentrations (cm^{-3} STP) of particles larger than the lower cut-point given in nm by the subscript. All data are out of cloud.

21.6% in the middle troposphere. The approximate order of magnitude difference between N_5 and N_{52} and the increase in NPF frequency suggests that new particles formed in this layer.

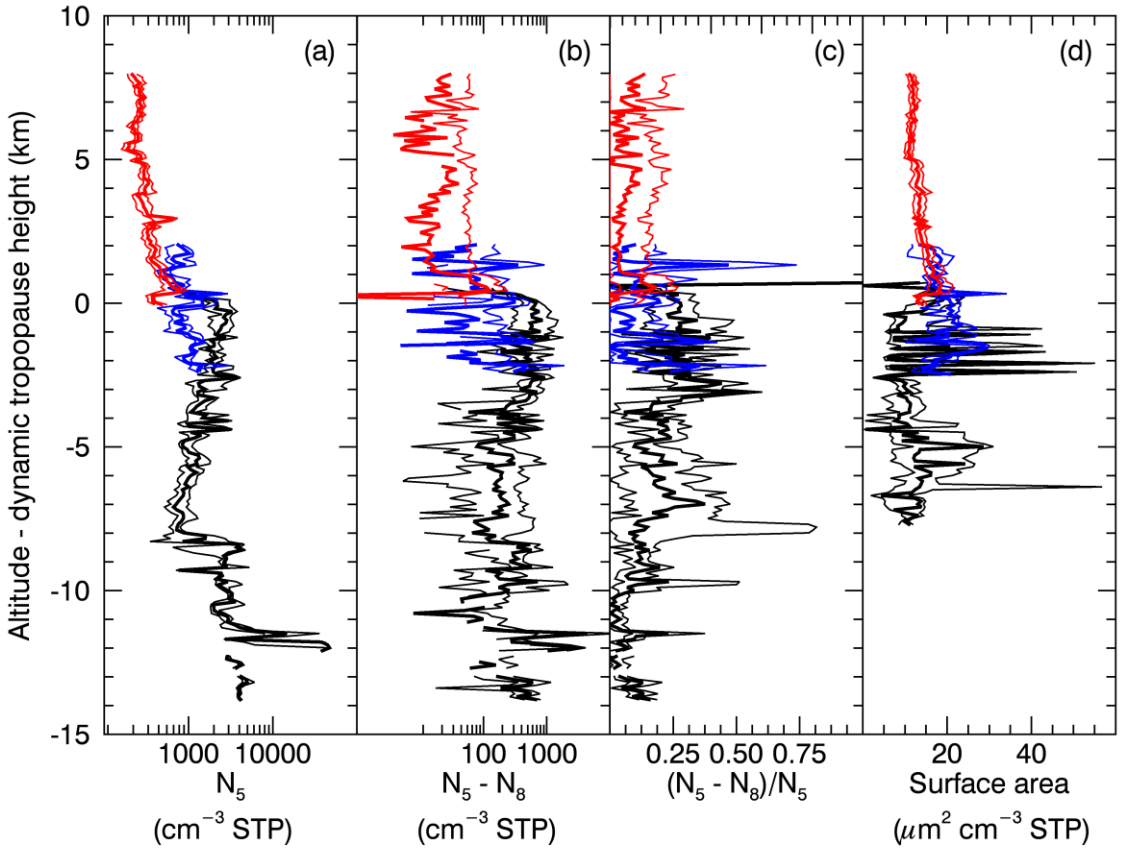

Figure 4.6. Vertical profile of aerosol concentrations in the troposphere (black), mixing (blue) and stratosphere (red). (a) NMASS N_5 concentration. (b) NMASS N_5-N_8 concentration. (c) NMASS (N_5-N_8)/ N_5 concentration. (d) FCAS total surface area concentration. The thick traces are median values and the thin traces are the 25 and 75 percentile values. All data are out of cloud.

The upper troposphere was defined as the layer from -4.7 km to +0.8 km. This layer was cloud impacted with distance to cloud at a median of 3 km compared to the

middle troposphere and mixing layer with a median of 6 km and 12 km respectively. At the very top of the layer, the distance to cloud increased to a median of 45 km at -0.7 km and down to 1 km at the dynamic tropopause. This was likely due to the aircraft flying within and in the proximity of cirrus clouds that form at the dynamic tropopause. Relative humidity was the highest with median values of 35% and 54% of relative humidity with respect to water and ice, respectively. Total particle number concentrations (N_5) increased to a median of 1999 cm^{-3} with a relatively high ultra-fine concentration (N_5-N_8) of 476 cm^{-3} and (N_5-N_8)/N_5 of 0.24. Surface area attained its lowest median value of 9.7 μm^2 cm^{-3} compared to 13.7 μm^2 cm^{-3} in the middle troposphere and 18.6 μm^2 cm^{-3} in the mixing layer. The upper troposphere was also a region with vertical wind shear where the wind velocity increased from 20 ms^{-1} at -4.6 km to 45 ms^{-1} at 0.4 km. Trace mixing ratios of CO were approximately equal to those in the middle troposphere (~ 100 ppbv) but higher than the mixing layer (63 ppbv). The fraction of (N_5-N_8)/N_5 was at its highest indicating that aerosol in the fine fraction was most significant in concentration. The fraction of measurements with NPF was 52.7%, making this layer most important for new particle formation.

The mixing layer was approximately centered at the dynamic tropopause as shown in Figure 4.8b. It was identified using O_3 - CO correlations as discussed in Section 4.2.2. The mixing layer was located from -2.5 km to +2.1 km relative to the dynamic tropopause (i.e. the mixing layer is 4.6 km deep). Total aerosol concentrations (N_5) had a median of 794 cm^{-3} in this layer with the fine fraction concentration at 88 cm^{-3} and (N_5-N_8)/N_5 of 0.11. A vertical wind shear gradient was present, with wind velocity at the top

and bottom of the layer of 15 ms^{-1} increasing to 45 ms^{-1} in the middle of the layer. The mixing layer was drier than the surrounding air in the upper troposphere. CO trace gas concentrations were also lower compared to the upper troposphere. On average, the mixing layer was the layer with the greatest surface area of 18.6 μm^2 cm^{-3}. The frequency of NPF was suppressed (10.7%) when compared to the upper troposphere (52.7%). Within the mixing layer a region of reduced $(N_5\text{-}N_8)/N_5$ ranging from median values of 0.01 to 0.1 was identified just below the dynamic tropopause (from -1.0 km to -0.2 km). This coincided with a region of low CO, a peak in relative humidity and maximum winds. This is thought to be the jet stream core due to the local maximum in the wind velocity (51 ms^{-1} at -0.5 km) and the anomalous drop in CO mixing ratio to 60 ppbv. Within the jet stream core NPF appeared to be suppressed, but it is enhanced immediately above (at 0 km) and below (at -1.4 km) the core where $(N_5\text{-}N_8)/N_5$ peaked at 0.2 and 0.37 respectively. The NPF peak below the core at -1.4 km coincided with a local drop in surface area from 26.4 μm^2 cm^{-3} at -1.4 km to 12.4 μm^2 cm^{-3} at -1.3 km. This is also a region of intense wind shear where the wind velocity increased from 18.5 ms^{-1} at -2 km to 34.8 ms^{-1} at -1.5 km. Above the jet core, a peak in CO mixing ratio of 97 ppbv was observed at 0.3 km. This coincided with relatively high relative humidity, wind shear (with a drop in wind speed from 36 ms^{-1} to 22 ms^{-1}) and a distinct peak in surface area (from 18.3 μm^2 cm^{-3} at 0.2 km to 28.2 μm^2 cm^{-3} at 0.3 km). This peak in surface area may have been related to cloud as the distance to cloud, and CO mixing ratio showed a large variability in this region.

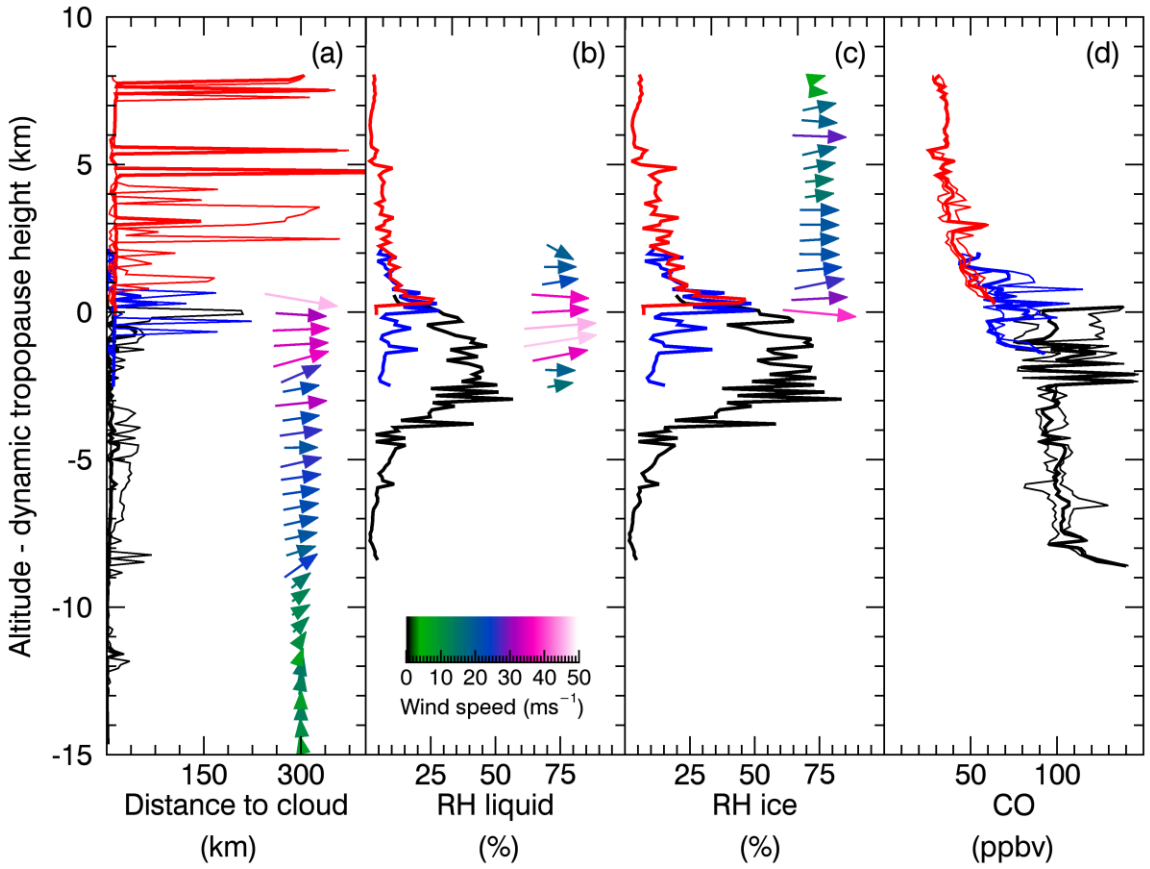

Figure 4.7. Vertical profile of meteorological variables in the troposphere (black), mixing (blue) and stratosphere (red). (a) Nearest distance to/from cloud along flight path. (b) Relative humidity with respect to water. (c) Relative humidity with respect to ice. (d) CO trace gas mixing ratio. The vectors in (a), (b) and (c) show the wind direction and wind speed for the troposphere, mixing and stratosphere respectively. The thick traces in (a) and (d) are median values, and the thin traces are the 25 and 75 percentile values. All data are out of cloud.

In the stratosphere (above the dynamic tropopause) N_5 and N_5-N_8 concentrations were at their lowest and the ratio $(N_5\text{-}N_8)/N_5$ ranged from median values of 0 to 0.18. The fraction of measurements with NPF was very small, with the only significant NPF occurring between 0.4 km and 0.9 km. This was a region of enhanced wind shear, relative humidity, and surface area. An increase in surface area was observed from 12.9 μm^2 cm^{-3}

at 0.3 km to 18.7 μm^2 cm^{-3} at 0.4 km. A distinct peak in CO mixing ratio to 59 ppbv was also observed at 3 km. This peak seemed to be related to cloud, and although a peak in N_5 was observed, this was not associated with significant NPF.

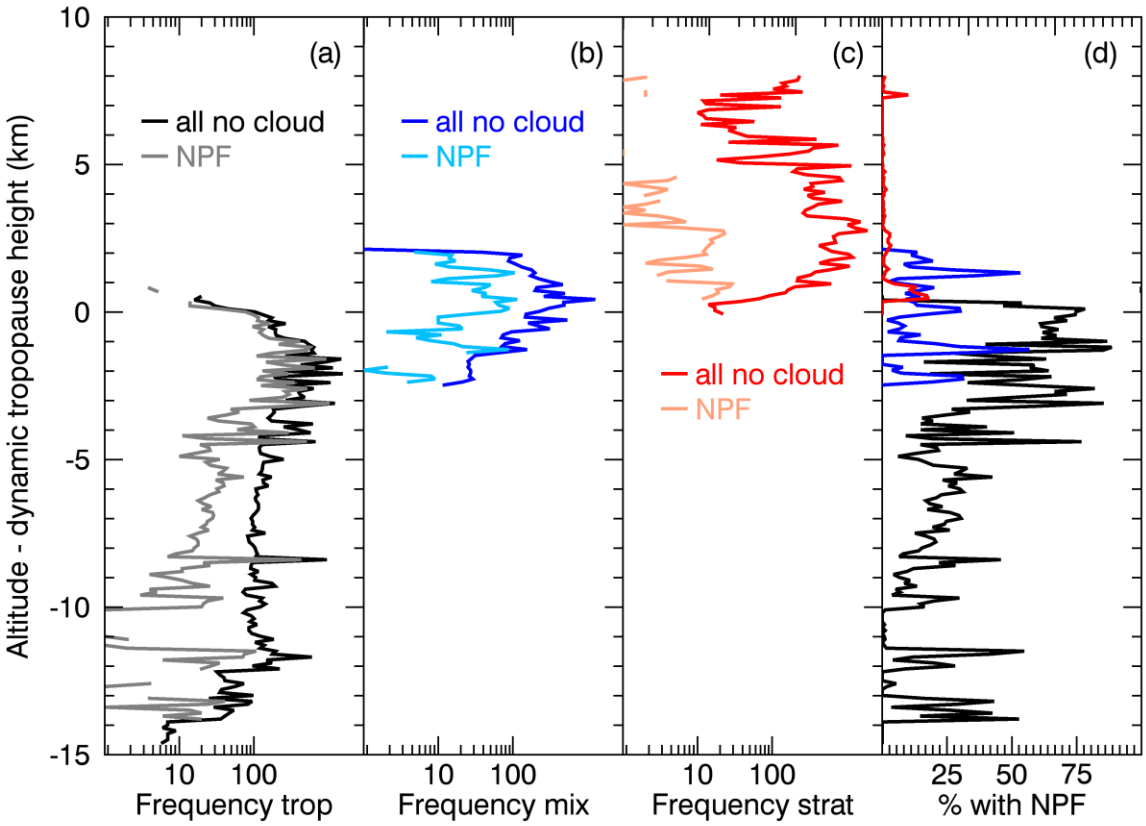

Figure 4.8. (a) Frequency of NPF in the troposphere. (b) Frequency of NPF in the mixing layer. (c) Frequency of NPF in the stratosphere. (d) Percentage of observations with NPF in the troposphere (black), mixing (blue) and stratosphere (red). All data are out of cloud.

In general, it was observed that the total aerosol concentration varied over two orders of magnitude from a few hundred in the stratosphere to occasionally more than 4×10^4 cm^{-3} near the surface. The lowest median values for total aerosol concentration (N_5) were found in the stratosphere between +5.0 km and +8.0 km relative to the dynamic

tropopause. Ultra-fine particles ranged from a few tens in the stratosphere to a few thousand cm^{-3} in the boundary layer. The ratio of ultra-fine particles to total particles (N_5-N_8)/N_5 was highest in the upper troposphere and most variable in the middle troposphere. In the stratosphere, the aerosol concentrations showed less variability. Surface area was also less variable in the stratosphere. The highest median layer surface area was in the mixing layer and the lowest in the upper troposphere. The upper troposphere was the layer with the highest N_5 in the free troposphere (excluding the boundary layer), the highest ultra-fine aerosol concentration, highest relative humidity, lowest surface area, lowest distance to cloud and highest fraction of measurements with NPF. The presence of ultra-fine particles in the upper troposphere was an indication of recent NPF by gas to particle conversion. Variability in surface area, CO, relative humidity, N_5, N_5-N_8, (N_5-N_8)/N_5 and percentage of NPF, seemed to be sensitive to the distance to cloud and the jet stream core. Therefore, it is quite evident that clouds and cloud edges in the upper troposphere had an impact on ultra-fine particles and new particle formation. The wind speed shear identified a region of intense mixing within the mixing layer due to the intense velocity gradient at the edges of the jet core. This region is also thought to be important for new particle formation.

Table 4.1. Median, mean and standard deviation values for observed parameters in different layers sampled during MACPEX. Distance in square brackets is relative to the dynamic tropopause.

	Boundary layer [-14.6 to -8.4 km]			Middle [-8.3 to -4.7 km]			Upper troposphere [-4.7 to +0.8 km]			Mixing layer [-2.5 to +2.1 km]			Stratosphere [0.0 to +8.0 km]		
	Med	$\bar{x}$	σ	Med	$\bar{x}$	σ	Med	$\bar{x}$	σ	Med	$\bar{x}$	σ	Med	$\bar{x}$	σ
N_5 (cm^{-3})	3685	6908	10889	928	1207	1483	1999	2322	1914	794	984	735	331	373	317
N_5-N_8 (cm^{-3})	354	848	2258	152	324	701	476	735	1327	88	181	494	17	46	237
(N_5-N_8)/N_5	0.1	0.12	0.11	0.16	0.22	0.22	0.24	0.27	0.19	0.11	0.15	0.16	0.05	0.1	0.12
Surface area (μm^2 cm^{-3})	16.5	16.6	1.8	13.7	17.0	12.2	9.7	16.7	16.2	18.6	19.1	5.3	13.6	13.9	2.7
Distance to cloud (km)	2	9	17	6	15	19	3	17	34	12	34	58	14	62	110
RH liquid (%)	2.8	2.9	0.8	4.7	6.9	5.9	34.8	33.5	17.0	13.0	16.3	10.8	6.6	7.3	4.1
RH ice (%)	2.7	2.8	0.8	6.1	8.7	7.8	54.0	52.3	27.1	23.7	29.6	20.0	12.3	13.6	7.8
CO (ppbv)	135	132	7	102	104	16	100	107	24	63	69	16	40	41	9
Fraction with	3.7	10.6	14.7	21.6	21.5	8.2	52.7	48.8	26.1	10.7	14.6	13.4	0.5	1.6	3.6

Med=median.
$\bar{x}$=mean.
σ=standard deviation.

4.4 Aerosol Size Distributions Relative to the Tropopause

Aerosol particles vary considerably in size, concentration, and distribution in space and time. Figure 4.9 shows the observed aerosol size distribution for the five different layers described in the previous section. The number of size distributions in each plot is shown in each panel. All out-of-cloud 1 Hz size distributions were used in calculating the median and mean. The highest layer, the stratosphere (ST), is in the top panel and the lowest layer, the boundary layer (BL), is in the bottom panel. The size distributions without NPF (left panel in Figure 4.9) are separated from those with NPF (right panel in Figure 4.9).

In the analysis of these size distributions, it was apparent that the median best represents the size distribution spectra. Much variability was observed in the size distributions between layers especially in the nucleation mode and at the tail end of the accumulation mode. In the boundary layer, the aerosol size distribution had a maximum at about 0.2 μm both in non-NPF and NPF cases. Four orders of magnitude difference were observed in the concentration of particles with and without NPF at 0.004 μm. The NPF case clearly showed more particles in the fine particle fraction as well as in particles < 0.07 μm in diameter. This was most apparent when comparing the median values for the size distribution (thick blue line). In the boundary layer non-NPF cases the median size distribution had a single mode, and that mode was in the accumulation mode. The accumulation mode contained on average an equal number of particles in the non-NPF and NPF case. Fine and ultra-fine particle modes were absent unless NPF was present.

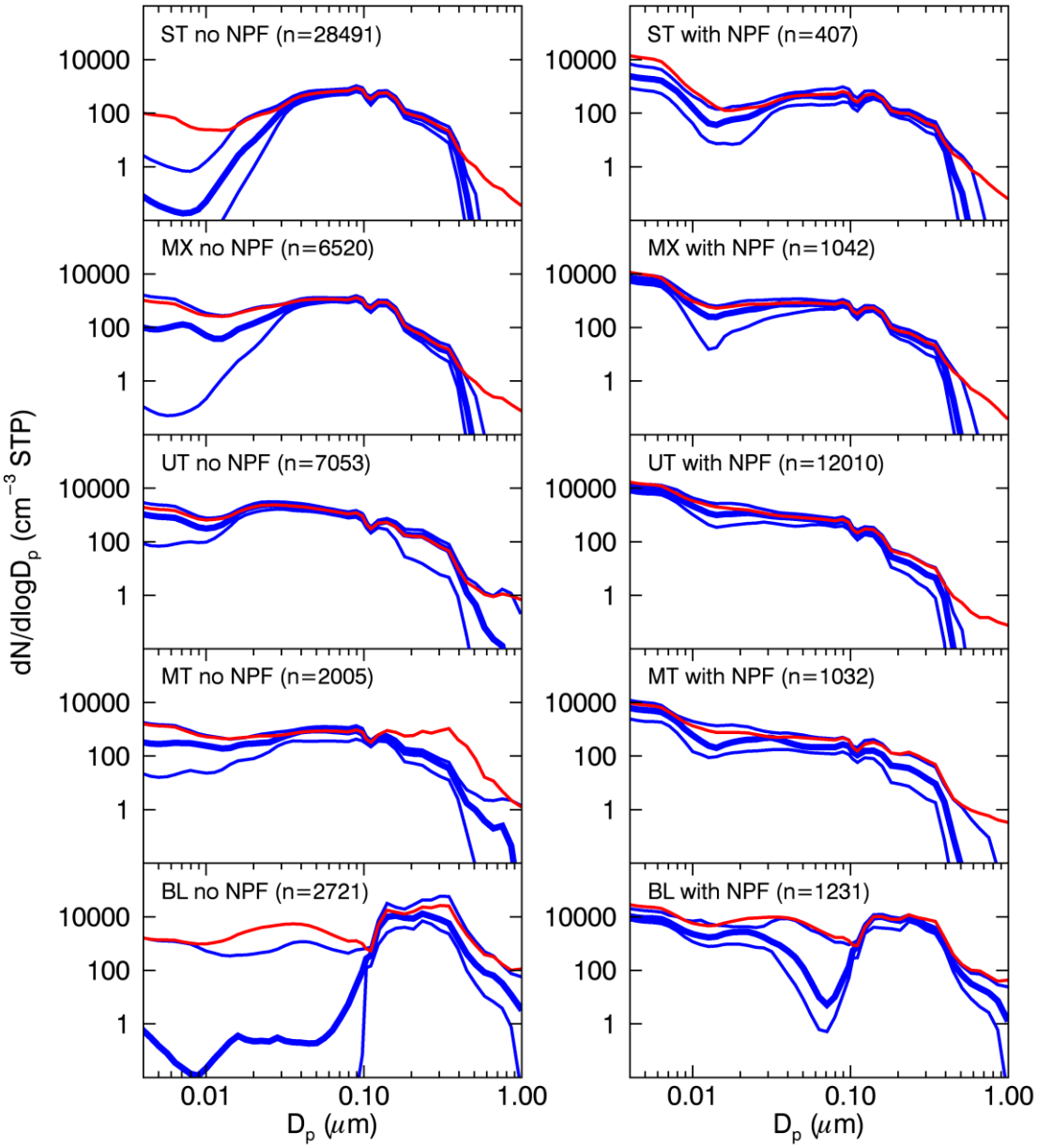

Figure 4.9. Measured aerosol size distributions with no NPF (left) and with NPF (right). Data were classified into five layers: stratosphere (ST), mixing layer (MX), upper troposphere (UT), middle troposphere (MT) and boundary layer (BL). The number of samples (n) is listed for each layer. The red line is the mean. The thick blue line is the median, and the thin blue lines are the 25 and 75 percentile values. All data are out of cloud.

This suggests that any particles in the nucleation mode quickly grew into the accumulation mode by coagulation and condensation.

In the middle troposphere, the concentration of accumulation mode particles was much lower, and fewer particles were measured at the tail end of the distribution. Comparing size distributions measured with non-NPF and NPF it was observed that a tail was largely absent in the NPF case. A nucleation mode was clearly distinguishable in the NPF case. The maximum in the aerosol size distribution was shifted to smaller sizes. In the middle troposphere, it was located at 0.06 μm in the non-NPF case and 0.026 μm in the NPF case (excluding the nucleation mode). Similar aerosol size distributions were observed in the upper troposphere, although the concentration of accumulation mode particles was slightly lower than in the middle troposphere due to fewer particles in the tail end of the distribution. Many more particles were measured in the fine fraction when compared to the middle troposphere. The maximum in the aerosol size distribution shifted further to smaller diameters in the upper troposphere and was 0.025 μm in the non-NPF case and 0.02 μm in the NPF case (excluding the nucleation mode). It was very clear that in the middle and upper troposphere, cases with NPF had fewer particles in the accumulation mode and tail end of the distribution. The variability in the size distributions was small especially for those with NPF in the upper troposphere.

In the mixing layer, the maximum of the size distribution shifted to larger sizes at 0.09 μm. There was a large similarity between the accumulation mode measured in non-NPF and NPF cases in the 0.04 μm and 0.5 μm diameter range. Two orders of magnitude difference were observed in the concentration of particles at 0.004 μm with and without

NPF and this increased to four in the stratosphere. In both the mixing layer and the stratosphere there was no significant difference between the number of particles in the tail end of the distribution for cases with and without NPF.

4.5 Discussion

Variability in surface area, CO mixing ratio, relative humidity and distance to cloud, all seemed to have an impact on the frequency of measurements with NPF. In the mixing layer, NPF was also related to the intensity of the wind shear at the jet stream core. The latter was associated with mixing processes around the jet which was found to occur at the dynamic tropopause, and the enhancement in NPF was located just above and below the jet core where wind speed was a maximum. It has been reported that in the tropical tropopause layer, vertical mixing occurs due to vertical shear in the tropical flanks of the subtropical jet and is controlled by the local horizontal strain and vertical shear rates due to wind (Konopka et al., 2007). To some extent this offers an explanation for upward transport of trace gases from the upper troposphere to the mixing layer. Above the mixing layer and in the stratosphere, the variability in CO mixing ratio, surface area, total particle number and ratio of ultra-fine particles to total particles was very low. From the low variability in these measured parameters, it can be deduced that the stratosphere is an aged layer that is not interacting strongly with the layer below it. The exception was the layer between 0.4 km and 0.9 km above the dynamic tropopause, a region of enhanced wind shear, relative humidity and surface area. In this region the frequency of NPF was high and then dropped at higher altitudes above the tropopause.

The fraction of measurements with NPF was quite significant in the middle troposphere (22%), upper troposphere (53%) and mixing layer (11%). In the stratosphere, the fraction of measurements with NPF was very small (0.5%) and no significant particle formation occurs. These layers are characterized by different properties and a single clear pathway to NPF is not immediately apparent.

Previous studies have shown that the upper troposphere is an active region photochemically due to the convective transport of radical precursors (Prather and Jacob, 1997; Collins et al., 1999). Studies have also shown that deep convection is an important transport process for tropospheric chemistry, providing an efficient mechanism for removing pollutants from the boundary layer and lifting them to higher altitudes (e.g. Lu and Turco, 1994; Hauf et al., 1995; Wang and Prinn, 2000). As mentioned earlier, CO is mainly produced by anthropogenic processes and therefore shows high concentration in the boundary layer and decreases with altitude. It is an inert tracer because of its low solubility and long lifetime. The decrease in CO mixing ratio from 135 ppbv in the boundary layer to 102 ppbv and 100 ppbv in the middle troposphere and upper troposphere indicates dilution of the boundary layer air when transported upward. Figure 4.7d showed that the mixing ratio of CO in the upper troposphere when the distance to cloud is very small was equal to that measured at the top of the boundary layer. These enhancements in CO appeared as peaks between -2.4 km and -1.0 km and coincided with frequent cloud penetrations and peaks in relative humidity and surface area. Immediately above this layer, at -1.0 km to 0 km, the variability above and below the median was large with 75 percentile values exceeding 120 ppbv in CO mixing ratio between -0.9 km

and 0.2 km, indicating that boundary layer CO was measured all the way up to the dynamic tropopause. Recall Figure 4.1 where few data points with mixing ratios of CO > 120 ppbv occurred along mixing lines branching the tropospheric air to the stratospheric air. This tropospheric-stratospheric mixing feature and the enhanced mixing associated with the jet stream are mechanisms that lift boundary layer CO deep into the mixing layer. Figure 4.7d shows that peaks in CO mixing ratio were measured in the mixing layer at 0.3 km (75 percentile of 107 ppbv) and 0.8 km (75 percentile of 115 ppbv).

Intense mixing has also been reported to occur in tropopause folds where the rapid transfer of subtropical air and tropospheric air enhances the mixing of boundary layer tracers (such as CO) into the lower stratosphere and promotes the generation of new particles (Zahn et al., 2000). Turbulence within folds is related to shear instability beneath the jet stream (Hartjenstein, 2000) and from deep convection that often reaches the tropopause (Browning and Reynolds, 1994). Recall in Chapter 2 Figure 2.6 that instances with drops in PV, identified as tropopause folds, were located in the PV contours on at least two days (20 April and 26 April). It is believed that these tropopause folds occurred frequently during MACPEX, especially during days with deep convection, and that NPF in the mixing layer was also associated with these folds. However, these tropopause folds were observed to occur very close to the convection and it was difficult to separate NPF data points associated with the fold from those associated with convection.

In addition to tropospheric-stratospheric mixing and tropopause folding, the enhancement in CO in the upper troposphere and the mixing layer may be due to

convective transport of boundary layer air. The aircraft mission was targeting cirrus clouds, some of which developed along the axis of the jet stream and others along the outflow regions of deep convective clouds. In the case of deep convection, it is possible for boundary layer CO, along with other trace gases, to vent into the upper troposphere and mixing layer. Mari et al. (2000) performed a modeling study and suggest that air with high levels of boundary layer trace gases can detrain from the plume of young (less deep) convection and subsequently entrained into deeper convection. The resulting convective ladder effect can transfer air from the boundary layer into the upper troposphere with little dilution. This ladder effect fits the CO vertical profile shown in Figure 4.7d where frequent young convection detrains boundary layer trace gases into the upper troposphere and less frequent deep convection further lofts these tracers deep into the mixing layer. It can be stated that the enhancement of boundary layer trace gases by convective transport results in the high frequency of NPF in the upper troposphere. It follows that the less frequent entrainment by deep convection of boundary layer trace gases from the upper troposphere into the mixing layer would lead to a lower frequency of NPF. The question is whether the process of NPF by gas-to-particle conversion is casually connected to the presence of convective clouds, or if it was just coincidence that the enhancement in CO is related to the occurrence of ultra-fine particles?

The role of deep convection in pumping gas precursors such as dimethyl sulfide and SO_2 in the nucleation of sulfate aerosol in convective outflow has been the subject of previous studies (e.g. Chatfield and Crutzen, 1984; Rodhe, 1999). Intense updrafts are associated with deep convection, with updraft velocities reaching 10 to 20 ms^{-1}, and

capable of lofting gases from the sub-cloud layer to the tropopause in the time scale of a few convective cycles. Also associated with convection is the large amount of precipitation that originates from ice particles that form in the middle troposphere and precipitate through the cloud and out of cloud base in the boundary layer. This precipitation scavenges trace gas species and aerosol particles. The updraft entrains air at all levels but in large volume at cloud base and within the boundary layer. As supercooled cloud particles freeze, energy is released, and the updrafts intensify, which entrains more air. Cloud detrainment occurs mostly at cloud top and in the anvil near the tropopause. Mari et al. (2000) model deep convective updrafts and study the entrainment and detrainment of trace gas species. They found that in deep convective outflows H_2O_2 was enhanced while HNO_3 was depleted. A substantial fraction of SO_2 was scavenged by aqueous reaction with H_2O_2 and O_3 leading to depletion of SO_2 in the convective outflow.

The question on whether NPF by gas-to-particle conversion is connected to the presence of convective clouds and tropospheric-stratospheric mixing is investigated further by plotting boxplots of observed parameters in each layer. Figure 4.10 shows boxplots with sample minimum, lower quartile, median, upper quartile, and sample maximum. Data with no NPF are shown in blue and data with NPF are shown in red for each layer. As expected, NPF cases had the largest median values in ultra-fine particles throughout the atmosphere. New particle formation was related to surface area as all NPF cases had a lower surface area when compared to non-NPF cases. Clouds appeared to have a stronger impact in the mixing layer than in the upper troposphere. In the mixing layer, NPF cases had higher CO mixing ratio, higher relative humidity and smaller

distance to cloud. This is a very clear indication of cloud outflow impacting processes that are connected to NPF.

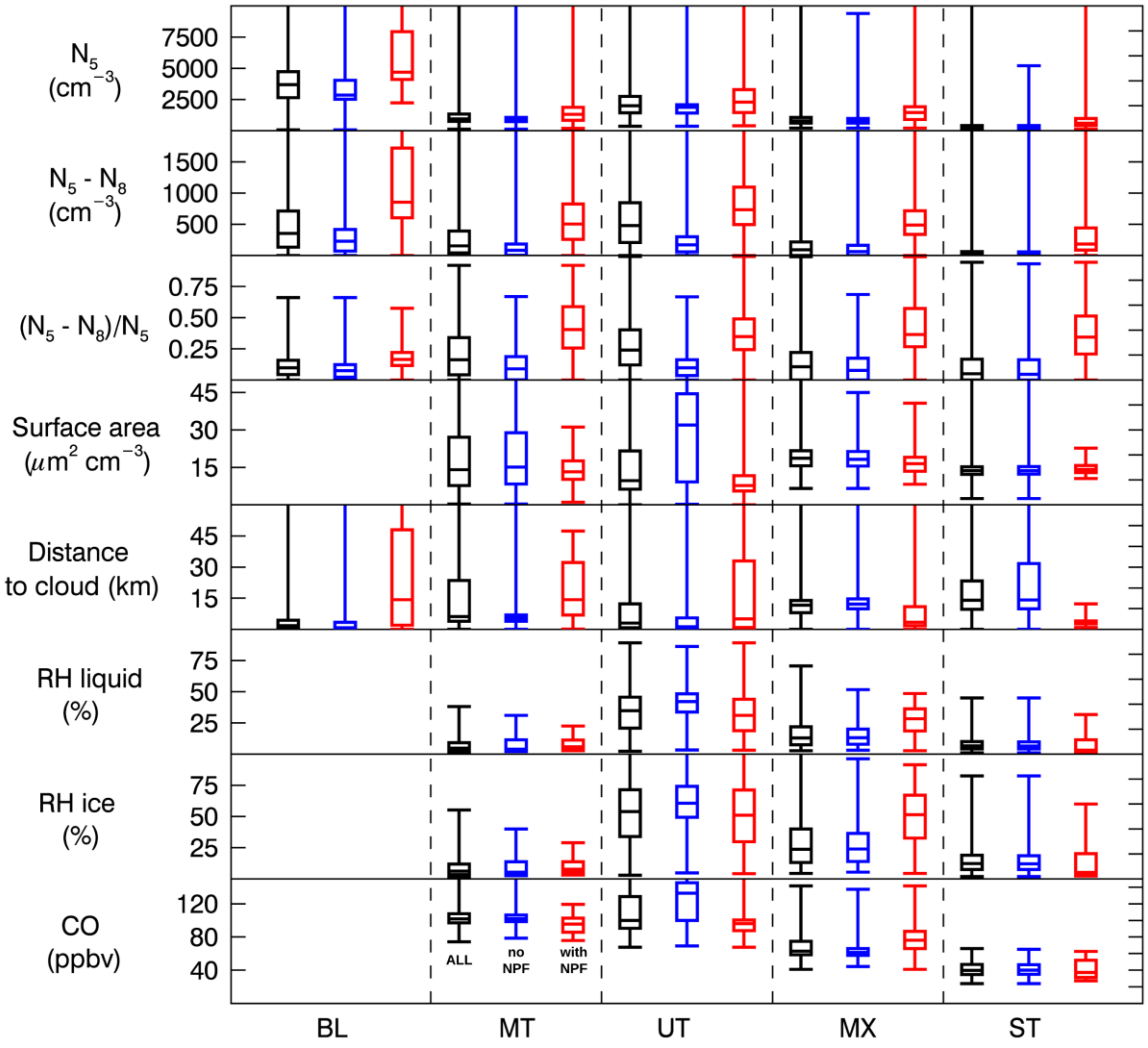

Figure 4.10. Sample minimum, lower quartile, median, upper quartile, and sample maximum for observed parameters in different layers sampled during MACPEX. The different layers are labeled as boundary layer (BL), middle troposphere (MT), upper troposphere (UT), mixing layer (MX) and stratosphere (ST). Boxplots for all data (black), data with no NPF (blue) and data with NPF (red) are shown for each layer. All data are out of cloud. All number and surface area concentrations are at STP.

In the middle troposphere and the upper troposphere, the impact of cloud was less apparent. There could be several reasons for this including the occurrence of NPF through different pathways where one pathway produced more frequent NPF far away from clouds. For example, if SO_2 is substantially depleted in cloud outflow, low concentration of SO_2 may not be sufficient for NPF in the upper troposphere and middle troposphere but adequate in the mixing layer. Also, the transport and scavenging of trace gases through clouds is dependent on cloud microphysics. The incorporation of soluble tracers in ice particles is determined by the mechanism of ice formation, such as homogeneous or heterogeneous nucleation of ice particles. These processes occur at different temperatures and different heights and supersaturation within the cloud. Glaciation could account for total scavenging of a certain gas species. When ternary NPF is involved, these ice microphysics processes could determine how NPF proceeds.

To make a stronger conclusion on the impact of convection on NPF, the days when the jet stream was sampled (20110403, 20110414, and 20110416) were separated from those days with convection (20110420, 20110425, and 20110426). Figure 4.11 shows the jet stream cases and convective cases in each layer. The legend in the figure describes the sequence of the box and whiskers. The boxplot distributions for the jet stream cases and convective cases were similar except for a few salient differences. In general, the convective cases were associated with higher concentrations of CO in the upper troposphere and the mixing layer. These samples also had higher surface area than those sampled near the jet stream, especially in the upper troposphere. The strong convective updrafts associated with deep convection are likely to contain some

concentration of interstitial aerosol (i.e. aerosol particles that are unactivated and not scavenged by precipitation). This interstitial aerosol is ejected in cloud outflow and acts to increase the surface area and suppress nucleation. Higher SO_2 concentrations are therefore required for NPF near convection. In jet stream cases the cirrus forms in small updrafts and thus exhibit a comparably low surface area concentration and aerosol nucleation is possible at lower SO_2 mixing ratio. In the mixing layer, the convective clouds had a strong impact on NPF at small distances from cloud. A signal in $(N_5\text{-}N_8)/N_5$ emerges for convective clouds with NPF indicating that the ultra-fine mode is significant in concentration. Ultra-fine particles were also higher in concentration in the upper troposphere. This is related to high CO and proximity to cloud. NPF occurred at low surface area in the upper troposphere, even though convective cases had higher surface area than the jet stream cases.

In summary, when considering jet stream cases and convective cases together, this analysis confirms that high relative humidity and low surface area concentration triggers new particle formation. The frequency of NPF in the upper troposphere was higher than that in the mixing layer, and the mechanism that precedes NPF was linked to the distance from cloud. When considering the convective cases separately, it was very clear that the contribution of ultra-fine mode particles was significant in those NPF events that occurred in the upper troposphere and mixing layer. Surface area suppressed NPF in the upper troposphere, but nucleation still occurred possibly due to the high mixing ratio of SO_2 that could be present by the transport of polluted boundary layer air into the upper troposphere, along with other precursor gases that may stabilize the

clusters for initial growth of newly formed particles. It is also possible that enhanced concentrations of OH around cloud edges increases the concentration of H_2SO_4 and subsequently a possible enhancement in nucleation rates. It is plausible that binary homogeneous nucleation in the vicinity of clouds and in regions of enhanced mixing is the nucleation mechanism that is most active.

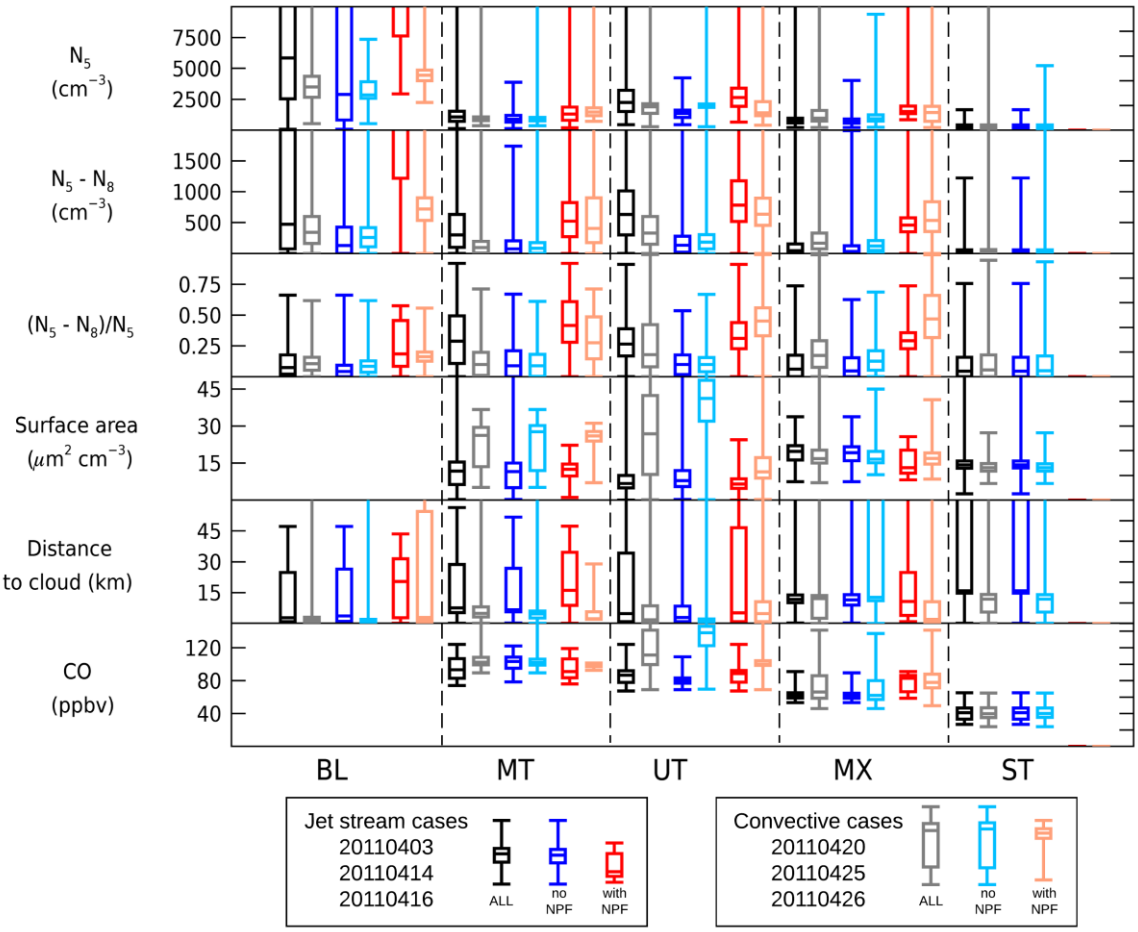

Figure 4.11. Sample minimum, lower quartile, median, upper quartile, and sample maximum for observed parameters in different layers for jet stream cases and convective cases. The different layers are labeled as boundary layer (BL), middle troposphere (MT), upper troposphere (UT), mixing layer (MX) and stratosphere (ST). All data are out of cloud. All number and surface area concentrations are at STP.

In Chapter 5 I modeled the impact of NPF on aerosol growth and investigated the impact of the evolution of the size distribution on CCN number concentration. In Chapter 6 the results are synthesized into a coherent picture that combines these observations with the model results.

Chapter Five: Modeling the Evolution of Aerosol Size Distributions

5.1 Introduction

Aerosol size distributions evolve under the effect of several physical processes, such as nucleation, condensational growth, and coagulation. In some cases, the aerosols grow and increase in number to add or modify the preexisting concentration of cloud condensation nuclei (CCN) and subsequently the concentration of cloud droplets. However, particles nucleated at nanometer sizes must undergo growth before they can become CCN, and the loss by scavenging limits the number concentration of particles. The role of aerosols in cloud formation by serving as CCN has been the subject of study as early as the late 19th century (Aitken, 1880). As mentioned in Chapter 1, understanding the CCN activation properties of the aerosol population is important due to the direct and indirect effects on climate. A higher concentration of CCN leads to more numerous cloud droplets in a given cloud and an increase in albedo (Twomey, 1977; Ackerman et al., 2000), increase in cloud lifetime (Albrecht, 1989), and decrease in precipitation efficiency (Rosenfeld, 1999; Andreae et al., 2004), resulting in a net cooling effect on the global scale.

When studying cloud formation, a focus is the growth of a population of droplets in a rising parcel of air. When a parcel rises, it expands, cools adiabatically, and reaches water saturation. Further uplift produces supersaturations that initially increases at a rate proportional to the updraft velocity. As the supersaturation increases with the updraft

velocity, aerosols are “activated” into CCN, starting with the most efficient (i.e. the larger and more soluble aerosols). Activation starts from the larger sizes down to the smaller diameter aerosols until the supersaturation is depleted. The diameter at which 50% of all aerosol activate is called the critical diameter. An aerosol particle will activate into a CCN droplet only if the water vapor supersaturation surrounding the particle exceeds its critical supersaturation. Once this occurs, water vapor rapidly condenses on the droplet resulting in a decrease of the ambient supersaturation as the growing droplet depletes the gas phase water. When air becomes supersaturated, all aerosol particles with critical supersaturation values below or equal to the ambient supersaturation will activate into a CCN droplet. The supersaturation is typically inhomogeneous in space and time. The factors controlling critical supersaturation include size, chemical composition, shape, surface tension, and temperature of the aerosol particle. Inclusion of this information in numerical models is needed for the improvement in accuracy of the predictions of the indirect effect of aerosols that calculate CCN concentrations at various supersaturations (i.e. CCN spectrum). For ease of calculation, most climate models use parameterized empirical functions to retrieve a CCN spectrum. If these empirical functions incorporate limited information of the controlling supersaturation, the model is inaccurate. More details of activation efficiency are included in global aerosol models which results in better predictions of CCN spectra (Spracklen et al., 2005). However, global climate models do not carry CCN activity or even the aerosol size distribution as a prognostic variable due to the poor understanding of activation efficiencies in complex mixtures representative of ambient aerosols.

A process that might affect the concentration of CCN, especially over the remote ocean where primary particles are less abundant, is the formation of new aerosol particles by nucleation and their subsequent growth. NPF has been recognized as a potentially significant contributor to CCN globally (Lihavainen et al., 2003; Laaksonen et al., 2005; Kerminen et al., 2005; Kuang et al., 2009; Merikanto et al., 2009). Several model studies, including Pierce and Adams (2009), Merikanto et al. (2009) and Yu and Luo (2009), have shown that growth of nanometer-sized particles nucleated in the free troposphere and boundary layer are an important source of tropospheric CCN, contributing between 23 and 70% of all CCN globally. The remaining fraction of CCN is from the emission of primary particles. The study by Merikanto et al. (2009) separates the sources of nucleation to global CCN and suggests that 35% of CCN at 0.2% supersaturation in global low-level clouds were created in the free and upper troposphere. Figure 5.1 from Merikanto et al. (2009) shows the relative contributions of all nucleated particles to global CCN. Primary particles dominate the CCN contribution in polluted regions over land. In the Southern Ocean sea salt is a primary source of CCN. In marine sub-tropical regions that are distant from continental primary sources and that have low sea salt emissions, boundary layer CCN are entrained from the upper troposphere. The upper troposphere makes a large contribution (> 60%) to boundary layer CCN in persistent marine stratocumulus regions. These stratiform clouds are highly sensitive to any additional CCN that might originate from upper tropospheric nucleation. Any additional CCN would modify the cloud microphysical properties, the cloud albedo and hence forcing.

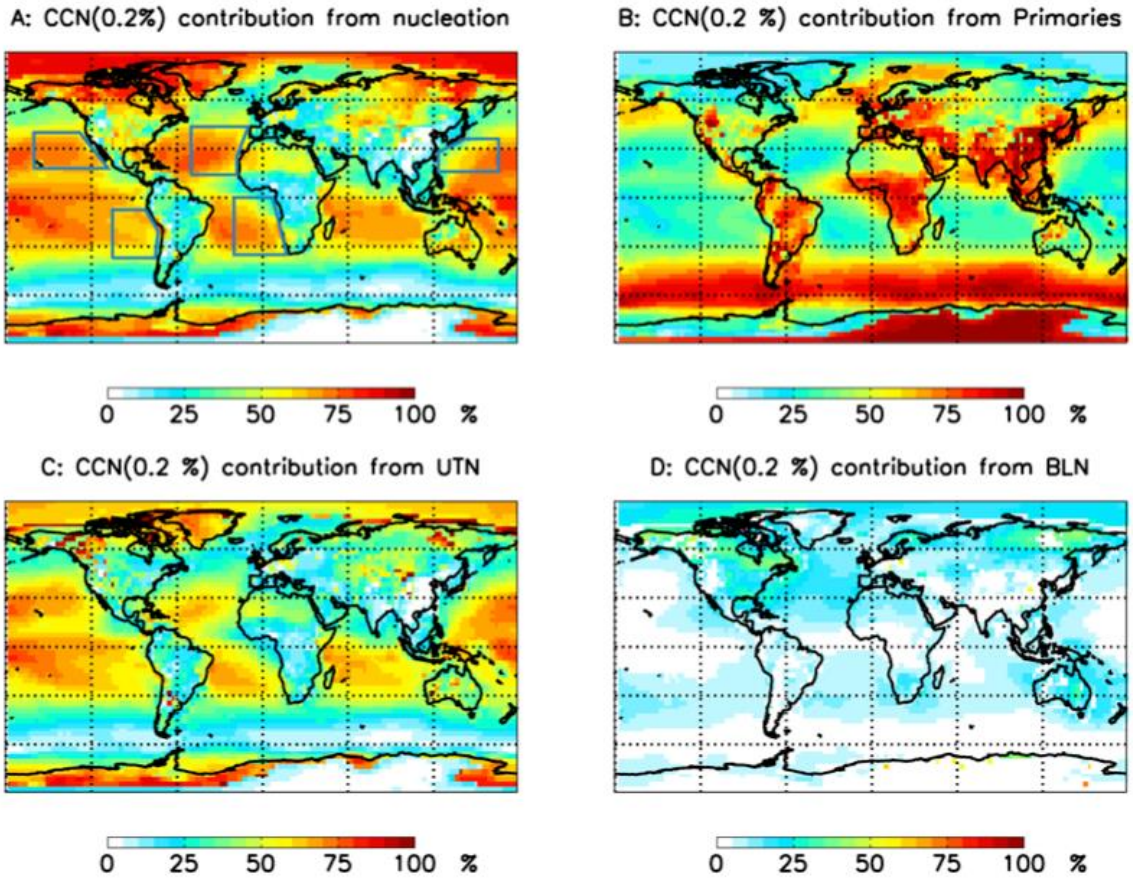

Figure 5.1. Relative average contributions to cloud condensation nuclei concentrations at 460 - 1100 m above ground level with 0.2% supersaturation of **A**: all nucleation particles (sum of panels **C** and **D**). Regions with persistent stratocumulus decks are highlighted with blue lines; **B**: primary particles; **C**: upper tropospheric nucleated (UTN) particles; **D**: boundary layer nucleated (BLN) particles.

Source: Merikanto, J., Spracklen, D. V., Mann, G. W., Pickering, S. J., & Carslaw, K. S. (2009). Impact of nucleation on global CCN. Atmospheric Chemistry and Physics, 9(21), 8601-8616.

The principal aim of this chapter was to get some idea of the potential importance of CCN production resulting from NPF in the upper troposphere, mixing layer and the stratosphere. The objective was to provide model estimates of aerosol growth following

the formation of new particles and corresponding concentrations based on microphysical processes. The investigation was based on the aerosol size distributions measured in each of these layers and the evolution of these size distributions along a forward trajectory over a four-day period. Model of Aerosols and Ions in the Atmosphere (MAIA) developed by Lovejoy et al. (2004) and Kazil et al. (2007) was applied. This was done to model the aerosol formation and growth processes. Here I discuss MAIA's output aerosol size distributions and the location and strength of NPF events in the northern mid-latitudes to evaluate the possible contribution of nucleated aerosol to the preexisting aerosol and CCN concentrations.

5.2 Modeling Studies

In this part of the work, I investigate the production of "potential" CCN resulting from NPF. As mentioned earlier, a quantitative determination of a CCN concentration as a function of supersaturation is not possible without direct CCN measurements. Alternatively detailed information on the size distribution, supersaturation, chemical composition and mixing state is required. Also, the chemical composition data and mixing information need to be size-resolved for CCN closure. Since such information is rarely available, a surrogate for CCN was used. Two quantities, CCN_{50} and CCN_{100}, namely the concentration of aerosols greater than 50 nm and 100 nm in diameter, respectively, were selected to represent the number of "potential" CCN along the modeled forward trajectory. The decision to use these size thresholds can be justified. The critical supersaturation needed to activate aerosols in the 50 to 100 nm diameter size

range is between 0.2 and 0.6% for dry ammonium sulfate aerosol (Seinfeld and Pandis, 1998), with 50 nm particles activating at 0.6% and 100 nm activating at 0.2%. These supersaturations are in the range of those estimated for marine stratocumulus and convective clouds (e.g., Pringle et al., 2010; Krüger et al., 2014). Ditas et al. (2012) calculate a 50% activation diameter of 115 nm at a critical supersaturation of 0.16% in marine stratocumulus clouds. Hammer et al. (2014) found that the activation diameter varies from 65 nm to 113 nm at a critical supersaturation range of 0.21 to 0.61% in cumulus clouds at a high-alpine site in Switzerland. Wiedensohler et al. (2009) investigated a NPF event in a highly polluted airmass at a regional site south of Beijing. They calculated the range in activation diameter to be between 62 nm and 84 nm in the 0.26 to 0.46% supersaturation range. The variation in activation diameters is apparent but the range between 50 nm and 100 nm captures the critical supersaturation that is relevant for convective and stratiform clouds. What is most important for this work is the impact of CCN in the North Atlantic. In a modeling study Pringle et al. (2010) report that in the North Atlantic the regional annual mean activation diameter at 60 nm is 0.37% and that at 120 nm is 0.13%. It is also well known that higher supersaturations are reached in convective clouds as compared to marine stratus clouds due to the higher intensity updrafts. Therefore, CCN_{50} and CCN_{100} provide a "first-order" estimate of the potential CCN concentration that might be activated in convective clouds and marine clouds, respectively. Low and mid-level stratus clouds are the most relevant in changes to the radiative balance as they cover much larger area than convective clouds and therefore are

more significant in accounting for a change in albedo for a given CCN concentration increase (Charlson et al., 1992).

5.2.1 Description of the model.

The model used in this work is the highly-resolved aerosol microphysics model MAIA (Lovejoy et al., 2004; Kazil et al., 2007). It is based on advanced numerical, thermodynamic and kinetic approaches compared to parameterizations which are currently used in aerosol modules in global climate models. The MAIA model higher complexity compared to aerosol formation rate parameterizations comes at a higher numerical cost. It is suitable for a small number of case study experiments and would not be adequate for a multi-physics type ensemble approach in studying the effect of various aerosol processes on CCN formation. In this work, I apply a modeling sensitivity study to broaden the impact of this dissertation.

MAIA simulates microphysical processes to calculate reference particle formation rates of neutral and charged (negative) H_2SO_4/H_2O aerosol particles for a given set of constant parameters (pressure, ionization rate, temperature, relative humidity, preexisting aerosol H_2SO_4 condensational sink, and gas phase H_2SO_4 concentration) until the time derivative of the aerosol concentrations falls below a given threshold (Kazil and Lovejoy, 2007). The aerosol concentrations and the formation rate are then assumed to be good approximations of their steady state values. Production of H_2SO_4 is calculated under the assumption that the reaction SO_2 + OH is the rate limiting step of the oxidation chain

$SO_2 \rightarrow H_2SO_4$ (Lovejoy et al., 1996). The ionization rate at ambient conditions is calculated with the theoretical cosmic ray ionization code of O'Brien (2005).

As input parameters for MAIA, in situ data, assumed mixing ratios of SO_2 and forward particle trajectories from HYSPLIT model (Stein et al., 2015) were used. The SO_2 is only specified as an initial value and is then depleted by OH oxidation as time proceeds. The model calculates the SO_2 concentration at the trajectory locations before integrating the evolution of the aerosol size distribution (J. Kazil, personal communication, March 22, 2017). For example, if the trajectory is descending (increasing pressure and air number concentration), the SO_2 concentration might increase, even though OH oxidation depletes SO_2. It is important to note that SO_2 does not mix with environmental air outside of the parcel and is not removed by scavenging processes such as wet removal by cloud water.

MAIA represents the aerosol size distribution with a hybrid kinetic-sectional scheme. In the kinetic scheme, the model solves the differential equations for the concentrations of each aerosol particle containing up to 21 H_2SO_4 molecules. For particles with a larger H_2SO_4 content and to account for diameters up to ~ 1 μm, the model uses 99 geometric size sections and solves the differential equations for the concentrations of aerosol particles within each size range (Kazil et al., 2007). The size distribution within geometric size sections is resolved with linear functions. The system of differential equations for the aerosol concentrations is integrated with the VODE (Variable-coefficient Ordinary Differential Equation) solver (Brown et al., 1989).

MAIA describes nucleation of sulfate aerosol and growth of the freshly nucleated particles using laboratory thermochemical data (Gibbs' free energy of formation) for the uptake and loss of gas phase H_2SO_4 and H_2O by neutral and charged molecular clusters (Curtius et al., 2001; Lovejoy and Curtius, 2001; Froyd and Lovejoy, 2003a,b; Hanson and Lovejoy, 2006). This is essential for the description of the nucleation process. The MAIA model calculates the hydrated H_2SO_4 dimer $(H_2SO_4)_2(H_2O)_x$ and trimer $(H_2SO_4)_3(H_2O)_y$ formation explicitly based on laboratory experiments by Hanson and Lovejoy (2006). The thermochemical data for H_2SO_4 and H_2O uptake and loss by large aerosol particles (> 5 sulfuric acid molecules) originate from the liquid drop model and H_2SO_4 and H_2O vapor pressures over bulk solutions based on Giauque et al. (1960) and Clegg et al. (1995). The thermochemical data for uptake and loss of gas phase H_2SO_4 and H_2O by intermediate sized particles are an interpolation of the data for the small (neutral clusters with 2 and charged clusters with 5 sulfuric acid molecules) and large particles (with many more than 2 or 5 sulfuric acid molecules) (Lovejoy et al., 2004; Kazil et al., 2007; Kokkola et al., 2009). The rate coefficients for H_2SO_4 uptake and loss by the aerosol particles, for the coagulation of the aerosol particles among themselves, and for the recombination of the negatively charged aerosol with cations are calculated with the Fuchs formula that describes Brownian coagulation (Fuchs, 1965) and maintains thermodynamic equilibrium of water down to the low temperatures found in the UTLS.

In summary, the major characteristics of MAIA processing modules are:

- Describes the size distribution using a hybrid kinetic-sectional, fixed center, first order approximation of size distribution inside geometric size sections. The model uses 21 kinetic and 99 geometric size sections.

- Detailed representation of new particle formation by ion-induced and neutral binary nucleation of sulfuric acid and water. Sulfate is the sole chemical compound treated in the nucleation process. The conversion rate of $SO_2 \rightarrow H_2SO_4$ by OH oxidation was calculated over the given trajectory.

- Experimental cluster ion thermodynamic parameters determine the initial steps of molecular cluster formation from the gas phase.

- Calculates nucleation rates as well as formation rates of particles of a given size.

- Calculates condensation of gas phase compounds to the preexisting aerosol.

- Calculates coagulation of the aerosol particles amongst themselves.

- Maintains thermodynamic equilibrium between liquid water and water vapor down to the very low temperatures occurring in the UTLS.

MAIA is a parcel model and neglects non-microphysical processes such as gravitational settling and scavenging by clouds and precipitation. Gravitational settling is a process that removes super-micron coarse particles when the simulation time extends over several days. Neglecting gravitational settling can cause an overestimation of particle numbers in the coarse mode. The scavenging of aerosol by clouds and precipitation is one of the major processes for aerosol removal. To estimate the interactions between aerosol, clouds and rain, cloud and raindrop size distributions are needed to estimated scavenging coefficients. This is not possible as the HYSPLIT forward trajectory does not produce cloud and raindrop size distributions. Scavenging of aerosol particles by cloud and rain can remove particles from the accumulation and the coarse mode. Since this modeling experiment is idealized, one can assume that the size distribution does not encounter any cloud and precipitation in the forward trajectory. Also, forecasting convective precipitation is difficult, requires detailed cloud microphysics models with fine resolution (< 5 km) and the multi-day scale of the forward trajectory would require a large domain. Therefore, it is computationally expensive and impractical to obtain any reasonable cloud and raindrop size distributions along the four-day forward trajectory.

MAIA treats sulfate as the sole aerosol chemical component and considers only nucleation of H_2SO_4 - H_2O. The exact nucleation mechanisms in the UTLS remain unidentified even after the recent CLOUD (Cosmics Leaving Outdoor Droplets) chamber experiments concluded that amines could explain part of the atmospheric nucleation process (Almeida et al., 2013). Whether organics have an impact on NPF in the UTLS is

unknown. The problem with identifying the "true" nucleation process is that it is highly variable and may involve ternary compounds that need to be measured in the atmosphere. The parameterizations used in MAIA are based on controlled laboratory experiments of ion-induced nucleation of H_2SO_4 and H_2O and the effect of amines and other organics are not included.

5.2.2 Input data.

MAIA requires thermodynamic data, SO_2 mixing ratio, aerosol size distribution and forward particle trajectories from the HYSPLIT model to run a single event. The model operates offline on HYSPLIT trajectories generated with a separate code. The simulations were initiated at altitudes representative of the upper troposphere, mixing layer and the stratosphere, and forward trajectories were calculated from altitudes originating from each of these three layers. For each layer, two size distributions are run (25 percentile and 75 percentile size distribution values), with and without NPF, and with three concentrations of SO_2. This amounts to 12 runs for each layer, with a total of 36 runs. The initial thermodynamic data and aerosol size distributions were obtained from aircraft measurements during MACPEX.

The HYSPLIT model was run for each layer (i.e. upper troposphere, mixing layer and the stratosphere) by inputting the date, time, aircraft position and thermodynamic data as measured by the aircraft for an instance that is representative of each layer. HYSPLIT runs the trajectory using the National Weather Service's National Centers for Environmental Protection (NCEP) Global Data Assimilation System (GDAS) reanalysis data that contain basic meteorological fields such as u- and v-wind components, pressure,

temperature, H_2O vapor mixing ratio, solar flux and humidity with respect to water. The data is at 0.5-degree resolution and is output every 1 hour for 96 hours (4 days). The HYSPLIT model calculation method is a hybrid between the Lagrangian approach and the Eulerian methodology (Stein et al., 2015). Data from the HYSPLIT output file were used to calculate thermodynamic and meteorological input parameters for MAIA and a forward trajectory input file was generated for each layer.

Figure 5.2 shows the forward trajectory used for the upper tropospheric layer cases which are based on the location of an NPF event on the 26 April 2011. All 12 upper tropospheric cases use this trajectory. This means that the air parcel trajectory does not change for each of the 12 upper tropospheric runs. Similarly, HYSPLIT forward trajectories are produced for the mixing layer and the stratospheric layer, each using a different starting point at the beginning of the trajectory. All the MAIA input data are shown in Appendix C.

The evolution of the size distribution was affected by varying the initial SO_2 mixing ratio which modifies the aerosol size distribution through oxidation of SO_2 by the hydroxyl radical OH to produce gaseous H_2SO_4. During MACPEX the mixing ratio of SO_2 was not measured. To obtain estimates of SO_2 in the northern mid-latitudes, I utilize data from the Studies of Emissions and Atmospheric Composition, Clouds and Climate Coupling by Regional Surveys (SEAC4RS) campaign. As in MACPEX, SEAC4RS was also based out of Ellington Field in Houston Texas, but the research flights were conducted in August and September of 2013 and concentrated on the southeastern United States.

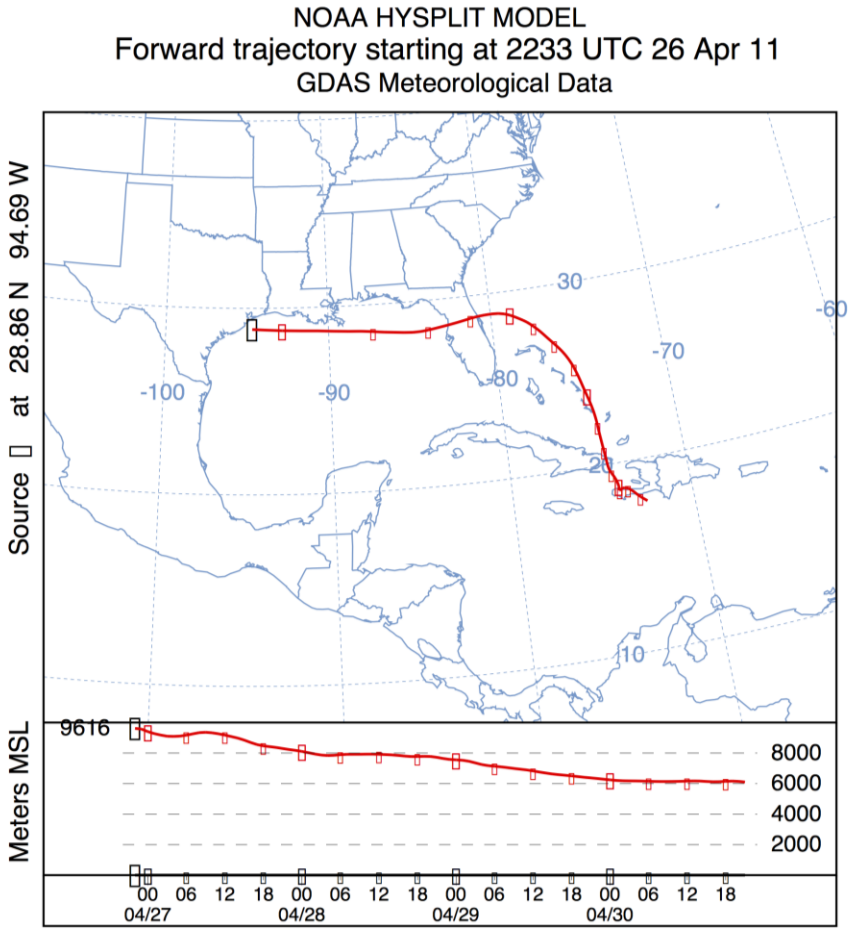

Figure 5.2. NOAA HYSPLIT forward-trajectory for an air parcel in the upper troposphere at 22:33 UTC on 4/26/2011 following an NPF event (event number 22). Note that for all cases forward-trajectories are computed for a four-day period. The lower part of the figure shows the vertical movement of the air mass trajectory. MAIA input variables are computed along this forward trajectory.

Figure 5.3 shows the flight tracks of two aircraft on the project, the NASA DC3, and NASA ER2. The flights between N25° and N35° have good overlap with MACPEX. Figure 5.4 shows the vertical profile of SO_2 mixing ratios up to 13 km altitude. Most of the flights were conducted around deep convective clouds in the southeastern US where deep moisture coincided with the subtropical jet stream. The meteorological sampling conditions in SEAC4RS were quite similar to those encountered during MACPEX. In

both campaigns, the convection was associated with the subtropical jet except for a few cases in MACPEX when the polar jet was sampled.

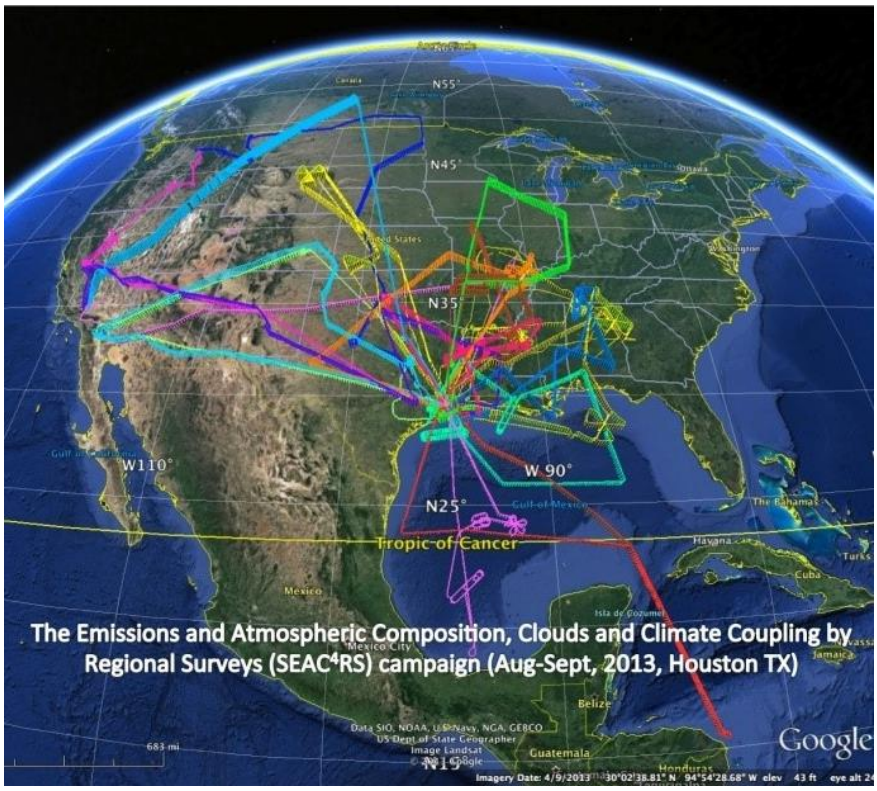

Figure 5.3. Research aircraft flight tracks during NASA SEAC4RS campaign in August and September 2013.

Since part of this dissertation is concerned with the impacts of cloud on NPF, it is important to consider SO_2 mixing ratios in the upper troposphere that are associated with cloud outflow. While not widely observed, SO_2 mixing ratios in the ppb range (1000 ppt is equal to 1 ppb) have been observed in the upper troposphere (Arnold et al., 1997). A process that produces such high concentrations of SO_2 is the convective lifting of polluted boundary layer air which often contains SO_2 in the ppb range. As discussed in Chapter 4, this is a plausible mechanism for boundary layer trace gases to get entrained in

deep convection and exhaust in the outflow region high into the upper troposphere and the mixing layer. Figure 5.4 shows the vertical profile of SO_2 during SEAC4RS with the thick red line as the median. The green lines represent SO_2 thresholds of 60 pptv and 1385 pptv (1.385 ppbv). The layer between 6 to 10 km shows that background SO_2 mixing ratios reach a maximum of ~ 60 pptv. It is also apparent that occasional peaks reach ~ 1385 pptv. These peaks are due to convective outflow (G. Huey, personal communication, March 16, 2017).

In this idealized study where the impact of NPF on potential CCN is of interest, a 60 pptv threshold to look at the maximum effect of non-cloud impacted NPF was used (i.e. NPF that occurs at some distance away from cloud). The 60 pptv mixing ratio also represents cases when SO_2 is depleted by cloud processing after it is entrained in convective updrafts. For cloud impacted NPF, a threshold of 1385 pptv was used. The 1385 pptv represents the maximum SO_2 that is entrained through convective cloud with little dilution. In this case, the NPF is assumed to occur very close to convective cloud outflow. Finally, 0 pptv of SO_2 was used to simulate a very clean (or pre-industrial) type conditions. In the latter MAIA does not form any new H_2SO_4 molecules as the reaction $SO_2 + OH$ is the rate limiting step of the oxidation chain $SO_2 \rightarrow H_2SO_4$. Therefore, the 0 pptv SO_2 case does not produce any new particles at any point during the simulation.

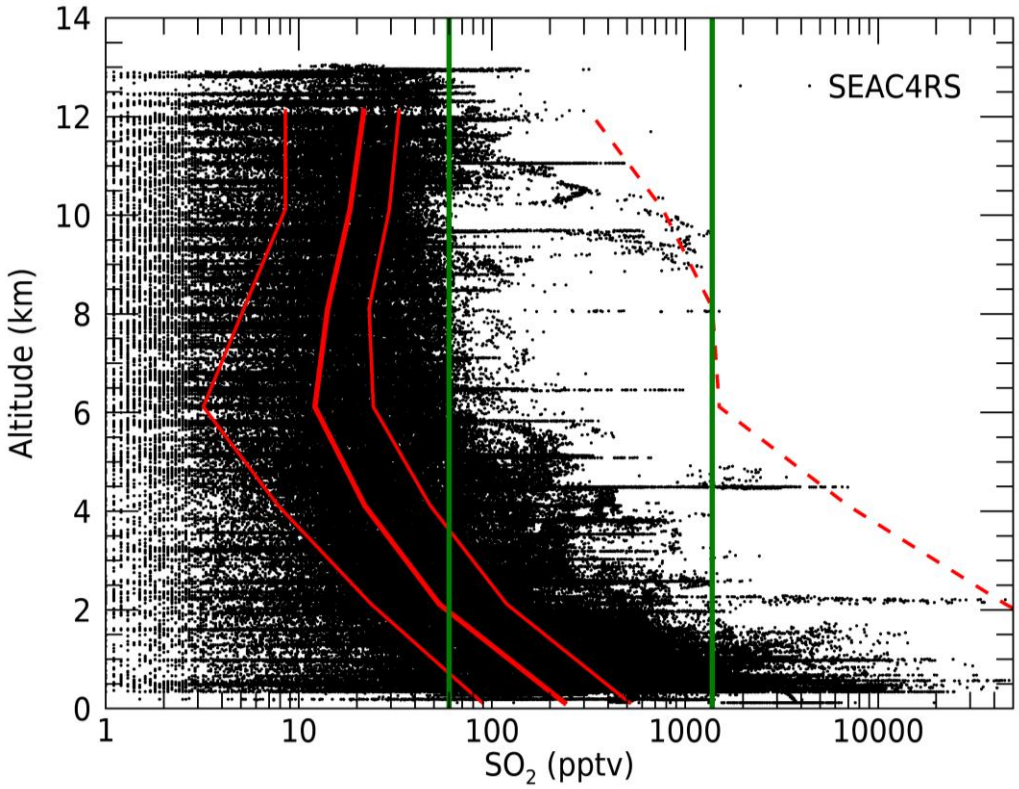

Figure 5.4. Vertical profile of SO_2 (black) during NASA SEAC4RS campaign. The thick red line is the median, and the thin red lines are the 25 and 75 percentile values binned at 2 km altitude bins. The dotted red line is the 100 percentile. The green lines represent SO_2 thresholds of 60 and 1385 pptv. (Use of SO_2 data with permission from Greg Huey at Georgia Tech.)

A two-mode lognormal fit was applied to the 25 percentile and the 75 percentile value of each size distribution, with and without NPF, in the upper troposphere, mixing layer, and stratosphere (i.e. a total of 12 lognormal fits). Since the surface area of the preexisting aerosol is a sink for gaseous H_2SO_4 and the newly formed particles, the surface area of the lognormal fit was carefully matched with measurements. An example of the fitting procedure is shown in Figure 5.5. The fitting was done manually (trial and error) by matching the shape of the size distribution. The size distribution was divided into two segments at 11 nm, with particles in the sub-11 nm threshold to form the

"Aitken mode." The particles greater than 11 nm form the "accumulation mode." The surface area was computed for each of these modes, and the area of the mode from the measured size distribution was then compared to that computed from the fit. As can be seen in Figure 5.5, there are no measurements with an aerosol diameter smaller than 4 nm so the criteria to fit the Aitken mode was to match the peak concentration to the mode median diameter. The criteria to match the accumulation mode was both to match the

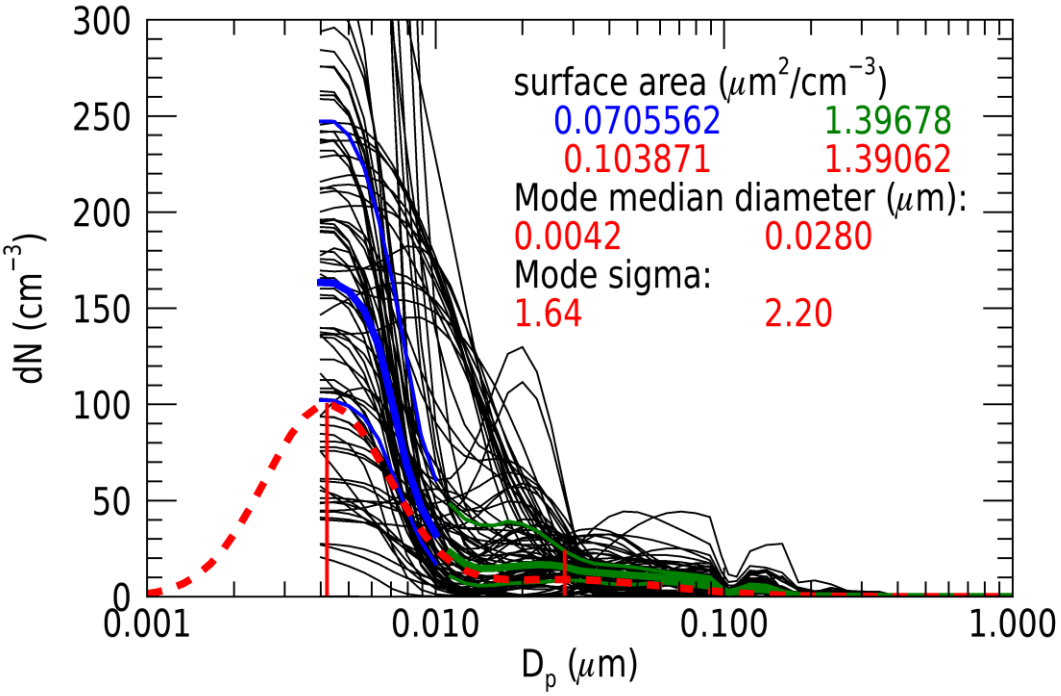

Figure 5.5. Two mode lognormal fit to the 25 percentile value of the measured aerosol size distributions with NPF in the upper troposphere (UT). The number of samples (n) is 12010. One size distribution is plotted every 120 samples (black lines). The thick blue/green line is the median. The thin blue/green lines are the 25 and 75 percentile values. The blue lines are the Aitken mode. The green lines are the accumulation mode. The red dotted line is the two-mode lognormal fit to the 25 percentile value. The text on the plot shows the surface area in the Aitken and accumulation mode (in blue and green respectively), the surface area for the fit in each mode (in red), the fit mode mean diameters and the fit mode standard deviation. All data are out of cloud.

peak concentration to the mode median diameter and to set the ratio of the measured surface area to the fit surface area to unity.

The 25 and 75 percentile values of the size distribution for each layer were chosen with the aim to cover a representative and realistic range of the measured size distributions within each layer. The SO_2 was prescribed at 0 pptv, 60 pptv or 1385 pptv to represent 'clean', 'high background', and 'cloud impacted' levels, respectively. Table 5.1 shows the settings for MAIA runs in the upper troposphere (UT), mixing layer (MX) and stratosphere (ST). The moments of the lognormal fits that was derived from the campaign averaged measurements are listed. Table 5.1 lists 12 instances of inputs for MAIA runs. Each of these instances was run at 0, 60 and 1385 pptv which make the total number of runs equal 36.

Once the HYSPLIT trajectories and the size distribution lognormal fits were calculated, a run parameter file for each of the 36 cases was created. Thermodynamic and meteorological input parameters were calculated for MAIA, and a forward trajectory input file was generated for each layer. For calculating aerosol microphysical properties, the run parameter file specifies the ambient conditions of the initial aerosol size distribution. OH and SO_2 concentrations were specified for the calculation of the H_2SO_4 production rate. The concentration of OH was prescribed by a diurnal cycle with a noon OH concentration of 10^6 molecules cm^{-3} based on a global average integrated with respect to the mass of air from the surface to 100 hPa within ± 32° latitude and to 200 hPa outside that region (Spivakovsky et al., 2000). A zero OH concentration was assumed at nighttime. The parameters needed to run the MAIA microphysical model

calculations are shown in Figure 5.6. The ion production rate (IPR) was calculated for the air-parcel geographic position and thermodynamic conditions (O'Brien, 2005). These data are used in MAIA to produce the modeled size distributions.

Table 5.1. MAIA model input parameters. Trajectory data are for 26 April 2011. The percentile values used for the size distribution (SD) are campaign median values with NPF or without NPF. The mode geometric median diameter (D), geometric standard deviation (σ) and surface area (area) were calculated. SO_2 input was 0, 60 and 1385 pptv for each case (not shown). All trajectories were run for 96 hours.

Layer	NPF (y/n)	SD % ile	Trajectory start (UTC)	Aitken mode			Accumulation mode		
				D (nm)	σ	area ($\mu m^2\ cm^{-3}$)	D (nm)	σ	area ($\mu m^2\ cm^{-3}$)
UT	n	25	22:33	4.20	1.60	1.7×10^{-3}	35.00	1.70	2.431
UT	y	25	22:33	4.20	1.64	0.104	28.00	2.20	1.391
UT	n	75	22:33	4.20	1.50	0.039	32.00	1.92	8.582
UT	y	75	22:33	4.20	1.64	0.262	20.20	2.20	3.153
MX	n	25	21:09	7.00	1.50	2.1×10^{-6}	64.00	1.62	2.355
MX	y	25	21:09	4.20	1.51	0.041	70.00	1.84	2.264
MX	n	75	21:09	4.20	1.50	0.011	64.00	1.83	5.338
MX	y	75	21:09	4.20	1.51	0.095	50.00	1.84	4.044
ST	n	25	18:50	4.20	1.35	6.6×10^{-9}	80.00	1.62	1.344
ST	y	25	18:50	4.20	1.45	0.006	78.00	1.75	1.786
ST	n	75	18:50	4.20	1.35	1.3×10^{-5}	80.00	1.75	3.345
ST	y	75	18:50	4.20	1.45	0.051	74.00	1.75	4.180

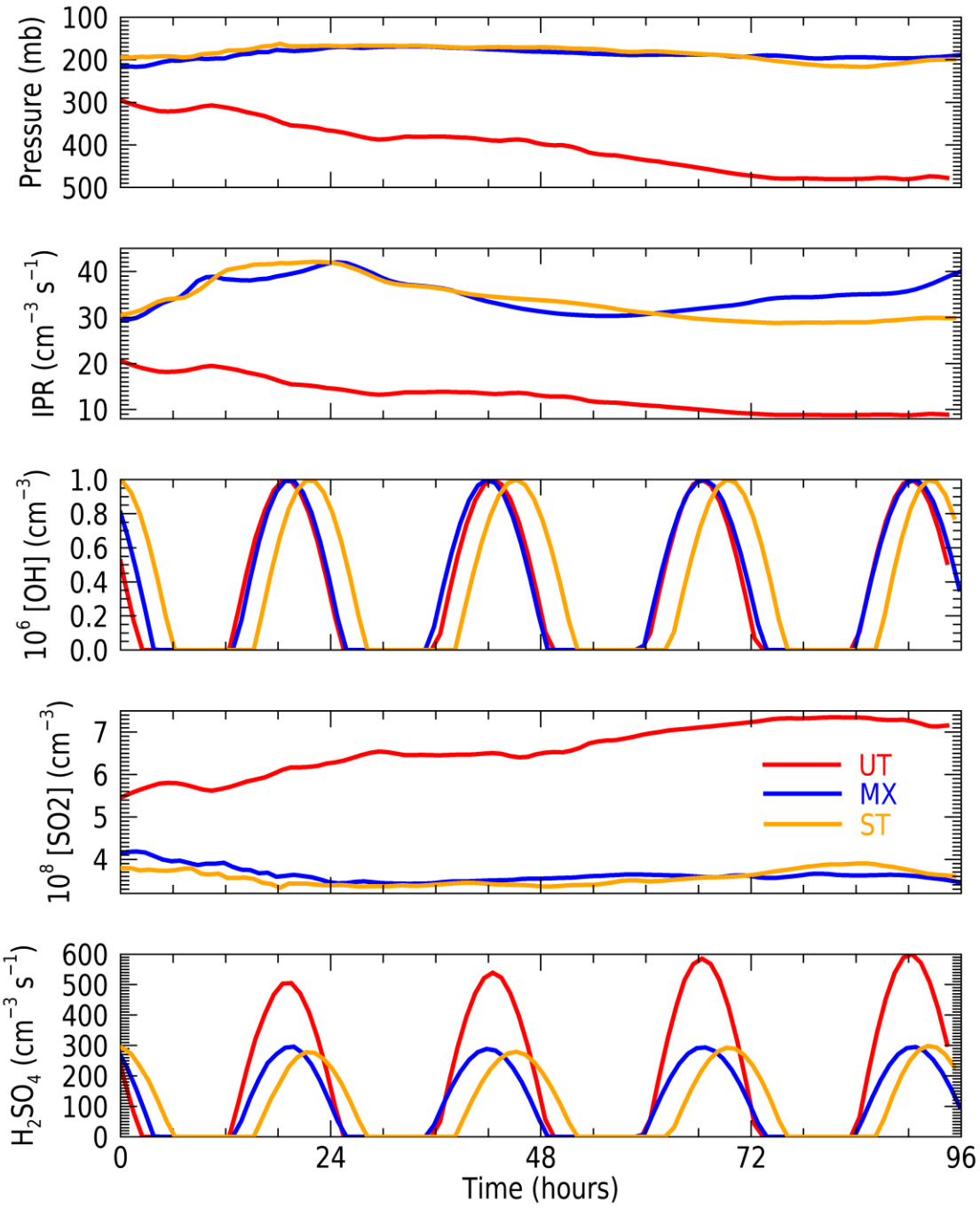

Figure 5.6. MAIA model input data for the upper troposphere (NPF event number 22 on 4/26/2011), mixing layer (NPF event number 18 on 4/26/2011) and stratosphere (NPF event number on 4/26/2011). In the cases shown here the SO_2 mixing ratio at the beginning of the trajectory was 60 pptv. The traces show (top to bottom) atmospheric pressure along the trajectory, ion production rate (IPR), OH concentration, SO_2 concentration and H_2SO_4 production. IPR, [OH], [SO_2] and H_2SO_4 are used to calculate nucleation rate in the model.

In summary, the input data for the MAIA runs were generated by:

- HYSPLIT derived estimates of temperature, relative humidity, pressure, water vapor mixing ratio and concentration of air along a forward trajectory of air mass transport,

- estimates of available OH (which is parameterized as a cosine of the solar zenith angle, in an approximation of the diurnal cycle of OH in the troposphere after Spivakovsky et al., 2000),

- cosmic ray induced ion production rates, calculated by a model of energetic particle transport in the Earth's atmosphere (O'Brien, 2005), which accounts for variations in cosmic ray intensity as a function of latitude and altitude,

- calculated preexisting aerosol surface area in the Aitken and accumulation mode based on lognormal fits to measured size distributions,

- prescribed initial SO_2 mixing ratios of 0 pptv, 60 pptv or 1385 pptv, representing 'clean', 'high background' and 'cloud impacted' levels, respectively.

One limitation of this approach is that both MAIA and HYSPLIT do not take into account the mixing of air masses with the surrounding air. During uplift or when detrainment occurs, it is very likely that the lifted air mass is diluted due to mixing with background air. The single trajectories resulting from HYSPLIT and the results from

MAIA simulations cannot reflect changes in SO_2 mixing ratios or aerosol surface area concentrations due to dilution or removal processes in the real atmosphere. Thus, the MAIA simulations in this work serve as a sensitivity study and establish thresholds that relate to an expected maximum effect. The 25 and 75 percentile values of the size distribution used as input, with and without NPF, and the range in SO_2 should compensate for the neglected mixing and dilution processes by producing a range of results that best simulate the real atmosphere.

5.2.3 Output data.

The output data from one of the simulated cases is shown in Figure 5.7. This case is the upper troposphere 25 percentile size distribution with NPF and an SO_2 mixing ratio of 1385 pptv at the beginning of the trajectory (case number 6UT25y1385). The corresponding HYSPLIT forward trajectory is shown in Figure 5.2. The size distributions are shown in Figure 5.5. The red traces in Figure 5.6 are the trajectory data for this case. Along the trajectory, the nucleation rate coefficients were recalculated whenever temperature or relative humidity (over water) change by more than 0.4 °C or 1%, respectively, whichever occurs first. All the MAIA output data are shown in Appendix C.

The MAIA output frequency for all calculated parameters is at 60 seconds. Figure 5.7 shows the H_2SO_4 condensation sink equal ~ 10^{-4} at the beginning of the trajectory and ~ 10^{-3} towards the end. H_2SO_4 vapor concentration in molecules cm^{-3} shows the same diurnal variability as OH. The peak in H_2SO_4 decreases slightly along the trajectory as SO_2 is consumed by OH during the day. The particle formation rate also follows a diurnal variability as in H_2SO_4 and OH. As the aerosol surface area density changes due to

growth and coagulation of the preexisting aerosol, so does the H_2SO_4 condensation sink. The condensation sink has a clear impact on particle formation as the particle formation rate decreases as condensation sink increases. As expected, the number of particles in the 3 to 4 nm range show the same trend as the new particle formation rate. These small particles act as a sink for the H_2SO_4 vapor and coagulate with the larger particles in the accumulation mode. The size distribution clearly shows typical nucleation events which exhibit a characteristic "banana-shaped" evolution of the aerosol size distribution, similar to what has been observed and reported at ground measurements sites. The growth of the nucleation and Aitken mode into the accumulation mode is also evident and when the accumulation mode crosses the 50 nm and 100 nm diameter, CCN_{50} and CCN_{100} increase. When comparing the potential CCN from the start (0 hr) to end (96 hr), CCN_{50} and CCN_{100} increase by a factor of 60 and 14, respectively. When CCN_{50} and CCN_{100} at 96 hr are compared to their corresponding values in the 0 SO_2 case (case number 4UT25y0) the percentage increase in CCN_{50} and CCN_{100} at 96 hr are 4140% and 847% respectively.

The increase in particle formation rate is temporally staggered when compared to the increase in the H_2SO_4 vapor. A time delay is observed, especially at higher condensation sink rates, for particles to reach a diameter of 3 nm. This is the time it takes for the molecular clusters to grow to a stable (but very small) diameter and for further growth. This can be seen very clearly in Figure 5.7c at hour 42. The cluster growth starts at hour 36 following the increase in H_2SO_4 vapor concentration, but the critical cluster size is not reached until hour 42 when the cluster size reaches a diameter of 3 nm and continuous to grow. As the condensation sink increases and the H_2SO_4 vapor

concentration decreases, the cluster cannot grow above its critical size and no further condensation growth is observed at hour 48. Therefore, NPF is governed by the abundance of H_2SO_4, the number of clusters formed and the time that is needed for the particles to grow to the nucleation mode (> 3 nm).

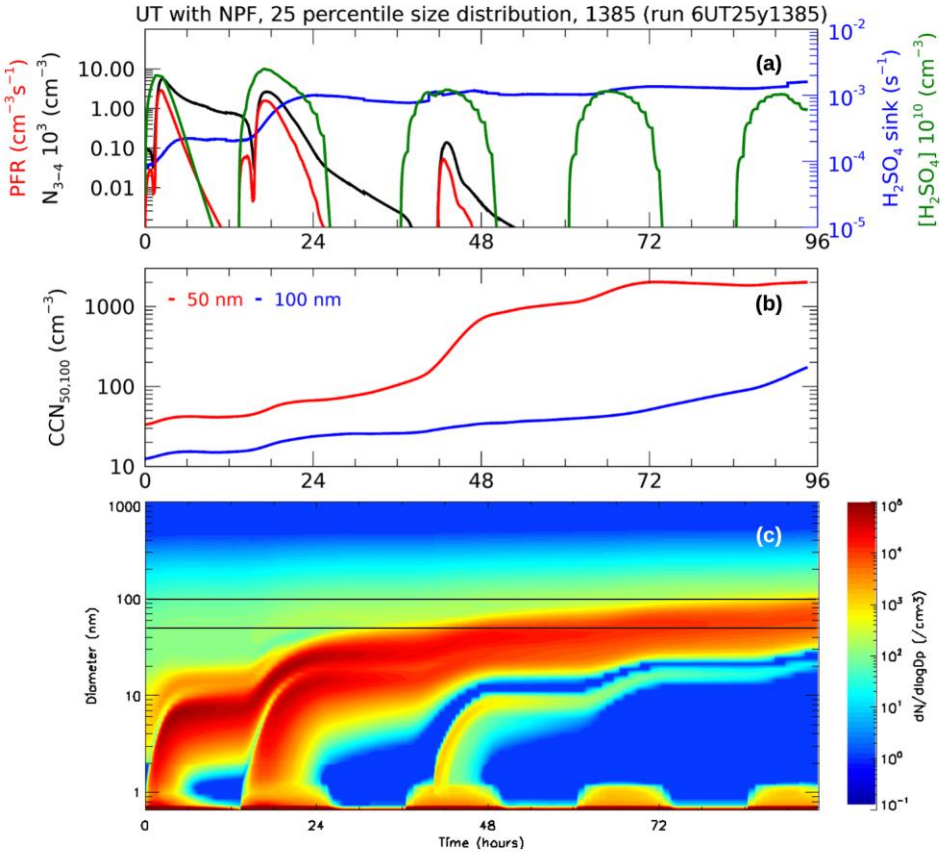

Figure 5.7. MAIA model output data for upper troposphere 25 percentile size distribution with NPF and SO_2 mixing ratio of 1385 pptv at the start of the trajectory (case number 6UT25y1385). Panel (a) shows the number concentration of aerosol in the 3 to 4 nm diameter size range (black), the particle formation rate of aerosol > 3 nm (red), H_2SO_4 condensation sink (blue) and H_2SO_4 concentration (green). Panel (b) shows the potential CCN at 50 nm and 100 nm activation diameter. Panel (c) shows the modeled aerosol size distribution with the horizontal lines indicating the 50 nm and 100 nm activation diameter threshold for potential CCN.

5.3 Results

The modeled abundance of H_2SO_4, the condensation sink, and the particle formation rate can give a good indication of whether the thermodynamic environment is conducive to the formation of new particles. Nucleation events can be associated with high H_2SO_4 vapor concentration, low H_2SO_4 sink, and high particle formation rate (PFR). In this study I investigate the potential for new particle formation and subsequent growth in the upper troposphere, mixing layer and the stratosphere. The results of the MAIA simulations are shown in Figure 5.8. In this figure, the simulations are grouped by layer, with the upper troposphere cases in Figure 5.8a, mixing layer in Figure 5.8b and stratosphere in Figure 5.8c. Each panel displays the H_2SO_4 vapor concentration, the condensation sink, and the particle formation rate for aerosol diameter > 3 nm predicted by MAIA as a function of time along a four-day forward trajectory. The different colored traces show the runs with 0 pptv SO_2 (in blue), 60 pptv SO_2 (in red) and 1385 pptv SO_2 (in black). Table 5.2, 5.3 and 5.4 provide further details on the magnitude of the particle formation and growth for each of the MAIA runs in this analysis.

As expected, no new particles formed with 0 pptv SO_2 in the model. The model does not produce any H_2SO_4 at 0 pptv SO_2 since SO_2 + OH is the rate limiting step of the oxidation chain $SO_2 \rightarrow H_2SO_4$. These simulations serve as a baseline for CCN production in a clean environment that might resemble the pre-industrial era. An interesting feature in Table 5.2, 5.3 and 5.4 is the large variability in CCN_{50} and CCN_{100} both in absolute terms and compared to the corresponding baseline 0 pptv SO_2 model run. In general, high values of PFR in the range 0.83 to 42 particles cm^{-3} s^{-1} were predicted by the model in the

1385 pptv SO_2 cases with the maximum occurring in the stratosphere. Moderate PFR were predicted at 60 SO_2 in the range 0.04 to 0.2 particles cm^{-3} s^{-1} with a maximum in the stratosphere. Figure 5.8 shows periodically high PFR in the stratosphere and the mixing layer at 1385 pptv SO_2. As mentioned earlier, the periodicity follows the abundance of H_2SO_4 vapor and the condensation sink.

In the troposphere PFR had a maximum of 2.9 particles cm^{-3} s^{-1} leading to the net production of some 14,000 to 35,000 particles cm^{-3} at 1385 pptv SO_2 during the four-day period of the simulation. At 60 pptv SO_2 the maximum PFR was 0.004 particles cm^{-3} s^{-1} and a net particle production up to ~100 particles cm^{-3}. The highest particle formation occurred in the first 24 hours. After the first 24-hour period, particle formation rate decreased in magnitude along the trajectory with no new particles forming after 48 hours. Figure 5.8a shows an increase in the H_2SO_4 sink at hour 18 and hour 42. This is also evident in Figure 5.7a. The increments in the condensation sink term gradually cut off the production of new particles. It is clear that simulated NPF in the troposphere is extremely sensitive to surface area. Figure 5.7c shows that new particles grow up to hour 48, but subsequent nucleation did not grow clusters greater than 1.2 nm in diameter. In the troposphere new particle formation was suppressed over time as the aerosol size distribution evolves. The condensational growth of nucleated and preexisting particles in the nucleation mode was rapid, especially in those cases with NPF. The size distributions with NPF were found to contribute significantly to CCN when compared to size distributions without NPF. The percentage increase in CCN_{50} and CCN_{100} at 96 hours ranged from 7% to 44% for all simulations at 60 pptv SO_2. These percentages were much

higher at 1385 pptv SO_2 and represented the maximum effect on CCN by parcels that are impacted by convective cloud outflow. In this case, the increase in CCN ranged from 187% to 4140%.

The nucleation activity in the mixing layer contrasts with that in the troposphere. Particle formation rates were much higher with a maximum of 23.3 particles cm^{-3} s^{-1} and a net particle production of ~ 460,000 particles cm^{-3}. The particle formation events were longer in duration than those in the upper troposphere by a factor of at least two, making this layer extremely important for the production of new particles. Figure 5.8b shows that PFR was of high intensity at 1385 pptv SO_2. At 60 pptv SO_2 the PFR was suppressed in the first 42 hours. New particles only formed after the condensation sink decreased at hour 38. The number of new particles formed at 60 pptv was less than 0.5% of those formed at 1385 pptv. Size distributions with NPF at 60 pptv SO_2 did not appear to contribute much to CCN. Careful examination of the modeled size distributions for the 60 pptv SO_2 cases shows that the impact of the nucleation mode particles is only due to coagulation with the accumulation mode. Nucleated particles did not grow much above 5 nm in most cases with 60 pptv SO_2. Although the mixing layer is very important for NPF, at background SO_2 levels (60 pptv) significant concentration of new particles only formed at a 25 percentile size distribution suggesting that high surface area becomes a factor in suppressing the growth of nucleated clusters. The percentage increase in CCN_{50} and CCN_{100} at 60 pptv SO_2 ranged from 2% to 12%. In the cases with 1385 pptv SO_2 the corresponding CCN increases were in the range 55% to 3098%.

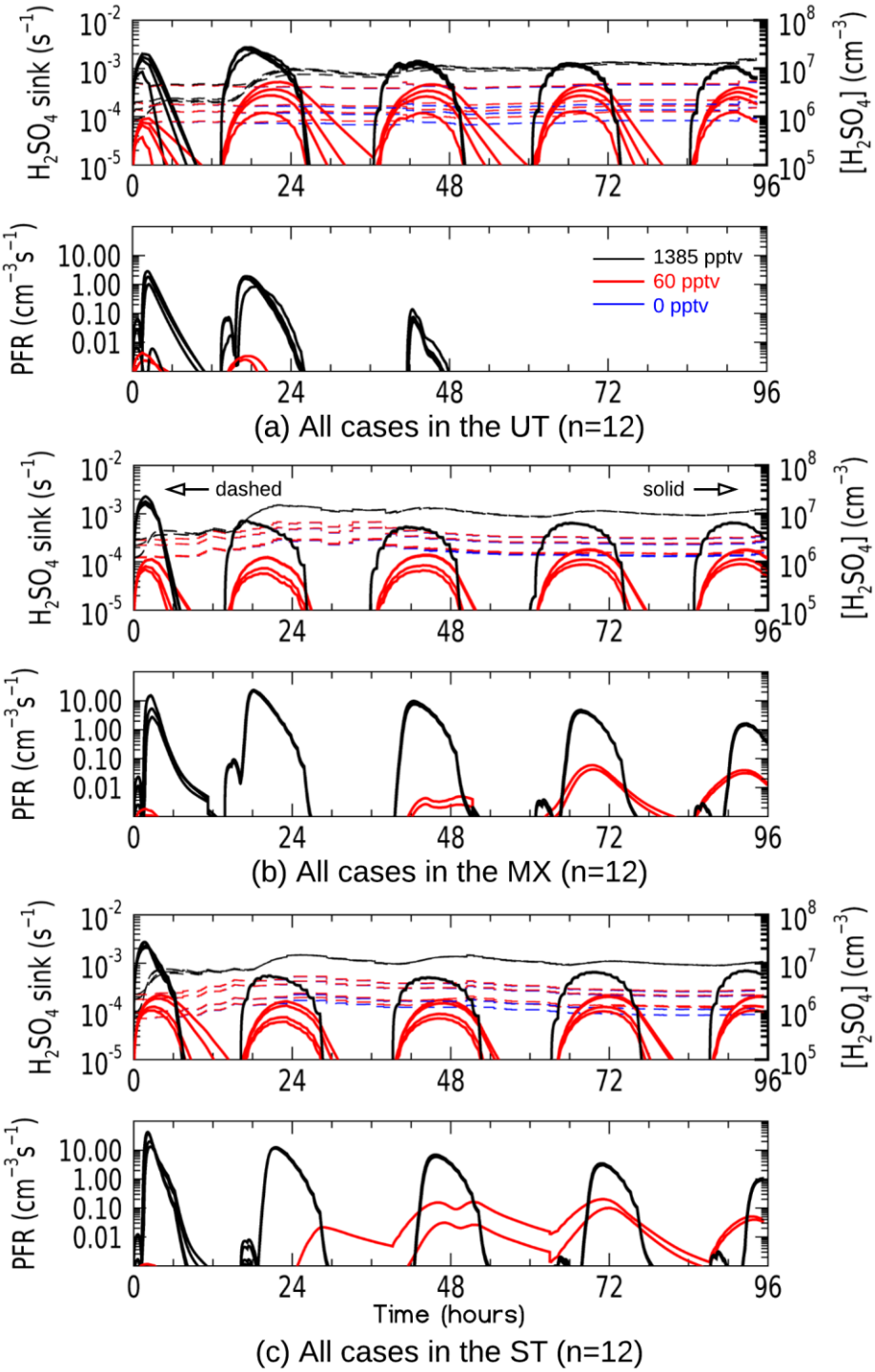

Figure 5.8. MAIA model output data for all 36 cases in the upper troposphere (a), mixing layer (b) and stratosphere (c). Runs with 0 pptv SO_2 are shown in blue, 60 pptv SO_2 in red and 1385 pptv SO_2 in black.

The highest PFR in all the simulations was in the stratosphere (27ST25n1385 case). Particle formation rates ranged 13 to 42 particles cm^{-3} at 1385 pptv SO_2 with a net particle production up to ~430,000 particles cm^{-3}. High PFR was associated with the 25 percentile size distribution. Both the 27ST25n1385 case and the 30ST25y1385 case produced high PFR. The particle formation in the 75 percentile size distribution cases was less than half that in the 25 percentile cases, but the duration of the events was a few hours longer. Since the trajectory was the same, these differences are not due to thermodynamics. It is noted in Table 5.3 that this difference was due to higher peaks in H_2SO_4 vapor in the 25 percentile cases. This higher PFR in the 25 percentile case occurred in the first two hours of simulation. Although the maximum condensation sink values were almost equal, the 75 percentile case provides a more rapid increase in condensation sink in the first four hours before the maximum is reached. This accounted for the difference in the simulated PFR. Careful examination of Figure 5.9a in the 0 to 3 hr range shows this difference. One possible reason for this is that the additional particles in the Aitken mode act as an immediate sink to the H_2SO_4 vapor as they grow by condensation in the first 3 hrs. The model size distributions for run 30ST25y1385 and run 36ST75y1385 are shown if Figure 5.9b and 5.9c respectively. Although the lower stratosphere produces the largest number of new particles, the impact of aerosol on boundary layer clouds may be less important because of the time required for these particles to make it into the boundary layer. The percentage increase in CCN_{50} and CCN_{100} at 60 pptv SO_2 range was from 2% to 10%. In the cases with 1385 pptv SO_2 the CCN increases ranged from 35% to 4550%.

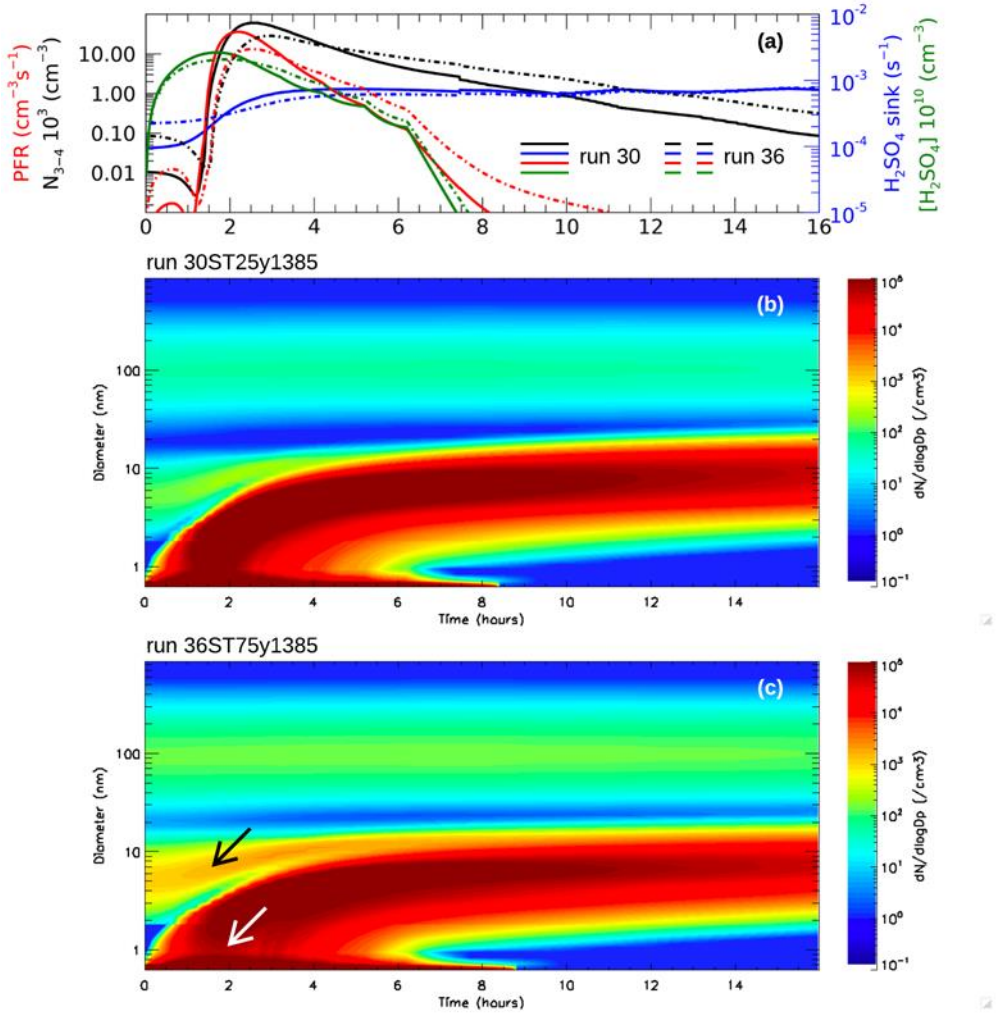

Figure 5.9. MAIA model output data for run 30ST25y1385 and run 36ST75y1385 in the stratosphere. The 25 percentile size distribution with NPF is compared with the 75 percentile size distribution with NPF at SO_2 mixing ratio of 1385 pptv. Panel (a) shows the number concentration of aerosol in the 3 to 4 nm diameter size range (black), the particle formation rate of aerosol > 3 nm (red), H_2SO_4 condensation sink (blue) and H_2SO_4 concentration (green) for both runs. Panel (b) and (c) show the modeled aerosol size distribution. The arrows in (c) point out enhanced growth by condensation of the Aitken mode (black arrow) and a reduction in particle formation (white arrow).

Table 5.2. MAIA model results for cases in the upper troposphere[†]

Run	H_2SO_4 10^5 (cm^{-3})	H_2SO_4 sink (10^{-4} s^{-1})	PFR 10^{-3} ($cm^{-3}s^{-1}$)	Particles formed (cm^{-3})	NPF duration (hrs)	CCN_{50} 0 hr (cm^{-3})	CCN_{50} 96 hr (cm^{-3})	CCN_{100} 0 hr (cm^{-3})	CCN_{100} 96 hr (cm^{-3})	CCN_{50} increase (%)	CCN_{100} increase (%)
1UT25n0	0	1.5	0	0	0	95	130	24	36		
2UT25n60	37	1.9	0.04	0	0	95	169	24	49	30	36
3UT25n1385	274	15.8	1931	32884	26.6	95	1900	24	202	1360	464
4UT25y0	0	0.9	0	0	0	33	47	12	18		
5UT25y60	52	1.5	2.5	84	8.9	33	68	12	24	44	35
6UT25y1385	249	16.0	2858	34884	27.8	33	2006	12	171	4140	847
7UT75n0	0	5.1	0	0	0	268	328	86	126		
8UT75n60	13	5.5	0.4	4	0.02	268	352	86	136	7	8
9UT75n1385	218	14.8	835	13397	22.5	268	942	86	374	187	196
10UT75y0	0	2.0	0	0	0	92	128	27	39		
11UT75y60	28	2.6	4.3	102	10.0	92	161	27	48	26	21
12UT75y1385	274	15.6	1870	29087	27.5	92	1845	27	187	1345	373

[†]Values listed for H_2SO_4 concentration, H_2SO_4 sink, and particle formation rate (PFR) are the trajectory maxima. Particles formed is the sum of PFR per unit time. NPF duration is calculated by summing the time steps with PFR > 0.01 cm^{-1} s^{-1}. CCN percent increase is calculated as 100×(CCN 60 [or 1385] SO_2 – CCN 0 SO_2)/CCN 0 SO_2.

Table 5.3. MAIA model results for cases in the mixing layer†

Run	H_2SO_4 10^5 (cm^{-3})	H_2SO_4 sink (10^{-4} s^{-1})	PFR 10^{-3} ($cm^{-3}s^{-1}$)	Particles formed (cm^{-3})	NPF duration (hrs)	CCN_{50} 0 hr (cm^{-3})	CCN_{50} 96 hr (cm^{-3})	CCN_{100} 0 hr (cm^{-3})	CCN_{100} 96 hr (cm^{-3})	CCN_{50} increase (%)	CCN_{100} increase (%)
13MX25n0	0	3.0	0	0	0	65	58	38	35		
14MX25n60	18	3.0	43	1608	35.6	65	60	38	39	4	12
15MX25n1385	226	15.0	21116	465782	57.8	65	1080	38	59	1766	69
16MX25y0	0	2.9	0	0	0	39	35	25	23		
17MX25y60	18	3.0	59	2250	41.4	39	36	25	25	4	9
18MX25y1385	228	15.0	21005	463491	59.0	39	1117	25	38	3098	64
19MX75n0	0	6.7	0	0	0	107	92	66	59		
20MX75n60	9	6.8	0.2	2	0.02	107	95	66	62	2	4
21MX75n1385	156	15.2	22514	461709	60.0	107	497	66	92	439	55
22MX75y0	0	5.1	0	0	0	114	98	56	51		
23MX75y60	11	5.2	1.8	26	3.1	114	103	56	55	5	7
24MX75y1385	179	15.1	23357	463063	60.6	114	757	56	98	669	90

†Values listed for H_2SO_4 concentration, H_2SO_4 sink, and particle formation rate (PFR) are the trajectory maxima. Particles formed is the sum of PFR per unit time. NPF duration is calculated by summing the time steps with PFR > 0.01 cm^{-1} s^{-1}. CCN percent increase is calculated as 100×(CCN 60 [or 1385] SO_2 – CCN 0 SO_2)/CCN 0 SO_2.

Table 5.4. MAIA model results for cases in the stratosphere†

Run	H_2SO_4 10^5 (cm^{-3})	H_2SO_4 sink (10^{-4} s^{-1})	PFR 10^{-3} ($cm^{-3}s^{-1}$)	Particles formed (cm^{-3})	NPF duration (hrs)	CCN_{50} 0 hr (cm^{-3})	CCN_{50} 96 hr (cm^{-3})	CCN_{100} 0 hr (cm^{-3})	CCN_{100} 96 hr (cm^{-3})	CCN_{50} increase (%)	CCN_{100} increase (%)
25ST25n0	0	1.7	0	0	0	26	27	19	20		
26ST25n60	22	1.9	201	13071	70.4	26	27	19	22	2	10
27ST25n1385	275	14.8	42059	434065	46.4	26	1248	19	38	4550	93
28ST25y0	0	2.2	0	0	0	30	31	21	22		
29ST25y60	20	2.4	100	4049	52.1	30	32	21	24	3	8
30ST25y1385	264	14.8	36160	420154	47.9	30	1195	21	38	3765	72
31ST75n0	0	4.2	0	0	0	54	54	39	40		
32ST75n60	13	4.2	0.3	2	0.02	54	55	39	42	2	4
33ST75n1385	228	14.7	19853	387265	50.1	54	947	39	54	1640	35
34ST75y0	0	5.2	0	0	0	77	77	53	54		
35ST75y60	10	5.3	1.1	18	2.1	77	78	53	56	2	4
36ST75y1385	207	14.7	13162	377465	53.7	77	767	53	75	900	39

†Values listed for H_2SO_4 concentration, H_2SO_4 sink, and particle formation rate (PFR) are the trajectory maxima. Particles formed is the sum of PFR per unit time. NPF duration is calculated by summing the time steps with PFR > 0.01 cm^{-1} s^{-1}. CCN percent increase is calculated as 100×(CCN 60 [or 1385] SO_2 – CCN 0 SO_2)/CCN 0 SO_2.

5.4 Discussion

This chapter has explored the sensitivity of CCN number concentration to new particle formation events in the upper troposphere, mixing layer and lower stratosphere. Understanding the formation of CCN from new particles is a crucial step to understanding the global CCN budget and the influence of primary emissions on climate through the modification of cloud microphysical properties. A modeling study of particle growth and CCN formation was done based on measured size distributions and modeled growth for the number distribution of particles that grew to 50 nm and 100 nm and assumed CCN-active. The model was applied to 12 measured size distributions in the upper troposphere, mixing layer and the stratosphere. Half of the size distributions were associated with recent NPF, and the other half were not. These size distributions were then inputted into the aerosol microphysical model MAIA and each run at an SO_2 concentration of 0, 60 and 1385 pptv producing modeled size distributions over a four-day forward trajectory. A total of 36 simulations were run.

A few studies have utilized MAIA to investigate new particle formation. One study used MAIA to examine whether ion-induced and neutral aerosol formation from sulfuric acid and water can explain the measured concentrations of nucleation mode particles (Weigel et al., 2011). Weigel et al. (2011) found that in most cases the predictions of the number of nucleation mode particles was in reasonable agreement with in situ observations. In another study Kazil et al. (2007) pair MAIA with a detailed 1D cirrus model (which describes ice crystal nucleation) to investigate whether neutral and charged sulfuric acid and water nucleation processes are active within non-convective

cirrus clouds. Kokkola et al. (2009) use MAIA as a reference model for an intercomparison of three different aerosol microphysics modules implemented in a climate model. All these studies used different initial gas phase mixing ratios of SO_2 and reported good results.

As an upper limit to the possible effect of changes in ion-induced binary nucleation of sulfuric acid and water, the total nucleation rate was perturbed by changing the SO_2 concentration, which has been shown to generate particle concentrations and NPF events in reasonable agreement with global observations (Spracklen et al., 2005; Spracklen et al., 2006; Merikanto et al., 2009; Yu and Luo, 2009; Spracklen et al., 2010). In this study, high SO_2 concentrations lead to a rapid growth of the newly formed particles out of the nucleation mode. In most cases, the formation of new particles was followed by gradual condensational growth to larger diameters, but this did not necessarily result in an increase of particle diameters greater than 50 nm and 100 nm. The number of potential CCN (CCN_{50} and CCN_{100}) varied significantly between the different model runs. In the cases considered in this study, neutral nucleation overwhelmingly dominates over charged nucleation. In fact, charged nucleation is negligible in the model output. Kazil et al. (2007) also found that neutral nucleation dominates in the UTLS and explain that the charged nucleation rate may be underestimated in MAIA.

In absolute terms, the highest increase in CCN was predicted to occur in the stratosphere. Intense NPF was predicted with high particle formation rates associated with the 25 percentile values of the size distribution in the stratosphere. The intense nucleation was associated with a more rapid increase in condensation sink in the 75

percentile case when compared to the 25 percentile case. In general, it appears that NPF proceeds readily and with high intensity in the lower stratosphere if SO_2 is present at high mixing ratios. The increases in potential CCN are extreme at 1385 pptv SO_2, but these are thought to have a very limited impact on free tropospheric and boundary layer clouds. Regardless, overshooting tops associated with large mesoscale convective systems are often observed above the tropopause in the mid-latitudes, and these cloud tops are thought to be responsible in hydrating the lower stratosphere by the geyser-like injection of ice particles and subsequent evaporation (Corti et al., 2008; Khaykin et al., 2009). It is feasible that high concentrations of SO_2 are also injected into the stratosphere through the convective ladder effect (Mari et al., 2000). Once SO_2 is present in high concentrations, MAIA predictions show that NPF should proceed with high intensity and episodically for several days.

The impact of particle formation on CCN is more relevant in the mixing layer and the troposphere. The mixing layer was found to be important for NPF. Particle formation events are of long duration and high intensity, especially at 1385 pptv SO_2. At 60 pptv SO_2, the impact of nucleation mode particles was only due to coagulation with the accumulation mode. It also appeared that nucleation was suppressed by size distributions with high surface area. At background 60 pptv SO_2 the increase in CCN reached 12% in the mixing layer and at 1385 pptv SO_2 the increase in CCN was 3098%.

In the upper troposphere new particle formation was suppressed and limited to the first 48 hours into the simulation. It was apparent that nucleation was very sensitive to the condensation sink. The size distributions with NPF were found to contribute significantly

to CCN when compared to size distributions without NPF. The percentage increase in CCN ranged from 7% to 44% at 60 pptv SO_2 and 187% to 4140% at 1385 pptv SO_2 in the upper troposphere. New particles formed 29% of the time over the four-day period, compared to twice that amount of time in the mixing layer and stratosphere. However, NPF events in the upper troposphere during MACPEX were frequent and therefore their CCN impact is most relevant. Convective cloud outflow is most likely to eject high concentrations of SO_2 in the upper troposphere, and if the condensation sink does not increase over time, a large number of new particles can form that can become CCN-active. In the NPF cases, the condensational growth of the nucleation mode is rapid and so is the growth of molecular clusters. This can be seen by the signature "banana" profiles in the modeled size distributions that are quite steep indicating fast growth. Any additional SO2 has a large impact on NPF in the upper troposphere. This NPF is likely to add new potential CCN and increase the concentration of CCN-active particles, especially in the instance when the preexisting surface area is low.

In the real atmosphere, the contribution of sulfuric acid to the formation of potential CCN is likely to differ from those reported in this study. The concentration of SO_2 and probably also of OH will deviate from what is assumed. Other differences between the model and real atmosphere may be due to:

- the uncertainty errors of the HYSPLIT air mass trajectory calculations, particularly estimates of temperature, relative humidity, pressure, water vapor mixing ratio and concentration, which are important in determining the SO_2 concentration and the ion production rate along the trajectory,

- the uncertainty in the model input parameters, particularly in the selection of SO_2 thresholds,
- the uncertainty due to the loss and removal of SO_2 inside clouds along the trajectory (which may play a major role since MACPEX targeted cirrus clouds and deep convective outflow),
- the mixing and dilution of SO_2 outside of the parcel trajectory,
- the uncertainty in particle nucleation rates due to other processes not included in MAIA such as ternary nucleation and heterogeneous nucleation on ice surfaces within cloud edges,
- the contribution of other condensed species in stabilizing the cluster and enhancing initial cluster growth.

In this study I simulate the forward trajectory up to four days. Increasing the time beyond that would have increased model errors and increased the probability that nucleation mode particle numbers would be unrealistically high, considering that in reality cloud formation is likely to interact with the airmass. In the four-day period, the HYSPLIT trajectories remained at high altitude, and it is, therefore, uncertain whether the simulated parcels would end up in the boundary layer.

Nevertheless, the results indicate very clearly that NPF is a significant source of potential CCN in the mid-latitudes. Particle formation is strongest at high SO_2 concentrations in the lower stratosphere and the mixing layer. The duration of NPF is

also relatively high with particle formation occurring up to 73% and 63% of the time in the stratosphere and the mixing layer, respectively. Particle formation in the upper troposphere is rapid and frequent in the first 48 hours. The fast growth of nucleated clusters, especially in the cases with NPF, produces a particle mode that becomes CCN-active within 24-hours.

Chapter Six: Conclusion

6.1 Theme of Dissertation

This research combined field measurements and observations with extensive data analysis and modeling to study new particle formation (NPF) in the mid-latitude upper troposphere (UT) and lower stratosphere (LS). The specific objectives of this dissertation were to: (1) successfully deploy a set of aerosol instruments on an airborne field campaign, (2) develop a new stringent and statistically significant criterion that identifies NPF events from measurements of aerosols in the nucleation mode, (3) identify the tropopause layer by using gas tracer relationships to examine stratospheric-tropospheric exchange, (4) examine the formation and intensity of NPF in relation to the origin of the air in which they were observed, (5) examine the formation and intensity of NPF in the vicinity of cloud, and (6) model the formation of new particles and their subsequent growth into a CCN active size range (concentration of aerosols > 50 nm and > 100 nm).

The main theme of this dissertation is new particle formation, a process where new particles form and grow by the condensation of condensable molecules created in reactions in the atmosphere involving gas-phase precursors. This process modifies the aerosol size distribution. It is widely believed that these processes contribute to the direct and indirect effect that aerosols have on climate.

In this dissertation, certain questions were addressed, and they relate to the understanding of aerosol new particle formation and particle growth in the mid-latitude

upper troposphere. Based on the analysis, modeling and the current knowledge of nucleation mechanisms and particle growth, different science questions were addressed: (1) when, where and how often does NPF occur in the UTLS (in spring over the continental US near the jet stream)? (2) what is the role of airmass origin in the tropopause layer in the formation of new particles? (3) what is the impact of deep convection on NPF in the UT? (4) what is the impact of the newly formed particles on the concentration of potential CCN (based on a modeling study)?

6.2 Key Findings

6.2.1 Timing, location, and frequency of new particle formation in the UTLS.

The UTLS is defined around the discontinuity that occurs at the tropopause. The air below the tropopause is the troposphere, and that above is the stratosphere. The dynamic tropopause at 2.5 potential vorticity units (PVU) best defines the chemical transition between the airmass in the troposphere that is rich in CO and the airmass in the stratosphere that is rich in O_3. A mixing layer was found to occur between the troposphere and the stratosphere, and it was approximately centered at the dynamic tropopause (see Figure 4.4). The mixing occurred between the dynamic and thermal tropopause near the jet stream, where the tropopause layer was discontinuous due to the separation in air mass that occurs at the jet. To analyze the MACPEX data, many of the measured parameters were averaged and normalized to the dynamic tropopause.

In total for the six MACPEX flights, 188 NPF events were detected in-cloud and out-of-cloud (see Figure 3.11). Out of the 188 events, 121 were traversed in a flight

distance greater than 1 km. A quarter of the NPF events (47 events) were detected for a distance greater than 15 km. The event that covered the largest distance extended to 119 km. It is believed that most of the nucleation occurs during daytime as OH concentration has a diurnal cycle with a maximum noon concentration and minimum nighttime concentration. Out of all the MACPEX out-of-cloud data, 22% contained NPF. The fraction of measurements with NPF was quite significant in the middle troposphere (22%), upper troposphere (53%) and mixing layer (11%) (see median values in Figure 4.8). NPF in the boundary layer was episodic (4%) and limited to the near-surface layer. The upper troposphere was the most important for new particle formation (see Figure 4.6 and 4.7). This layer was cloud impacted, with high relative humidity with respect to ice (54%), high ultra-fine aerosol concentration (476 cm^{-3}) and low surface area (9.7 μm^2 cm^{-3}). The ratio of ultra-fine particles to total particle number was highest in the upper troposphere at a median of 0.24 and was contained within 3 km below the dynamic tropopause. The upper troposphere was also a region with vertical wind shear and strong mixing. Trace mixing ratios of CO were approximately equal to those in the middle troposphere and higher than the mixing layer. A vertical wind shear gradient was present in the mixing layer and resembled the wind profile that is characteristic of the jet stream, with the highest velocity at the central core. The mixing layer was drier (24% RH_{ice}) than the surrounding air in the upper troposphere and surface area was relatively high (18.6 μm^2 cm^{-3}). CO trace gas concentrations were also lower compared to the upper troposphere. The frequency of NPF was suppressed (10.7%) when compared to the upper troposphere (52.7%). NPF appeared to be enhanced immediately above and below the jet

stream core, in areas of intense wind shear. In the stratosphere, the fraction of measurements with NPF was very small (0.5%) and no significant particle formation occurs because it is too dry (12% RH_{ice}).

New particle formation in the upper troposphere was triggered by high relative humidity and low surface area. The frequency of NPF in the upper troposphere was higher than that in the mixing layer, and NPF was linked to the distance from cloud. Surface area suppressed NPF in the upper troposphere, but nucleation and growth still occurred possibly due to the high mixing ratio of SO_2 that could be present by the transport of polluted boundary layer air into the upper troposphere. New particles formed in regions with strong mixing, such as those in the vicinity of deep convection and near the jet stream.

6.2.2 Role of airmass origin on new particle formation in the tropopause layer.

New particle formation in the UTLS is most commonly attributed to homogeneous nucleation of sulfuric acid and water vapor. Other gases may be involved in the nucleation process, but there is much uncertainty in nucleation processes that involve other species. Many of the critical factors that determine how binary nucleation proceeds depends on the sulfuric acid vapor concentration, preexisting particle surface area, temperature and relative humidity. Easter and Peters (1993) found that turbulent fluctuations of temperature and water vapor showed new particle formation peaking at conditions of lower temperature and higher relative humidity. Bigg (1997) suggested that

small fluctuations in these quantities cause a change in the particle formation rate even when the mean nucleation rate is below the threshold for binary homogeneous nucleation. These fluctuations are caused by turbulence or rapid mixing resulting in a decrease in temperature and increase in relative humidity. Nilsson and Kulmala (1998) suggested that mixing alone can dominate the effect proposed by Easter and Peters (1993). Based on the current knowledge of nucleation mechanisms and meteorological analysis (see Section 2.2.2 and 2.2.3), it is believed that the measurements with NPF in the upper troposphere and mixing layer are subject to enhancements in the nucleation rates by mixing processes.

Mixing is the sudden transfer of air with different properties or the mixing of air masses of different origin. Mixing can also occur at cloud edges especially in intense convective clouds with large updrafts and downdrafts. Mixing takes place in the mixing layer where tropospheric air exchanges with stratospheric air. This transfer of air was observed at the dynamic tropopause where mixing between the troposphere and the stratosphere results in linear mixing lines (see Figure 4.1). The linearity of these mixing curves indicates a rapid and frequent exchange of the tropospheric and stratospheric air masses. This mixing was contained approximately 2 km above and 2 km below the dynamic tropopause (or the 2.5 PVU surface). A vertical wind shear gradient was observed at the top of the upper troposphere and in the mixing layer (see Figure 4.7). Dynamical processes such as mid-latitude cyclogenesis, a dynamic process that induces the development of cyclonic circulation, was observed during MACPEX and can serve as triggers for airmass mixing and play a major role in the upward transport of pollutants into the upper troposphere. During MACPEX, cyclogenesis was frequently occurring as

the aircraft often conducted measurements near the jet stream. Strong mixing events such as mid-latitude tropopause folds were also observed (see Figure 2.6). These folds coincide with the frontal zone beneath the jet stream in the mixing layer.

It has been established that the upper troposphere and mixing layer is actively producing new particles and that certain regions with mixing, such as wind shear zones, are favored locations for particle formation. It is believed that tropopause folds frequently occurred during MACPEX and that NPF in the mixing layer was associated with these folds. However, tropopause folds were observed to occur very close to convection and it was difficult to separate NPF data points associated with folds from those associated with convection.

6.2.3 Impact of deep convection on new particle formation.

This study confirms that high relative humidity and low preexisting particle number concentration triggers new particle formation in the upper troposphere. New particle formation was also associated with high concentrations of CO which could be an indicator that a high precursor gas mixing ratio was present. This was most apparent in the upper troposphere and mixing layer, particularly in instances when the air parcel was in the vicinity of cloud. Surface area suppressed particle formation in the upper troposphere as those cases with no NPF were associated with high surface area. It is also possible that enhanced concentrations of OH around cloud edges increases the concentration of H_2SO_4 and subsequently a possible enhancement in nucleation rates.

The cases with deep convection were associated with higher concentrations of CO in the upper troposphere and the mixing layer. It is hypothesized that a convective ladder effect transferred air from the boundary layer into the upper troposphere with little dilution. This ladder effect fits the CO vertical profile shown in Figure 4.7d where high CO values in the upper troposphere and mixing layer indicate frequent mixing with the boundary layer. This feature was associated with high frequency of NPF in the upper troposphere and mixing layer (see Figure 4.11). Measurements in the vicinity of convection also had higher surface area than those sampled near the jet stream. It is hypothesized that strong convective updrafts are likely to contain interstitial aerosol. This interstitial aerosol is ejected in cloud outflow and acts to increase the surface area and suppress nucleation. Higher SO_2 concentrations are therefore required for particle formation near deep convection with intense updrafts.

6.2.4 Impact of new particle formation on cloud condensation nuclei.

In this dissertation, I have investigated the production of "potential" CCN resulting from NPF along a modeled forward trajectory. A modeling study of particle growth and CCN formation was done based on measured size distributions and modeled growth for the number distribution of particles assumed CCN-active. The model used in this work is the highly-resolved aerosol microphysics model MAIA (Lovejoy et al., 2004; Kazil et al., 2007). MAIA simulates microphysical processes to calculate reference particle formation rates of H_2SO_4/H_2O aerosol particles and growth by condensation and coagulation. As an upper limit to the possible effect of changes in ion-induced binary

nucleation of sulfuric acid and water, the total nucleation rate was changed by setting SO_2 concentrations to 0 pptv to simulate a very clean (or pre-industrial) type conditions, 60 pptv threshold to look at the maximum effect of non-cloud impacted NPF and 1385 pptv threshold to represent the maximum SO_2 that is entrained through convective cloud with little dilution.

In absolute terms, the highest increase in CCN was predicted to occur in the lower stratosphere. It appears that NPF proceeds readily and with high intensity in the lower stratosphere if SO_2 is present at high mixing ratios. The increases in potential CCN are extreme at 1385 pptv SO_2, but these are thought to have a very limited impact on free tropospheric and boundary layer clouds. In the mixing layer it was found that particle formation events are of long duration and high intensity. At 60 pptv SO_2, nucleation was suppressed by size distributions with high surface area. In the upper troposphere new particle formation was suppressed and limited to the first 24 to 48 hours into the simulation. It was apparent that nucleation is very sensitive to the condensation sink and the size distributions with NPF were found to contribute significantly to CCN when compared to size distributions without NPF.

The results suggest that NPF is a source of potential CCN. NPF events in the upper troposphere during MACPEX were frequent and therefore their CCN impact is most relevant. Convective cloud outflow is most likely to eject high concentrations of SO_2 in the upper troposphere, and if the condensation sink does not increase over time, a large number of new particles can form that can become CCN active. In the NPF cases, the condensational growth of the nucleation mode is rapid and so is the growth of

molecular clusters. Any additional SO_2 has a large impact on NPF in the upper troposphere. This NPF is likely to add new potential CCN and increase the concentration of CCN active particles, especially in the instance when the preexisting surface area is low. The fast growth of nucleated clusters, especially in the cases with NPF, produces a particle mode that becomes CCN active within 24-hours.

6.3 Outstanding Scientific Questions

New particle formation in the UTLS is most commonly attributed to homogeneous nucleation of sulfuric acid and water vapor. Other gases may be involved in the nucleation process, but there is some uncertainty in nucleation processes that involve other species. The precise identity of vapors participating in nucleation and growth by condensation in the UTLS remains unknown. Several studies have deployed instrumentation on airborne platforms to investigate the formation and growth of particles in different environments and discuss the importance of various mechanisms of particle formation and growth between the different environments. While several mechanisms have been proposed for new particle formation, the importance of each mechanism is still the center of much debate. One major problem hampering our understanding of new particle formation is that these new particles are smaller than the lowest detection limit of the instrument. Another issue is that there are a very small number of new particle formation observations in the region close to the tropopause, due to the capabilities of research platforms to fly consistently at this high altitude equatorward of the mid-latitudes.

While the existence of NPF and growth to potential CCN has certainly been established beyond all doubt as a relatively common phenomenon in the UTLS, the present work fails to establish with any certainty the exact mechanisms involved in the observed particle formation. It can be said that mesoscale and synoptic features enhance mixing and facilitate the formation of new particles in the northern mid-latitudes. These new particles can grow to produce a particle mode that becomes CCN-active within 24-hours. Until more detailed studies are made it is not possible to estimate whether NPF could account for a significant fraction of cloud-active CCN. However, it seems so likely that the synoptic meteorology, mesoscale dynamics, and the identified mixing processes lead to particle formation as described and that these grow to become CCN. Whether these additional CCN participate in cloud formation and cloud modification will have to be studied by detailed high-resolution bin-microphysics on a synoptic scale.

References

Ackerman, A. S., Toon, O. B., Stevens, D. E., Heymsfield, A. J., Ramanathan, V., & Welton, E. J. (2000). Reduction of tropical cloudiness by soot. Science, 288(5468), 1042-1047.

Aitken, J. (1888) "On the Number of Dust Particles in the Atmosphere." Nature News. Nature Publishing Group, 37, 428-430.

Albrecht, B. A. (1989). Aerosols, Cloud Microphysics, and Fractional Cloudiness. Science, 245(4923), 1227-1231.

Almeida, J., Schobesberger, S., Kürten, A., Ortega, I. K., Kupiainen-Määttä, O., Praplan, A. P., ... & David, A. (2013). Molecular understanding of Sulphuric Acid-amine Particle Nucleation in the Atmosphere. Nature, 502(7471), 359-363.

Al-Saadi, J. A., Thornhill, A., Alston, E. J., Chen, G., Fahey, D. W., Jensen, E. J., & Mace, G. G. (2012). MACPEX Water Measurement Comparison. In AGU Fall Meeting Abstracts (Vol. 1, p. 0071).

Anastasio, C., & Martin, S. T. (2001). Atmospheric nanoparticles. Reviews in Mineralogy and Geochemistry, 44(1), 293-349.

Andreae, M. O., Rosenfeld, D., Artaxo, P., Costa, A. A., Frank, G. P., Longo, K. M., & Silva-Dias, M. A. F. (2004). Smoking rain clouds over the Amazon. Science, 303(5662), 1337-1342.

Arnold, F. (2008). Atmospheric Ions and Aerosol Formation. Space Science Reviews, 1(137), 225-239.

Arnold, F., Schneider, J., Gollinger, K., Schlager, H., Schulte, P., Hagen, D. E., ... & Van Velthoven, P. (1997). Observation of upper tropospheric sulfur dioxide-and Acetone-pollution: Potential Implications for Hydroxyl Radicaland Aerosol Formation. Geophysical Research Letters, 24(1), 57-60.

Barry, R. G., & Chorley, R. J. (2009). Atmosphere, weather and climate. Routledge.

Bigg, E. K. (1997). A mechanism for the formation of new particles in the atmosphere. Atmospheric Research, 43(2), 129-137

Birmili, W., & Wiedensohler, A. (2000). New particle formation in the continental boundary layer: Meteorological and gas phase parameter influence. Geophysical Research Letters, 27(20), 3325-3328.

Bloom, S. C., Takacs, L. L., Da Silva, A. M., & Ledvina, D. (1996). Data assimilation using incremental analysis updates. Monthly Weather Review, 124(6), 1256-1271.

Boering, K. A., Daube, B. C., Wofsy, S. C., Loewenstein, M., Podolske, J. R., & Keim, E. R. (1994). Tracer-tracer relationships and lower stratospheric dynamics: CO2 and N2O correlations during SPADE. Geophysical Research Letters, 21(23), 2567-2570.

Brock, C. A. (1998). A fast-response nuclei mode spectrometer for determining particle size distribution in the 3-100 nm diameter range: technical description, Denver, CO: Technical Report, University of Denver.

Brock, C. A., Hamill, P., Wilson, J. C., Jonsson, H. H., & Chan, K. R. (1995). Partical formation in the upper tropical troposphere: A source of nuclei for the stratospheric aerosol. Science, 270(5242), 1650.

Brown, P. N., Byrne, G. D., & Hindmarsh, A. C. (1989). VODE: A variable-coefficient ODE solver. SIAM Journal on Scientific and Statistical Computing, 10(5), 1038-1051.

Browning, K. A., & Reynolds, R. (1994). Diagnostic study of a narrow cold-frontal rainband and severe winds associated with a stratospheric intrusion. Quarterly Journal of the Royal Meteorological Society, 120(516), 235-257.

Buseck, P. R., & Adachi, K. (2008). Nanoparticles in the atmosphere. Elements, 4(6), 389-394.

Charlson, R. J., & Schwartz, S. E. (1992). Climate Forcing by Anthropogenic Aerosols. Science, 255(5043), 423.

Chatfield, R. B., & Crutzen, P. J. (1984). Sulfur dioxide in remote oceanic air: Cloud transport of reactive precursors. Journal of Geophysical Research: Atmospheres, 89(D5), 7111-7132.

Clarke, A. D., Davis, D., Kapustin, V. N., Eisele, F., Chen, G., Paluch, I., ... & Mauldin, L. (1998). Particle nucleation in the tropical boundary layer and its coupling to marine sulfur sources. Science, 282(5386), 89-92.

Clarke, A. D., Kapustin, V. N., Eisele, F. L., Weber, R. J., & McMurry, P. H. (1999). Particle production near marine clouds: Sulfuric acid and predictions from classical binary nucleation. Geophysical Research Letters, 26(16), 2425-2428.

Clegg, S. L., & Brimblecombe, P. (1995). Application of a Multicomponent Thermodynamic Model to Activities and Thermal Properties of 0-40 mol kg-1

aqueous sulfuric acid from< 200 to 328 K. Journal of Chemical and Engineering Data, 40(1), 43-64.

Clement, C. F., & Ford, I. J. (1999). Gas-to-particle conversion in the atmosphere: II. Analytical models of nucleation bursts. Atmospheric Environment, 33(3), 489-499.

Clement, C. F., Ford, I. J., Twohy, C. H., Weinheimer, A., & Campos, T. (2002). Particle production in the outflow of a mid-latitude storm. Journal of Geophysical Research: Atmospheres, 107(D21).

Collins, W. J., Stevenson, D. S., Johnson, C. E., & Derwent, R. G. (1999). Role of convection in determining the budget of odd hydrogen in the upper troposphere. Journal of Geophysical Research: Atmospheres, 104(D21), 26927-26941.

Corti, T., Luo, B. P., De Reus, M., Brunner, D., Cairo, F., Mahoney, M. J., ... & Schiller, C. (2008). Unprecedented evidence for deep convection hydrating the tropical stratosphere. Geophysical Research Letters, 35(10).

Cotton, R., Osborne, S., Ulanowski, Z., Hirst, E., Kaye, P. H., & Greenaway, R. S. (2010). The ability of the Small Ice Detector (SID-2) to characterize cloud particle and aerosol morphologies obtained during flights of the FAAM BAe-146 research aircraft. Journal of Atmospheric and Oceanic Technology, 27(2), 290-303.

Crutzen, P. J. (1979). The role of NO and NO2 in the chemistry of the troposphere and stratosphere. Annual Review of Earth and Planetary Sciences, 7(1), 443-472.

Curtius, J. (2009). Nucleation of atmospheric particles. In EPJ Web of Conferences (Vol. 1, pp. 199-209). EDP Sciences.

Curtius, J., Froyd, K. D., & Lovejoy, E. R. (2001). Cluster Ion Thermal Decomposition: Experimental Kinetics Study, Ab Initio Calculations and Master Equation Modeling for HSO4-(H2SO4) x (HNO3) y. The Journal of Physical Chemistry A, 105(48), 10867-10873.

Cziczo, D. J., Froyd, K. D., & Murphy, D. M. (2012). The chemical composition of cirrus forming aerosol: Lessons from the MACPEX field study. In AGU Fall Meeting Abstracts (Vol. 1, p. 01P).

Danielsen, E. F. (1968). Stratospheric-tropospheric exchange based on radioactivity, ozone and potential vorticity. Journal of the Atmospheric Sciences, 25(3), 502-518.

Davis, S. M., Hallar, A. G., Avallone, L. M., & Engblom, W. (2007). Measurement of total water with a tunable diode laser hygrometer: Inlet analysis, calibration procedure, and ice water content determination. Journal of Atmospheric and Oceanic Technology, 24(3), 463-475.

DeFelice, T. P., & Cheng, R. J. (1998). On the phenomenon of nuclei enhancement during the evaporative stage of a cloud. Atmospheric Research, 47, 15-40.

de Reus, M., Krejci, R., Williams, J., Fischer, H., Scheele, R., & Ström, J. (2001). Vertical and horizontal distributions of the aerosol number concentration and size distribution over the northern Indian Ocean. Journal of Geophysical Research. D. Atmospheres, 106, 28.

de Reus, M., Ström, J., Kulmala, M., Pirjola, L., Lelieveld, J., Schiller, C., & Zöger, M. (1998). Airborne aerosol measurements in the tropopause region and the dependence of new particle formation on preexisting particle number concentration. Journal of Geophysical Research: Atmospheres, 103(D23), 31255-31263.

Ditas, F., Shaw, R. A., Siebert, H., Simmel, M., Wehner, B., & Wiedensohler, A. (2012). Aerosols-cloud microphysics-thermodynamics-turbulence: evaluating supersaturation in a marine stratocumulus cloud. Atmospheric Chemistry and Physics, 12(5), 2459-2468.

Dusek, U., Frank, G. P., Hildebrandt, L., Curtius, J., Schneider, J., Walter, S., ... & Borrmann, S. (2006). Size matters more than chemistry for cloud-nucleating ability of aerosol particles. Science, 312(5778), 1375-1378.

Easter, R. C., & Peters, L. K. (1993). Binary homogeneous nucleation: Temperature and relative humidity fluctuations and non-linearity (No. PNL-SA--21486; CONF-930133--9). Pacific Northwest Lab., Richland, WA (United States)

Field, P. R., Heymsfield, A. J., & Bansemer, A. (2006). Shattering and particle interarrival times measured by optical array probes in ice clouds. Journal of Atmospheric and Oceanic Technology, 23(10), 1357-1371.

Fischer, H., Wienhold, F. G., Hoor, P., Bujok, O., Schiller, C., Siegmund, P., ... & Lelieveld, J. (2000). Tracer correlations in the northern high latitude lowermost stratosphere: Influence of cross-tropopause mass exchange. Geophysical Research Letters, 27(1), 97-100.

Frey, W., Borrmann, S., Kunkel, D., Weigel, R., Reus, M. D., Schlager, H., ... & Krämer, M. (2011). In situ measurements of tropical cloud properties in the West African Monsoon: upper tropospheric ice clouds, Mesoscale Convective System outflow, and subvisual cirrus. Atmospheric Chemistry and Physics, 11(12), 5569-5590.

Froyd, K. D., & Lovejoy, E. R. (2003a). Experimental thermodynamics of cluster ions composed of H2SO4 and H2O. 1. Positive ions. The Journal of Physical Chemistry A, 107(46), 9800-9811.

Froyd, K. D., & Lovejoy, E. R. (2003b). Experimental thermodynamics of cluster ions composed of H2SO4 and H2O. 2. Measurements and ab initio structures of negative ions. The Journal of Physical Chemistry A, 107(46), 9812-9824

Fuchs, N. A., Daisley, R. E., Fuchs, M., Davies, C. N., & Straumanis, M. E. (1965). The mechanics of aerosols. MacMillan , N.Y. , Chapter 7

Fueglistaler, S., Dessler, A. E., Dunkerton, T. J., Folkins, I., Fu, Q., & Mote, P. W. (2009). Tropical tropopause layer. Reviews of Geophysics, 47(1).

Gao, R. S., Ballard, J., Watts, L. A., Thornberry, T. D., Ciciora, S. J., McLaughlin, R. J., & Fahey, D. W. (2012). A compact, fast UV photometer for measurement of ozone from research aircraft. Atmospheric Measurement Techniques, 5(9), 2201.

Gao, R., Rollins, A., Thornberry, T. D., Hall, E., Jordan, A., Hurst, D. F., ... & Fahey, D. W. (2011). Quantifying consistency and biases between aircraft, balloon and remote sensing measurements of UT/LS water vapor during the WB-57 NASA MACPEX mission. In AGU Fall Meeting Abstracts (Vol. 1, p. 0135).

Giauque, W. F., Hornung, E. W., Kunzler, J. E., & Rubin, T. R. (1960). The thermodynamic properties of aqueous sulfuric acid solutions and hydrates from 15 to 300 K. 1. Journal of the American Chemical Society, 82(1), 62-70.

Griggs, D. J., & Noguer, M. (2002). Climate change 2001: the scientific basis. Contribution of working group I to the third assessment report of the intergovernmental panel on climate change. Weather, 57(8), 267-269.

Hallar, A. G., Lowenthal, D. H., Chirokova, G., Borys, R. D., & Wiedinmyer, C. (2011). Persistent daily new particle formation at a mountain-top location. Atmospheric Environment, 45(24), 4111-4115.

Hammer, E., Bukowiecki, N., Gysel, M., Jurányi, Z., Hoyle, C. R., Vogt, R., ... & Weingartner, E. (2014). Investigation of the effective peak supersaturation for liquid-phase clouds at the high-alpine site Jungfraujoch, Switzerland (3580 m asl). Atmospheric Chemistry and Physics, 14(2), 1123-1139.

Hanson, D. R., & Lovejoy, E. R. (2006). Measurement of the thermodynamics of the hydrated dimer and trimer of sulfuric acid. The Journal of Physical Chemistry A, 110(31), 9525-9528.

Hartjenstein, G. (2000). Diffusive decay of tropopause folds and the related cross-tropopause mass flux. Monthly Weather Review, 128(8), 2958-2966.

Hauf, T., Schulte, P., Alheit, R., & Schlager, H. (1995). Rapid vertical trace gas transport by an isolated mid-latitude thunderstorm. Journal of Geophysical Research: Atmospheres, 100(D11), 22957-22970.

Hinds, W. C. (2009). Aerosol technology: properties, behavior, and measurement of airborne particles. 2nd Edition, John Wiley & Sons.

Holton, J. R. (1992). An introduction to dynamic meteorology. International Geophysics Series, San Diego, New York: Academic Press, c1992, 3rd ed.

Holton, J. R., Haynes, P. H., McIntyre, M. E., Douglass, A. R., Rood, R. B., & Pfister, L. (1995). Stratosphere-troposphere exchange. Reviews of Geophysics, 33(4), 403-439.

Hoor, P., Fischer, H., Lange, L., Lelieveld, J., & Brunner, D. (2002). Seasonal variations of a mixing layer in the lowermost stratosphere as identified by the CO-O3 correlation from in situ measurements. Journal of Geophysical Research: Atmospheres, 107(D5).

Ilotoviz, E., Khain, A. P., Benmoshe, N., Phillips, V. T., & Ryzhkov, A. V. (2016). Effect of aerosols on freezing drops, hail, and precipitation in a mid-latitude storm. Journal of the Atmospheric Sciences, 73(1), 109-144.

Jensen, E. J., Lawson, R. P., Bergman, J. W., Pfister, L., Bui, T. P., & Schmitt, C. G. (2013). Physical processes controlling ice concentrations in synoptically forced, midlatitude cirrus. Journal of Geophysical Research: Atmospheres, 118(11), 5348-5360.

Jensen, E. J., Toon, O. B., Pfister, L., & Selkirk, H. B. (1996). Dehydration of the upper troposphere and lower stratosphere by subvisible cirrus clouds near the tropical tropopause. Geophysical Research Letters, 23(8), 825-828.

Jonsson, H. H., Wilson, J. C., Brock, C. A., Knollenberg, R. G., Newton, T. R., Dye, J. E., ... & Woods, D. C. (1995). Performance of a focused cavity aerosol spectrometer for measurements in the stratosphere of particle size in the 0.06–2.0-μm-diameter range. Journal of Atmospheric and Oceanic Technology, 12(1), 115-129.

Kazil, J., & Lovejoy, E. R. (2004), Tropospheric ionization and aerosol production: A model study, J. Geophys. Res., 109, D19206, doi:10.1029/2004JD004852.

Kazil, J., & Lovejoy, E. R. (2007). A semi-analytical method for calculating rates of new sulfate aerosol formation from the gas phase. Atmospheric Chemistry and Physics, 7(13), 3447-3459.

Kazil, J., Lovejoy, E. R., Jensen, E. J., & Hanson, D. R. (2007). Is aerosol formation in cirrus clouds possible? Atmospheric Chemistry and Physics, 7(5), 1407-1413.

Kerminen, V. M., Lihavainen, H., Komppula, M., Viisanen, Y., & Kulmala, M. (2005). Direct observational evidence linking atmospheric aerosol formation and cloud droplet activation. Geophysical Research Letters, 32(14).

Kerminen, V. M., Pirjola, L., & Kulmala, M. (2001). How significantly does coagulational scavenging limit atmospheric particle production?. Journal of Geophysical Research: Atmospheres, 106(D20), 24119-24125.

Khaykin, S., Pommereau, J. P., Korshunov, L., Yushkov, V., Nielsen, J., Larsen, N., ... & Williams, E. (2009). Hydration of the lower stratosphere by ice crystal geysers over land convective systems. Atmospheric Chemistry and Physics, 9(6), 2275-2287.

Kim, J. H., Yum, S. S., Shim, S., Yoon, S. C., Hudson, J. G., Park, J., & Lee, S. J. (2011). On aerosol hygroscopicity, cloud condensation nuclei (CCN) spectra and critical supersaturation measured at two remote islands of Korea between 2006 and 2009. Atmospheric Chemistry and Physics, 11(24), 12627.

Kirkby, J., Curtius, J., Almeida, J., Dunne, E., Duplissy, J., Ehrhart, S., ... & Kupc, A. (2011). Role of sulphuric acid, ammonia and galactic cosmic rays in atmospheric aerosol nucleation. Nature, 476(7361), 429-433.

Kojima, T., Buseck, P. R., Wilson, J. C., Reeves, J. M., & Mahoney, M. J. (2004). Aerosol particles from tropical convective systems: Cloud tops and cirrus anvils. Journal of Geophysical Research: Atmospheres, 109(D12).

Kokkola, H., Hommel, R., Kazil, J., Niemeyer, U., Partanen, A. I., Feichter, J., & Timmreck, C. (2009). Aerosol microphysics modules in the framework of the ECHAM5 climate model–intercomparison under stratospheric conditions. Geoscientific Model Development, 2, 97-112.

Konopka, P., Günther, G., Müller, R., dos Santos, F. H. S., Schiller, C., Ravegnani, F., ... & Pan, L. L. (2007). Contribution of mixing to upward transport across the tropical tropopause layer (TTL). Atmospheric Chemistry and Physics, 7(12), 3285-3308.

Korhonen, P., Kulmala, M., Laaksonen, A., Viisanen, Y., McGraw, R., & Seinfeld, J. H. (1999). Ternary nucleation of H2SO4, NH3, and H2O in the atmosphere. Journal of Geophysical Research: Atmospheres, 104(D21), 26349-26353.

Krebsbach, M., Schiller, C., Brunner, D., Günther, G., Hegglin, M. I., Mottaghy, D., ... & Wernli, H. (2006). Seasonal cycles and variability of O3 and H2O in the UT/LMS during SPURT. Atmospheric Chemistry and Physics, 6, 109-125.

Krüger, M. L., Mertes, S., Klimach, T., Cheng, Y. F., Su, H., Schneider, J., ... & Rose, D. (2014). Assessment of cloud supersaturation by size-resolved aerosol particle and cloud condensation nuclei (CCN) measurements. Atmospheric Measurement Techniques, 7(8), 2615-2629.

Kuang, C., McMurry, P. H., & McCormick, A. V. (2009). Determination of cloud condensation nuclei production from measured new particle formation events. Geophysical Research Letters, 36(9).

Kuang, C., McMurry, P. H., McCormick, A. V., & Eisele, F. L. (2008). Dependence of nucleation rates on sulfuric acid vapor concentration in diverse atmospheric locations. Journal of Geophysical Research: Atmospheres, 113(D10).

Kulmala, M., & Kerminen, V. M. (2008). On the formation and growth of atmospheric nanoparticles. Atmospheric Research, 90(2), 132-150.

Kulmala, M., Korhonen, P., Napari, I., Karlsson, A., Berresheim, H., & O'Dowd, C. D. (2002). Aerosol formation during PARFORCE: Ternary nucleation of H2SO4, NH3, and H2O. Journal of Geophysical Research: Atmospheres, 107(D19).

Kulmala, M., Petäjä, T., Mönkkönen, P., Koponen, I. K., Maso, M. D., Aalto, P. P., ... & Kerminen, V. M. (2005). On the growth of nucleation mode particles: source rates of condensable vapor in polluted and clean environments. Atmospheric Chemistry and Physics, 5(2), 409-416.

Kulmala, M., Reissell, A., Sipilä, M., Bonn, B., Ruuskanen, T. M., Lehtinen, K. E., ... & Ström, J. (2006). Deep convective clouds as aerosol production engines: Role of insoluble organics. Journal of Geophysical Research: Atmospheres, 111(D17).

Kulmala, M., Vehkamäki, H., Petäjä, T., Dal Maso, M., Lauri, A., Kerminen, V. M., ... & McMurry, P. H. (2004). Formation and growth rates of ultrafine atmospheric particles: a review of observations. Journal of Aerosol Science, 35(2), 143-176.

Laakso, L., Mäkelä, J. M., Pirjola, L., & Kulmala, M. (2002). Model studies on ion-induced nucleation in the atmosphere. Journal of Geophysical Research: Atmospheres, 107(D20).

Laaksonen, A., Hamed, A., Joutsensaari, J., Hiltunen, L., Cavalli, F., Junkermann, W., ... & Facchini, M. C. (2005). Cloud condensation nucleus production from nucleation events at a highly polluted region. Geophysical Research Letters, 32(6).

Lawson, R. P., O'Connor, D., Zmarzly, P., Weaver, K., Baker, B., Mo, Q., & Jonsson, H. (2006). The 2D-S (stereo) probe: Design and preliminary tests of a new airborne, high-speed, high-resolution particle imaging probe. Journal of Atmospheric and Oceanic Technology, 23(11), 1462-1477.

Lee, K. W., Chen, J., & Gieseke, J. A. (1984). Log-normally preserving size distribution for Brownian coagulation in the free-molecule regime. Aerosol Science and Technology, 3(1), 53-62.

Lee, S. H., Reeves, J. M., Wilson, J. C., Hunton, D. E., Viggiano, A. A., Miller, T. M., ... & Lait, L. R. (2003). Particle formation by ion nucleation in the upper troposphere and lower stratosphere. Science, 301(5641), 1886-1889.

Lee, S. H., Wilson, J. C., Baumgardner, D., Herman, R. L., Weinstock, E. M., LaFleur, B. G., ... & Strawa, A. (2004). New particle formation observed in the tropical/subtropical cirrus clouds. Journal of Geophysical Research: Atmospheres, 109(D20).

Lihavainen, H., Kerminen, V. M., Komppula, M., Hatakka, J., Aaltonen, V., Kulmala, M., & Viisanen, Y. (2003). Production of "potential" cloud condensation nuclei associated with atmospheric new-particle formation in northern Finland. Journal of Geophysical Research: Atmospheres, 108(D24).

Liu, X., Zhang, K., Comstock, J. M., Wan, H., & Wang, M. (2013). Investigating the Impact of Updraft Velocity on Cirrus Cloud Properties Using the CAM5 Model Constrained with Field Measurements. In AGU Fall Meeting Abstracts.

Liu, X., Zhang, K., Wang, M., Comstock, J. M., Mitchell, D. L., Mace, G. G., & Jensen, E. J. (2012). Constraining Climate Forcing of Ice Nucleation with SPartICus/MACPEX Observations. In AGU Fall Meeting Abstracts (Vol. 1, p. 0279).

Lovejoy, E. R., & Curtius, J. (2001). Cluster ion thermal decomposition (II): Master equation modeling in the low-pressure limit and fall-off regions. Bond energies for HSO4-(H2SO4) x (HNO3) y. The Journal of Physical Chemistry A, 105(48), 10874-10883.

Lovejoy, E. R., Curtius, J., & Froyd, K. D. (2004). Atmospheric ion-induced nucleation of sulfuric acid and water. Journal of Geophysical Research: Atmospheres, 109(D8).

Lovejoy, E. R., Hanson, D. R., & Huey, L. G. (1996). Kinetics and products of the gas-phase reaction of SO_3 with water. The Journal of Physical Chemistry, 100(51), 19911-19916.

Lu, R., & Turco, R. P. (1994). Air pollutant transport in a coastal environment. Part I: Two-dimensional simulations of sea-breeze and mountain effects. Journal of the Atmospheric Sciences, 51(15), 2285-2308.

Lucchesi, R. (2012). File specification for MERRA products. GMAO Office Note No. 1 (Version 2.3).

Luebke, A., Avallone, L. M., & Kraemer, M. (2012). On the relationship between vertical velocity and cirrus ice crystal number, size, and water content during MACPEX. In AGU Fall Meeting Abstracts (Vol. 1, p. 0280).

Mari, C., Jacob, D. J., & Bechtold, P. (2000). Transport and scavenging of soluble gases in a deep convective cloud. Journal of Geophysical Research, 105, 22.

Markowski, G. R. (1987). Improving Twomey's algorithm for inversion of aerosol measurement data. Aerosol science and technology, 7(2), 127-141.

McFarquhar, G. M., & Heymsfield, A. J. (1996). Microphysical characteristics of three anvils sampled during the Central Equatorial Pacific Experiment. Journal of the Atmospheric Sciences, 53(17), 2401-2423.

McMurry, P. H., & Friedlander, S. K. (1979). New particle formation in the presence of an aerosol. Atmospheric Environment (1967), 13(12), 1635-1651.

Merikanto, J., Napari, I., Vehkamäki, H., Anttila, T., & Kulmala, M. (2007). New parameterization of sulfuric acid-ammonia-water ternary nucleation rates at tropospheric conditions. Journal of Geophysical Research: Atmospheres, 112(D15).

Merikanto, J., Spracklen, D. V., Mann, G. W., Pickering, S. J., & Carslaw, K. S. (2009). Impact of nucleation on global CCN. Atmospheric Chemistry and Physics, 9(21), 8601-8616.

Minnis, P., Kratz, D. P., Coakley, J. A. J., King, M. D., Arduini, R., Garber, D. P., ... & Young, D. F. (1995). Clouds and the Earth's Radiant Energy System (CERES) algorithm theoretical basis document, volume III: Cloud analyses and radiance inversions (subsystem 4). NASA RP, 1376, 135-176.

Modgil, M. S., Kumar, S., Tripathi, S. N., & Lovejoy, E. R. (2005). A parameterization of ion-induced nucleation of sulphuric acid and water for atmospheric conditions. Journal of Geophysical Research: Atmospheres, 110(D19).

Murphy, D. M., Cziczo, D. J., Hudson, P. K., Thomson, D. S., Wilson, J. C., Kojima, T., & Buseck, P. R. (2004). Particle generation and resuspension in aircraft inlets when flying in clouds. Aerosol Science and Technology, 38(4), 401-409.

Nash, E. R., Newman, P. A., Rosenfield, J. E., & Schoeberl, M. R. (1996). An objective determination of the polar vortex using Ertel's potential vorticity. Journal of Geophysical Research: Atmospheres, 101(D5), 9471-9478.

Nilsson, E. D., & Kulmala, M. (1998). The potential for atmospheric mixing processes to enhance the binary nucleation rate. Journal of Geophysical Research: Atmospheres, 103(D1), 1381-1389.

O'Brien, K. (2005). The theory of cosmic-ray and high-energy solar- particle transport in the atmosphere, the natural radiation environment VII. In: McLaughlin Simopoulos, J.P., Simopoulos, E.S., Steinhäusler, F. (Eds.), Proceedings of the Seventh International Symposium on the Natural Radiation Environment, Rhodes, Greece, 20-24 May, 2002. Elsevier.

O'Dowd, C. D., Geever, M., Hill, M. K., Smith, M. H., & Jennings, S. G. (1998). New particle formation: Nucleation rates and spatial scales in the clean marine coastal environment. Geophysical Research Letters, 25(10), 1661-1664.

Pan, L. L., Bowman, K. P., Shapiro, M., Randel, W. J., Gao, R. S., Campos, T., ... & Barnet, C. (2007a). Chemical behavior of the tropopause observed during the Stratosphere-Troposphere Analyses of Regional Transport experiment. Journal of Geophysical Research: Atmospheres, 112(D18).

Pan, L. L., Randel, W. J., Gary, B. L., Mahoney, M. J., & Hintsa, E. J. (2004). Definitions and sharpness of the extratropical tropopause: A trace gas perspective. Journal of Geophysical Research: Atmospheres, 109(D23).

Pan, L. L., Wei, J. C., Kinnison, D. E., Garcia, R. R., Wuebbles, D. J., & Brasseur, G. P. (2007b). A set of diagnostics for evaluating chemistry-climate models in the extratropical tropopause region. Journal of Geophysical Research: Atmospheres, 112(D9).

Penner, J. E., Andreae, M. O., Annegarn, H., Barrie, L., Feichter, J., Hegg, D., ... & Pitari, G. (2001). Aerosols, their direct and indirect effects. In Climate Change 2001: The Scientific Basis. Contribution of Working Group I to the Third Assessment Report of the Intergovernmental Panel on Climate Change (pp. 289-348). Cambridge University Press.

Pierce, J. R., & Adams, P. J. (2009). Uncertainty in global CCN concentrations from uncertain aerosol nucleation and primary emission rates. Atmospheric Chemistry and Physics, 9(4), 1339-1356.

Ploeger, F., Gottschling, C., Griessbach, S., Grooß, J. U., Guenther, G., Konopka, P., ... & Ungermann, J. (2015). A potential vorticity-based determination of the transport barrier in the Asian summer monsoon anticyclone. Atmospheric Chemistry and Physics, 15(22), 13145-13159.

Plumb, R. A. (1996). A "tropical pipe" model of stratospheric transport. Journal of Geophysical Research: Atmospheres, 101(D2), 3957-3972.

Prather, M. J., & Jacob, D. J. (1997). A persistent imbalance in HOx and NOx photochemistry of the upper troposphere driven by deep tropical convection. Geophysical Research Letters, 24(24), 3189-3192.

Pringle, K. J., Tost, H., Pozzer, A., Pöschl, U., & Lelieveld, J. (2010). Global distribution of the effective aerosol hygroscopicity parameter for CCN activation. Atmospheric Chemistry and Physics, 10(12), 5241-5255.

Pruppacher, H. R., & Klett, J. D. (1997). Microphysics of Clouds and Precipitation: With an Introduction to Cloud Chemistry and Cloud Electricity, 954 pp.

Radke, L. F., & Hobbs, P. V. (1991). Humidity and particle fields around some small cumulus clouds. Journal of the Atmospheric Sciences, 48(9), 1190-1193.

Ramanathan, V. C. P. J., Crutzen, P. J., Kiehl, J. T., & Rosenfeld, D. (2001). Aerosols, climate, and the hydrological cycle. Science, 294(5549), 2119-2124.

Reeves, J. M., Wilson, J. C., Brock, C. A., & Bui, T. P. (2008). Comparison of aerosol extinction coefficients, surface area density, and volume density from SAGE II and in situ aircraft measurements. Journal of Geophysical Research: Atmospheres, 113(D10).

Reiter, R. (1992). Phenomena in atmospheric and environmental electricity (Vol. 541). Amsterdam: Elsevier.

Reus, M., Ström, J., Kulmala, M., Pirjola, L., Lelieveld, J., Schiller, C., & Zöger, M. (1998). Airborne aerosol measurements in the tropopause region and the dependence of new particle formation on preexisting particle number concentration. Journal of Geophysical Research: Atmospheres, 103(D23), 31255-31263.

Rienecker, M. M., Suarez, M. J., Gelaro, R., Todling, R., Bacmeister, J., Liu, E., ... & Bloom, S. (2011). MERRA: NASA's modern-era retrospective analysis for research and applications. Journal of Climate, 24(14), 3624-3648.

Riley, D. and Spolton, L. (1981). World weather and climate (2nd ed.). Cambridge: Cambridge University Press.

Rodhe, H. (1999). Human impact on the atmospheric sulfur balance. Tellus A: Dynamic Meteorology and Oceanography, 51(1), 110-122.

Rollins, A. W., Thornberry, T. D., Gao, R. S., Smith, J. B., Sayres, D. S., Sargent, M. R., ... & Jordan, A. F. (2014). Evaluation of UT/LS hygrometer accuracy by intercomparison during the NASA MACPEX mission. Journal of Geophysical Research: Atmospheres, 119(4), 1915-1935.

Rosenfeld, D. (1999). TRMM observed first direct evidence of smoke from forest fires inhibiting rainfall. Geophysical Research Letters, 26(20), 3105-3108.

Rosenfeld, D., Andreae, M. O., Asmi, A., Chin, M., Leeuw, G., Donovan, D. P., ... & Lau, W. (2014). Global observations of aerosol-cloud-precipitation-climate interactions. Reviews of Geophysics, 52(4), 750-808.

Rosenfeld, D., Lohmann, U., Raga, G. B., O'Dowd, C. D., Kulmala, M., Fuzzi, S., ... & Andreae, M. O. (2008). Flood or Drought: How Do Aerosols Affect Precipitation? Science, 321, 1309.

Schmitt, C. G., Schnaiter, M., Heymsfield, A. J., Yang, P., Hirst, E., & Bansemer, A. (2016). The Microphysical Properties of Small Ice Particles Measured by the Small Ice Detector-3 Probe during the MACPEX Field Campaign. Journal of the Atmospheric Sciences, 73(12), 4775-4791.

Schröder, F., & Ström, J. (1997). Aircraft measurements of sub micrometer aerosol particles (> 7 nm) in the mid-latitude free troposphere and tropopause region. Atmospheric Research, 44(3-4), 333-356.

Scott, D. C., Herman, R. L., Webster, C. R., May, R. D., Flesch, G. J., & Moyer, E. J. (1999). Airborne Laser Infrared Absorption Spectrometer (ALIAS-II) for in situ atmospheric measurements of N2O, CH4, CO, HCl, and NO2 from balloon or remotely piloted aircraft platforms. Applied Optics, 38(21), 4609-4622.

Seinfeld, J. H., & Pandis, S. N. (1998). Atmospheric Chemistry and Physics: From Air Pollution to Climate Change, John Wiley & Sons, New York, 1326 pp.

Shapiro, M. A. (1980). Turbulent mixing within tropopause folds as a mechanism for the exchange of chemical constituents between the stratosphere and troposphere. Journal of the Atmospheric Sciences, 37(5), 994-1004.

Shapiro, M. A., Hampel, T., & Krueger, A. J. (1987). The Arctic tropopause fold. Monthly Weather Review, 115(2), 444-454.

Shaw, G. E. (1989). Production of condensation nuclei in clean air by nucleation of H2SO4. Atmospheric Environment (1967), 23(12), 2841-2846.

Solomon, S., Garcia, R. R., & Stordal, F. (1985). Transport processes and ozone perturbations. Journal of Geophysical Research: Atmospheres, 90(D7), 12981-12989.

Spivakovsky, C. M., Logan, J. A., Montzka, S. A., Balkanski, Y. J., Foreman-Fowler, M., Jones, D. B. A., ... & Wofsy, S. C. (2000). Three-dimensional climatological distribution of tropospheric OH: Update and evaluation. Journal of Geophysical Research: Atmospheres, 105(D7), 8931-8980.

Spracklen, D. V., Carslaw, K. S., Kulmala, M., Kerminen, V. M., Mann, G. W., & Sihto, S. L. (2006). The contribution of boundary layer nucleation events to total particle concentrations on regional and global scales. Atmospheric Chemistry and Physics, 6(12), 5631-5648.

Spracklen, D. V., Carslaw, K. S., Merikanto, J., Mann, G. W., Reddington, C. L., Pickering, S., ... & Boy, M. (2010). Explaining global surface aerosol number concentrations in terms of primary emissions and particle formation. Atmospheric Chemistry and Physics, 10(10), 4775-4793.

Spracklen, D. V., Pringle, K. J., Carslaw, K. S., Chipperfield, M. P., & Mann, G. W. (2005). A global off-line model of size-resolved aerosol microphysics: I. Model development and prediction of aerosol properties. Atmospheric Chemistry and Physics, 5(8), 2227-2252.

Stein, A. F., Draxler, R. R., Rolph, G. D., Stunder, B. J. B., Cohen, M. D., & Ngan, F. (2015). NOAA's HYSPLIT atmospheric transport and dispersion modeling system. Bulletin of the American Meteorological Society, 96(12), 2059-2077.

Stocker, T. F., Qin, D., Plattner, G. K., Tignor, M., Allen, S. K., Boschung, J., ... & Midgley, P. M. (2013). IPCC, 2013: Summary for policymakers in climate change 2013: the physical science basis, contribution of working group I to the fifth assessment report of the intergovernmental panel on climate change. New York: Intergovernmental Panel on Climate Change.

Ström, J., Fischer, H., Lelieveld, J., & Schröder, F. (1999). In situ measurements of microphysical properties and trace gases in two cumulonimbus anvils over western Europe. Journal of Geophysical Research: Atmospheres, 104(D10), 12221-12226.

Twohy, C. H., Clement, C. F., Gandrud, B. W., Weinheimer, A. J., Campos, T. L., Baumgardner, D., ... & Tan, D. (2002). Deep convection as a source of new particles in the mid-latitude upper troposphere. Journal of Geophysical Research: Atmospheres, 107(D21).

Twomey, S. (1977). The influence of pollution on the shortwave albedo of clouds. Journal of the Atmospheric Sciences, 34(7), 1149-1152.

Wang, C., & Prinn, R. G. (2000). On the roles of deep convective clouds in tropospheric chemistry. Journal of Geophysical Research: Atmospheres, 105(D17), 22269-22297.

Wang, Y., Liu, S. C., Anderson, B. E., Kondo, Y., Gregory, G. L., Sachse, G. W., ... & Thompson, A. M. (2000). Evidence of convection as a major source of condensation nuclei in the northern mid-latitude upper troposphere. Geophysical Research Letters, 27(3), 369-372.

Weber, R. J., Chen, G., Davis, D. D., Mauldin, R. L., Tanner, D. J., Eisele, F. L., ... & Bandy, A. R. (2001). Measurements of enhanced H_2SO_4 and 3–4 nm particles near a frontal cloud during the First Aerosol Characterization Experiment (ACE 1). Journal of Geophysical Research: Atmospheres, 106(D20), 24107-24117.

Weber, R. J., Clarke, A. D., Litchy, M., Li, J., Kok, G., Schillawski, R. D., & McMurry, P. H. (1998). Spurious aerosol measurements when sampling from aircraft in the vicinity of clouds. Journal of Geophysical Research-all Series-, 103, 28-337.

Weber, R. J., Marti, J. J., McMurry, P. H., Eisele, F. L., Tanner, D. J., & Jefferson, A. (1997). Measurements of new particle formation and ultrafine particle growth rates at a clean continental site. Journal of Geophysical Research-All Series-, 102, 4375-4385.

Weber, R. J., McMurry, P. H., Mauldin, R. L. I. I. I., Tanner, D. J., Eisele, F. L., Clarke, A. D., & Kapustin, V. N. (1999). New particle formation in the remote troposphere: A comparison of observations at various sites. Geophysical Research Letters, 26(3), 307-310.

Weigel, R., Borrmann, S., Kazil, J., Minikin, A., Stohl, A., Wilson, J. C., ... & Lovejoy, E. R. (2011). In situ observations of new particle formation in the tropical upper troposphere: the role of clouds and the nucleation mechanism. Atmospheric Chemistry and Physics, 11, 9983-10010.

Weigelt, A., Hermann, M., Van Velthoven, P. F. J., Brenninkmeijer, C. A. M., Schlaf, G., Zahn, A., & Wiedensohler, A. (2009). Influence of clouds on aerosol particle number concentrations in the upper troposphere. Journal of Geophysical Research: Atmospheres, 114(D1).

Weinstock, E. M., Smith, J. B., Sayres, D. S., Pittman, J. V., Spackman, J. R., Hintsa, E. J., ... & Anderson, J. G. (2009). Validation of the Harvard Lyman-α in situ water vapor instrument: Implications for the mechanisms that control stratospheric water vapor. Journal of Geophysical Research: Atmospheres, 114(D23).

Whitby, K. T. (1978). The physical characteristics of sulfur aerosols. Atmospheric Environment (1967), 12(1-3), 135-159.

Wiedensohler, A., Cheng, Y. F., Nowak, A., Wehner, B., Achtert, P., Berghof, M., ... & Takegawa, N. (2009). Rapid aerosol particle growth and increase of cloud condensation nucleus activity by secondary aerosol formation and condensation: A case study for regional air pollution in northeastern China. Journal of Geophysical Research: Atmospheres, 114(D2).

Wilson, J. C., Blackshear, E. D., & Hyun, J. H. (1983a). An improved continuous-flow condensation nucleus counter for use in the stratosphere. Journal of Aerosol Science, 14(3), 387-391.

Wilson, J. C., Hyun, J. H., & Blackshear, E. D. (1983b). The function and response of an improved stratospheric condensation nucleus counter. Journal of Geophysical Research: Oceans, 88(C11), 6781-6785.

Wilson, J. C., Jonsson, H. H., Brock, C. A., Toohey, D. W., Avallone, L. M., Baumgardner, D., ... & Osborn, M. (1993). In situ observations of aerosol and chlorine monoxide after the 1991 eruption of Mount Pinatubo: Effect of reactions on sulfate aerosol. Science, 261(5125), 1140-1143.

Wilson, J. C., Lee, S. H., Reeves, J. M., Brock, C. A., Jonsson, H. H., Lafleur, B. G., ... & Toon, G. (2008). Steady-state aerosol distributions in the extra-tropical, lower stratosphere and the processes that maintain them. Atmospheric Chemistry and Physics, 8(22), 6617-6626.

Wilson, J. C., Stolzenburg, M. R., Clark, W. E., Loewenstein, M., Ferry, G. V., Chan, K. R., & Kelly, K. K. (1992). Stratospheric sulfate aerosol in and near the Northern Hemisphere polar vortex: The morphology of the sulfate layer, multimodal size distributions, and the effect of denitrification. Journal of Geophysical Research: Atmospheres, 97(D8), 7997-8013.

World Meteorological Organization (1957). Meteorology—A three-dimensional science: Second session of the commission for aerology. WMO Bull., IV, 134–138.

Xu, Z., & Mace, G. G. (2017). Ice Particle Mass–Dimensional Relationship Retrieval and Uncertainty Evaluation Using the Optimal Estimation Methodology Applied to the MACPEX Data. Journal of Applied Meteorology and Climatology, 56(3), 767-788.

Young, L. H., Benson, D. R., Montanaro, W. M., Lee, S. H., Pan, L. L., Rogers, D. C., ... & Bowman, K. P. (2007). Enhanced new particle formation observed in the northern mid-latitude tropopause region. Journal of Geophysical Research: Atmospheres, 112(D10).

Yu, F., & Luo, G. (2009). Simulation of particle size distribution with a global aerosol model: contribution of nucleation to aerosol and CCN number concentrations. Atmospheric Chemistry and Physics, 9(20), 7691-7710.

Yu, F., & Turco, R. P. (2001). From molecular clusters to nanoparticles: Role of ambient ionization in tropospheric aerosol formation. Journal of Geophysical Research: Atmospheres, 106(D5), 4797-4814.

Yu, F., Luo, G., Bates, T. S., Anderson, B., Clarke, A., Kapustin, V., ... & Wu, S. (2010). Spatial distributions of particle number concentrations in the global troposphere: Simulations, observations, and implications for nucleation mechanisms. Journal of Geophysical Research: Atmospheres, 115(D17).

Zahn, A., Brenninkmeijer, C. A. M., & Van Velthoven, P. F. J. (2004). Passenger aircraft project CARIBIC 1997–2002, Part I: the extratropical chemical tropopause. Atmospheric Chemistry and Physics Discussions, 4(1), 1091-1117.

Zahn, A., Brenninkmeijer, C. A. M., Maiss, M., Scharffe, D. H., Crutzen, P. J., Hermann, M., ... & Van Velthoven.P.F.J. (2000). Identification of extratropical two-way troposphere-stratosphere mixing based on CARIBIC measurements of O_3, CO, and ultrafine particles. Journal of Geophysical Research, 105, 1527-1535.

Zhang, R. (2010). Getting to the critical nucleus of aerosol formation. Science, 328(5984), 1366-13.

Zhang, R., Khalizov, A., Wang, L., Hu, M., & Xu, W. (2011). Nucleation and growth of nanoparticles in the atmosphere. Chemical Reviews, 112(3), 1957-2011.

Zhang, R., Suh, I., Zhao, J., Zhang, D., Fortner, E. C., Tie, X., ... & Molina, M. J. (2004). Atmospheric new particle formation enhanced by organic acids. Science, 304(5676), 1487-1490.

Zöger, M., Afchine, A., Eicke, N., Gerhards, M. T., Klein, E., McKenna, D. S., ... & Woyke, T. (1999). Fast in situ stratospheric hygrometers: A new family of balloon-borne and airborne Lyman α photofragment fluorescence hygrometers. Journal of Geophysical Research: Atmospheres, 104(D1), 1807-1816.

Appendix A: MACPEX Campaign Upper Air Meteorological Analysis

During MACPEX most of the flight time was at high altitude in the region of the tropopause. An understanding of the upper air meteorology is needed to lay the foundation for the analysis done in this dissertation. In the mid-latitudes, the upper troposphere is often under the influence of an intense wind core called the jet stream. The jet stream is a semi-continuous ribbon of fast-moving air, connected with the zone of maximum slope, in a region where folding or fragmenting of the tropopause occurs (Barry and Chorley, 2009). The maximum wind in the jet stream is commonly referred to as a "jet streak". Figure A1 shows a north-south three-dimensional cross-section of the mid-latitude jet stream where winds can reach 150 kts (278 km/h) in the jet streak. Strong vertical and horizontal wind shear is found along the jet stream which produces areas of divergence and convergence. The synoptic pattern of the jet stream is associated with principal troughs of Rossby waves. The jet stream meanders along the troughs and ridges of low pressure and high pressure systems.

The tropopause is the transition layer in between the troposphere and the stratosphere. The height of the tropopause does not uniformly decrease from the equator poleward. The tropopause height decreases in "breaks" or "folds" that occur in the jet stream. These jets are not stationary but shift with the seasons, moving closer to the equator in winter and poleward in summer. The mid-latitudes are often impacted by the polar jet and the subtropical jet. Mid-latitude mesoscale convective systems and severe thunderstorms are caused by the polar jet stream trough "digging" into the warm and humid sub-tropical airmass. At the surface this movement is referred to as a front.

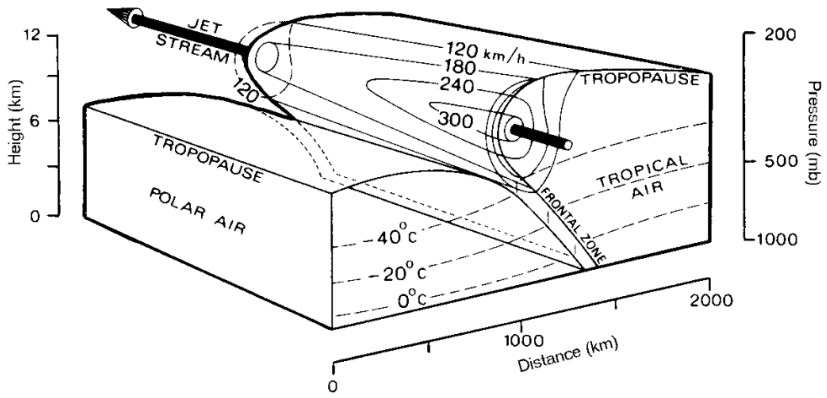

Figure A1. Structure of the mid-latitude jet stream showing the distribution of temperature, pressure and wind velocity with distance. The flow rotates counter-clockwise around the jet along the direction of flow.

Source: Riley, D. and Spolton, L. (1981). World weather and climate (2nd ed.). Cambridge: Cambridge University Press.

These fronts lead to instability and are often associated with cloud formation and precipitation. In the spring, cold fronts cause deep convection in the mid-latitudes especially when accompanied by cold air advection and divergence in the upper troposphere. This divergence is associated with the entrance region of the jet streak. Figure A2 shows a north-south cross-section with three westerly jet streams in the northern hemisphere. In this figure, the arctic front jet stream is at 70° N, the polar front at 45° N and the subtropical jet at 25° N. The position of these fronts varies with the movement of the Rossby waves and the seasonal amplification of the troughs and ridges.

The jet streams are important distributors of air as they create massive areas of mixing between the troposphere and the stratosphere. It is, therefore, important to analyze the MACPEX data with knowledge on the sampling conditions relative to the jet stream. Figures A3 – A8 show the 250 mb geopotential surface, which is the gravity-adjusted

height at which 250 mb occurs. The 250 mb geopotential surface occurs at an altitude that is very close to the tropopause in spring (~ 10 km), and most suitable for analysis of the jet stream. Isotachs are contours on the geopotential surface that connect points with equal wind speed. In Figures A3 – A8 the 00:00 GMT maps are produced using the available upper air data with a first guess from the 18:00 GMT North American Mesoscale Forecast System (NAM) 6-hour forecast. These analyses were used to compile the meteorological classification listed in Chapter 2 Table 2.1.

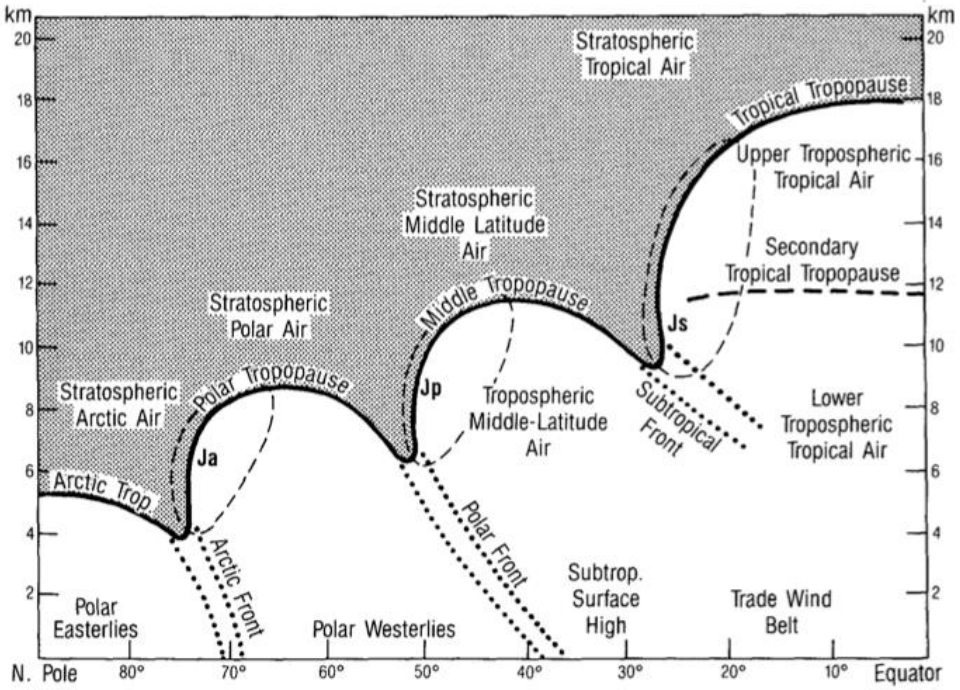

Figure A2. The "threefold" structure of the tropopause as described by Shapiro et al., (1987). The potential vorticity discontinuity tropopause is shown as the heavy solid line. The thin dashed line defines the three primary jet streams; the Arctic (Ja), the polar (Jp) and the subtropical (Js).

Source: Shapiro, M. A., Hampel, T., & Krueger, A. J. (1987). The Arctic tropopause fold. Monthly weather review, 115(2), 444-454.

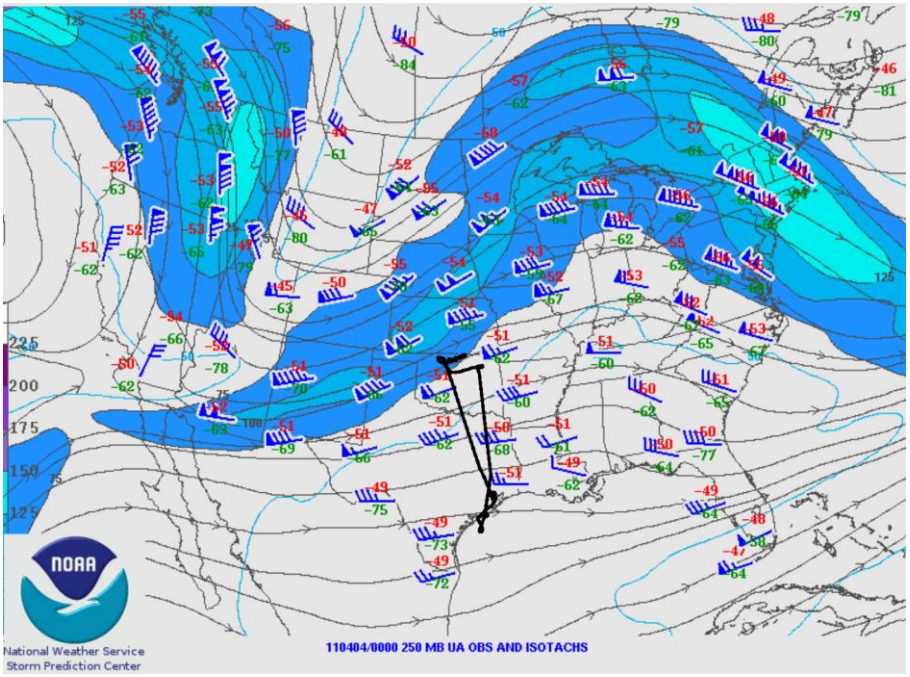

Figure A3. Streamlines and isotachs at the 250 mb geopotential height. The wind barbs show the wind speed and direction at each upper air station. The red value is the temperature, and the green is the dewpoint temperature (°C) at 250 mb. The WB-57F flight track is shown in black. Analysis is valid at 00:00 GMT on 20110404.

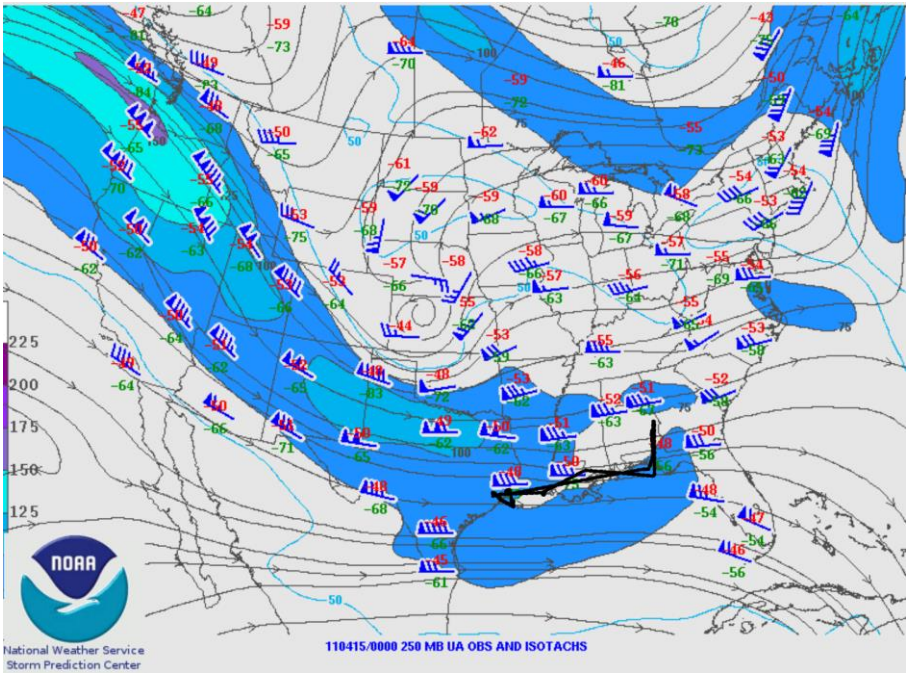

Figure A4. Same as Figure A3. Analysis is valid at 00:00 GMT on 20110415.

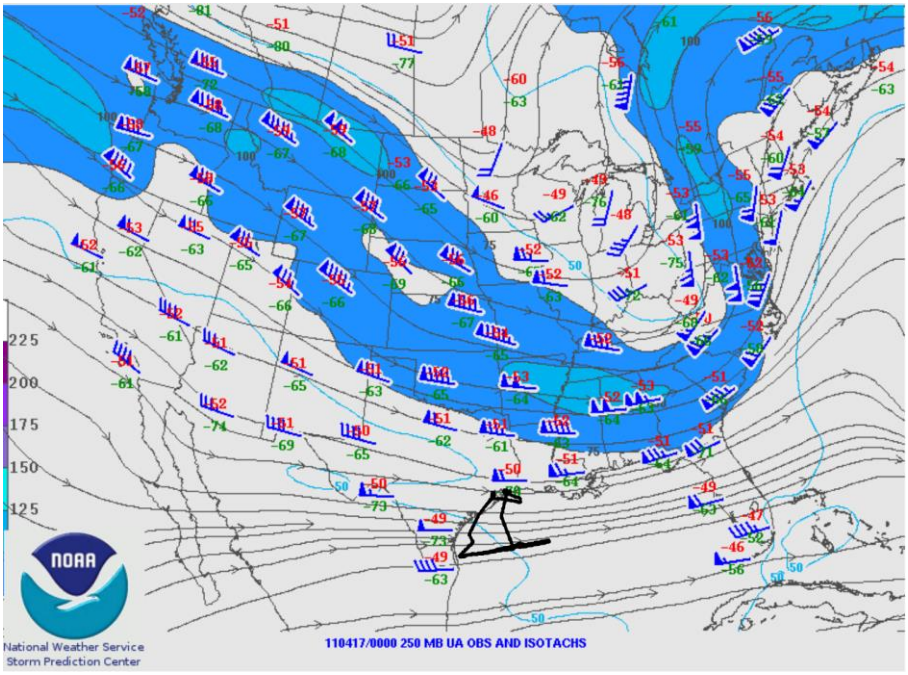

Figure A5. Same as Figure A3. Analysis is valid at 00:00 GMT on 20110417.

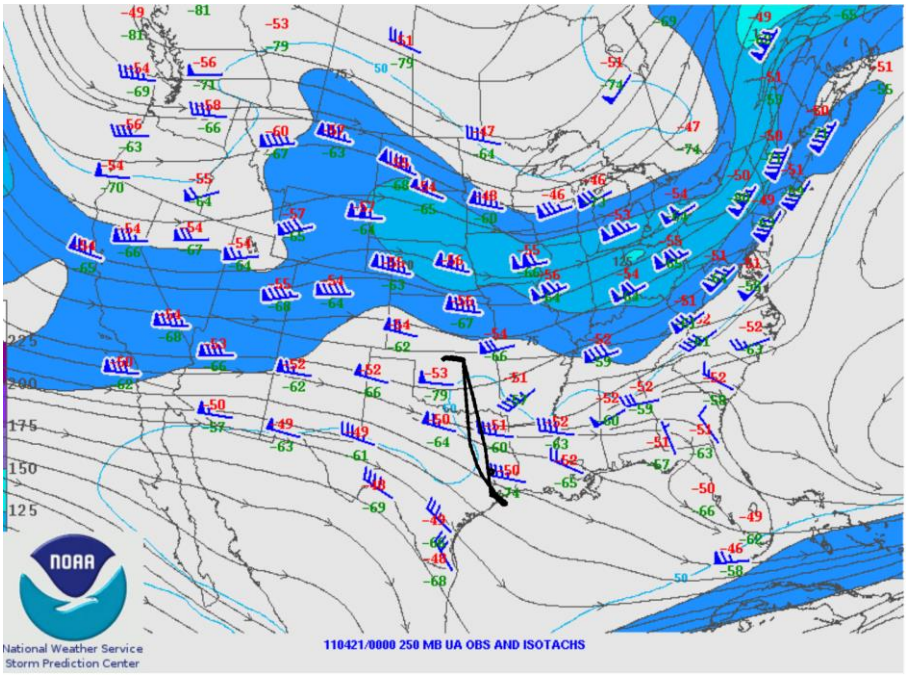

Figure A6. Same as Figure A3. Analysis is valid at 00:00 GMT on 20110421.

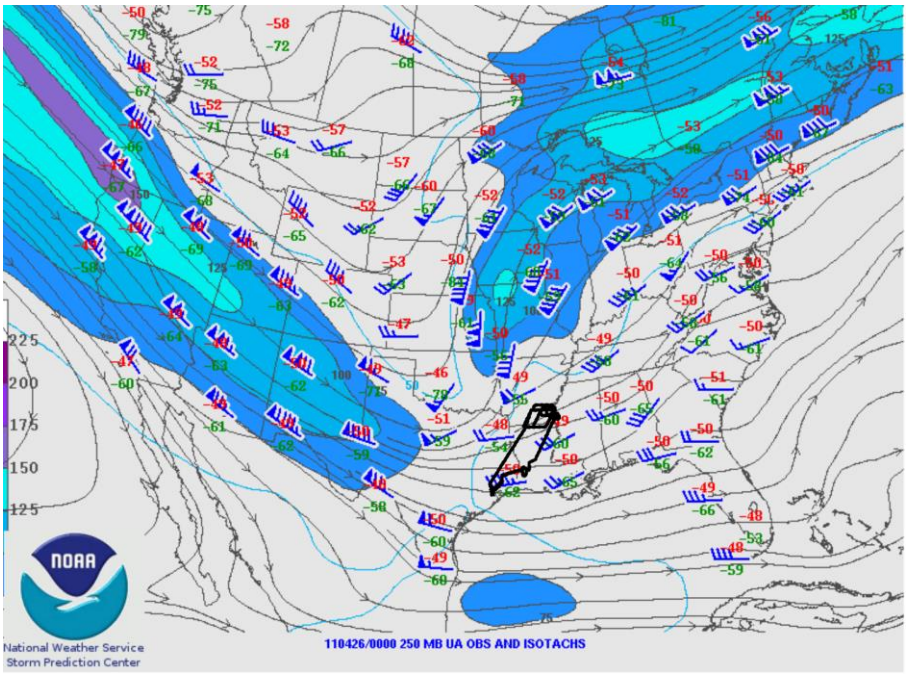

Figure A7. Same as Figure A3. Analysis is valid at 00:00 GMT on 20110426.

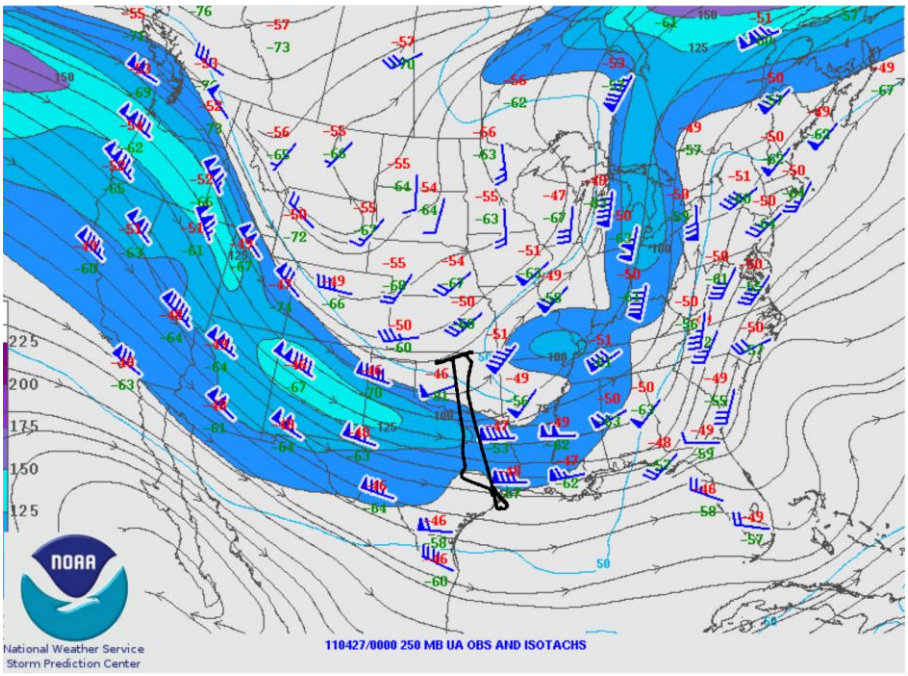

Figure A8. Same as Figure A3. Analysis is valid at 00:00 GMT on 20110427.

The images were obtained from the NOAA National Centers for Environmental Information, https://www.ncdc.noaa.gov

Appendix B: Species Vertical Structure and Time Series

The meteorological variability from flight to flight during the MACPEX mission was significant. On 3 April, 14 April and 16 April the aircraft sampled cirrus cloud associated with jet stream dynamics. On 20 April, 25 April and 26 April sampling of cirrus cloud was associated with convection. In most cases, the polar jet was sampled except on 14 April and 16 April when the subtropical jet was near the Gulf of Mexico and presented a sampling opportunity. In this Appendix, supplementary information is given to show the vertical structure and time series of the species sampled by the aircraft.

Figure B1 shows the vertical structure of temperature, PV, CO and O_3 for each flight. The diagnosis of the thermal tropopause and the dynamic tropopause is also shown. The magenta lines show instances when the change of the temperature lapse rate indicated the presence of a thermal tropopause and the green lines show the dynamic tropopause diagnosed by the 2.5 PVU surface. In most cases, the tropopause is above 11 km, except for 26 April when a tropopause as low as 9 km was observed. This was the case when the aircraft sampled the polar airmass behind the surface front (see Figure A8). Here a complex vertical structure is observed due to sampling of different tropopause heights at different points in time during the flight. Figures B2 – B7 show the time series for the measured species for each flight. This is most useful in understanding the instances when the aircraft penetrated the tropopause and in relating NPF events with other species. Some of the NPF events are numbered. The thermal tropopause and dynamic tropopause height can be compared to the aircraft altitude and the sequence of NPF events to relate the position of the aircraft with the conditions present during NPF.

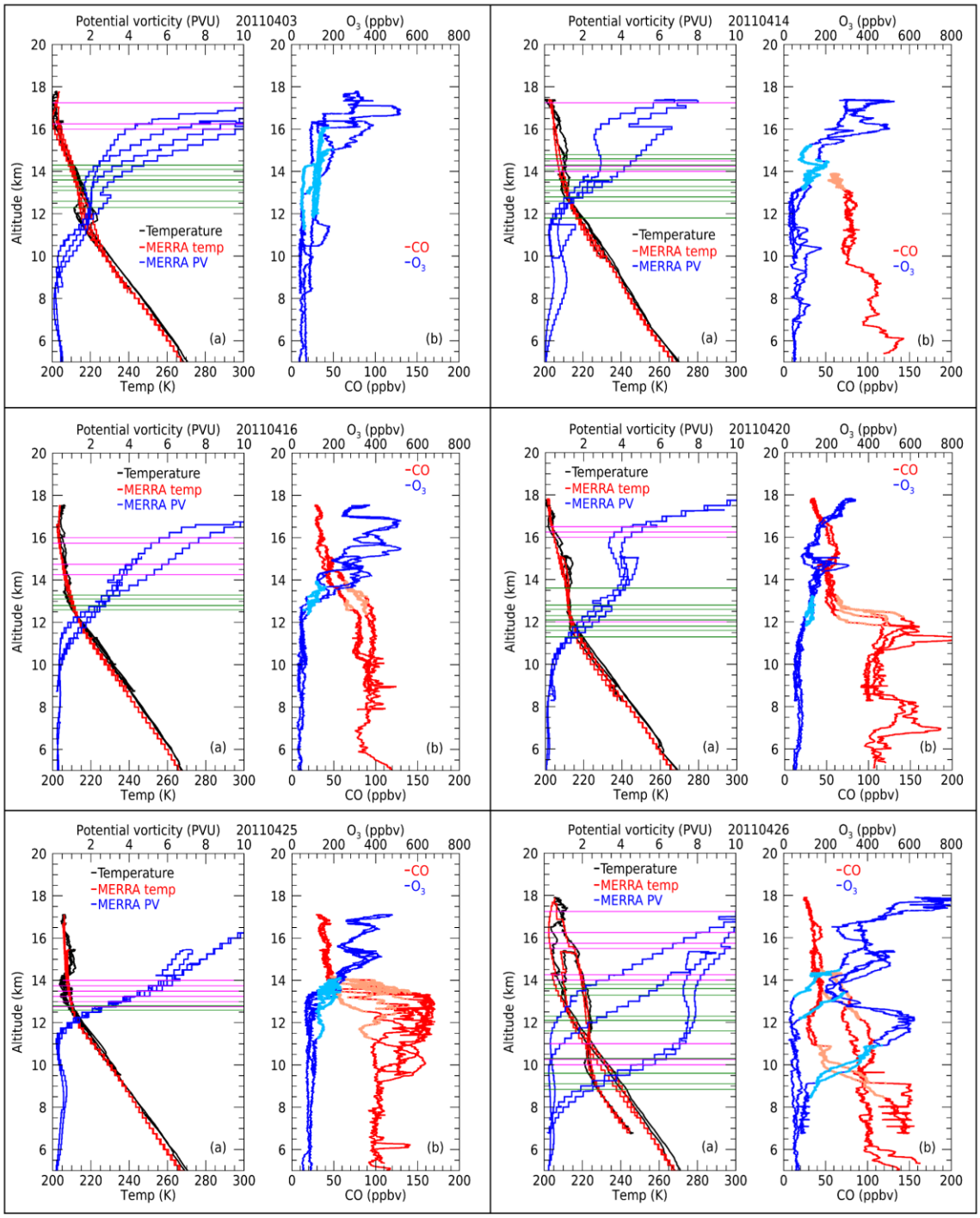

Figure B1. (a) Measured temperature (black), MERRA temperature (red); MERRA PV (blue). Thermal (magenta) and dynamic tropopause (green) are horizontal lines. (b) The CO trace in the mixing layer is colored light red and that of O_3 light blue. The thermal and dynamic tropopause are plotted every 1000 samples (~ 16 minutes).

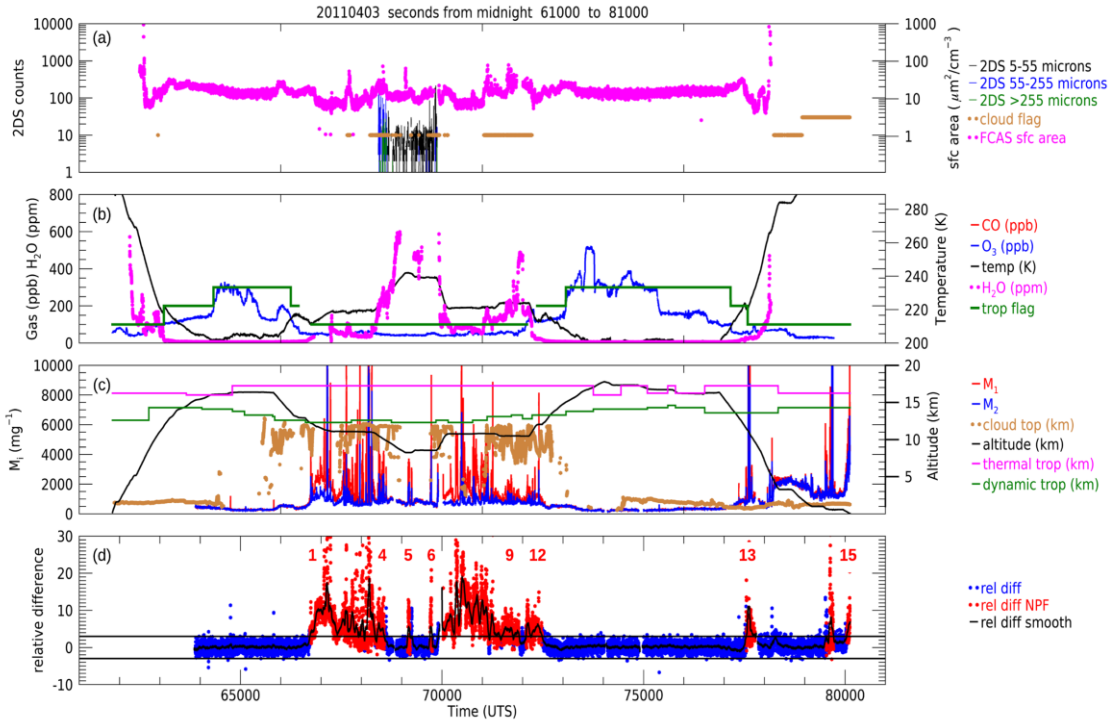

Figure B2. Time series for 20110403. (a) 2DS particle counts, cloud flag and FCAS surface area; (b) CO mixing ratio, O_3 mixing ratio, temperature, H_2O vapor mixing ratio, tropopause flag; (c) NMASS channel 1 mixing ratio (M_1), channel 2 mixing ratio (M_2), VISST cloud top, aircraft altitude, thermal tropopause, dynamic tropopause; (d) relative difference, NPF events.

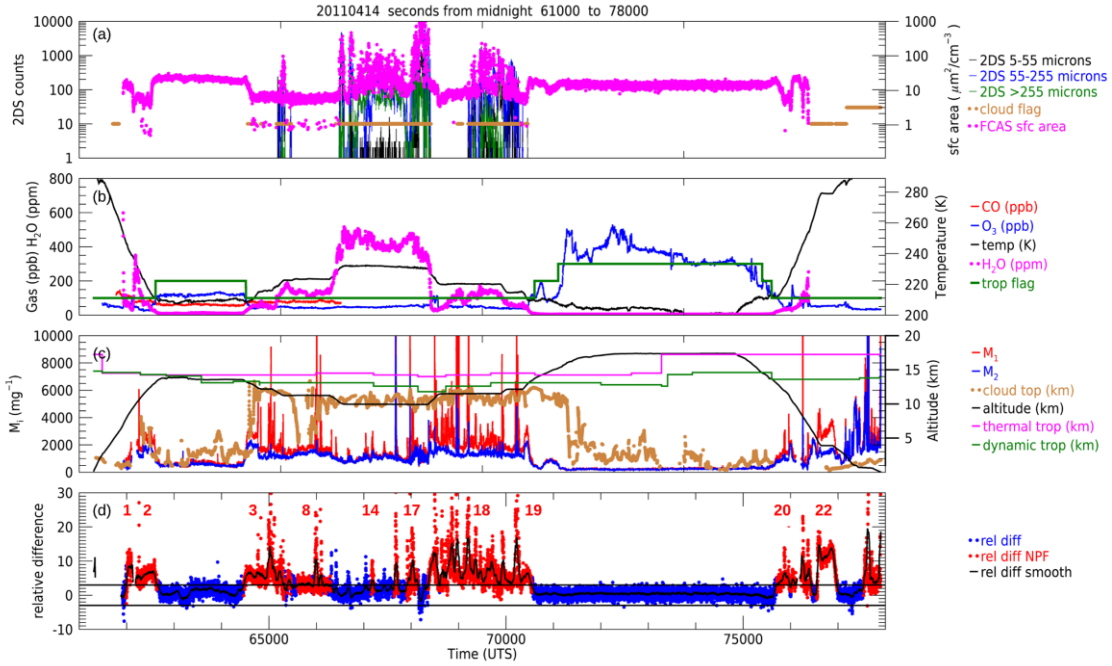

Figure B3. As in Figure B2 for 20110414.

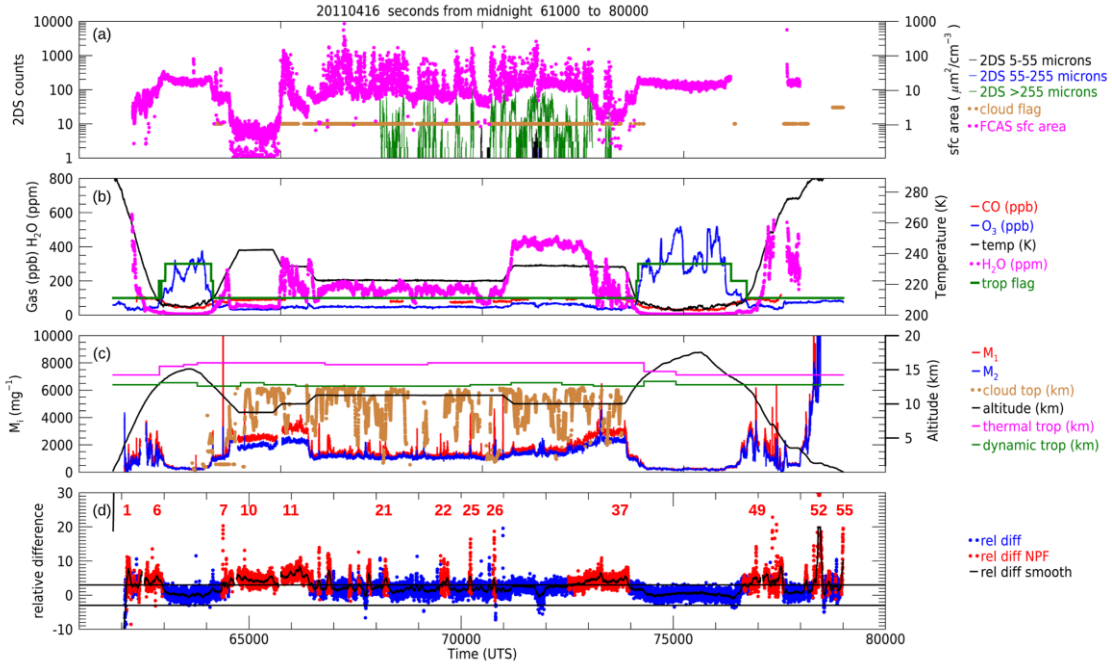

Figure B4. As in Figure B2 for 20110416.

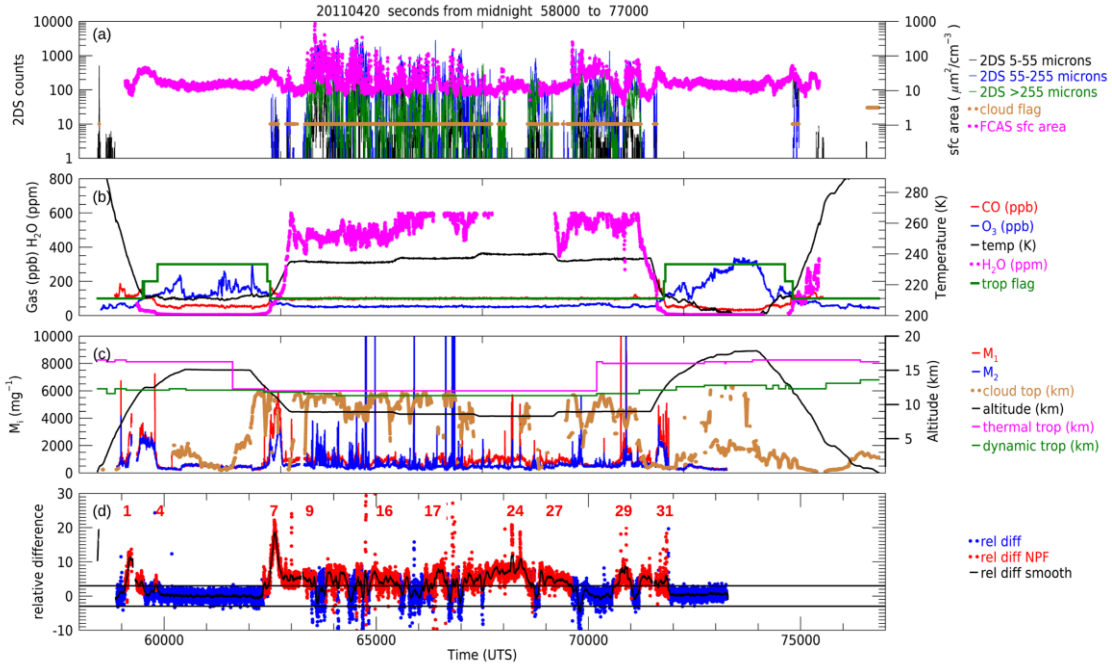

Figure B5. As in Figure B2 for 20110420.

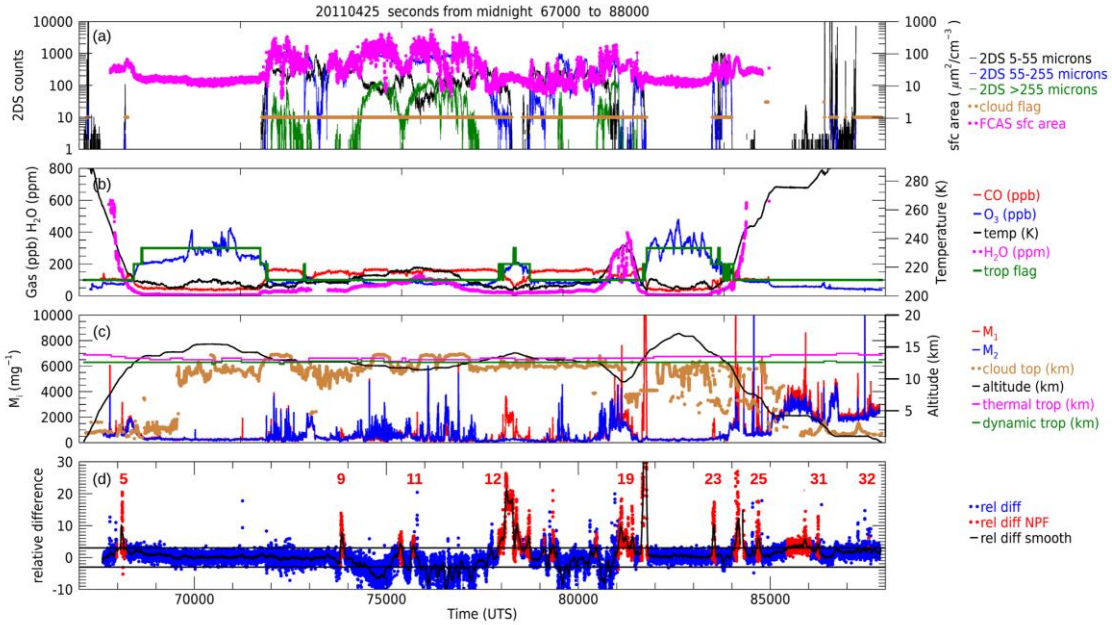

Figure B6. As in Figure B2 for 20110425.

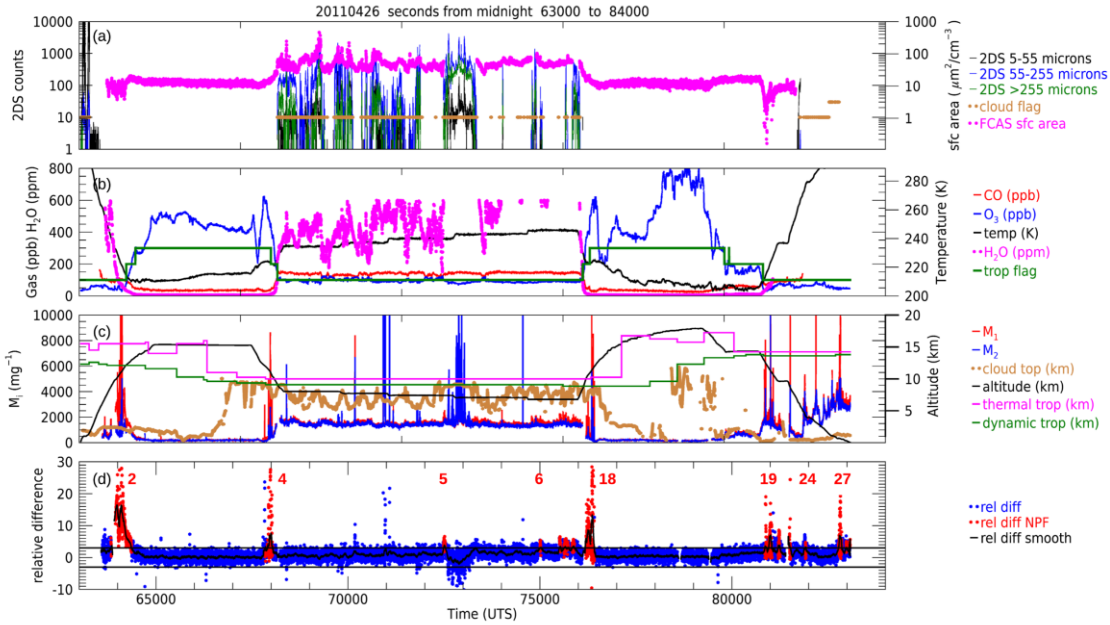

Figure B7. As in Figure B2 for 20110426.

Appendix C: MAIA Model Input and Output Data

The MAIA input consists of thermodynamic data from the research aircraft at the start of the trajectory, lognormal fits to the measured size distribution and HYSPLIT four-day forward trajectories. The HYSPLIT model was run by inputting position data from the aircraft at the start time of the trajectory. HYSPLIT runs the trajectory forward in time using the National Weather Service's National Centers for Environmental Protection (NCEP) Global Data Assimilation System (GDAS) reanalysis data that contain basic meteorological fields at 0.5 degree resolution. The HYSPLIT trajectory data was output every 1 hour for 96 hours (four days). The data contain pressure, temperature, relative humidity, water vapor mixing ratio and solar radiation flux. These data were used to calculate thermodynamic and meteorological input parameters for MAIA and a forward trajectory input file was generated for each layer. Figure C1, C2 and C3 show the forward trajectory used for the upper troposphere cases, the mixing layer cases and the stratosphere cases. These three trajectories use position data from NPF event locations at the corresponding layers on the 26 April 2011. The same trajectory was used for all simulations within the layer.

The MAIA model output is at 1 min intervals and consists of the ion production rate (IPR), water vapor mixing concentration, OH concentration, H_2SO_4 production rate, H_2SO_4 concentration, aerosol size distribution (from 0.6 nm to 860 nm), H_2SO_4 condensation sink, charged nucleation rate and neutral nucleation rate. Figures C4 to C39 show selected output for all 36 MAIA runs. In these figures panel (a) shows the number concentration of aerosol in the 3 to 4 nm diameter size range (black), the particle

formation rate of aerosol > 3 nm (red), H_2SO_4 condensation sink (blue) and H_2SO_4 concentration (green). Panel (b) shows the potential CCN at 50 nm and 100 nm activation diameter. Panel (c) shows the modeled aerosol size distribution with the horizontal lines indicating the 50 nm and 100 nm activation diameter for potential CCN.

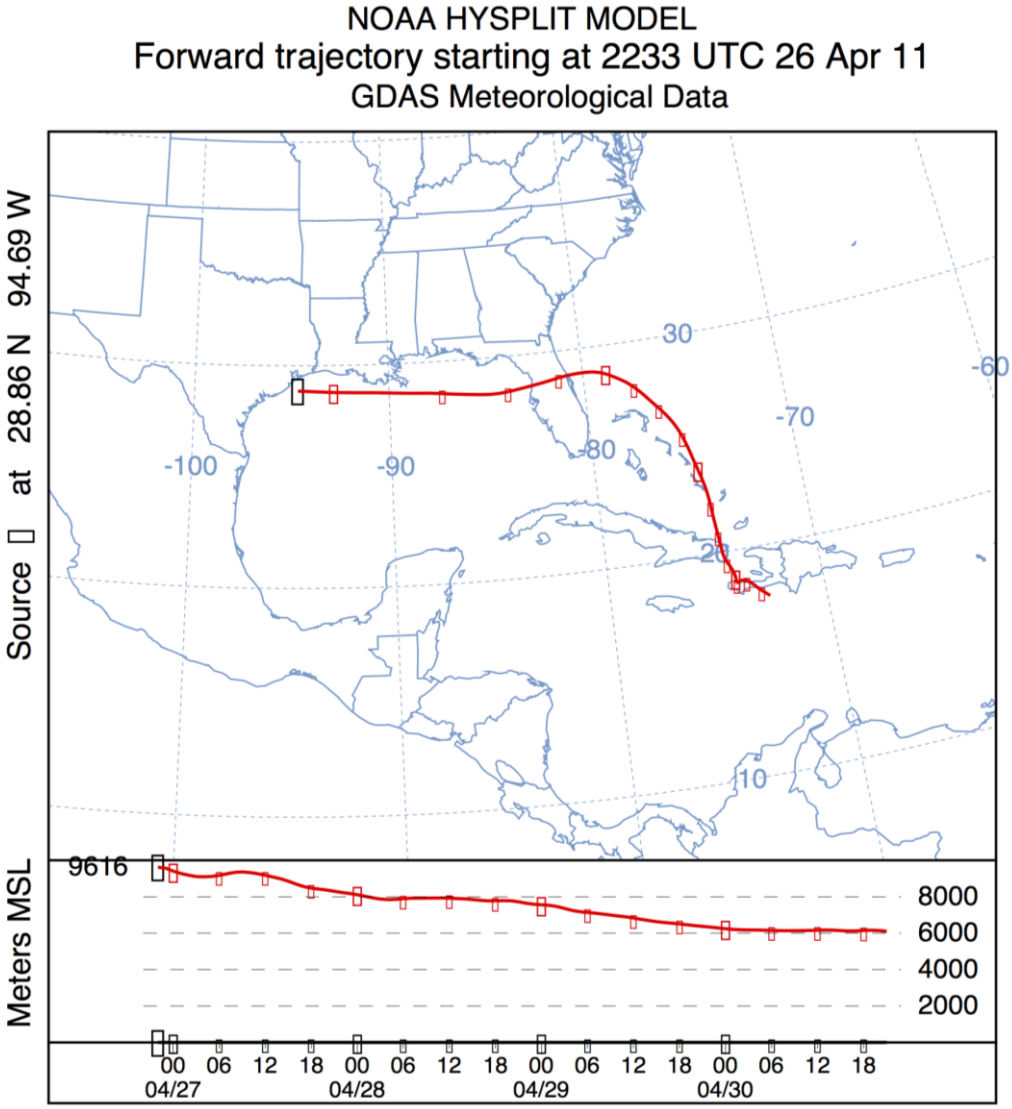

Figure C1. NOAA HYSPLIT forward-trajectory for an air parcel in the upper troposphere at 22:33 UTC on 4/26/2011 following an NPF event (event number 22). The lower part of the figure shows the vertical movement of the air mass trajectory. MAIA input variables are computed along this forward trajectory.

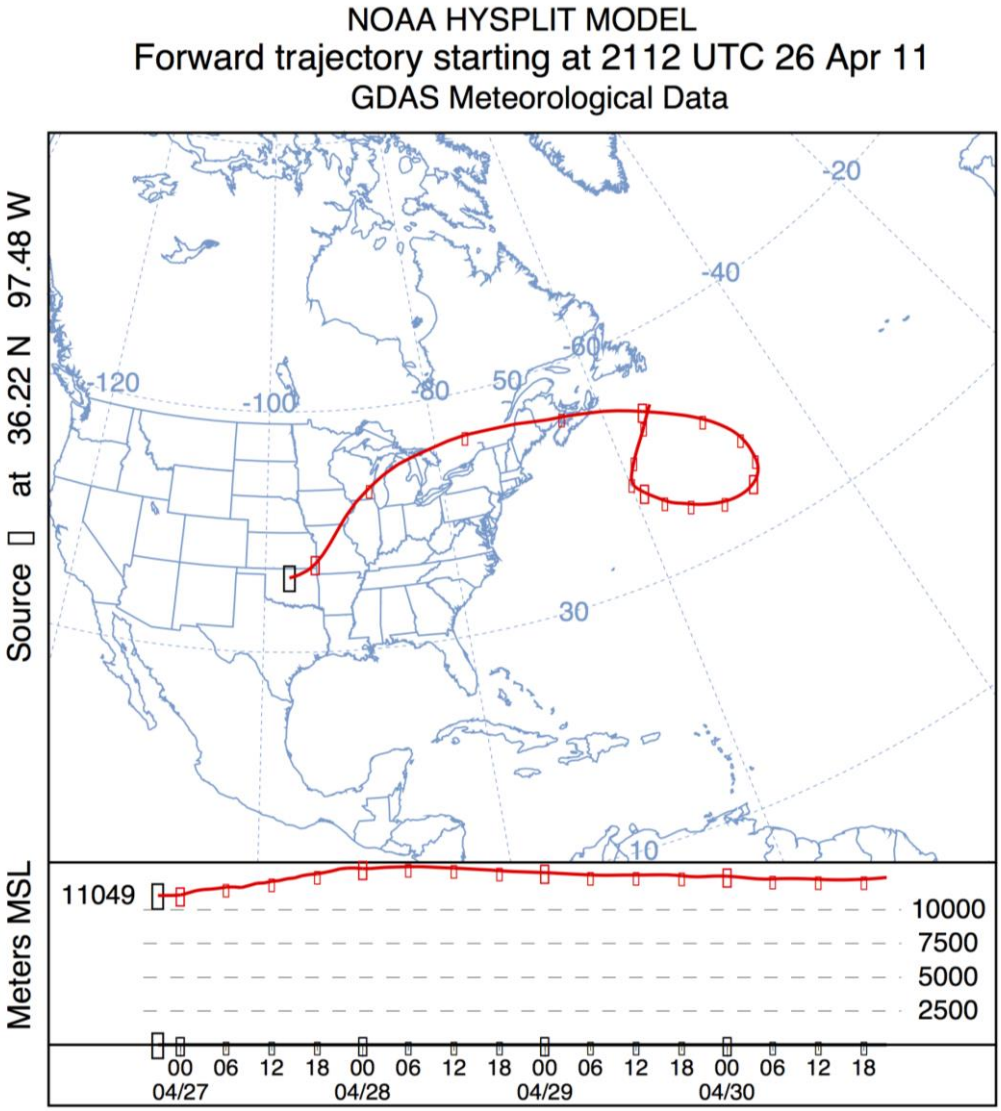

Figure C2. NOAA HYSPLIT forward-trajectory for an air parcel in the mixing layer at 21:12 UTC on 4/26/2011 following an NPF event (event number 18). The lower part of the figure shows the vertical movement of the air mass trajectory. MAIA input variables are computed along this forward trajectory.

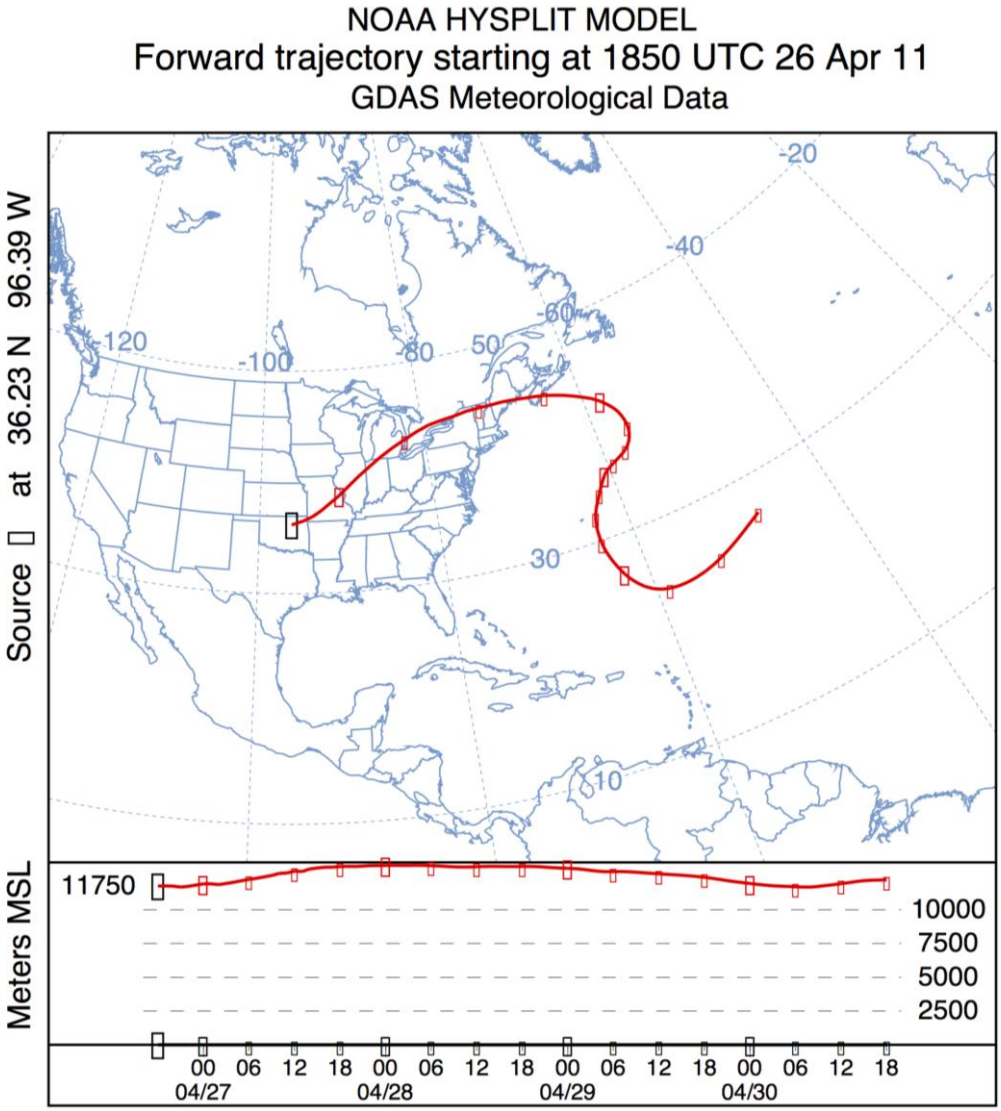

Figure C3. NOAA HYSPLIT forward-trajectory for an air parcel in the lower stratosphere at 18:50 UTC on 4/26/2011 following an NPF event (event number 3). The lower part of the figure shows the vertical movement of the air mass trajectory. MAIA input variables are computed along this forward trajectory.

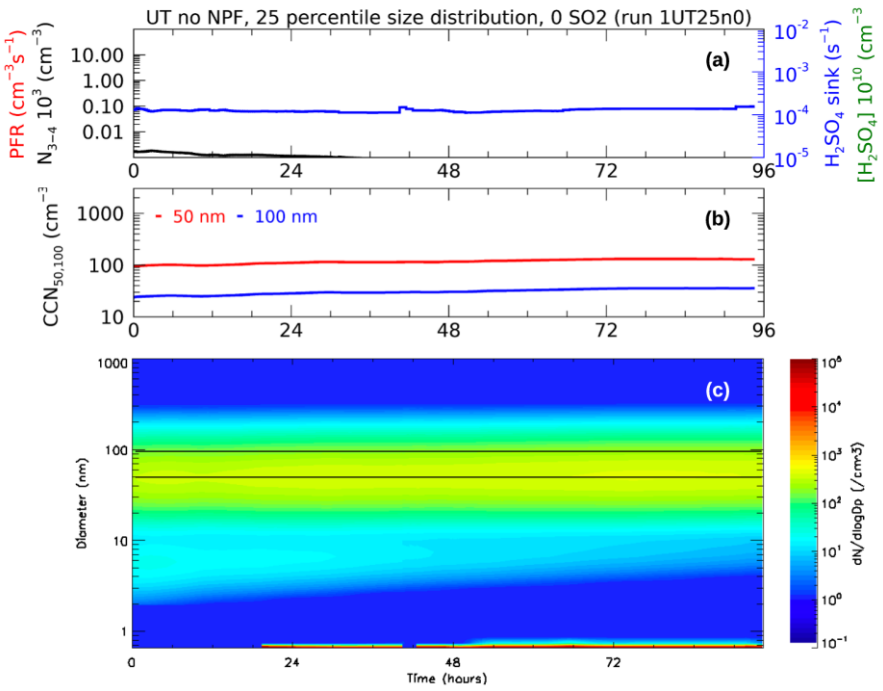

Figure C4. Run 1 – upper troposphere – no NPF – 25 percentile – 0 SO_2

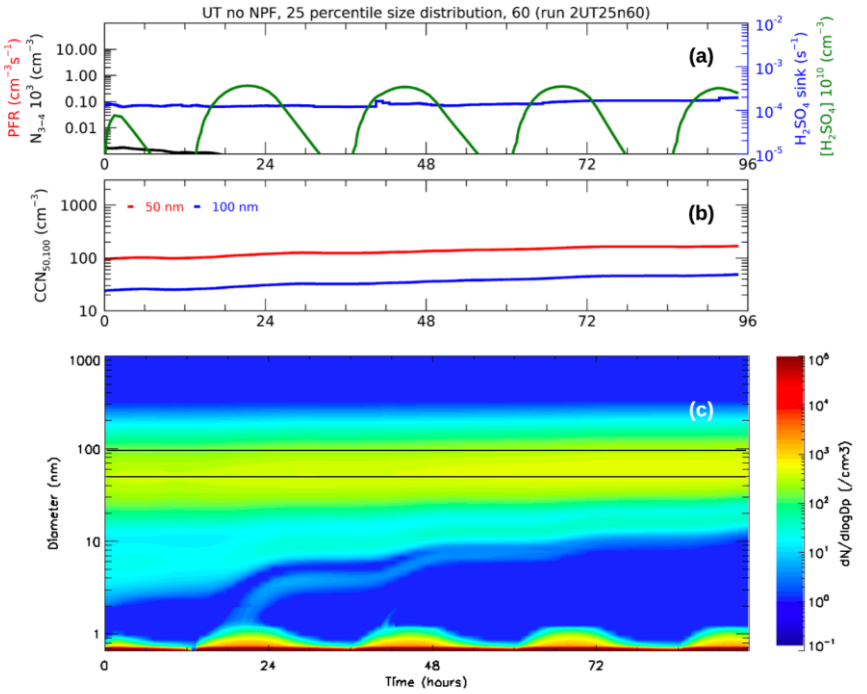

Figure C5. Run 2 – upper troposphere – no NPF – 25 percentile – 60 SO_2

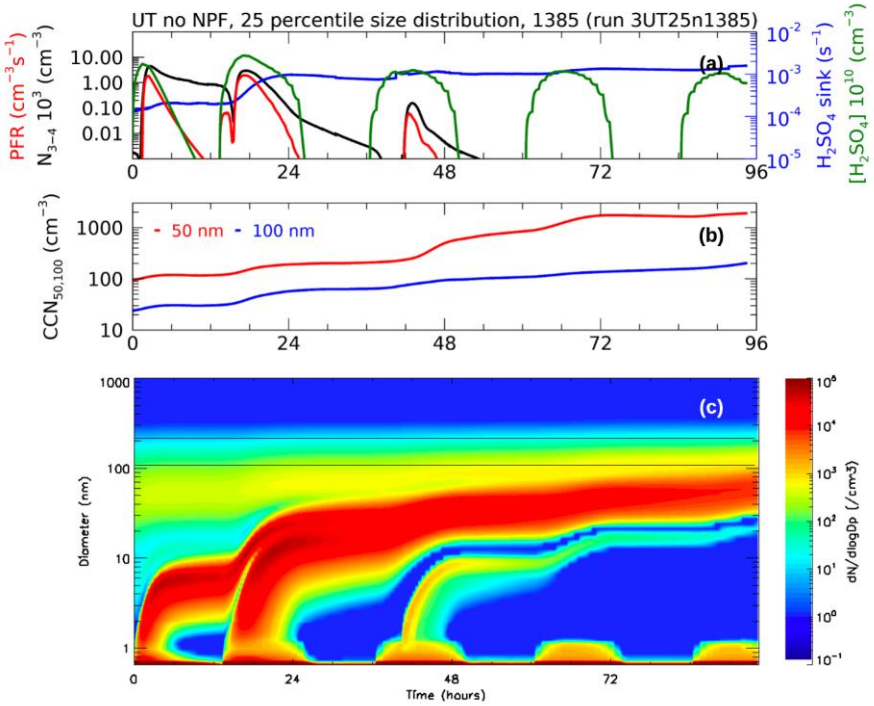

Figure C6. Run 3 – upper troposphere – no NPF – 25 percentile – 1385 SO2

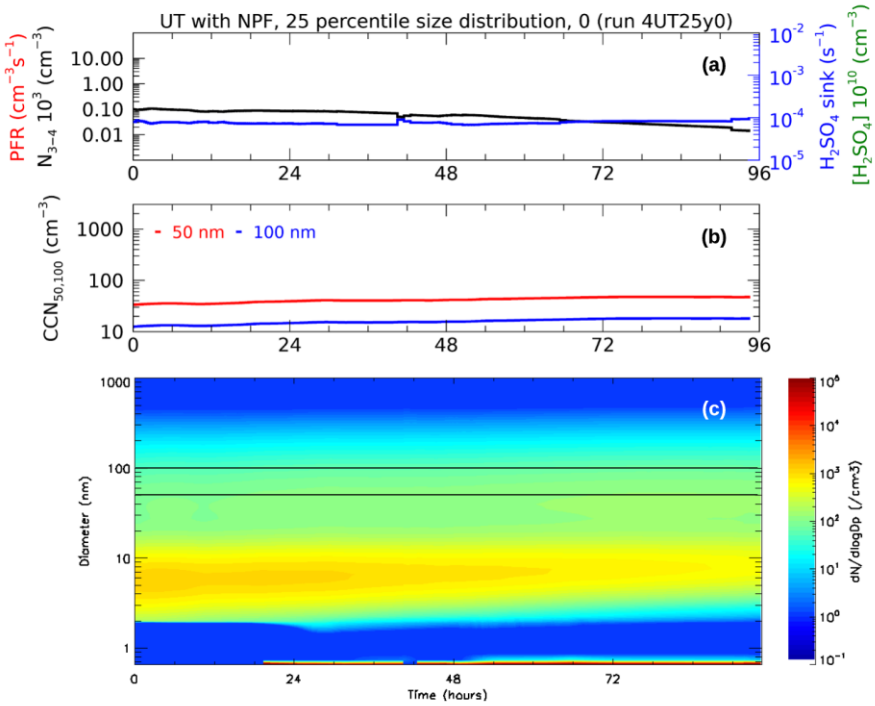

Figure C7. Run 4 – upper troposphere – with NPF – 25 percentile – 0 SO_2

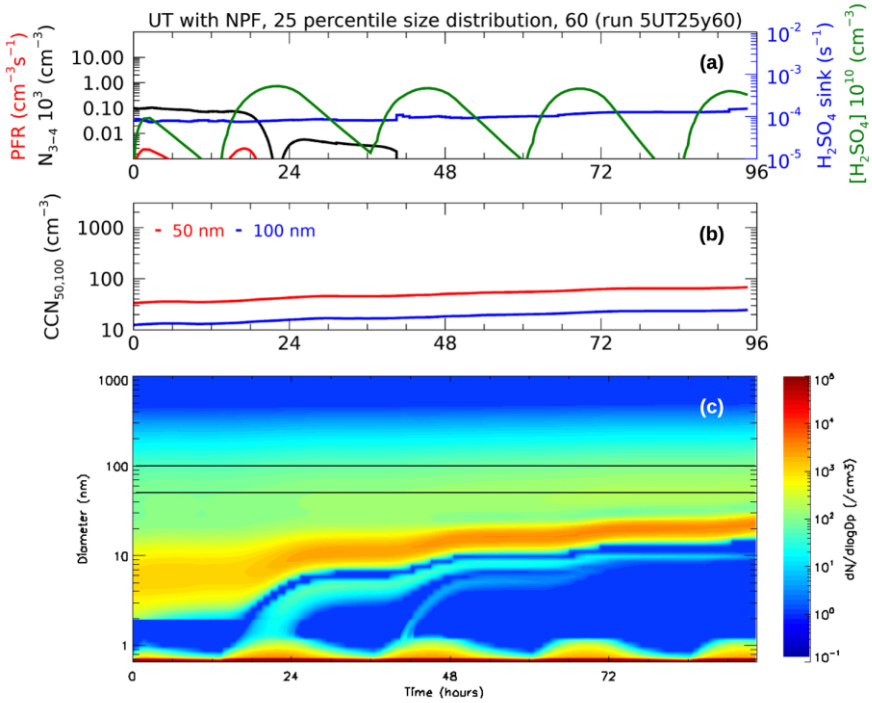

Figure C8. Run 5 – upper troposphere – with NPF – 25 percentile – 60 SO_2

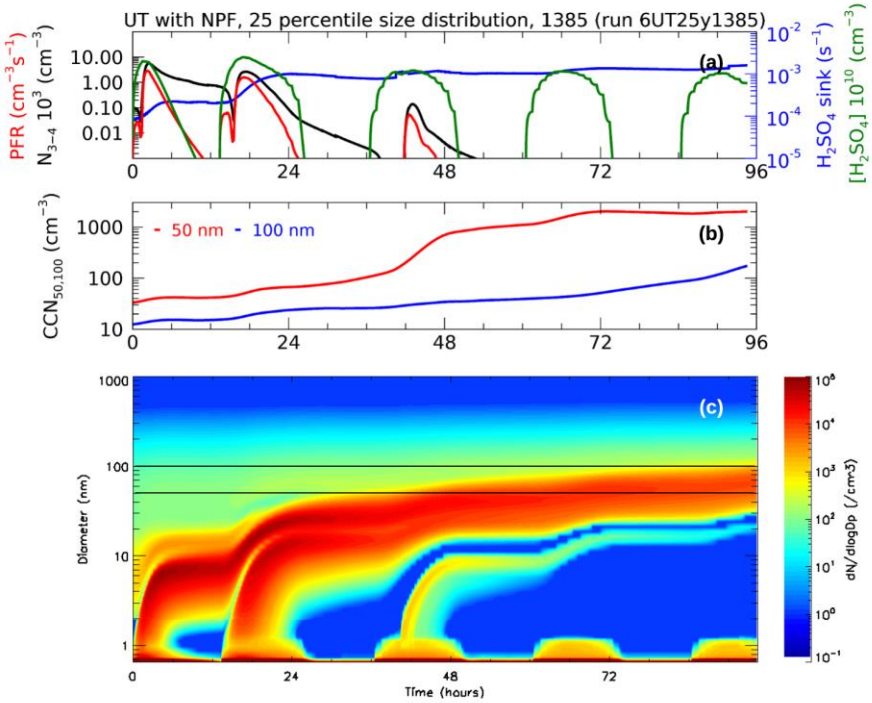

Figure C9. Run 6 – upper troposphere – with NPF – 25 percentile – 1385 SO_2

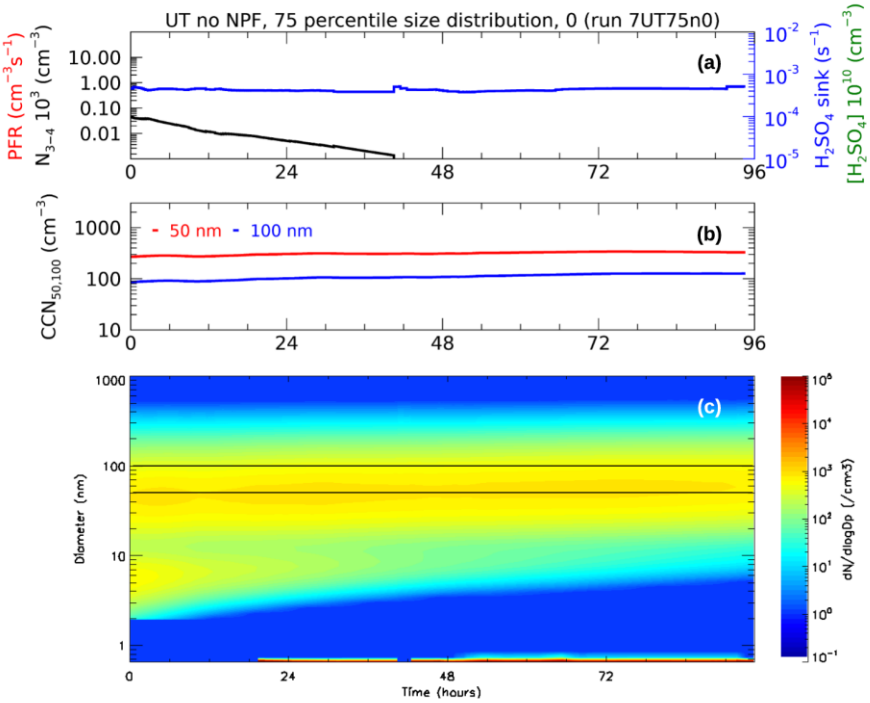

Figure C10. Run 7 – upper troposphere – no NPF – 75 percentile – 0 SO_2

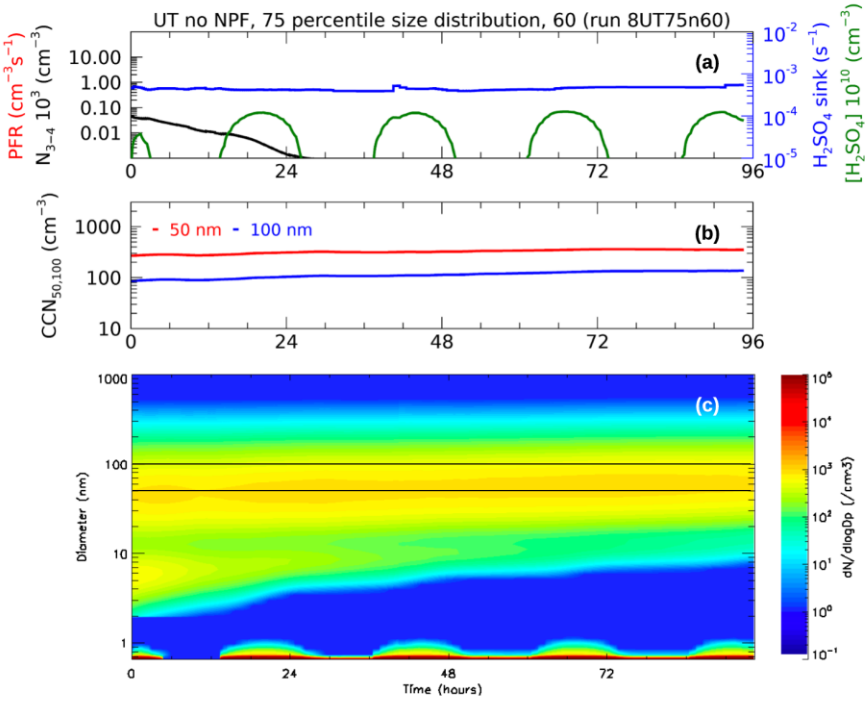

Figure C11. Run 8 – upper troposphere – no NPF – 75 percentile – 60 SO_2

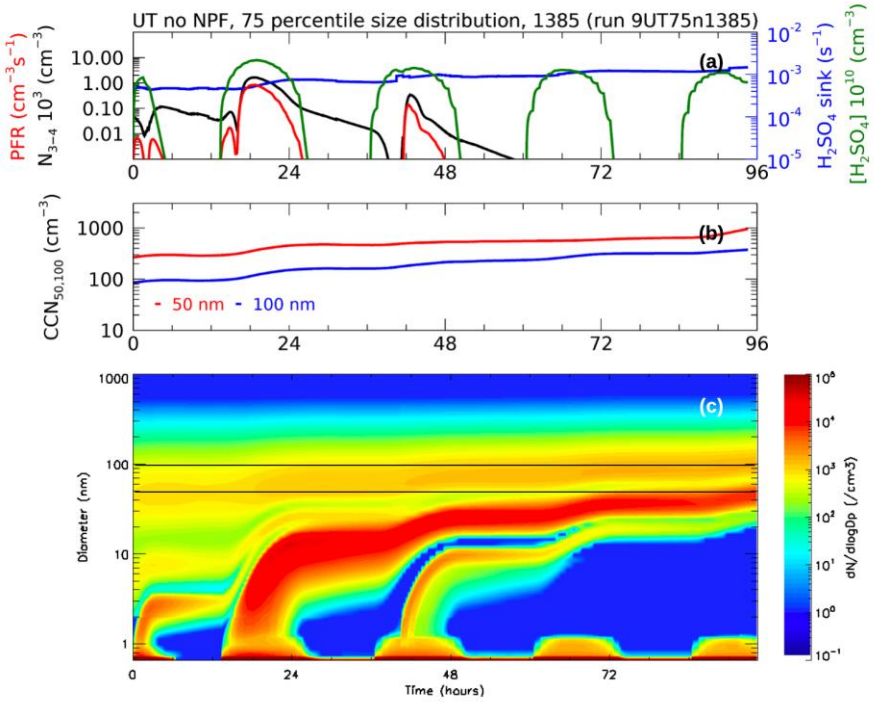

Figure C12. Run 9 – upper troposphere – no NPF – 75 percentile – 1385 SO_2

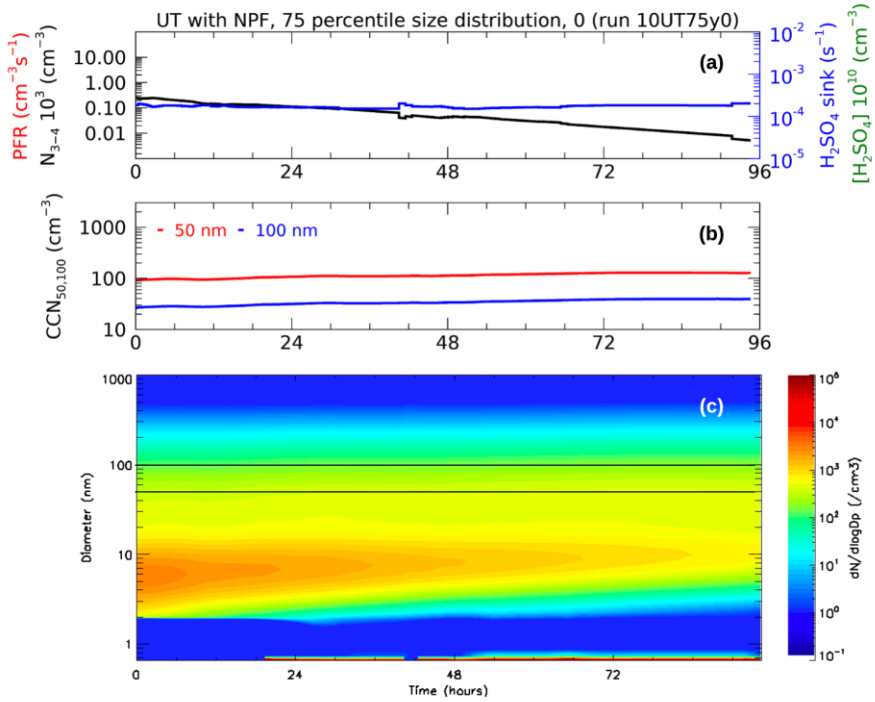

Figure C13. Run 10 – upper troposphere – with NPF – 75 percentile – 0 SO_2

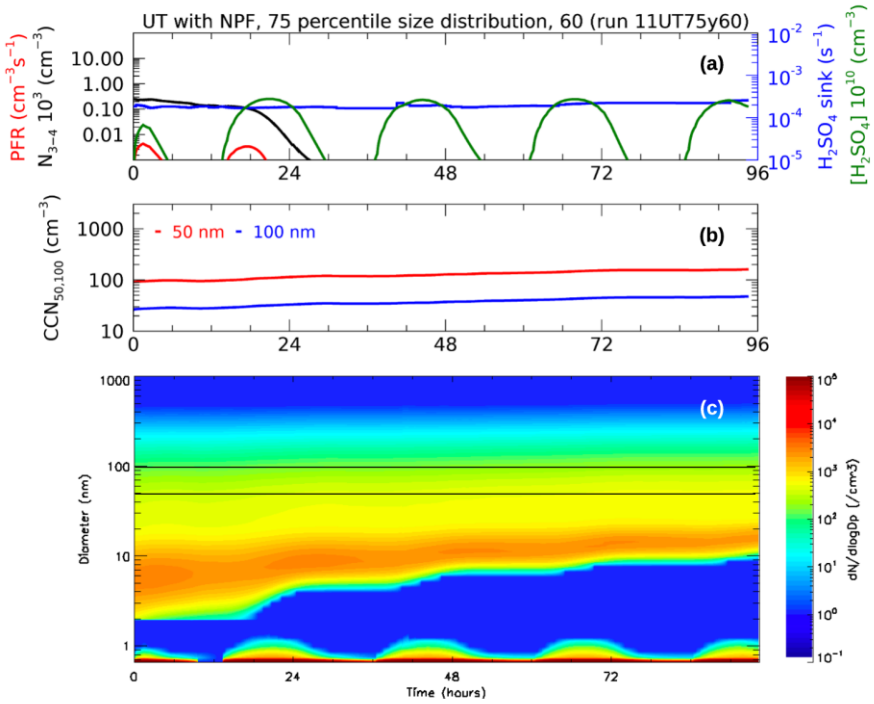

Figure C14. Run 11 – upper troposphere – with NPF – 75 percentile – 60 SO_2

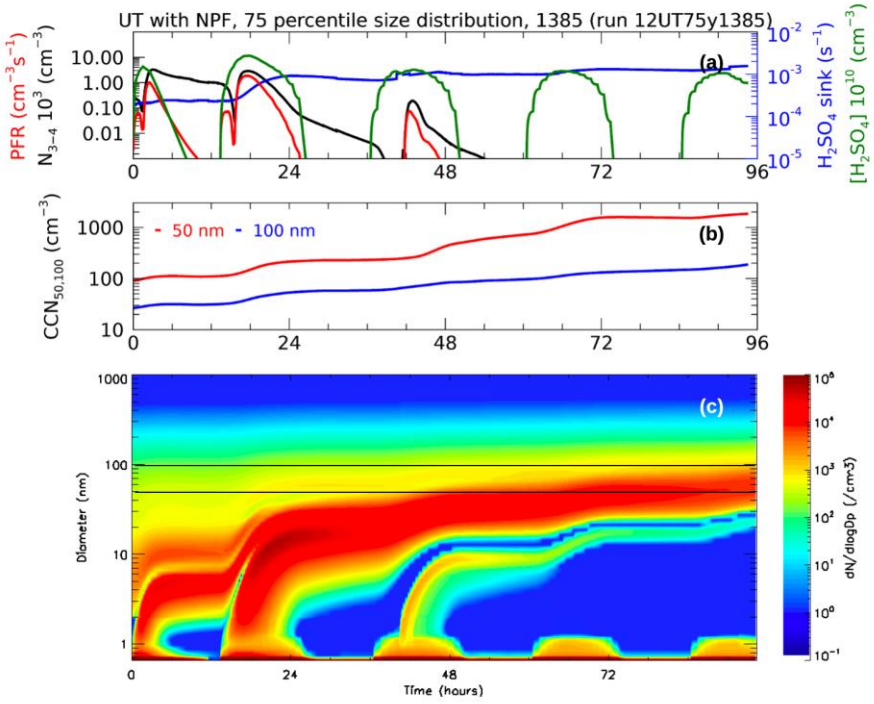

Figure C15. Run 12 – upper troposphere – with NPF – 75 percentile – 1385 SO_2

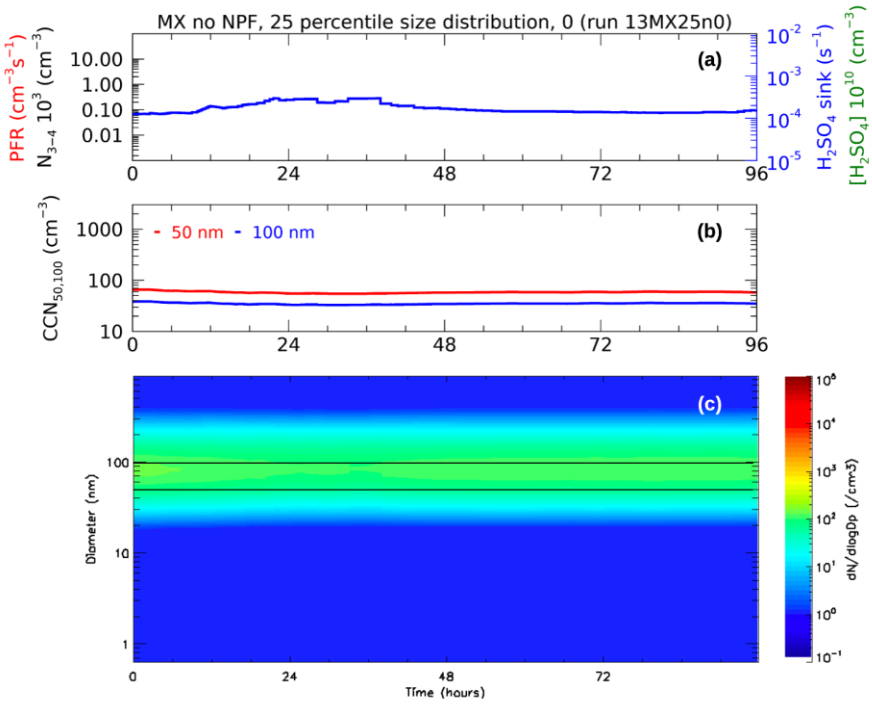

Figure C16. Run 13 – mixing layer – no NPF – 25 percentile – 0 SO_2

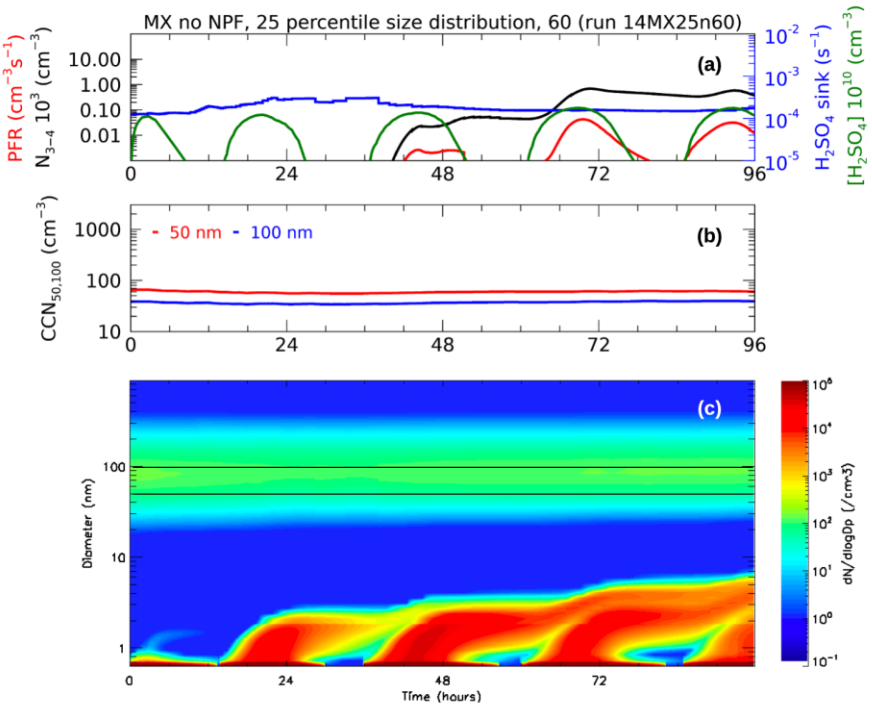

Figure C17. Run 14 – mixing layer – no NPF – 25 percentile – 60 SO_2

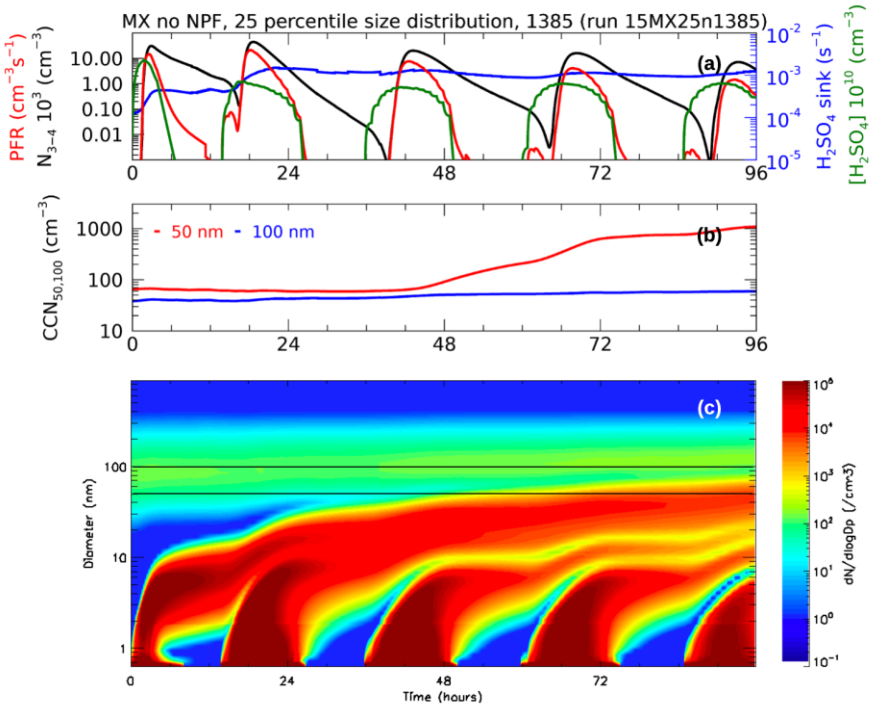

Figure C18. Run 15 – mixing layer – no NPF – 25 percentile – 1385 SO_2

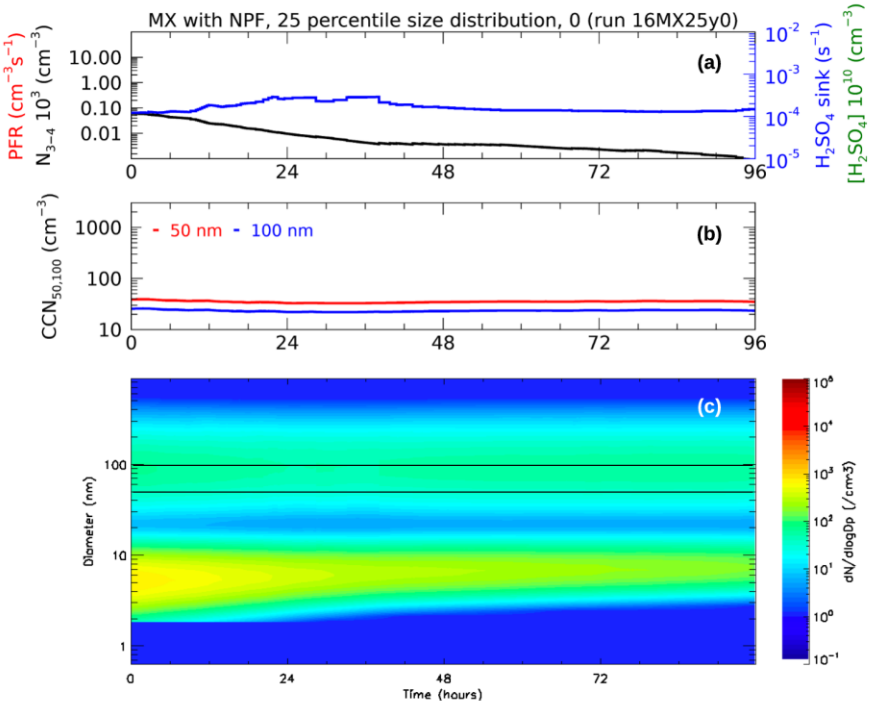

Figure C19. Run 16 – mixing layer – with NPF – 25 percentile – 0 SO_2

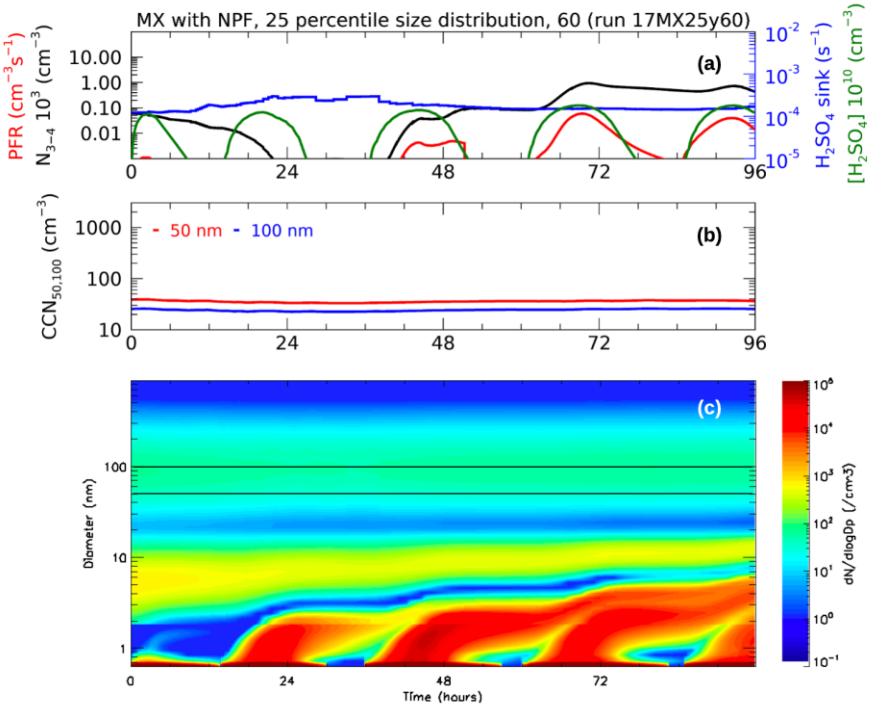

Figure C20. Run 17 –mixing layer – with NPF – 25 percentile – 60 SO_2

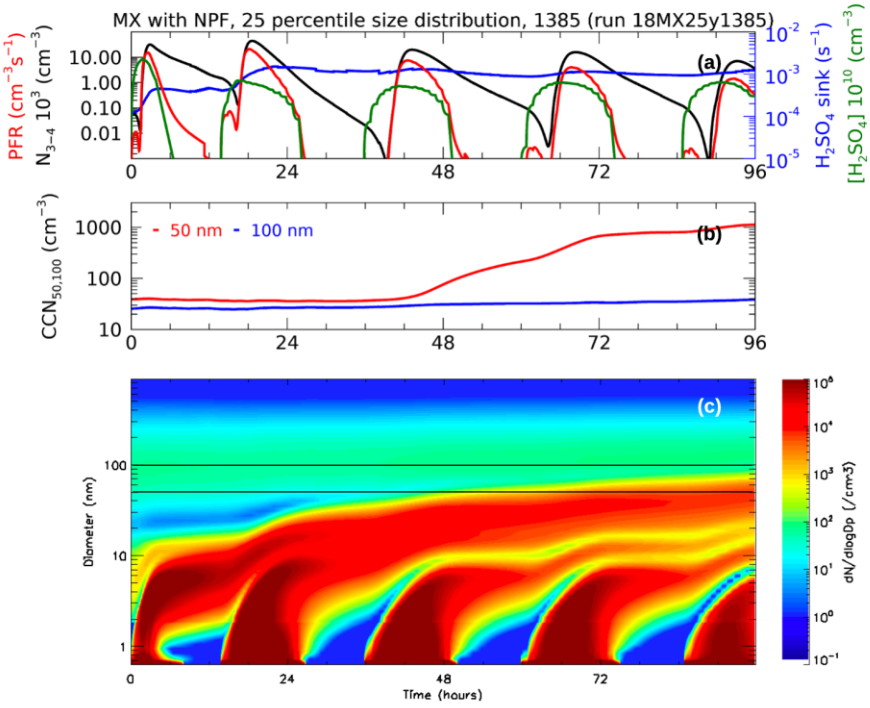

Figure C21. Run 18 –mixing layer – with NPF – 25 percentile – 1385 SO_2

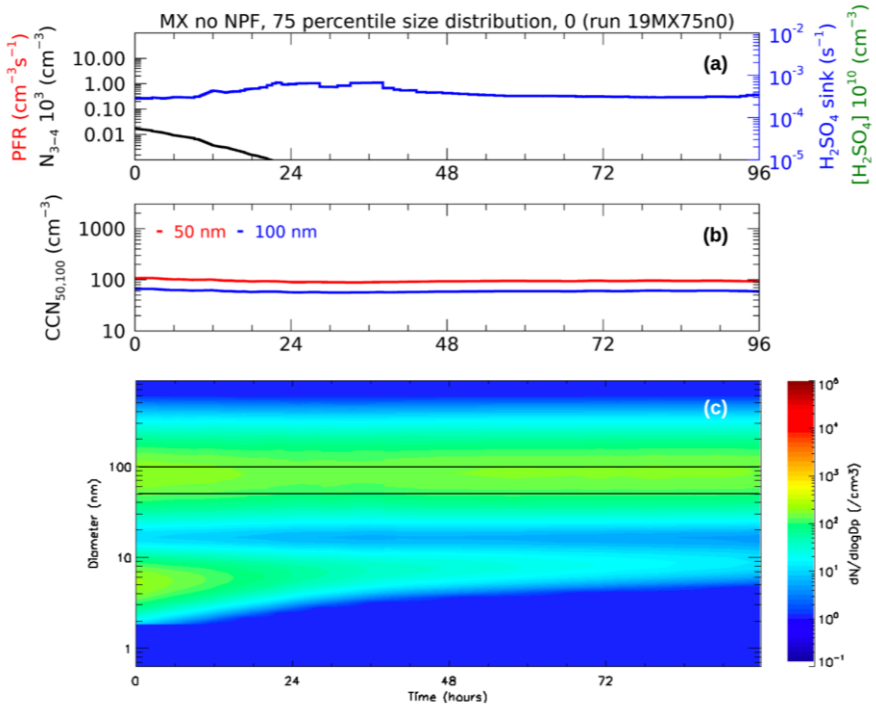

Figure C22. Run 19 – mixing layer – no NPF – 75 percentile – 0 SO_2

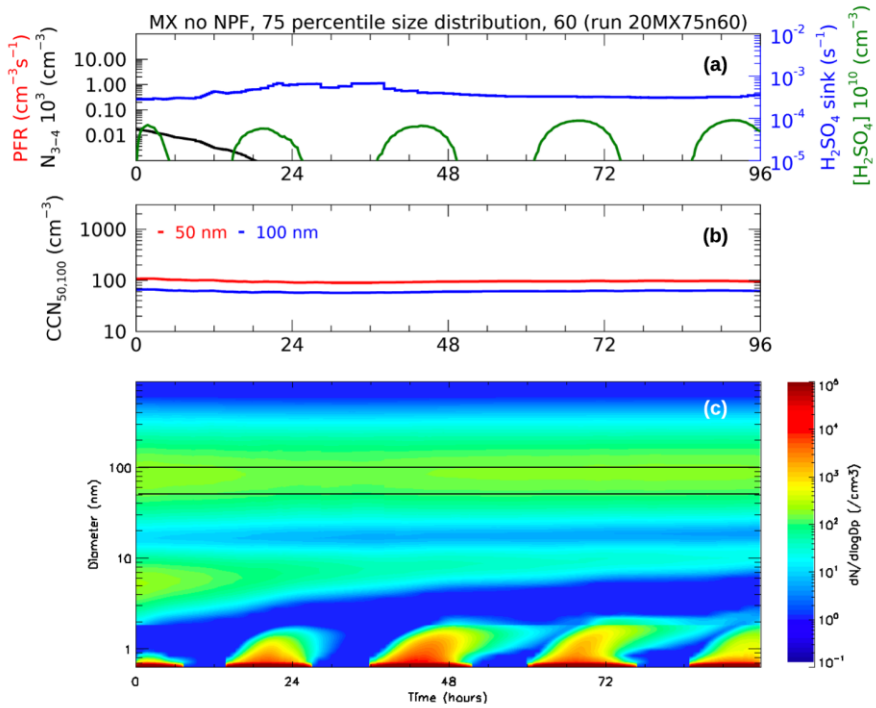

Figure C23. Run 20 – mixing layer – no NPF – 75 percentile – 60 SO_2

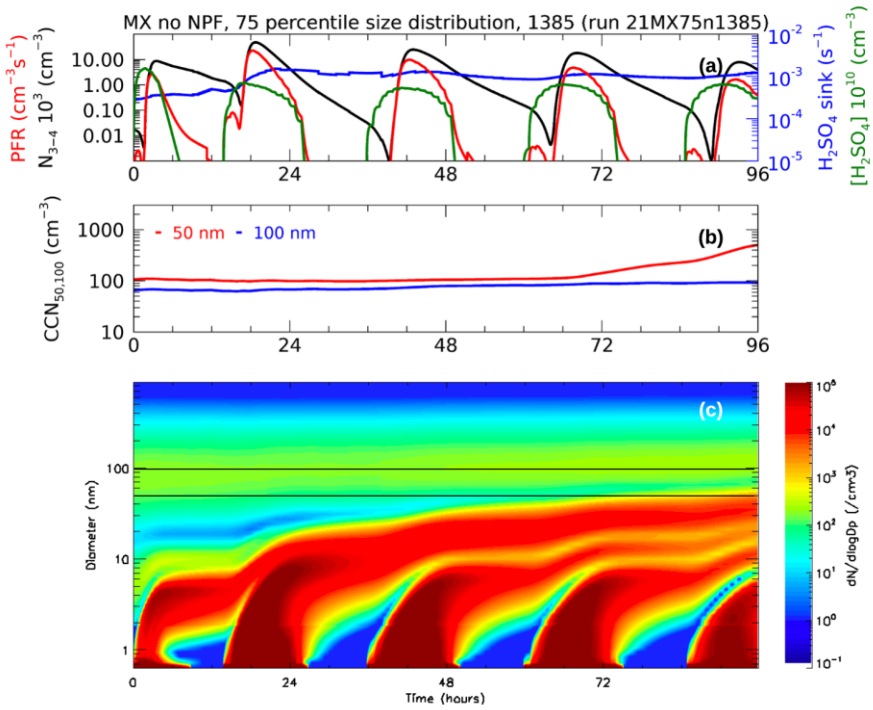

Figure C24. Run 21 – mixing layer – no NPF – 75 percentile – 1385 SO_2

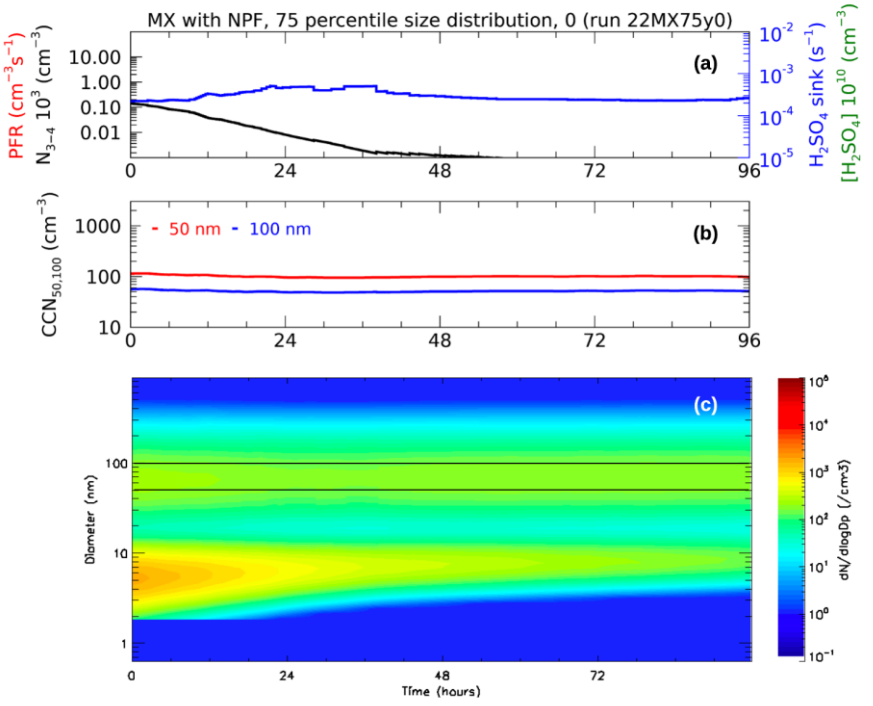

Figure C25. Run 22 – mixing layer – with NPF – 75 percentile – 0 SO_2

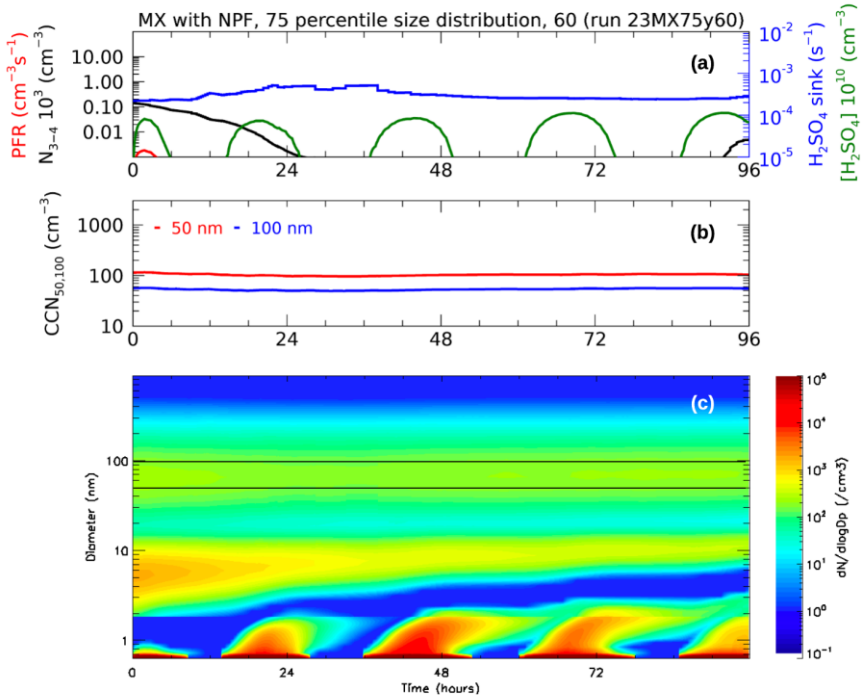

Figure C26. Run 23 – mixing layer – with NPF – 75 percentile – 60 SO_2

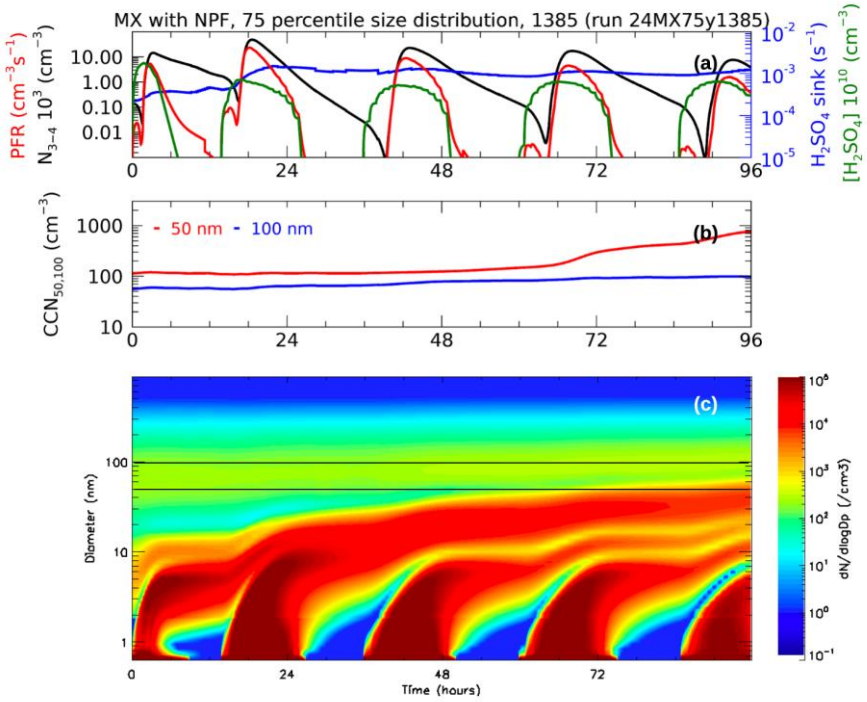

Figure C27. Run 24 –mixing layer – with NPF – 75 percentile – 1385 SO_2

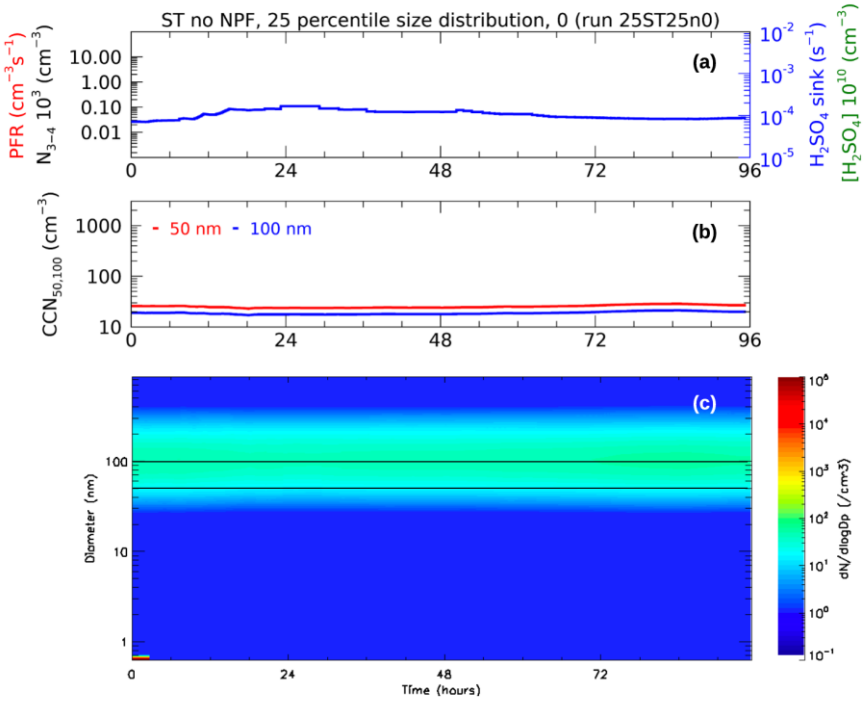

Figure C28. Run 25 – stratosphere – no NPF – 25 percentile – 0 SO_2

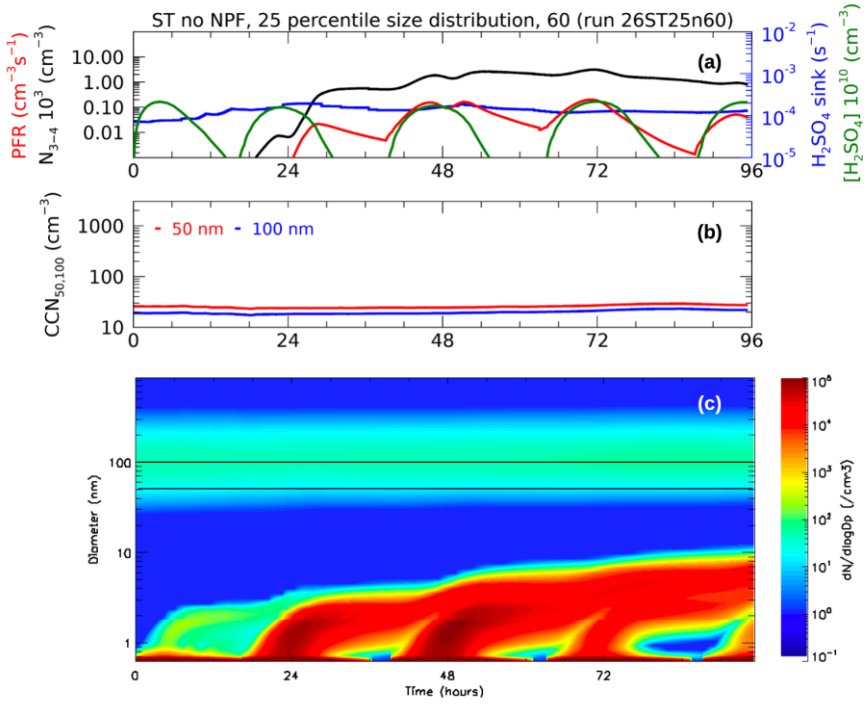

Figure C29. Run 26 – stratosphere – no NPF – 25 percentile – 60 SO_2

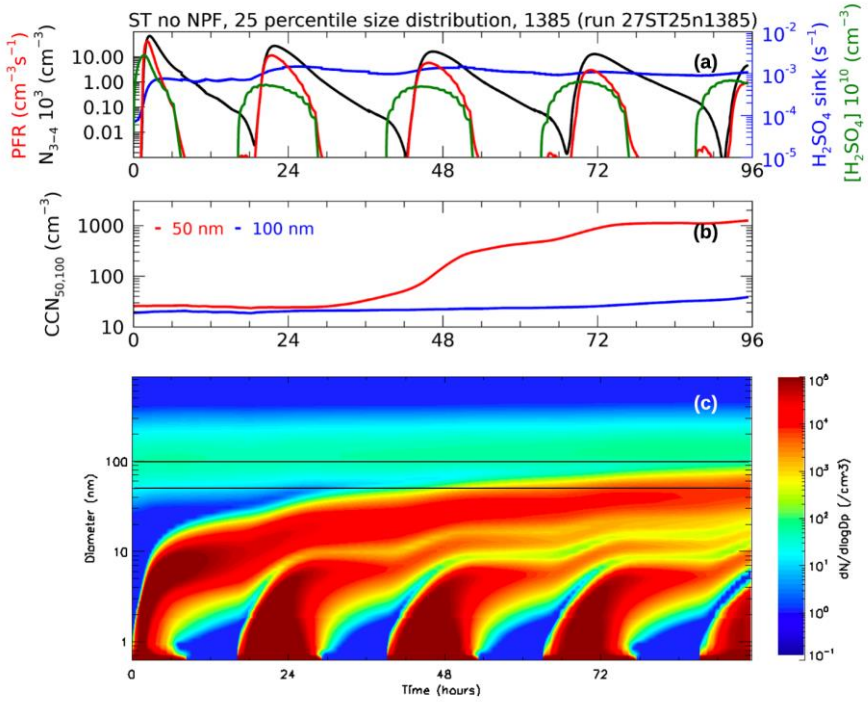

Figure C30. Run 27 – stratosphere – no NPF – 25 percentile – 1385 SO_2

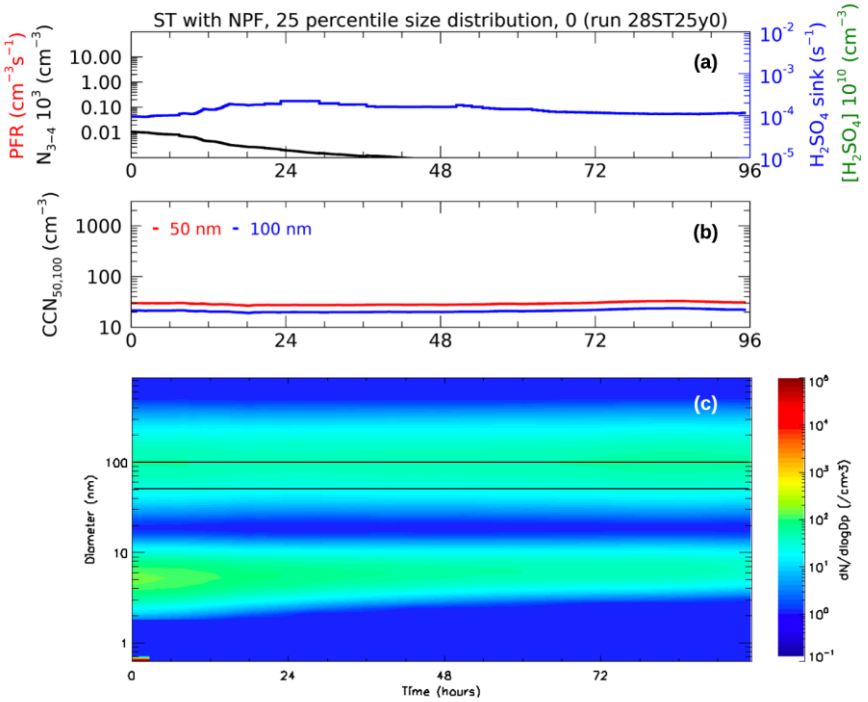

Figure C31. Run 28 – stratosphere – with NPF – 25 percentile – 0 SO_2

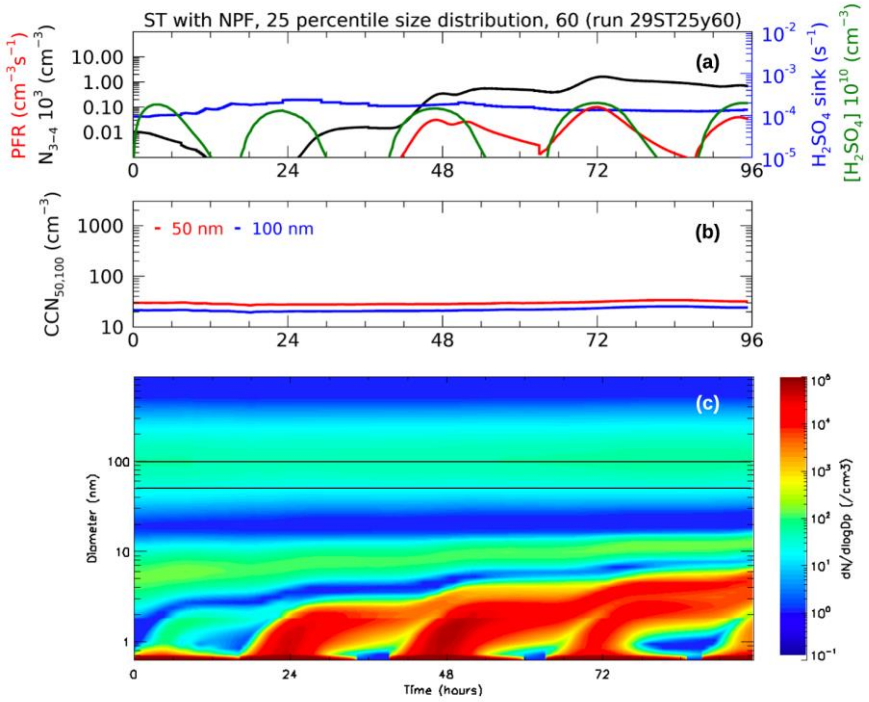

Figure C32. Run 29 – stratosphere – with NPF – 25 percentile – 60 SO2

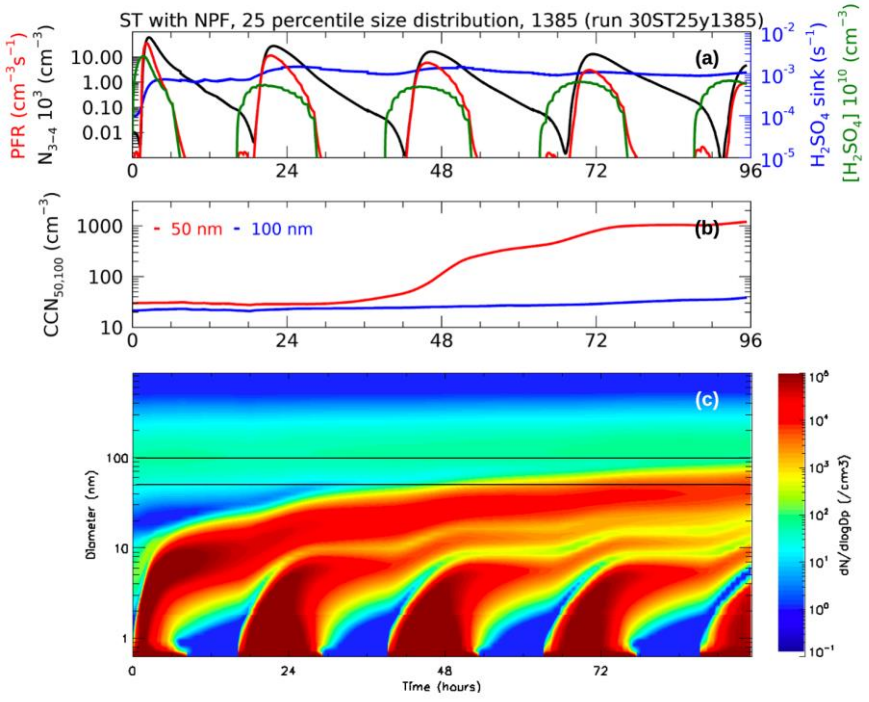

Figure C33. Run 30 – stratosphere – with NPF – 25 percentile – 1385 SO_2

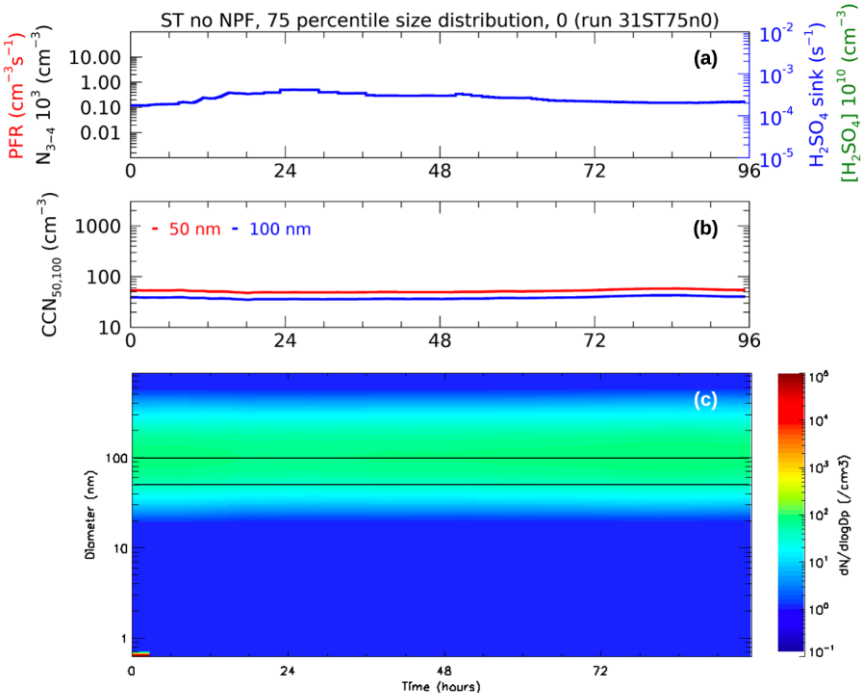

Figure C34. Run 31 – stratosphere – no NPF – 75 percentile – 0 SO_2

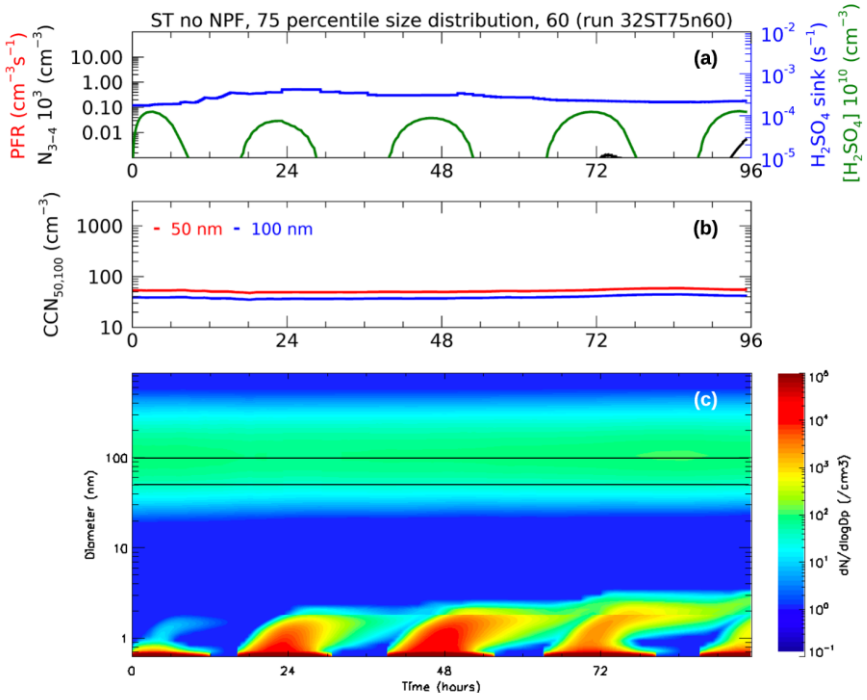

Figure C35. Run 32 – stratosphere – no NPF – 75 percentile – 60 SO_2

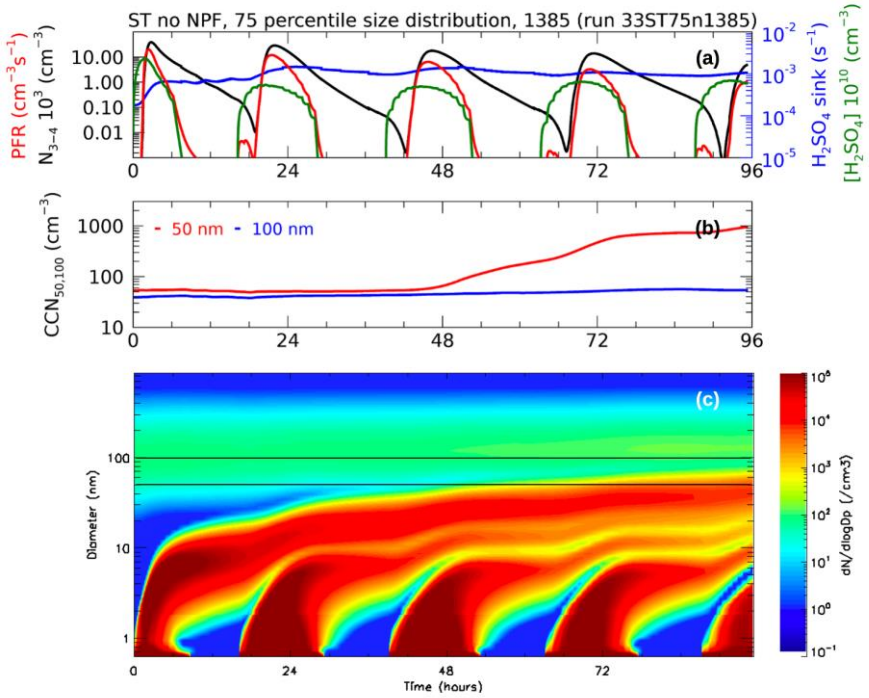

Figure C36. Run 33 – stratosphere – no NPF – 75 percentile – 1385 SO_2

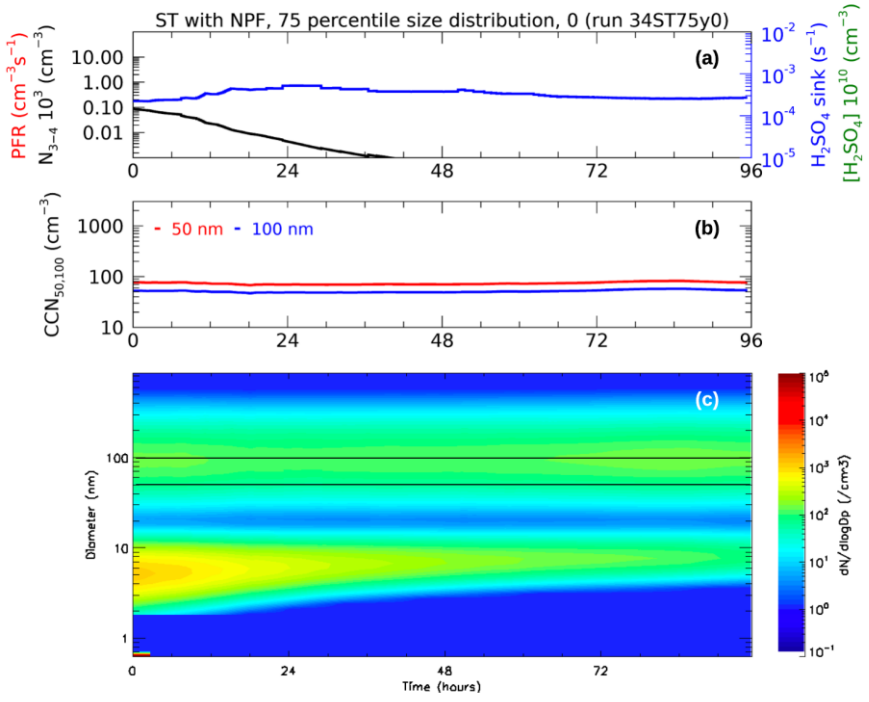

Figure C37. Run 34 – stratosphere – with NPF – 75 percentile – 0 SO_2

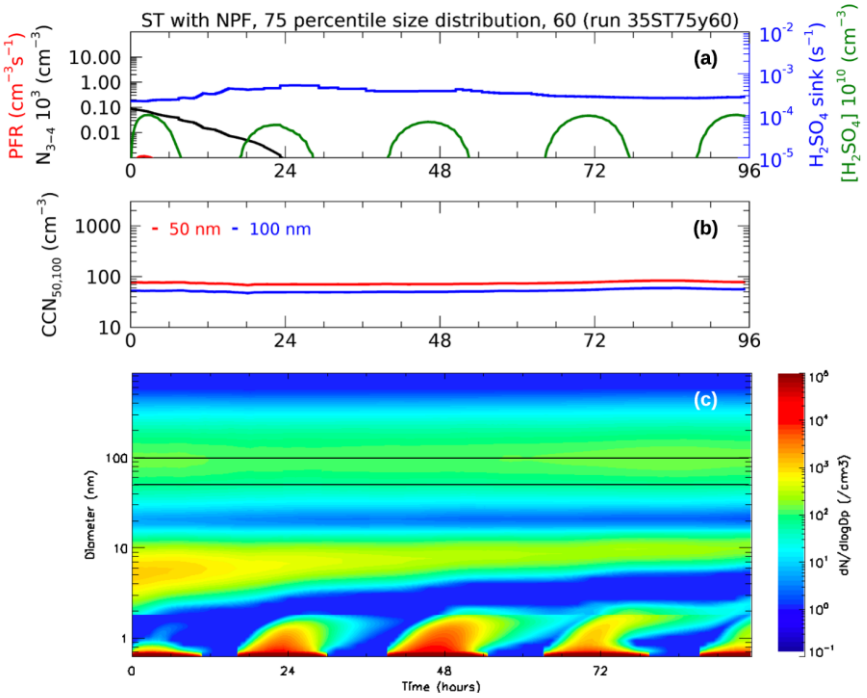

Figure C38. Run 35 –stratosphere – with NPF – 75 percentile – 60 SO_2

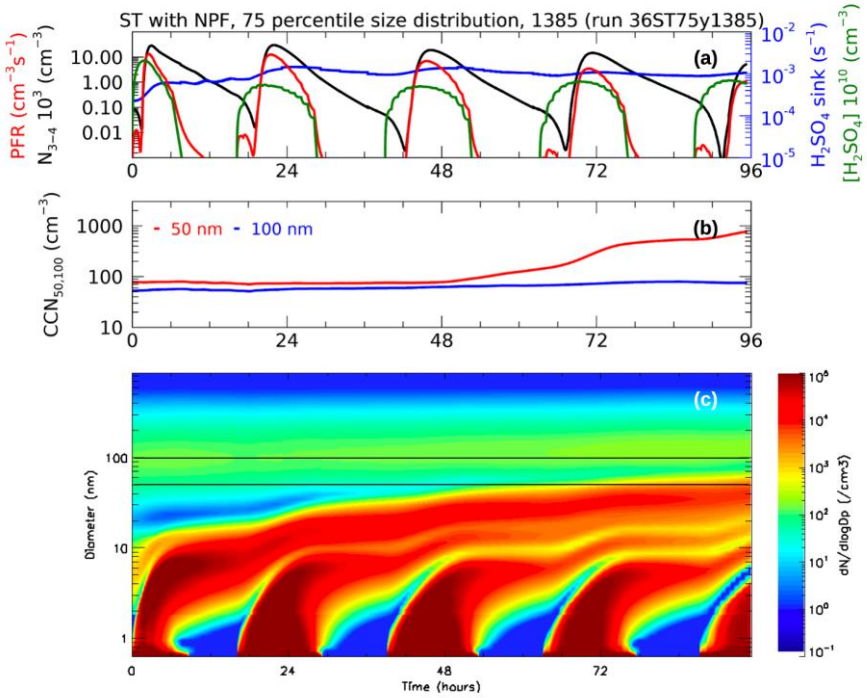

Figure C39. Run 36 – stratosphere – with NPF – 75 percentile – 1385 SO_2